Fonctionnalisation du phosphore blanc pour la synthèse de nanoparticules de phosphures métalliques et d'organophosphines

Koyel Bhattacharyya

Université Fédérale
Toulouse Midi-Pyrénées

THÈSE

En vue de l'obtention du

DOCTORAT DE L'UNIVERSITÉ DE TOULOUSE

Délivré par :

Université Toulouse 3 Paul Sabatier (UT3 Paul Sabatier)

Présentée et soutenue par :
Koyel Bhattacharyya

le 2 février 2017

Titre :

The Functionalization of White Phosphorus towards Metal Phosphide Nanoparticles and Organophosphines

---

École doctorale et discipline ou spécialité :

ED SDM : Chimie organométallique de coordination - CO 043

Unité de recherche :

Laboratoire Hétérochimie Fondamentale et Appliquée

Directeur/trice(s) de Thèse :

Dr. Nicolas Mézailles

Jury :

Dr. Chloé Thieuleux, Rapporteur
Dr. François Ribot, Rapporteur
Dr. Anne-Marie Caminade, Président

Table of Contents

List of Abbreviations

Co: Cobalt
DFT : Density functional theory
DOSY: Diffusion ordered spectroscopy
Fe: Iron
HOMO: Highest occupied molecular orbital
LUMO: Lowest unoccupied molecular orbital
MO: Molecular orbital
Ni: Nickel
NMR: Nuclear magnetic resonance
NPs : Nanoparticles
P_4: White phosphorus
THF: Tetrahydrofuran
TMS: Trimethylsilyl
TOP: Trioctylphosphine
WAXS: Wide-angle X-ray scattering
XRD : X-ray diffraction

Acknowledgments

There is a commonly used proverb in English that comes from the Igbo and Yoruba cultures of Nigeria. It goes: “It takes a village to raise a child.” It’s certainly taken a metaphorical village to get me to where I am today.

To that end, I must first and foremost thank my parents, who have always supported me and my scientific efforts, and have made my path in life easier (and tastier).

I would like to thank Professor Nicolas Mézailles for the opportunity to work on a very interesting set of chemical problems, and for inducting me into the world of nanoparticle chemistry. I would like to thank everyone in LHFA for their support or companionship, but in particular, the SHEN team. Noël and Marie asked many difficult questions during group meeting that helped reshape my way of thinking critically about my work. My colleagues, Alexia, Sébastien, Anthony le Grand, Florian, Anthony l’Autre, Pilar, Maria, and Julian, and my former colleagues, Anne-Frédérique, Samuel, Qian, and Mathieu, provided me not only with scientific support but also social support outside of the lab. They helped integrate this American into Toulousain life through conversations ranging from mechanistic discussions to impressions of famous French stand-up comedians. They made what might have been a lonely three years in France a very enjoyable sojourn in this country. I must especially thank my bay mate, Sébastien, for all of his help, including numerous vital discussions on nanoparticles, about which I knew nothing at all when I arrived.

I would like to thank the administrative and technical staff for all of their help in making sure that both the bureaucratic and scientific sides of the lab ran smoothly. I would like to gratefully acknowledge Christian for taking all of the TEM images, M. Bijani for taking DOSY NMR spectra and for taking the time to explain to me how DOSY works, and M. Lecante for his WAXS analyses and patient responses to my endless stream of confused e-mails.

Finally, I would like to thank my friends outside of the lab for trying to keep me sane; whether or not they succeeded is up for debate. In particular, I would like to thank my cats for being fuzzy. Finally, I must thank Brett for his numerous transatlantic flights to come see me, and for his constant, gentle support of my every endeavor.

“We are all in the gutter, but some of us are looking at the stars.”

Oscar Wilde

General Introduction

White phosphorus (P_4) is the most reactive allotrope of elemental phosphorus. Produced on a scale of nearly one million tonnes annually, it is used for various industrial processes, including the formation of phosphine, hypophosphite, and trichlorophosphine. P_4 is also valuable in the laboratory because of its high reactivity. However, the high reactivity of P_4 is a double-edged sword. It permits the use of mild reaction conditions to effect important transformations, but it renders P_4 very difficult to control. The goal of these doctoral studies, performed at the Laboratoire Hétérochimie Fondamentale et Appliquée (CNRS, Université Paul Sabatier, Toulouse), was to use this powerful reagent in a controlled fashion in order to access high-value products. This goal was approached from two directions: one using nanoparticles, and the other using a main-group hydride reducing agent.

The field of nanoparticle chemistry has exploded since the 1980s. Both metal(0) and metal phosphide nanoparticles have been growing in practical importance ever since. Here, we present a versatile method for the synthesis of metal(0) nanoparticles of nickel, iron, and cobalt, using a metal(II) diamide precursor. We examined the mechanism of the conversion of these molecular complexes to nanoparticles, particularly in the case of nickel, in order to understand the influence of each reaction component on the size, shape, and surface characteristics of particles. We used organometallic tools that are typically overlooked by nanomaterials scientists to examine the molecular precursors in detail. Preliminary investigations into the catalytic activity of these particles were performed, which showed the particles to be of practical interest.

The addition of white phosphorus to these metal(0) nanoparticles resulted in the formation of the corresponding metal phosphide nanoparticles. The mechanism of phosphorus incorporation into Ni(0) nanoparticles was examined, and the groundwork was laid for further investigations into the formation of iron and cobalt phosphide nanoparticles.

The molecular functionalization of white phosphorus currently typically relies on the use of bulky nucleophiles to prevent phosphorus oligomerization. This renders the resulting phosphorus compounds difficult to use in downstream applications. We were interested in converting white phosphorus to a product that could be turned into

various organophosphine compounds. In particular, we were interested in the formation of versatile P–H bonds. To our surprise, we found almost no reports of the use of hydride reagents to reduce white phosphorus, and the few available reports used expensive transition metal complexes to result in very modest yields of PH_3. We used a main-group element reagent, superhydride ($LiBEt_3H$), to form a borane-stabilized lithium phosphanide species. This species was shown to react with various electrophiles, such as trimethylsilylchloride or aroyl chlorides, to form the corresponding phosphine species. This stable source of PH_2^- was thus found to serve as a safe intermediate between white phosphorus and organophosphines.

Chapter I: Bibliographic Introduction on the Synthesis and Applications of Nickel(0) Nanoparticles

1. Historical overview of nanoparticles

Nanoparticles are generally defined as particles between 1 – 100 nm in diameter.[1] Within this size range, particles exhibit novel properties that differentiate them from their corresponding bulk materials. Although their appearances in the scientific literature have increased almost exponentially over the past two decades (Figure I-1), nanoparticles are not a human invention. They are also produced naturally, and have been used by humans for thousands of years.[2]

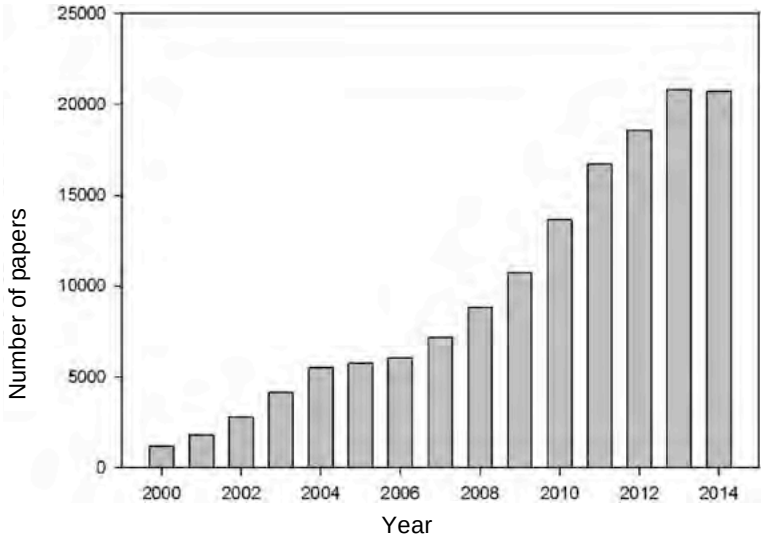

Figure I-1. The number of nanoscience papers indexed in Scopus between 2000 and 2014 with the keyword "Nanoparticles."[1]

The small sizes of nanoparticles result in unusual chemical, electrical, optical, and magnetic properties. The size-dependent properties of some nanoparticles have been well explored, beginning with the use of metal nanoparticles to color glass during the Bronze Age.[3, 4] The properties of colloidal gold were closely examined by Faraday in the mid-19th century.[5] Faraday synthesized the first pure sample of colloidal gold, and he concluded that the color came from the small size of the gold particles. To this day, modern research into the visible effects of the sizes of nanoparticles is deeply rooted in ancient tradition.

2. Modern nanoparticle research: Factors affecting nanoparticle properties

Figure I-1 shows the growth of synthetic nanoparticle research since the turn of the 21st century. Since the 1980s, the concept of quantum confinement, or the shift in the absorption and fluorescence bands caused by changing particle size, has been explored as a reason for the size-dependent electronic properties of nanoparticles.[6] Brus pioneered the idea that as a semiconducting material shrinks to the order of the material's exciton Bohr radius, or the distance between an electron-hole pair, its energy levels become discrete due to quantum confinement. The size of the particle thus affects its band gap. In 1985, Henglein used differently sized particles of Cd_3P_2 to demonstrate this principle.[7] A decade later, Bawendi expanded on this concept by creating a rainbow of fluorescence using (CdSe)ZnS nanoparticles.[8] Bawendi examined semiconductor nanoparticles, or quantum dots, whose electronic properties differ from both bulk materials and individual atoms or molecules (Figure I-2). The band gap determines the fluorescence emission energy of quantum dots, and the changing band gaps for differently sized particles results in the rainbow observed in Figure I-2 for monodisperse particles of sizes ranging from 2 nm (blue) to 8 nm (red).

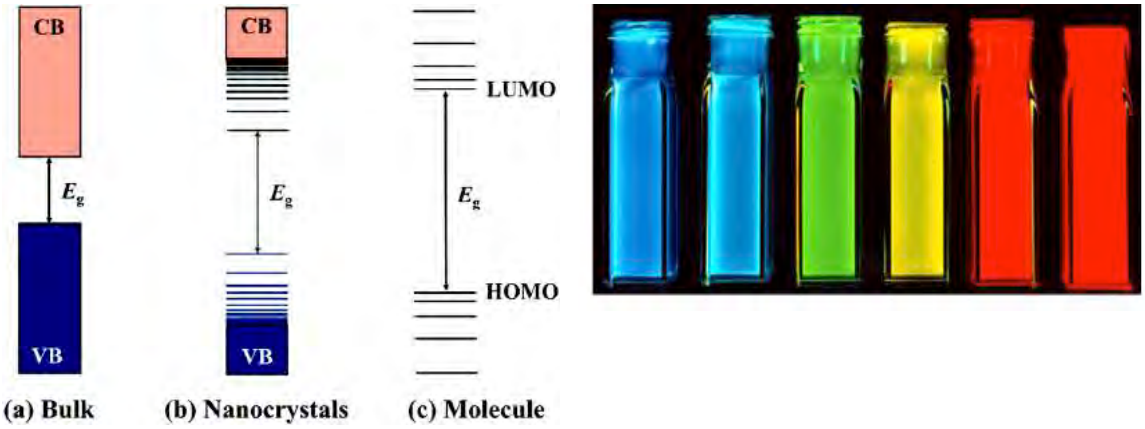

Figure I-2. Left: Comparison of electronic energy states of bulk, nanocrystalline, and molecular semiconductors (CB = conduction band; VB = valence band; E_g = band gap energy).[9] Right: Fluorescence of nanocrystalline samples of (CdSe)ZnS, with particle sizes ranging from 2 nm (left) to 8 nm (right).[7]

A greater understanding of size- and structure-dependent properties of nanoparticles has developed over the past decades.[10] Alivisatos noted variations in phase transition temperatures and electrical conductivity based on the size of

semiconductor nanoparticles. Size changes on the very smallest scale, from clusters of three to 50 atoms, result in unique bonding geometries that lead to changes in electronic structure.[11]

Internal structure also affects the properties of the nanoparticles, which changes with crystallinity of the particles. Silver nanoparticles have been found to enhance the efficiency of dye-sensitized solar cells differently based on their crystallinity, while the crystallinity of anatase (TiO_2) affects its ability to photodegrade phenol.[12]

Capping by organic ligands also affects surface-state passivation, nanocrystal solubility, and stability.[9] The arrangement of surface atoms and their saturation also affect their chemical reactivity. For example, CdSe particles capped by trioctylphosphine oxide (TOPO), which binds to the Cd sites, permits the nanoparticles to be dissolved in nonpolar solvents. TOPO and other stabilizing ligands also encourage the formation of more monodisperse particles.

Inorganic capping, meanwhile, may affect the electronic properties of the particles. The previously described CdSe nanoparticles with ZnS shells demonstrate this effect. The use of ZnS, which has a wider band gap than CdSe, leads to an enhancement of photoluminescence quantum yields.[13]

Thus, various factors affect the properties of nanoparticles, including size, crystallinity, and surface ligands. These different properties may be exploited by a variety of applications, as different types of nanoparticles are better suited for different uses.

By and large, however, nanoparticles are “black boxes,” with few aspects of the chemistry behind their synthesis having been well explored. We hoped to use what is already understood about the mechanism of synthesis of nanoparticles in general to more intelligently design the synthesis of new particles.

3. Mechanism of nanoparticle formation

The basic theory of chemical nanoparticle formation from the chemical reduction of a salt was described in 1950 by LaMer, who suggested that nanoparticle formation is comprised of two stages: a nucleation stage and a crystal growth stage (Figure I-3).[9,14] According to his model, reaction precursors dispersed in a medium first generate monomers. When the concentration of monomers in the mixture reaches

a level of super-saturation, nuclei form through the aggregation of monomers. Monomer aggregation continues on these pre-existing nuclei until the monomer concentration drops to below a critical level. The formation of new nuclei during the growth stage results in widening size distribution. Thus, separating the nucleation and growth stages is essential to a narrow size distribution.

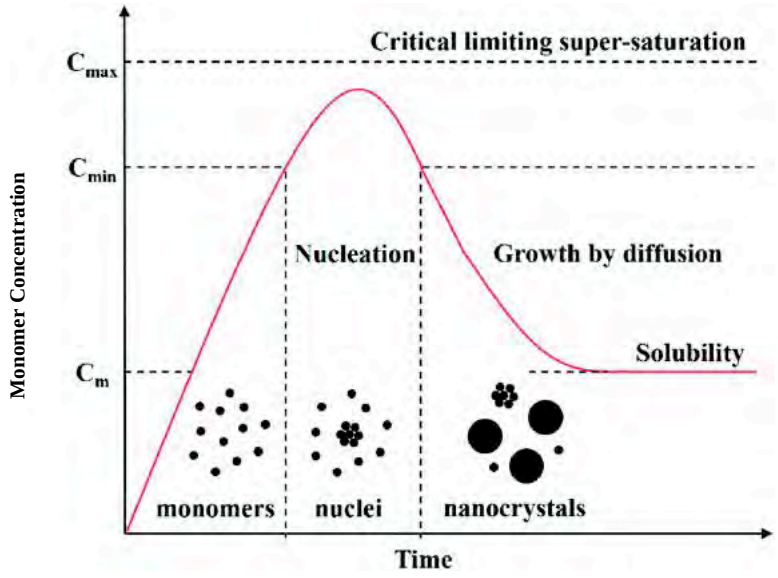

Figure I-3. LaMer model of nanoparticle growth.[9]

After formation of preliminary particles, the surface energy of the particles determines whether or not they continue to grow. A surface energy that is much higher than the entropy loss of a decreasing number of particles will lead to Ostwald ripening or coalescence, both of which may lead to the broadening of size distribution (Figure I-4).[15]

In the process of Ostwald ripening, smaller particles dissolve and redeposit onto larger particles. This process occurs because larger particles are more energetically favorable than smaller ones. Since surface atoms are much less energetically stable than those in the interior, smaller particles with a higher surface area-to-volume ratio also are higher in energy. The small, higher-energy particles can be digested in favor of addition to already-large particles. Particles that grow by Ostwald ripening have a single crystalline domain.

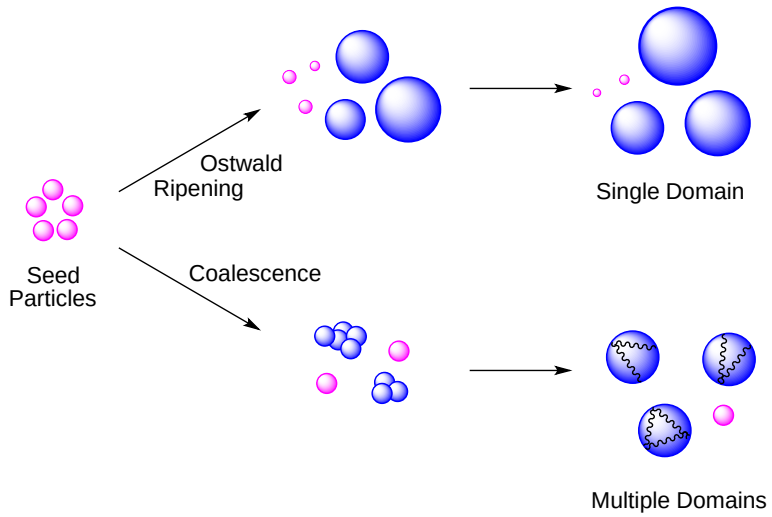

Figure I-4. Post-nucleation growth of particles.

Growth by coalescence, meanwhile, results when multiple particles aggregate into larger ones. In such cases, multiple crystalline domains are seen in the resulting particles. Orientated attachment is similar to coalescence, but requires an alignment of the crystalline faces for attachment to occur.

Because post-nucleation growth is highly dependent upon the surface energy of the particles, surface ligands are of great importance. They greatly affect the energetic stability of the surface atoms, and thus either inhibit ripening processes, or else guide them to a thermodynamically favorable size. For example, polydisperse gold colloids that are refluxed in the presence of excess thiol, amine, phosphine, or silane ligands have been observed to evolve into nearly monodisperse systems.[16]

4. Nanoparticle synthetic methods

Methods of nanoparticle synthesis can be fundamentally classified into two approaches.[17] In the bottom-up approach, nanomaterials are constructed from the basic building blocks of atoms or molecules. The top-down approach, meanwhile, requires the restructuring of a bulk material in order to form a nanomaterial, and is particularly ill suited for the formation of small nanoparticles. The bottom-up approach permits greater control over the exact properties of the final particles, and is better suited for the generation of uniform particles of a desired shape, size, and structure. Here, we will focus on bottom-up approaches to nanoparticle synthesis.

A variety of physical (mechanical) and chemical methods may be employed. Physical methods, which often result in large, polydisperse particles, include the mechanical crushing or pulverization of bulk metal, arc discharge between metal electrodes, vapor condensation, or spray pyrolysis. Such methods do not follow the growth theory posited by LaMer, shown in Figure I-3. Chemical methods, on which we have focused, involve the reduction of metal ions or the decomposition of precursors, followed by the aggregation of the reduced atoms. Although there are many methods of wet chemical nanoparticle formation, they typically involve either a metal(0) complex that decomposes to nanoparticles upon application of external energy, or oxidized metal salts that are reduced using reagents such as hydrogen or a chemical hydride. External energy may come in the form of light, electricity, heat, or sound.

Such methods tend to result in more narrow size distributions than physical methods. The size dependence of many properties of nanoparticles makes the synthesis of monodisperse particles, with a size distribution of less than ± 5 % standard deviation, of key importance.[18] Common wet chemical methods designed to make monodisperse nanoparticles include seed-mediated growth, homogeneous nucleation, and the addition of stabilizing ligands.

Seed-mediated growth permits the separation of the nucleation and growth processes; the importance of separating these processes has been described above. One method of seed-mediated growth separates the two steps manually. In a first step, metal salts are reduced quickly to produce small seeds, or nuclei, in the presence of a stabilizing agent. Particle growth is then induced by the repeated addition of small amounts of precursor and a weaker reducing agent. This method typically results in very long reaction times, as the second reducing agent must be weak enough to avoid the formation of new seeds.

A second method follows the same principle in a distinct, two-step fashion. Pre-formed nuclei are introduced into a reaction mixture, in addition to the monomers that will precipitate onto the surface of these nuclei. This method requires the introduction of monodisperse seeds in order to produce larger monodisperse particles. It also requires a dilute reaction mixture in order to avoid homogeneous nucleation.

Homogeneous nucleation may also be used to synthesize monodisperse nanoparticles. Two different procedures have been developed for homogeneous nucleation. One method, developed by Bawendi,[8] is known as hot-injection. The rapid

injection of excess precursor into a hot surfactant solution results in monomer supersaturation and consequent burst nucleation. This immediate burst nucleation causes the monomer concentration in solution to drop sharply, halting nucleation. One limitation of hot-injection synthesis is scalability. The method depends upon the instantaneous addition of precursor. Large volumes of precursor become inherently more difficult to add instantaneously, and the time lag of the addition can result in polydispersity.[19] Quick addition of large volumes into a very hot solution may also be difficult and hazardous.

A simpler method of homogeneous nucleation is known as the heat-up method.[20] In this procedure, all the reaction components are mixed before the entire solution is heated in order to incur decomposition. Size control using this method often relies on stopping the reaction before all of the monomer has been consumed, in order to avoid any ripening or coalescence mechanisms that would result in size divergence. This, of course, results in a loss of yield of conversion from precursor to nanoparticle.

Another method of achieving monodispersity is to introduce stabilizing ligands. Stabilizing agents, such as phosphines or thiols, affect the surface energy of the particles as described in section 4, and thus permit a more narrow size distribution. Indeed, there are various methods of controlling the sizes and size distributions of nanoparticles using ligands. In addition to the thermodynamic size control induced by surface ligands, strongly adsorbed stabilizers on the nanoparticle surface can limit the local quantity of reactants and thus inhibit further growth. Varying the stoichiometry of the ligands to the particles often permits size control. The use of thiol ligands on Au nanoparticles, for example, allows controlled size variation from one to four nm. However, the use of such ligands to control the size of the particle may have drawbacks in downstream applications. For example, such ligands might block catalytically active sites, making the particles less desirable, despite their monodispersity.

A big problem in nanoparticle synthesis is reproducibility. Very small criteria that would not typically matter in molecular synthesis, such as the speed of stirring, could result in vast differences in product.[21] The source of the reagents can also make a big difference in the size and shape of nanoparticles,[22] and small differences in solution aging, on the order of minutes, have been seen to have poorly understood effects.[23] A serious challenge remaining to us is the development of robust methods

that can withstand such seemingly negligible parameters. Further examination of the mechanisms outlined in section 3 may permit us to develop such robust methods. This grows increasingly necessary as the applications of nanoparticles grow more varied and integrate themselves into various aspects of modern technology and science.

5. Applications of nanoparticles

As nanoparticles become increasingly well understood, they become more commonly used.[2] TiO_2 nanoparticles, for example, aid in the quest for viable alternative fuel sources. They may be used for dye-sensitized solar cells, which have increased the price/performance ratio of solar cells to be competitive with fossil fuel electrical generation.[24]

Nanoparticles may serve as heterogeneous catalysts.[25] Catalysts are vital to the chemical manufacturing process, as well as to the processing of hazardous waste. The use of heterogeneous catalysts permits their easy separation after the reaction is complete, and often permits the use of harsher conditions without catalyst death. Nanoparticles in particular have demonstrated enhanced reactivity and selectivity, in part due to their high surface-to-volume ratio, which renders them more active. In addition to the advantages imbued by small particle size, nanoparticle catalytic activity is also determined by their composition, geometry, oxidation state, and environment. Different crystal facets may have improved adsorption or corrosion resistance. Rough surfaces and edge boundaries, which contain undercoordinated atoms, are particularly active in catalysis.

Nanoparticles catalyze a wide range of reactions. Rh nanoparticles are used for the hydrogenolysis of aromatic C–Cl bonds, and for the consequent hydrogenation of aromatic rings.[26] Pt nanoparticles have been used for decades to catalyze hydrosilylation.[27] However, both Rh and Pt are very high-cost metals, and much interest has focused on the use of lower-cost metals, such as Ni, Fe, and Co, for catalysis.

Ni_2P and several other transition metal phosphides are widely used for hydrodesulfurization (HDS) and hydrodenitrogenation (HDN) of petroleum feedstocks,[28] which are key processes needed to ensure clean fuel use for transportation. Organosulfur compounds may poison the catalysts that process these feedstocks. They can also be oxidized to SO_2 during the combustion process.

Similarly, organonitrogen compounds produce NO_x pollutants during combustion. These nanoparticle-catalyzed processes are thus vital to the petroleum industry.

Co nanoparticles of 8 nm are used to catalyze the formation of carbon nanotubes from acetylene.[29] Co particles of 3 – 10 nm may be used to catalyze the Fischer-Tropsch reaction, which converts syngas (a mixture of CO and H_2) into liquid fuel.[30] This same metal, in the form of large nanoparticles of 90 – 95 nm, catalyzes the aerobic oxidation of alcohols.[31] Fe(0), one of the most widely available elements on earth, is commonly used as a hydrogenation catalyst. Nanoparticles of 2 nm selectively hydrogenate unsaturated C–C and C=X bonds (Figure I-5).[32] Sixty-nm aggregates of smaller 3-nm Fe(0) nanoparticles catalyze the swift dehydrogenation of ammonia borane. In addition, the particles are magnetic, which leads to their easy separation from the reaction medium at the end of the catalysis.[33]

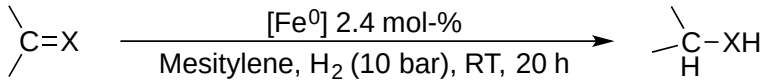

Figure I-5. Fe-catalyzed hydrogenation of C=X bonds.[25]

Nanoparticles are also becoming increasingly important as electrochemical catalysts. Oxide-derived, nanocrystalline Cu nanoparticles of 30 – 100 nm catalyze the electroreduction of CO_2 into multicarbon oxygenates at moderate overpotentials, particularly along grain boundaries.[34] Many metal phosphide nanoparticles, such as Ni_2P, CoP, and Fe_2P, are highly active hydrogen evolution catalysts, producing H_2 from water.[35] Co nanoparticles of 10 nm are also capable of catalyzing the oxygen evolution reaction at low overpotentials, oxidizing water to oxygen.[36] Together, hydrogen and oxygen evolution from water form a water-splitting electrochemical cell that can be used to generate electrical energy.

Of the many interesting properties that nanoparticles possess, magnetism is especially important for many practical applications. Nickel, iron, and cobalt are commonly used to make magnetic nanoparticles. As mentioned above, they may be useful in catalysis because of the ease of separation from a reaction mixture. Fe_3O_4 nanoparticles have been explored for biomedical purposes, as they can bind to various organic matter *in vivo*.[37] They can also be directed to a specific site using external magnetic fields, and can be heated using alternating magnetic fields for hyperthermia treatments. *In vivo* imaging using magnetic particles, which has been explored for

Fe_3O_4 nanoparticles of 4 nm, can be performed with a signal-to-noise ratio that is two orders of magnitude greater than that achieved using standard magnetic resonance imaging (MRI). Magnetic FeCo (15 nm) and FePt (3 – 10 nm) nanocrystal superlattices are of growing interest due to their potential implementation into nano- or microelectronic devices, particularly for magnetic information storage.[38]

With the introduction of more applications for nanoparticles has come an increasing understanding of their properties. Conversely, the more research that is performed on the mechanism of formation and growth of nanoparticles, the better we can tailor their formation to our needs.

One very versatile type of nanoparticles are those of nickel(0). The high availability and relatively low toxicity of Ni(0),[39] combined with its chemical versatility, make it a valuable metal.

6. Specific applications of nickel(0) nanoparticles

The bulk of the investigations into nanoparticle synthesis and mechanism in the present work were performed on nickel(0). Ni is a relatively inexpensive metal, and thus, using it as a substitute to more expensive metals like Pt is of great interest. Ni nanoparticles are valued for a variety of applications, ranging from catalysis[40] and magnetic properties[41] to the development of more complex nanomaterials.[42]

Ni(0) nanoparticles of 3.5 nm in size have been shown to catalyze the hydrosilylation of alkenes,[43] while particles of < 2 nm perform the transfer hydrogenation of carbonyl compounds (Figure I-6).[44]

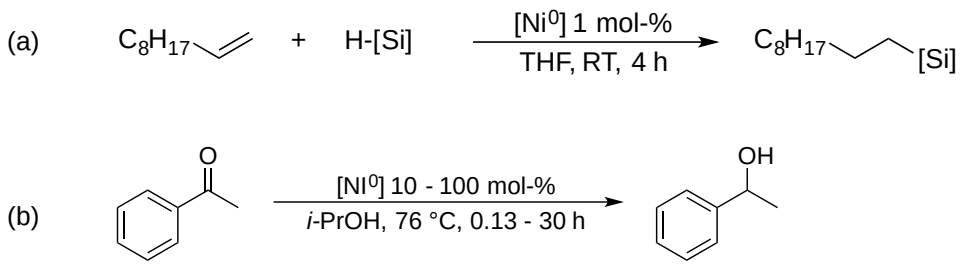

Figure I-6. (a) Hydrosilylation of alkenes, and (b) reduction of ketones by nickel(0) nanoparticles.[18,19]

Ni(0) nanoparticles have also been shown to reduce phenylacetylene exclusively to ethylbenzene under hydrogen, while the use of Ni_2P nanoparticles to

catalyze the reduction of phenylacetylene produces predominantly styrene.[45] This attenuation of the hydrogenation activity of Ni_2P may be attributed to the electron-withdrawing effect of phosphorus on nickel.

Water- and air-stable Ni nanoparticles of under 10 nm have also demonstrated high catalytic activity for hydrogen generation from ammonia borane.[40a] Ni nanoparticles of 15 – 18 nm are able to catalyze the formation of thioethers from the condensation of thiols and alcohols at a catalyst loading of 10 %.[40b]

Monodisperse, size-tunable, air-stable, magnetic Ni nanoparticles have been synthesized.[41a] The uses of magnetic nanoparticles have been outlined in Section 3. Size control was achieved by adjusting the reaction time or by changing the ratio of Ni precursor to organic ligand. The magnetic saturation of the particles increased significantly with increasing particle size, approaching the magnetization of bulk Ni. Further, moving from spherical Ni nanoparticles to nanocubes resulted in an up to ten-fold enhancement in magnetic saturation for particles of 11 – 13 nm.[41b] Moreover, the phase of the particles could be transformed from face-centered cubic (fcc) to hexagonal close-packed (hcp) by augmenting the temperature of the reaction. The importance of changing phase structure lies in the different properties of each phase, due in part to the difference in surface energy, as well as to differences in magnetic saturation.[41c] The hcp phase is metastable, and thus has been less completely studied than the more stable fcc phase. The magnetism of hcp particles has been shown to be different from that of the fcc Ni nanoparticles, though its magnetic saturation is lower than for fcc Ni.

The use of Ni nanoparticles to form more complex nanoparticles has been well examined. In examining the different reactivity of Ni nanoparticles on and without carbon support, carbon with crystal defects on the surface of the carbon support was found to migrate into the Ni nanoparticles.[42a] Supports are known to influence heat and mass transfer by metal-support interactions, but had not been known to affect the active metal surface. Surface carbon was found to dissolve into the Ni lattice, resulting in its expansion and forming nickel carbide at the surface of the nanoparticles. This results in a modification not only of the lattice size, but also of the electronic properties of the metal, influencing the catalytic activity of the particles.

Ni nanoparticles form myriad shapes and structures. Magnetic, urchin-like Ni nanoparticles have been observed to form self-assembled magnetic chains simply by heating.[42b] The formation of monodisperse vertically aligned nanofibers was

accomplished by synthesizing Ni nanoparticles with a monolayer of trioctylphosphine ligands.[42c] The trioctylphosphine was observed to decompose at the Ni surface and form a graphitic shell. Ni(0) nanoparticles heated in the presence of white phosphorus in a ratio of 1:3 phosphorus:nickel were found to form core-shell structures, with Ni_2P at the core and shells of Ni(0).[42d] Meanwhile, simple Ni_2P nanoparticles may be formed from Ni(0) and stoichiometric white phosphorus. A thick, self-generated carbon coating may then be obtained through a soft calcination step, using the nanoparticle ligands as a carbon source. These particles exhibit partially reversible insertion of Li in the nanoparticle lattice, which is a first step for the synthesis of nanoscale lithium batteries.[42e]

The extensive applications of Ni nanoparticles have spurred numerous methods of synthesis. Each application requires different sizes, shapes/phases, or surface ligands. Having a variety of synthetic methods permits the formation of particles tailored to each use.

7. Nickel(0) nanoparticles: Synthesis

The number of methods for the synthesis of metallic Ni nanoparticles is nearly as large as for all metal nanoparticles. One method of nanoparticle preparation employs the polyol method.[46] Ni nanoparticles of 13 – 25 nm in the hcp phase may be obtained by reduction of $Ni(NO_3)_2$ by polyethylene glycol (PEG) of molecular weights varying from 200 – 600 g/mol, using oleic acid and oleylamine as ligands to provide stabilization and solubility. The varying molecular weights permit heating to different temperatures, as they have different boiling points. PEG is also inexpensive and environmentally benign. Size control using the polyol method is obtained by controlling the various rate-determining steps of the reaction. Tuning the rate of reduction and the introduction of seed-induced heterogeneous nucleation permit control over the size of the resulting Ni nanoparticles.

A second method uses the electrochemical reduction.[47] A hydrogen coevolution method has been developed in which $Ni(NO_3)_2$ hydrate is placed in an electrochemical cell. Monodisperse Ni(0) particles of 20 – 600 nm are then precipitated onto a solid surface with the coevolution of hydrogen.

Another technique is known as the rapid expansion of supercritical fluid solutions.[48] A $NiCl_2$ solution in near-critical ethanol heated at 230 °C in a closed coil

may be expanded rapidly into a room-temperature solution of the reducing agent $NaBH_4$, resulting in nanoparticles of 6 nm.

The sol-gel technique involves the formation of the metal network through the polycondensation of a molecular precursor in a liquid.[49] Using this method, Ni particles of 6 nm may be synthesized by decomposing a $Ni(NO_3)_2$ hydrate precursor onto a potassium bromide matrix.

Microwave furnaces have also been used.[50] Using $Ni(CHO_2)_2$ as the precursor, a short, 15-minute microwave treatment at 300 °C results in the formation of Ni(0) nanoparticles of 10 nm.

Seeded growth has also been reported.[51] Pt seeds have been observed to serve as catalysts for the reduction of $NiCl_2$ by hydrazine in aqueous solution. Size control was achieved by controlling the ratio between Ni salt and platinum seeds, and was tunable within a range between 13 and 33 nm.

Organometallic Ni(0) precursors, such as bis(cyclooctadiene)nickel [$Ni(COD)_2$], may be decomposed in the presence of a ligand.[52] Small particles of under 5 nm are obtained by the decomposition of $Ni(COD)_2$ at modest temperatures under hydrogen. A disadvantage of using Ni(0) precursors, however, is their high air sensitivity.

Most simply for chemists, and most relevantly to the present work, nickel salts may be reduced by a reducing agent.[53] Various Ni(II) precursors, such as $NiCl_2$, Ni(acetylacetonate)$_2$ [$Ni(acac)_2$], or $Ni(NO_3)_2$, are reduced to Ni(0). This may be done at low temperatures using strong reducing agents, such as sodium borohydride.[54] Although this is a well-defined reaction between an electron source and an oxidized metal, the strength of the reducing agent makes nucleation swift and thus difficult to control. Alternatively, a weaker reducing agent, such as an amine or a carboxylic acid, may be used at high temperature.[55] This approach typically leads to the presence of a variety of intermediates, making the reactions harder to describe mechanistically, and blurring the distinction between nucleation and growth needed for a monodisperse particle size distribution.[56] The inherent complexity and polydispersity from this approach, however, may be regulated by the addition of ligands that permit the tailoring of nanoparticle sizes, while retaining the robustness and controllability of the slower nucleation process provided by a weak reducing agent.

Previous work in our group thoroughly examined a reaction belonging to that last class of synthetic methods.[56,57] Carenco developed a robust method for

consistently synthesizing size-tunable, monodisperse Ni nanoparticles through the reduction of $Ni(acac)_2$ by the mild reducing agent oleylamine, at high temperature and in the presence of TOP. The size of the particles was tunable between 2 – 30 nm in diameter by varying the stoichiometry of TOP and oleylamine to the amount of Ni (Figure I-7). It was found that increasing amounts of TOP in solution led to decreasing particle size due to the surface stabilization. Increasing amounts of oleylamine also led to decreased particle size. Because it served as the reducing agent, larger amounts of oleylamine led to faster nucleation, and thus to the fast production of many smaller nanoparticles.

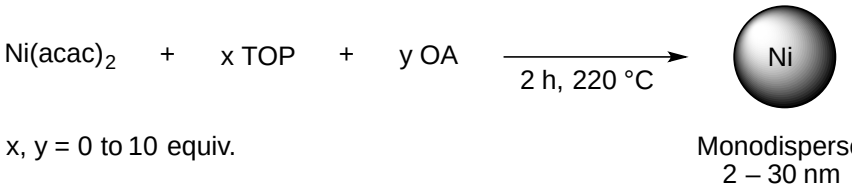

Figure I-7. Ni(0) nanoparticles from the high-temperature reduction of $Ni(acac)_2$ by oleylamine in the presence of TOP.

An associated mechanistic study revealed that water was formed by the dehydration of the acac ligands during the reaction (Scheme I-1).[57]

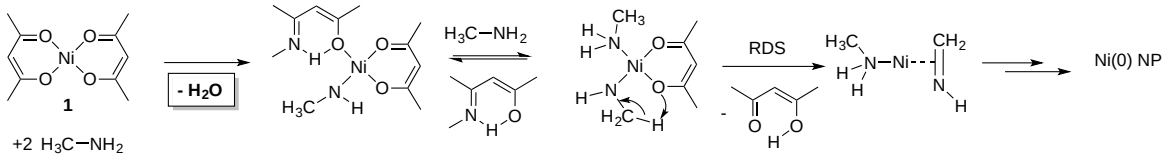

Scheme I-1. Mechanism of reduction of metal precursors to metal nanoparticles, leading to co-formation of water.

Although the presence of water does not impede the formation of Ni(0) nanoparticles, the consequent removal of water for downstream applications poses a challenge. Further, a coherent, generic synthesis of nanoparticles from other metal precursors would be prevented by the facile oxidation of other metal(0) species, such as iron, by water. Indeed, the reduction of iron(III) tris(acac) to form nanoparticles by this method results in Fe_3O_4 or other oxidized Fe species, rather than Fe(0).[58] We sought to develop a water-free method of nanoparticle synthesis that would retain the facility and robustness of Carenco's procedure while permitting us to extend the

procedure to a variety of metals, regardless of their susceptibility to oxidation by water.

The reduction of $Ni(acac)_2$ by oleylamine has been shown, through both calculations and experiments, to proceed through a Ni(II) species containing one acac ligand, one amide ligand, and one amine ligand (Scheme I-1). Most importantly, the formation of water and the reduction of Ni(II) to Ni(0) are two independent steps. Water is formed in the early stages of the reaction in a condensation reaction at the ligands, while Ni remains in the (II) oxidation state. The key reduction step involves a β-hydrogen transfer from the amide ligand to the acac ligand, resulting in the loss of one equivalent of acetylacetone (Scheme 1).

In order to retain the robustness of the reduction of $Ni(acac)_2$ while eliminating the production of water, we sought to begin directly from a $Ni(amide)_2$ species. Mechanistically, the reduction would rely on β-hydrogen transfer from one amide ligand to the other, as shown in Scheme I-1. While our work was in progress, Kovalenko, *et al.* successfully transformed a variety of most main-group metal chlorides into metal(0) nanoparticles (M = In, Ga, Bi, Sb, Zn, Cu, Sn and their alloys) by forming metal amide species *in situ*.[59] We thus chose to focus on nickel(II) bis(amide) species as the precursor, either synthesized independently or *in situ*.

8. Present work

In the following chapter, we will show that Ni(0) nanoparticles may be synthesized from Ni(II) diamide precursors in a highly reproducible and somewhat scalable fashion. The method may be extended to other metals, such as iron and cobalt. The effects of ligands of various coordinating strengths are examined, particularly the inverse relationship between the amount of the highly stabilizing trioctylphosphine (TOP) ligand and the size and polydispersity of the nanoparticles, and the direct relationship between the amount of oleylamine and the size and monodispersity of the particles. We also examine the role of a small inorganic salt, lithium bromide, on particle size and size distribution. The effects of various solvents are also explored in order to probe the role of each functional group on the reduction process and consequent nanoparticle formation.

Most interestingly, we have found a previously unreported effect of the polymerization of the starting material. In exploring the differences between nanoparticles obtained from isolated *vs. in situ*-synthesized bis(amide), we discovered that the ostensibly two-coordinate nickel complex forms more saturated nickel-amide polymers that must be degraded to monomers before the formation of nanoparticles. This, we presume, is in part the reason behind the mysterious solution aging effects described briefly in section 4. We examine the effect of this polymer on nanoparticle formation, and its role in the necessary division of nucleation and particle growth and thus on particle monodispersity. Finally, some preliminary catalysis with the Ni nanoparticles is explored in order to demonstrate the potential applications of this research.

9. References

[1] Shin, S.; Song, I.; Um, S. *Nanomaterials* **2015**, *5* (3), 1351–1365.

[2] Heiligtag, F. J.; Niederberger, M. *Mater. Today* **2013**, *16* (7–8), 262–271.

[3] Colomban, P. *J. Nano Res.* **2009**, *8*, 109–132. (b) Leonhardt, U. *Nat. Photonics* **2007**, *1* (4), 207–208.

[4] Zsigmondy, R. *Nobel Media AB 2014* **1926**.

[5] Faraday, M. *Trans. R. Soc.* **1857**, *147* (0), 145–181.

[6] Brus, L. *J. Phys. Chem.* **1986**, *90* (12), 2555–2560. (b) Brus, L. E. *J. Chem. Phys.* **1983**, *79* (1983), 5566.

[7] Weller, H.; Fojtik, A.; Henglein, A. *Chem. Phys. Lett.* **1985**, *117* (5), 485–488.

[8] Murray CB, Norris DJ, Bawendi, M. *J. Am. Chem. Soc.* **1993**, *115*, 8706–8715. (b) Dabbousi, B. O.; Rodriguez, J.; Mikulec, F. V; Heine, J. R.; Mattoussi, H.; Ober, R.; Jensen, K. F.; Bawendi, M. G. *J. Phys. Chem. B* **1997**, *101* (97), 9463–9475.

[9] Chang, J.; Waclawik, E. R. *RSC Adv.* **2014**, *4* (45), 23505–23527.

[10] (a) Röthlisberger, U.; Andreoni, W.; Parrinello, M. *Phys. Rev. Lett.* **1994**, *72* (5), 665–668. (b) Henglein, A. *Chem. Rev.* **1989**, *89* (8), 1861–1873. (c) Klabunde, K. J.; Sorensen, C. M.; Stoeva, S. I.; Prasad, B. L. V; Smetana, A. B.; Lin, X. M. *Met. Nanoclusters Catal. Mater. Sci. Issue Size Control* **2008**, *2*, 233–249.

[11] Alivisatos, A. P. *J. Phys. Chem.* **1996**, *100* (95), 13226–13239.

[12] Tanvi; Mahajan, A.; Bedi, R. K.; Kumar, S.; Saxena, V.; Aswal, D. K. *J. Appl. Phys.* **2015**, *117*, 083111-1–083111-6. (b) Wang, X.; Sø, L.; Su, R.; Wendt, S.; Hald, P.; Mamakhel, A.; Yang, C.; Huang, Y.; Iversen, B. B.; Besenbacher, F. *J. Catal.* **2014**, *310*, 100–108.

[13] Hines, M. A.; Guyot-Sionnest, P. *J. Phys. Chem.* **1996**, *100* (2), 468–471.

[14] LaMer, V.; Dinegar, R. *J. Am. Chem. Soc.* **1950**, *72* (8), 4847–4854. (b) Bönnemann, H.; Nagabhushana, K. S. *Met. Nanoclusters Catal. Mater. Sci. Issue Size Control* **2008**, 21–48.

[15] Thanh, N. T. K.; Maclean, N.; Mahiddine, S. *Chem. Rev.* **2014**, *114* (15), 7610–7630.

[16] Prasad, B. L. V; Stoeva, S. I.; Sorensen, C. M.; Klabunde, K. J. *Chem. Mater.* **2003**, *15* (4), 935–942.

[17] (a) Daniel, M. C.; Astruc, D. *Chem. Rev.* **2004**, *104* (1), 293–346. (b) *Nanoscale Materials*; Liz-marzan, L. M., Kamat, P. V, Eds.; Kluwer Academic Publishers: Boston, 2003. (c) Tavakoli, A.; Sohrabi, M.; Kargari, A. *Chem. Pap.* **2007**, *61* (3), 151–170. (d) Huber, D. L. *Small* **2005**, *1* (5), 482–501.

[18] (a) Park, J.; Joo, J.; Soon, G. K.; Jang, Y.; Hyeon, T. *Angew. Chem. Int. Ed.* **2007**, *46* (25), 4630–4660. (b) Polte, J. *CrystEngComm* **2015**, *17* (36), 6809–6830.

[19] (a) Dorfs, D.; Krahne, R.; Falqui, A.; Manna, L. *Compr. Nanosci. Technol.* **2011**, *1.08*, 219–270. (b) Zacharaki, E.; Kalyva, M.; Fjellvåg, H.; Sjåstad, A. O. *Chem. Cent. J.* **2016**, *10*, 10–11. (c) Barhoum, A.; Rehan, M.; Rahier, H.; Bechelany, M.; Van Assche, G. *ACS Appl. Mater. Interfaces* **2016**, *8* (16), 10551–10561.

[20] Van Embden, J.; Chesman, A. S. R.; Jasieniak, J. J. *Chem. Mater.* **2015**, *27* (7), 2246–2285.

[21] Karaagac, O.; Kockar, H. *J. Supercond. Nov. Magn.* **2012**, *25* (8), 2777–2781.
[22] Carenco, S. Doctoral Dissertation, l'Université Pierre et Marie Curie, **2011**.
[23] (a) Kettemann, F.; Wuithschick, M.; Caputo, G.; Kraehnert, R.; Pinna, N.; Rademann, K.; Polte, J. *CrystEngComm* **2015**, *17* (8), 1865–1870. (b) Guan, Z.; Luo, W.; Xu, Y.; Tao, Q.; Wen, X.; Zou, Z. *ACS Appl. Mater. Interfaces* **2016**, *8* (8), 5432–5438.
[24] Gratzel, M.; O'Regan, B. *Nature* **1991**, *354*, 56–58.
[25] (a) Cuenya, B. R. *Acc. Chem. Res.* **2013**, *46* (8), 1682–1691. (b) Cuenya, B. R. *Thin Solid Films* **2010**, *518* (12), 3127–3150. (c) Astruc, D. *Nanoparticles and Catalyis*, Wiley, 2008.
[26] Buil, M. L.; Esteruelas, M. A.; Niembro, S.; Oliván, M.; Orzechowski, L.; Pelayo, C.; Vallribera, A. *Organometallics* **2010**, *29* (19), 4375–4383.
[27] Lewis, L. N.; Lewis, N. *J. Am. Chem. Soc.* **1986**, *108* (23), 7228–7231.
[28] (a) Oyama, S. T.; Wang, X.; Lee, Y. K.; Chun, W. J. *J. Catal.* **2004**, *221* (2), 263–273. (b) Senevirathne, K.; Burns, A. W.; Bussell, M. E.; Brock, S. L. *Adv. Funct. Mater.* **2007**, *17* (18), 3933–3939.
[29] Huh, Y.; Green, M. L. H.; Kim, Y. H.; Lee, J. Y.; Lee, C. J. *Appl. Surf. Sci.* **2005**, *249* (1–4), 145–150.
[30] Trépanier, M.; Dalai, A. K.; Abatzoglou, N. *Appl. Catal. A Gen.* **2010**, *374* (1–2), 79–86.
[31] Mondal, A.; Mukherjee, D.; Adhikary, B.; Ahmed, M. A. *J. Nanoparticle Res.* **2016**, *18* (5), 117.
[32] Kelsen, V.; Wendt, B.; Werkmeister, S.; Junge, K.; Beller, M.; Chaudret, B. *Chem. Commun. (Camb).* **2013**, *49* (33), 3416–3418.
[33] Yan, J.; Zhang, X.; Han, S.; Shioyama, H.; Xu, Q. *Angew. Chemie Int. Ed.* **2008**, 2287–2289.
[34] (a) Li, C. W.; Ciston, J.; Kanan, M. W. *Nature* **2014**, *508* (7497), 504–507. (b) Feng, X.; Jiang, K.; Fan, S.; Kanan, M. W. *ACS Cent. Sci.* **2016**, *2* (3), 169–174.
[35] Callejas, J. F.; Read, C. G.; Woske, C. W.; Lewis, N. S.; Schaak, R. E. *Chem. Mater.* **2016**, *28* (17), 6017–6044.
[36] Wu, L.; Li, Q.; Wu, C. H.; Zhu, H.; Mendoza-Garcia, A.; Shen, B.; Guo, J.; Sun, S. *J. Am. Chem. Soc.* **2015**, *137* (22), 7071–7074.
[37] (a) Gupta, A. K.; Gupta, M. *Biomaterials* **2005**, *26* (18), 3995–4021. (b) Gleich, B.; Weizenecker, J. *Nature* **2005**, *435* (7046), 1214–1217.
[38] (a) Sun, S. et al. *Science (80).* **2000**, *287* (5460), 1989–1992. (b) Desvaux, C.; Amiens, C.; Fejes, P.; Renaud, P.; Respaud, M.; Lecante, P.; Snoeck, E.; Chaudret, B. *Nat. Mater.* **2005**, *4* (10), 750–753.
[39] Trumbo, P.; Yates, A. A.; Schlicker, S.; Poos, M. *Journal of the American Dietetic Association*. 2001, pp 294–301.
[40] (a) J.-M. Yan, X.-B. Zhang, S. Han, H. Shioyama, Q. Xu, *Inorg. Chem.* **2009**, *48*, 7389–7393. (b) A. Saxena, A. Kumar, S. Mozumdar, *Appl. Catal. A* **2007**, *317*, 210– 215.
[41] (a) Wang, H.; Jiao, X.; Chen, D. *J. Phys. Chem. C* **2008**, *112*, 18793– 18797. (b) LaGrow, A. P.; Ingham, B.; Cheong, S.; Williams, G. V. M.; Dotzler, C.; Toney, M. F.; Jefferson, D. A.; Corbos, E. C. ; Bishop, P. T.; Cookson, J.; Tilley, R. D. *J. Am. Chem. Soc.* **2012**, *134*, 855–858. (c) Han, M.; Liu, Q.; He, J.; Song, Y.; Xu, Z.; Zhu, J. M. *Adv. Mater.* **2007**, *19*, 1096–1100. (d) Jeon, Y. T.; Moon, J. Y.; Lee, G. H.; Park, J.; Chang, Y. *J. Phys. Chem. B* **2006**, *110* (3), 1187–1191.

[42] (a) Rinaldi, A.; Tessonnier, J.-P.; Schuster, M. E.; Blume, R.; Girgsdies, F.; Zhang, Q.; Jacob, T.; Abd Hamid, S. B.; Su, D. S.; Schlögl, R. *Angew. Chem.* **2011**, *123*, 3371–3375.; *Angew. Chem. Int. Ed.* **2011**, *50*, 3313– 3317. (b) Zhu, L.-P.; Liao, G.-H.; Zhang, W.-D.; Yang, Y.; Wang, L.-L.; Xie, H.-Y. *Eur. J. Inorg. Chem.* **2010**, 1283–1288. (c) Sarac, M. F.; Wilson, R. M.; Johnston-Peck, A. C.; Wang, J.; Pearce, R.; Klein, K. L.; Melechko, A. V.; Tracy, J. B. *ACS Appl. Mater. Interfaces* **2011**, *3*, 936–940. (d) Carenco, S.; Le Goff, X. F.; Shi, J.; Roiban, L.; Ersen, O.; Boissière, C.; Sanchez, C.; Mézailles, N. *Chem. Mater.* **2011**, *23*, 2270–2277. (e) Carenco, S.; Surcin, C.; Morcrette, M.; Larcher, D.; Mézailles, N.; Boissière, C.; Sanchez, C. *Chem. Mater.* **2012**, *24*, 688–697.

[43] Buslov, I.; Song, F.; Hu, X. *Angew. Chemie Int. Ed.* **2016**, *55*, 12295–12299.

[44] Alonso, F.; Riente, P.; Sirvent, J. A.; Yus, M. *Appl. Catal. A Gen.* **2010**, *378* (1), 42–51. (b) F. Alonso, P. Riente, M. Yus, *Tetrahedron Lett.* **2008**, *49*, 1939–1942.

[45] (a) Carenco, S.; Leyva-Pérez, A.; Concepción, P.; Boissière, C.; Mézailles, N.; Sanchez, C.; Corma, A. *Nano Today* **2012**, *7* (1), 21–28. (b) Chen, Y.; Li, C.; Zhou, J.; Zhang, S.; Rao, D.; He, S.; Wei, M.; Evans, D. G.; Duan, X. *ACS Catal.* **2015**, *5* (10), 5756–5765.

[46] (a) Hinotsu, T.; Jeyadevan, B.; Chinnasamy, C. N.; Shinoda, K.; Tohji, K. *J. Appl. Phys.* **2004**, *95* (11 II), 7477–7479. (b) Murray, C. B.; Sun, S.; Doyle, H.; Betley, T. *MRS Bull.* **2001**, *26* (12), 985–991. (c) Tzitzios, V.; Basina, G.; Gjoka, M.; Alexandrakis, V.; Georgakilas, V.; Niarchos, D.; Boukos, N.; Petridis, D. *Nanotechnology* **2006**, *17* (15), 3750–3755.

[47] Zach, M. P.; Penner, R. M. *Adv. Mater.* **2000**, *12* (12), 878–883.

[48] Sun, Y. P.; Rollins, H. W.; Guduru, R. *Chem. Mater.* **1999**, *11* (1), 7–9.

[49] (a) Yang, J.; Feng, B.; Liu, Y.; Zhang, Y.; Yang, L.; Wang, Y.; Wei, M.; Lang, J.; Wang, D.; Liu, X. *Appl. Surf. Sci.* **2008**, *254* (22), 7155–7158. (b) Chatterjee, A.; Chakravorty, D. *Appl. Phys. Lett.* **1992**, *60* (1), 138–140.

[50] Parada, C.; Mora, E.; Qu, F. D. C. *Chem. Marter.* **2006**, *18* (4), 2719–2725.

[51] Grzelczak, M.; Pérez-Juste, J.; Rodríguez-González, B.; Spasova, M.; Barsukov, I.; Farle, M.; Liz-Marzán, L. M. *Chem. Mater.* **2008**, *20* (16), 5399–5405.

[52] (a) Cordente, N.; Respaud, M.; Senocq, F.; Casanove, M.-J.; Amiens, C.; Chaudret, B. *Int. Lab.* **2004**, *31* (8), 154–161. (b) Ould Ely, T.; Amiens, C.; Chaudret, B.; Snoeck, E.; Verelst, M.; Respaud, M.; Broto, J. *Chem. Mater.* **1999**, *11* (l), 526–529. (c) Bradley, J. S.; Tesche, B.; Busser, W.; Maase, M.; Reetz, M. T. *J. Am. Chem. Soc.* **2000**, *122* (19), 4631–4636.

[53] (a) Wang, H.; Jiao, X.; Chen, D. *J. Phys. Chem. C* **2008**, *112*, 18793. (b) Chen,Y.; Luo, X.;Yue, G. H.; Luo, X.; Peng, D. L. *Mater.Chem.Phys.* **2009**, *113*, 412. (c) Green, M.; O'Brien, P. *Chem. Commun.* **2001**, 1912. (c) Park, J.; Kang, E.; Son, S.; Park, H.; Lee, M.; Kim, J.; Kim, K.; Noh, H.; Park, J.; Bae, C.; Park, J.; Hyeon, T. *Adv. Mater.* **2005**, *17*, 429. (d) Chen, Y.; Peng, D.; Lin, D.; Luo, X. *Nanotechnology* **2007**, *18*, 505703. Zhang, H. T.; Wu, G.; Chen, X. H.; Qiu, X. G. *Mater. Res. Bull.* **2006**, *41*, 495. (e) Goto, Y.; Taniguchi, K.; Omata, T.; Otsuka-Yao- Matsuo, S.; Ohashi, N.; Ueda, S.; Yoshikawa, H.; Yamashita, Y.; Oohashi, H.; Kobayashi, K. *Chem. Mater.* **2008**, *20*, 4156. (f) Han, M.; Liu, Q.; He, J. H.; Song, Y.; Xu, Z.; Zhu, J. M. *Adv. Mater.* **2007**, *19*, 1096.

[54] Hou, Y.; Gao, S. *J. Mater. Chem.* **2003**, *13*, 1510.

[55] Han, M.; Liu, Q.; He, J.; Song, Y.;Xu, Z.; Zhu, J. *Adv. Mater.* **2007**, *19*, 1096.
[56] Carenco, S.; Boissiere, C.; Nicole, L.; Sanchez, C.; Floch, P. Le; Mézailles, N. M. *Chem. Mater.* **2010**, *22* (4), 1340–1349.
[57] (a) Carenco, S., Labouille, S., Bouchonnet, S., Boissière, C., Le Goff, X.-F., Sanchez, C., Mézailles, N. *Chem. Eur. J.*, **2012**, *18*(44), 14165–73. (b) Hou, Y.; Kondoh, H.; Ohta, T.; Gao, S. *Appl. Surf. Sci.* **2005**, *241* (1–2), 218–222.
[58] Willis, A. L.; Chen, Z.; He, J.; Zhu, Y.; Turro, N. J.; O'Brien, S. *J. Nanomater.* **2007**, *14858*, 1–7. (b) Sun, S.; Zeng, H. *J. Am. Chem. Soc.* **2002**, No. 31, 8204–8205. (c) Nene, A. G.; Takahashi, M.; Somani, P. R. **2016**, 20–28.
[59] He, M.; Protesescu, L.; Caputo, R.; Krumeich, F.; Kovalenko. M. *Chem. Mater.* **2015**, *27*, 635–647.

Chapter II: Synthesis of Metal Nanoparticles by Reduction of Metal(II) Diamide Precursors

1. Water-free nickel(0) nanoparticles from nickel(II) diamide precursor

In order to achieve a water-free synthesis of metal(0) nanoparticles, as introduced in the previous chapter, we began by examining previous work in the group. We found that a nickel(II) acetylacetonate [$Ni(acac)_2$] species was reduced by oleylamine to form a molecular Ni(0) species $Ni(NH_2CH_2R)(HN{=}CHR)$ that then decomposed to form nanoparticles (NPs). This reaction produced water in a ligand-centered condensation reaction. We hoped to go through the same $M(NH_2CH_2R)(HN{=}CHR)$ intermediate without forming water.

While Ni(0) is not oxidized by the coproduction of water *in situ*, metals like Fe(0) oxidize in the presence of water.[1] Because our goal was to find a general method of synthesizing NPs from first-row transition metals, we developed a direct approach to form the $M(NH_2CH_2R)(HN{=}CHR)$ intermediate from a metal(II) diamide precursor (Scheme II-1).

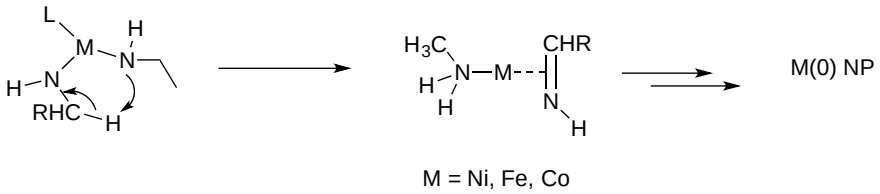

Scheme II-1. Formation of $M(NH_2CH_2R)(HN{=}CHR)$ intermediate from metal(II) diamide precursor to form metal(0) NPs to the exclusion of water.

We focused on Ni(0) NPs, and the process was later extended to Fe(0) and Co(0) NPs as well. Using commercially available $NiBr_2$(DME) (DME = 1,2-dimethoxyethane), complex **1** (1/n $[Ni(NHR)_2]_n$) was synthesized by simple reaction with lithium oleylamide (Scheme II-2). The concurrently formed lithium bromide (LiBr) was then precipitated from pentane. After drying, the product formed a dark purple oil. ^{1}H NMR spectroscopy showed alkyl and alkenyl peaks that were distinct from those of the starting oleylamine and from lithium oleylamide. The identity of the product was supported by elemental analysis.

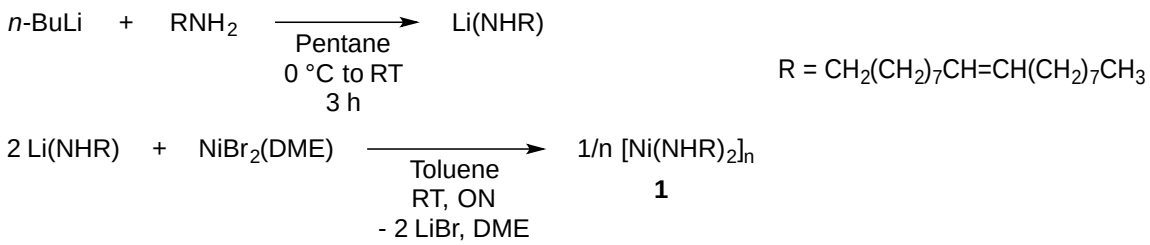

Scheme II-2. Synthesis of nickel(II) dioleylamide **1**.

The isolated precursor formed black Ni(0) NPs upon heating at 150 °C in toluene for 0.5 h (Figure II-1). Transmission electron microscopy (TEM) showed these nanoparticles to be polydisperse, of 4.8 ± 1.1 nm in diameter, as calculated by averaging the sizes of several hundred particles. The size of the particles was much smaller than those synthesized from $Ni(acac)_2$ (4.8 nm *vs.* 30 nm).[2] This polydispersity was consistent with poor ligand stabilization. Although size control was poor, the present synthesis showed that the nickel(II) diamide species could be reduced to Ni(0) NPs, and several directions were envisaged to probe the effects of ligands on the size and shape of the Ni NPs.

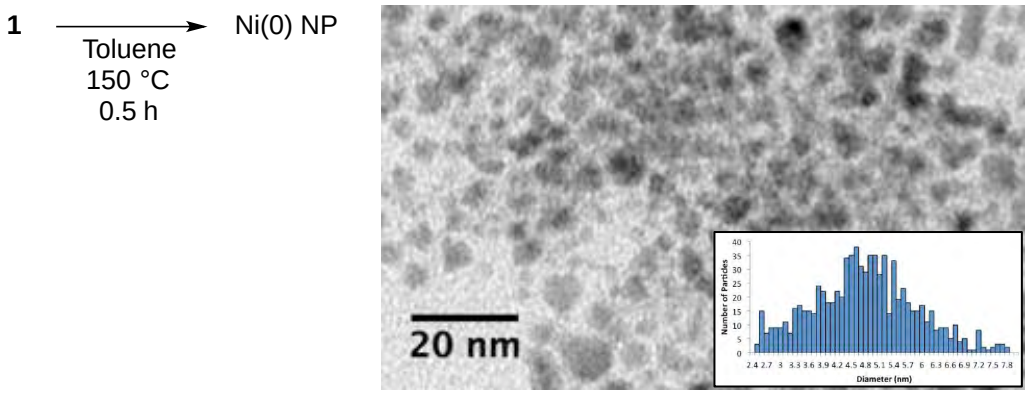

Figure II-1. Equation and TEM image of decomposition of complex **1** to Ni(0) NPs of D = 4.8 ± 1.1 nm.

2. Decomposition of complex 1 in the presence of free oleylamine (OAH)

Previous work showed oleylamine to be a poor ligand for Ni NPs synthesized from $Ni(acac)_2$ at 220 °C, because it desorbed easily from the metal surface.[2] Under milder reaction conditions (150 °C), however, ligand desorption would be less favorable.[3] We thus postulated that additional oleylamine could result in some control over size and shape. Different amounts of free oleylamine were thus added to the

reaction mixture. The addition of 0.1 or 0.5 equivalents made no observable difference in the resulting NPs by TEM. Upon addition of one equivalent of oleylamine, highly faceted, self-organizing NPs were observed. This reaction produces a bimodal distribution of NPs, focused around smaller, round particles of 5.9 ± 0.9 nm and larger, faceted particles of 9.5 ± 1.1 nm, with an average particle size of 7.5 nm (Figure II-2). One possible reason for this bimodal distribution is the presence of two different types of surface ligands. We postulate one of these ligands to be the poorly stabilizing oleylamine,[4] and the second to be the imine formed upon reduction of the metal center (Scheme II-1). This promising result suggested that the size and shape of the nanoparticles might be controllable *via* the use of additional, more strongly coordinating ligands.

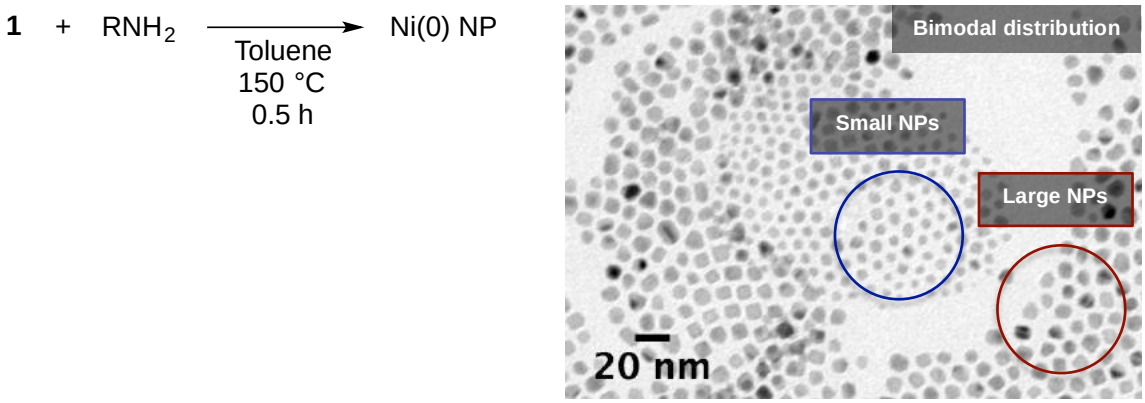

Figure II-2. Equation and TEM image of formation of Ni(0) NPs from the decomposition of nickel dioleylamide. Bimodal distribution of smaller nanoparticles of D = 5.9 ± 0.9 nm and larger, faceted nanoparticles of D = 9.5 ± 1.1 nm.

3. Decomposition of complex 1 in the presence of trioctylphosphine (TOP)

In order to further explore the changes in particle size and shape observed upon addition of one equivalent of oleylamine, the addition of more strongly coordinating ligands for the stabilization of Ni(0) was then examined. The addition of the highly stabilizing phosphine TOP was found to yield spherical, monodisperse nanoparticles. Varying the number of equivalents of TOP delivers the ability to control the size of the Ni(0) NPs from 4.2 nm to 10.9 nm (in contrast to the 9- to 25-nm diameters previously observed upon addition of 0.1 to 0.5 equivalents of TOP to Ni NPs obtained from $Ni(acac)_2$).[2] As seen in the TEM images in Figure II-3, the

addition of 0.2, 2, and 5 equivalents of TOP also resulted in the formation of a few tiny nanoparticles that could be easily separated by size-selective precipitation with a small amount of ethanol.

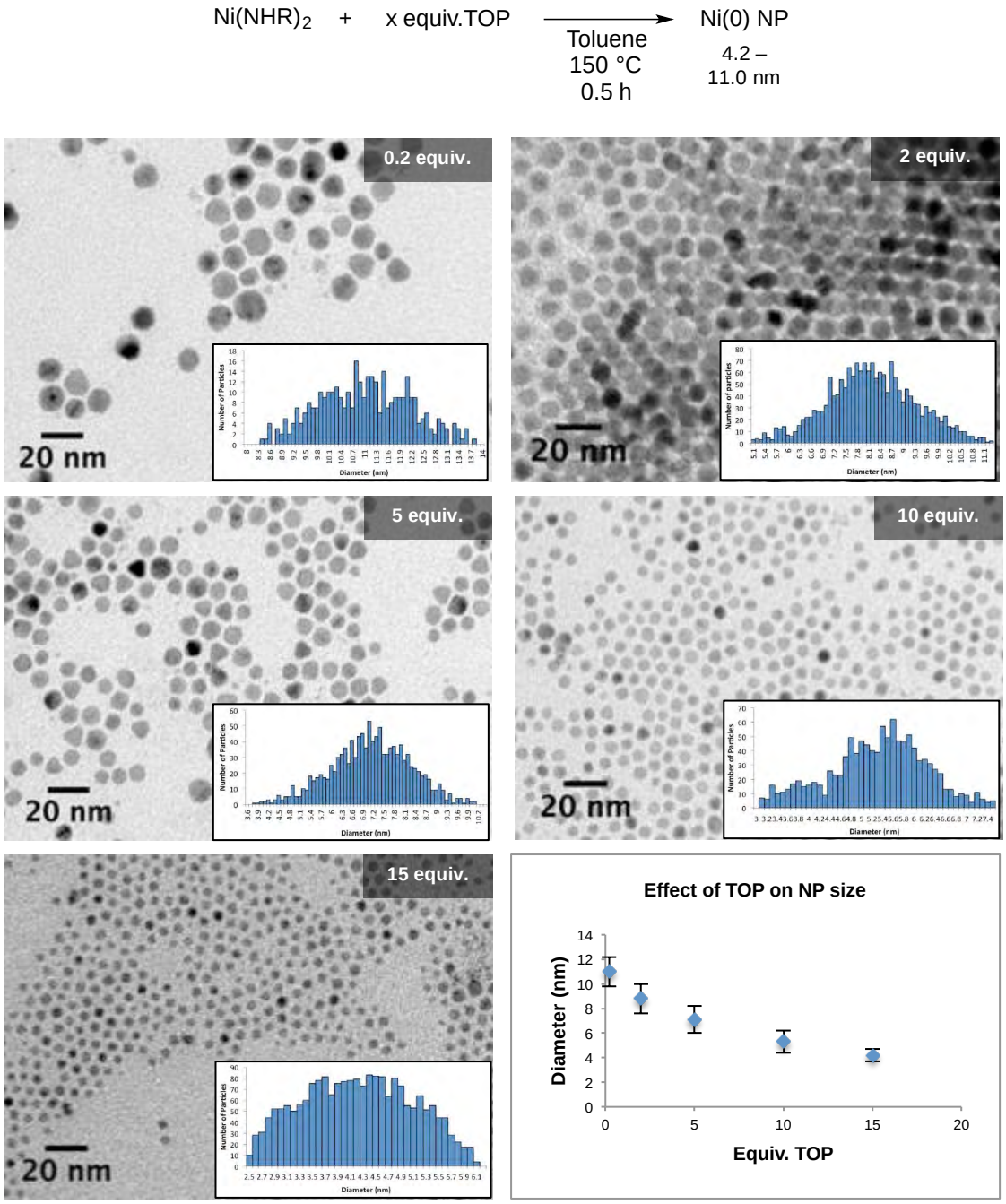

Figure II-3. Equation, TEM images, and summarizing graph of formation of Ni NPs from decomposition of nickel(II) dioleylamide to Ni(0) NPs with varying amounts of TOP. 0.2 equiv. (D = 11.0 ± 1.2 nm); 2 equiv. (D = 8.8 ± 1.2 nm); 5 equiv. (D = 7.1 ± 1.1 nm); 10 equiv. (D = 5.3 ± 0.9 nm); and 15 equiv. (D = 4.2 ± 0.5 nm) TOP examined.

Thus, we were able to obtain monodisperse, size-controlled Ni(0) nanoparticles from the decomposition of an easy-to-synthesize precursor without producing water. In the absence of excess oleylamine, the nickel diamide precursor decomposed in a poorly controlled manner, resulting in small, polydisperse NPs. The addition of one equivalent of excess oleylamine results in bimodal particles, while round, monodisperse particles are formed upon addition of TOP. As expected, an indirect correlation was observed between the amount of TOP and the size of the particles. While the amount of oleylamine correlated directly with the nucleation rate when $Ni(acac)_2$ was reduced by oleylamine at 220 °C,[2] an increase in the amount of oleylamine in the present system instead affected the size and faceting of the resulting particles. Consequently, we proposed the rate-determining step to be β-hydrogen transfer from one amide ligand to the other, both of which are already present in the starting complex. DFT calculations were performed to verify these experimental results (section 10).

4. Ni nanoparticles from *in situ* formation of nickel(II) dioleylamide

Having developed a robust method for the formation of Ni NPs, we sought to further simplify the synthesis. We thus investigated the formation of nanoparticles from nickel(II) dioleylamide formed *in situ* from the commercially available $NiBr_2$(DME), without consequent isolation. An experiment analogous to the reaction setup outlined in Figure II-3, using 0.2 equivalents of TOP, surprisingly produced small (D = 4.3 ± 1.0 nm) particles instead of the expected particles of D = 11.0 ± 1.2 nm. After some optimization, it was found that performing the reaction at a higher temperature using the much higher-boiling oleylamine as solvent resulted in the formation of larger particles (D = 11.0 ± 1.1), comparable in size and size dispersity to the particles obtained using 0.2 equivalents of TOP with isolated **1** (Figure II-4).

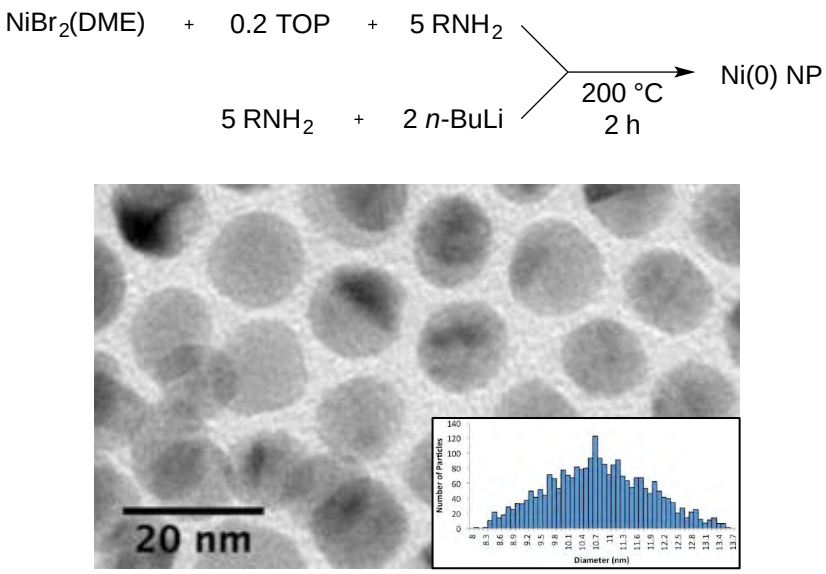

Figure II-4. Equation and TEM image of Ni NPs from $NiBr_2$(DME) (D = 11.0 ± 1.1 nm).

Despite the 11.0-nm diameter of the particles by TEM, X-ray diffractometry yielded a spectrum too broad to permit Scherrer analysis (Figure II-5).

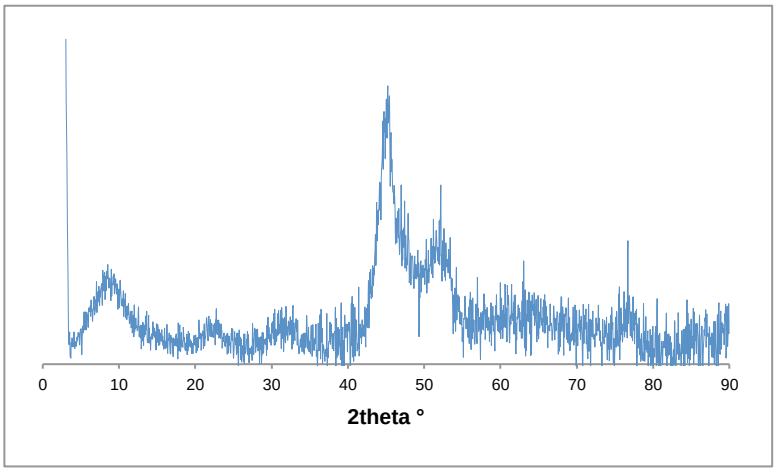

Figure II-5. X-ray diffractogram of Ni(0) NPs shown in Figure II-4 (D = 11 ± 1.1 nm).

Furthermore, the TEM images showed the presence of darker and lighter areas inside a single NP. Together, these data indicate that the NPs are not monocrystalline. This was confirmed by wide-angle X-ray scattering (WAXS), which showed that the particles are composed of crystalline domains of roughly 3 nm (Figure II-6).

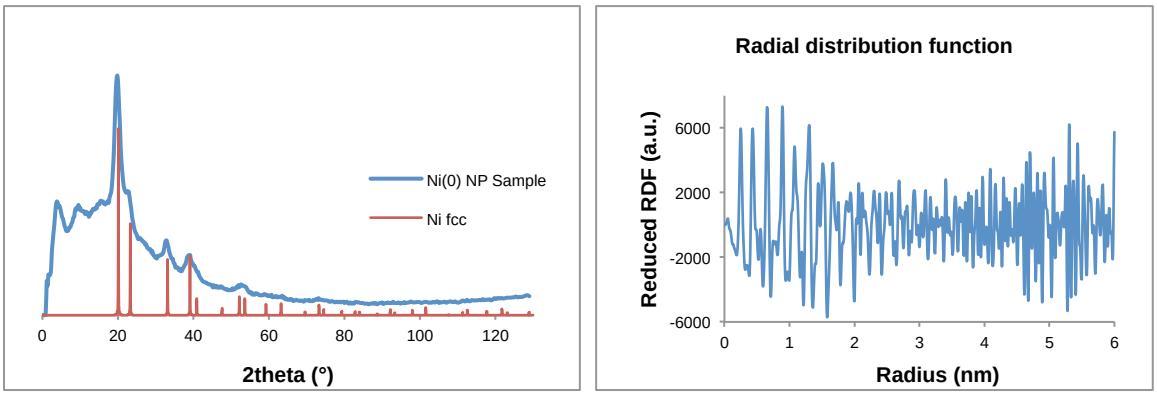

Figure II-6. Left: WAXS diffractogram of Ni(0) NPs shown in Figure II-4. Right: Radial distribution function of particles, revealing size of crystalline zones.

The radial distribution function describes density of atoms as a function of distance from a reference particle.[5] It is a measure of the probability of finding a coherent particle at a distance *r* from a reference particle. Coherence exists only within each individual crystalline domain. Thus, the local minimum of the radial distribution function, which should be considered as the baseline (noise level) of the plot, represents the diameter of each crystallite of which the global nanoparticles are composed.

The polycrystalline NP structure suggests that the particles grow through an aggregative mechanism.[6] As discussed in the previous chapter, a ripening mechanism would be expected to result in monocrystalline particles. Instead, the coalescence of many smaller particles, each with its own crystalline structure, would result in polycrystalline particles.

Indeed, analyzing particle formation over time shows that after 10 minutes, the particles are 3.0 ± 0.6 nm in size, in accordance with the individual crystalline domains (Figure II-7), before coalescing to form the particles shown in Figure II-4.

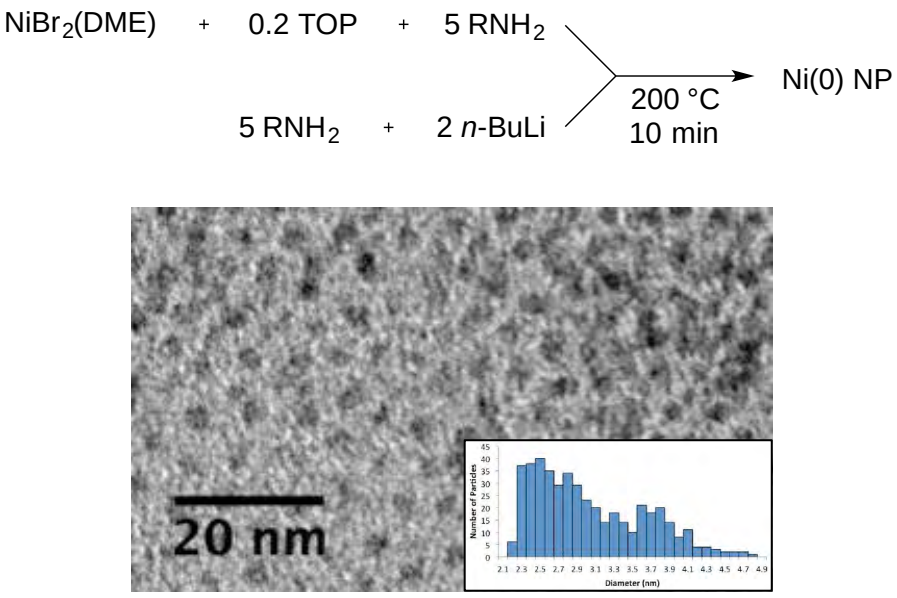

Figure II-7. Equation and TEM image of NPs from $NiBr_2$(DME) after 10 min. (D = 3.0 ± 0.6 nm).

5. Effect of temperature on nanoparticle growth and nucleation

In order to understand the effect of temperature on growth and nucleation, the decomposition of $NiBr_2$(DME) was also carried out at 100 °C and 150 °C rather than at 200 °C, keeping the other reaction parameters constant (0.2 equivalents of TOP, 10 total equivalents of NRH_2, 2 equivalents of *n*-BuLi; heated for 2 hours). Both lower temperatures resulted in incomplete conversion after two hours, as shown by the small mass of isolated NPs as well as the color of the supernatant after NP precipitation, which is clear upon complete conversion. Nonetheless, at 100 °C, the NPs that were isolated were much smaller than those obtained at 200 °C, with an average diameter of 3.8 ± 0.8 nm. Increasing the temperature to 150 °C resulted in particles closer to those obtained at 200 °C, though again smaller in size, with an average diameter of 8.6 ± 1.2 nm (Figure II-8). This suggests that while nucleation occurs at a lower temperature, growth is favored at higher temperatures.

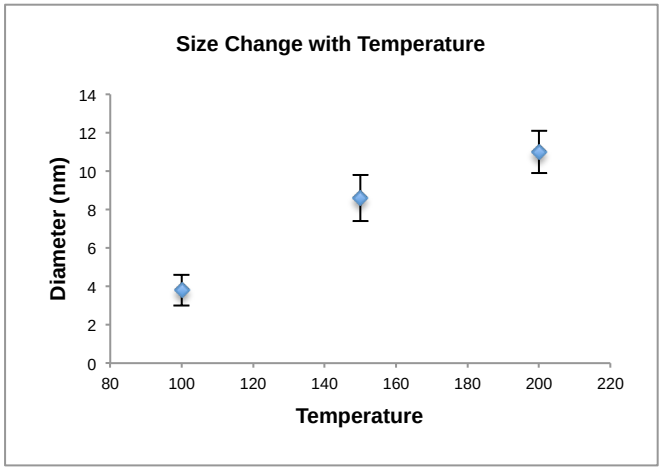

Figure II-8. Size change of Ni NPs with temperature.

Previous examples in the literature consistently indicate a direct correlation between temperature and NP size.[3,7] These reports suggest that at higher temperatures, ligands desorb from particle surfaces more easily, raising the surface energy of the particles. As described in the previous chapter, the process of particle growth occurs because of high-energy surfaces. A surface energy that is much higher than the entropy loss of a decreasing number of particles will lead to particle growth. The departure of stabilizing ligands leads to an increase in surface energy. Therefore, because high temperature encourages desorption of ligands from particle surfaces, NP growth correlates directly with temperature. This direct correlation between reaction temperature and size of the NPs is fully consistent with the aggregative mechanism proposed in section 4. It also provides another means of controlling the size of the nanoparticles.

6. Effect of precursor size on nanoparticle size and shape

The proposed precursor, nickel(II) dioleylamide, is a two-coordinate, 16-electron Ni(II) species when each amide ligand is treated as a three-electron donor using the covalent model of electron counting. Such a species is coordinatively unsaturated and is typically unstable, tending toward dimerization/oligomerization.[8] Few such stable species, in which dimerization is prevented by steric bulk, are known (Scheme II-3). Even the somewhat bulky nickel(II) bis(diphenylamide) forms dimers, typically through bridging amide groups. Nickel(II) dioleylamide has little steric protection, suggesting that it might also form aggregated species in solution. Thus, we

postulated that the species would be more accurately denoted as **1**, 1/n $[Ni(oleylamide)_2]_n$.

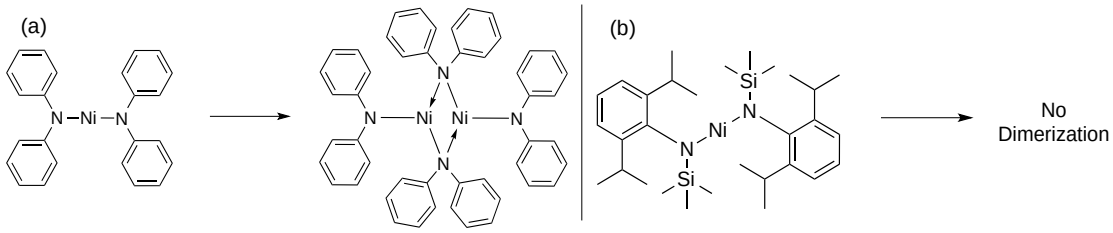

Scheme II-3. Literature examples of (a) dimerization of nickel(II) diamides, or (b) prevention of dimerization using bulky substituents.

In an attempt to identify the exact precursor to the Ni NPs, 2-D diffusion-ordered NMR studies (DOSY) were performed on $Ni(NHR)_2$-type precursors obtained under different conditions. In ^{1}H DOSY NMR spectra, molecules diffuse in accordance with their hydrodynamic radius r_H, a value that may be considered equivalent to the radius of a complex in solution given minimal solvent interactions.[9] The diffusion of a species in solution is indirectly proportional to its radius; thus, a larger diffusion coefficient D yields a smaller hydrodynamic radius. The two values are correlated by the following equation:

$$r_H = \frac{k_B T}{6\pi\eta D}$$

Equation II-1. Equation correlating hydrodynamic radius, r_H, and diffusion coefficient. D = diffusion coefficient (m^2/s), k_B = Boltzmann constant (1.38E-23 J/K), T = temperature (293 K), and η = viscosity (0.56E-3 Pa•s for toluene, 0.48E-3 Pa•s for THF).

The DOSY studies shown here were performed in the non-coordinating solvent toluene in order to reduce solvent effects. The isolated species **1** (synthesized and stored as a viscous oil for a few days to a few months) was shown to be an oligomeric species of about 6 nm radius (Figure II-9a). This was demonstrated by the diffusion coefficient of the diagnostic peak at 5.6 ppm (D = 6.06E-7 cm^2/s), corresponding to the alkenyl moiety of the oleyamine ligand. The streak shown in the DOSY spectrum supports the non-monodisperse nature of the species, and/or may

also be indicative of different conformations of the alkenyl chains in oligomeric species of the same size.

In contrast, a DOSY NMR spectrum of the *in situ*-synthesized **1** taken after 0.5 h showed it to be monomeric (Figure II-9b). The larger diffusion coefficient shown in Figure II-9b (D = 3.08E-6 cm^2/s) showed that the species corresponding to this coefficient diffused more quickly in solution, consistent with a hydrodynamic radius of about 1.3 nm.

The sample of unisolated **1**, whose NMR spectrum is shown in Figure II-9b, oligomerized in solution over three days at room temperature to form oligomers ranging in size from 2.5 to 13.1 nm in radius (Figure II-9c), as indicated by the much smaller diffusion coefficients (D = 1.55E-6 to 2.52E-7 cm^2/s). This room-temperature polymerization is supported by the size of the isolated complex **1** shown in Figure II-9a, which is typically synthesized by stirring at room temperature overnight.

We endeavored to understand whether the Ni(0) NPs formed after heating were the result of metal reduction within the framework provided by the oligomeric starting material, or whether the oligomers reformed monometallic species before the reduction took place. To do this, we examined the solutions of the oligomeric $[Ni(RNH)_2]_n$ after heating for a short period of time. This permitted the initiation of the reduction process, but stopped short of the production of too many nanoparticles.

Upon heating at 150 °C for five minutes, the size of the oligomers in the samples shown in Figures II-9a and II-9c reduced in size from much larger oligomers to monomeric species (Figure II-9d, which demonstrates the separation of the oligomers observed in Figure II-9c back to monomers of r_H = 0.9 nm, demonstrated by a diffusion coefficient of D = 4.27E-6 cm^2/s). This experiment suggests that regardless of the state of aggregation of the $[Ni(RNH)_2]_n$ species at the beginning of the reaction, the first step in the formation of NPs is the depolymerization of the oligomeric Ni(II) species to the monomeric form before the metal is reduced through β-hydrogen transfer.

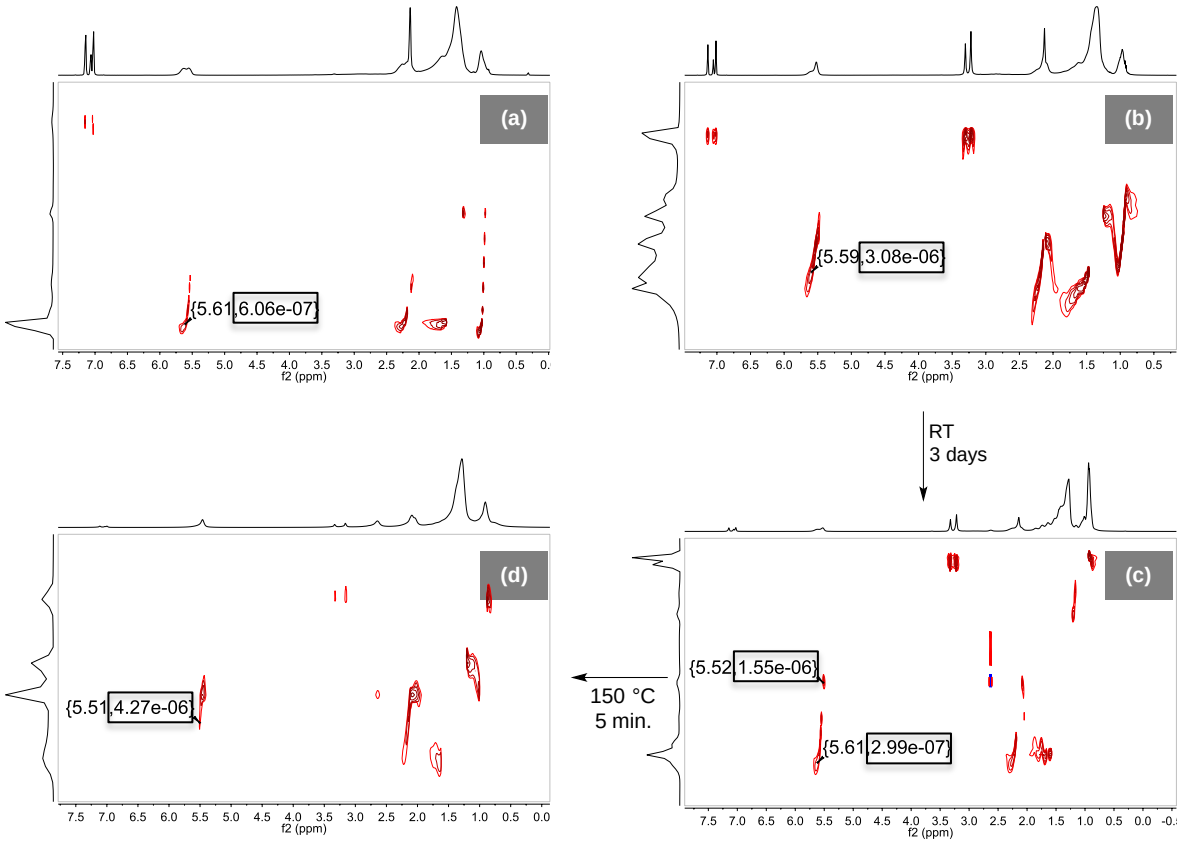

Figure II-9. DOSY NMR spectra in d_8-toluene of (a) Complex **1** (r_H = 6 nm); (b) $NiBr_2$(DME) after addition of a mixture of 2 equiv. *n*-BuLi and 2 equiv. oleylamine after 40 min. (r_H = 1.3 nm); (c) Sample b after three days at RT (r_H = 2.5 or 13.1 nm); and (d) Sample c heated to 150 °C for 5 min (r_H = 0.9 nm). The highlighted peaks are labeled with the coordinates of (chemical shift in ppm, diffusion coefficient in cm^2/s).

We hypothesized that the elimination of this first depolymerization step in the formation of NPs from **1** led to the differences in the particles obtained from isolated *vs in situ*-synthesized **1**. The procedure using isolated **1** employed toluene as solvent (Figure II-3), while the procedure using *in situ*-synthesized **1** to form NPs required the use of oleylamine as solvent (Figure II-4). Indeed, the addition of eight free equivalents of oleylamine to the reaction mixture shown above in Figure II-9b, which approximated the real conditions of NP synthesis, limited the growth of polymer size over three days to 2.2 nm instead of 13.1 nm obtained without the additional oleylamine, as demonstrated by a diffusion coefficient of D = 1.76E-6 cm^2/s (Figure II-10).

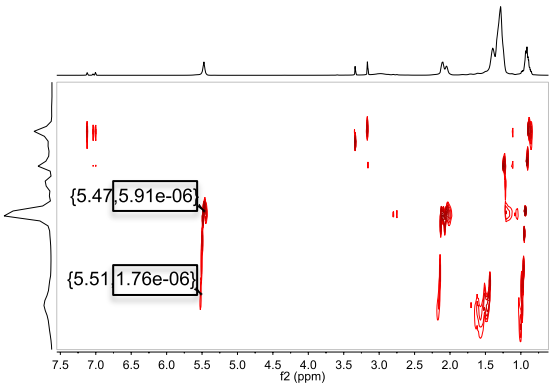

Figure II-10. DOSY NMR spectrum of $NiBr_2$(DME) after addition of a mixture of 2 equiv. *n*-BuLi and 10 equiv. oleylamine (*i.e.*, with eight free equivalents of oleylamine) after three days (r_H = 2.2 nm); free oleylamine also visible, with a diffusion coefficient of 5.91E-6, corresponding to r_H = 0.6 nm.

We expected the presence of eight equivalents of free oleylamine (solvent) to result in greater stabilization of the starting Ni(II) complex. This, in turn, would slow down the reduction of **1** to Ni(0) NPs, and thus lead to the same reaction pathway as that of the decomposition of isolated **1**. By more clearly separating the processes of depolymerization and nucleation, the resulting nanoparticles are expected to be more monodisperse.

In order to verify the theory of solution ripening, two sets of experiments were conducted. In a first test, **1** was synthesized *in situ* in a solution of toluene and aged overnight. It was then heated at 150 °C under the conditions used for isolated **1** (Figure II-11).

The resulting particles are not identical, but they are much closer in size and shape than they would have been without aging. While the aged solution does not produce a substantial amount of small, spherical nanoparticles as produced from the solution of isolated **1**, the faceted NPs are similar in size, size-dispersity, and faceting. In contrast, an unaged solution of *in situ*-synthesized **1** produced very different particles, as briefly discussed in section 4 (Figure II-12).

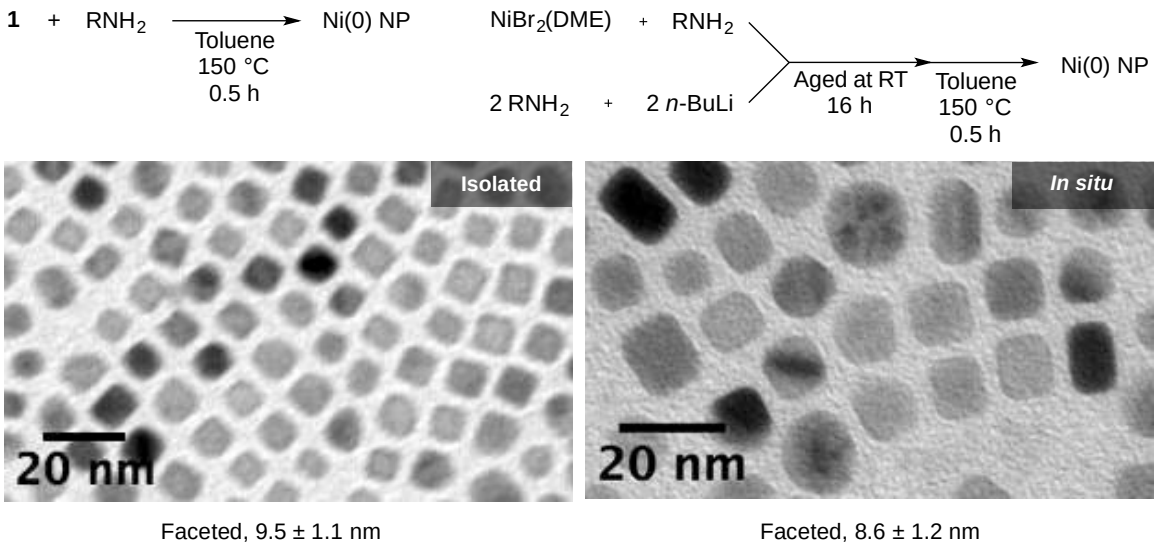

Figure II-11. Equation and TEM images of NPs resulting from isolated **1** (D = 9.5 ± 1.1 nm for larger, faceted particles) and an aged solution of **1** generated *in situ* (D = 8.6 ± 1.2 nm), at which point the two sets of precursor are expected to be similar in size.

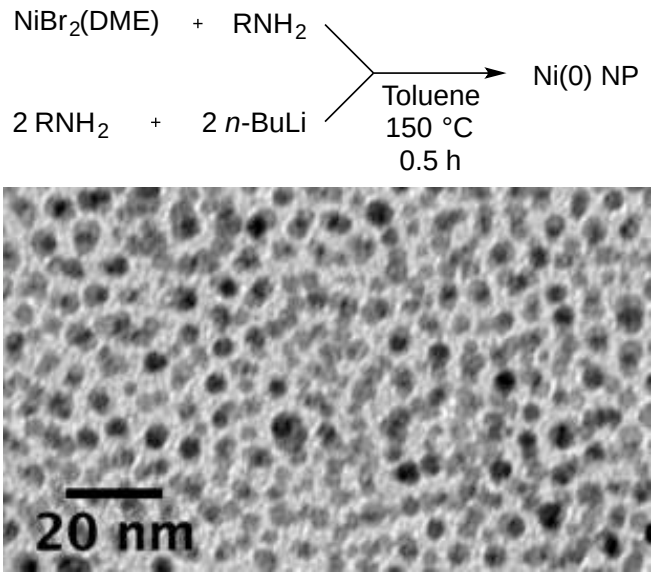

Figure II-12. Equation and TEM image of NPs resulting from an unaged solution of **1** (D = 3.4 ± 0.5 nm).

In a second test, a solution of **1** was synthesized in benzene, aged overnight, and then dried *in vacuo* (Figure II-13). The resulting mixture was redispersed in oleylamine and heated at 200 °C to form NPs. In a parallel reaction, isolated **1** was also dispersed in oleylamine and heated at 200 °C.

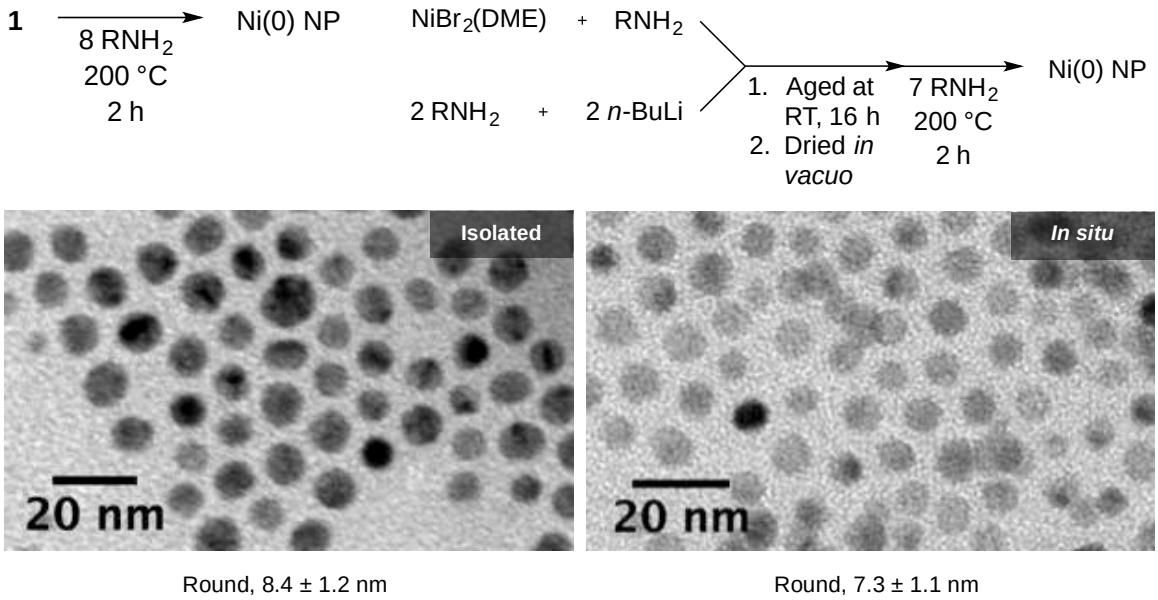

Figure II-13. Equation and TEM images of NPs resulting from isolated **1** (D = 8.4 ± 1.2 nm) and an aged solution of **1** generated *in situ* (D = 7.3 ± 1.1 nm), at which point the two sets of precursor are expected to be similar in size.

Once again, the resulting particles, though not identical, were similar in size, size-dispersity, and shape. These can be compared to the particles derived from unaged **1** (D = 11.0 ±1.1 nm), shown in Figure II-4 above.

These reactions strongly suggest that the starting oligomeric state of the precursor **1** has a significant impact on the shape and size of the resulting nanoparticles. We assume that the remaining differences may be attributed to factors such as the presence of LiBr and DME in solution.

Because literature examples of dimerization occur through bridging amido groups, we expected this to be the case for complex **1** as well. The presence of a double bond in complex **1** enabled us to verify the mode of coordination in the observed polymerization (Scheme II-4).

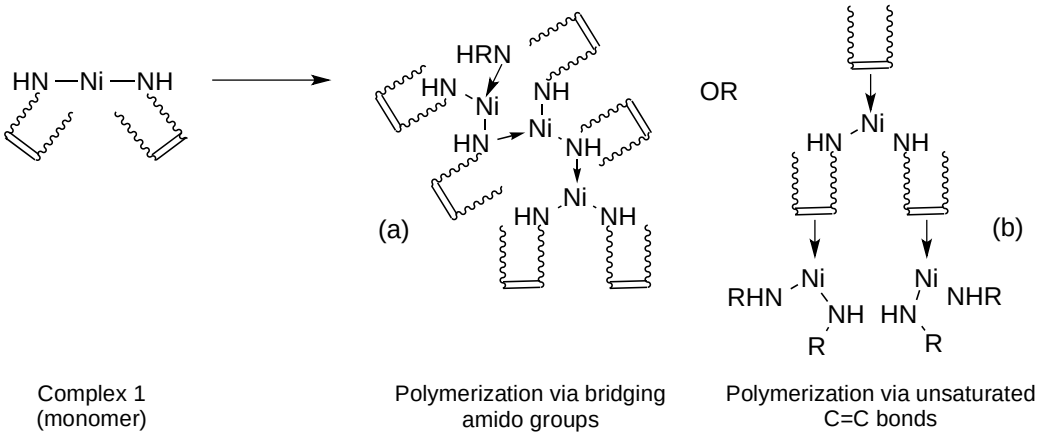

Scheme II-4. Examples of two possible modes of polymerization of **1** via bridging amido groups or coordination with unsaturated C=C bonds. A combination of both coordination modes is envisioned.

In order to better understand the coordination, a nickel(II) dihexadecylamide was prepared to reproduce the conditions of **1** in the absence of a double bond. The nickel(II) dihexadecylamide was synthesized using the same method as that used to prepare **1** (Scheme II-1). Oleylamine was replaced with hexadecylamine, and lithiation of the amine was followed by reaction with the nickel(II) salt. As in the case of oleylamine, oligomerization was observed by DOSY NMR. A DOSY NMR spectrum after 0.5 h indicated particles of r_H = 0.47 nm, using the peak indicated at 1.7 ppm (Figure II-14a). In comparison, a DOSY NMR spectrum after three days of aging at room temperature indicated particles of r_H = 3.4 nm, using the peak indicated at 1.6 ppm (Figure II-14b).

The size of the oligomeric nickel(II) dihexadecylamine was substantially smaller than the size of the oligomeric **1** seen after three days, which had a radius of 13.1 nm. This suggested that the coordination between nickel(II) dioleylamide monomers might in fact be through both the amide and alkenyl moieties, which permits the formation of larger oligomers.

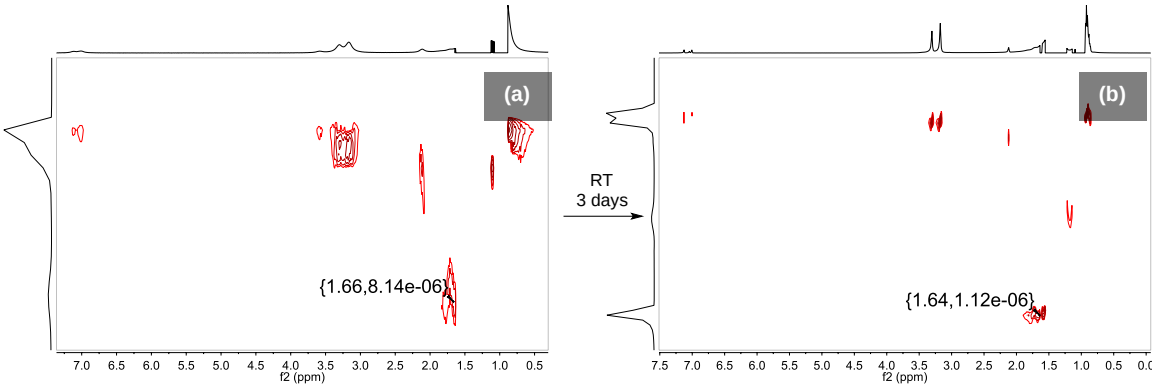

Figure II-14. DOSY NMR spectrum of Ni(hexadecylamide)$_2$ (a) after 0.5 h (r_H = 0.5 nm); and (b) after three days (r_H = 3.4 nm).

7. Effect of lithium bromide (LiBr) on nanoparticle size and shape

The procedures of NP synthesis beginning from either isolated or *in situ*-synthesized **1** differ not only in the oligomeric size of the nickel(II) precursor, but also in the presence of two equivalents of lithium bromide. When **1** is isolated, the LiBr that forms from the reaction between $NiBr_2$(DME) and lithium oleylamide is removed by suspension of the dried, crude reaction mixture and consequent filtration. Meanwhile, **1** synthesized *in situ* also resulted in the presence of unseparated LiBr.

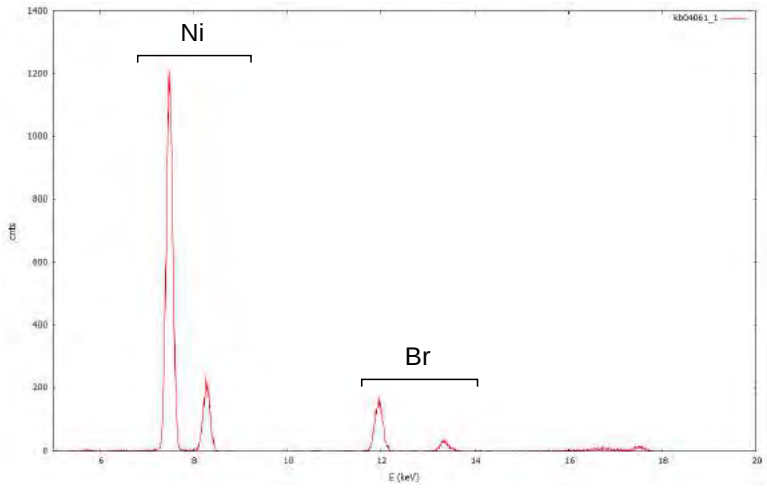

Figure II-15. X-ray fluorescence of sample of Ni NPs synthesized from *in situ*-synthesized **1**. Peaks at 7480 eV and 8267 eV correspond to Ni (K_α and K_β). Peaks at 11924 eV and 13292 eV correspond to Br.

While halide effects on the morphology or aggregation of nanoparticles due to anion surface adsorption have been observed for silver or gold,[10] such effects have never been studied for Ni NPs. X-ray fluorescence indicates the presence of bromide in the sample of Ni NPs derived from *in situ*-synthesized **1** (Figure II-15).

We thus studied the effect of added LiBr on the size and morphology of the Ni NPs obtained from isolated **1**. The isolated species was reduced to Ni NPs under conditions ostensibly resembling those used for *in situ*-synthesized **1**. The effect was dramatic: the addition of just two equivalents of free LiBr led to particles of 3.2 ± 1.2 nm in diameter, instead of the expected 11.0 ± 1.1 nm.

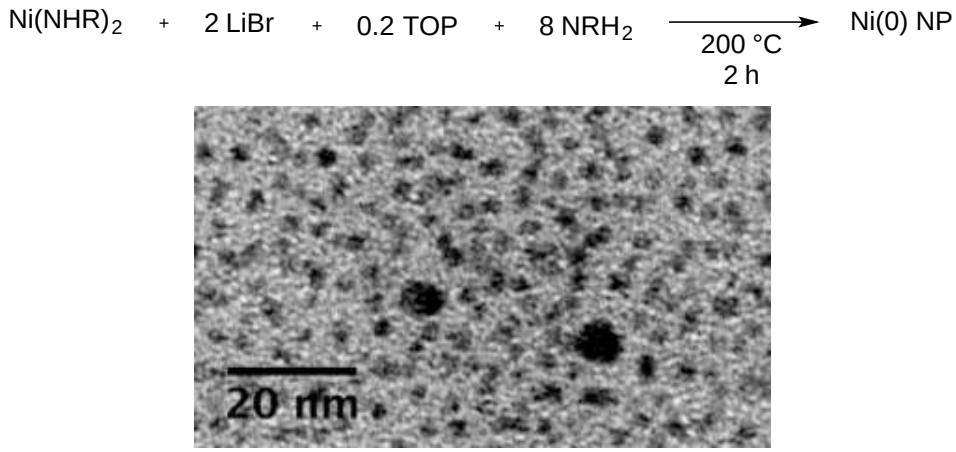

Figure II-16. Equation and TEM image of addition of 2 equiv. LiBr to isolated **1** before decomposition to Ni(0) NPs (D = 2.7 ± 0.5 nm).

Notably, these particles were very different from those obtained using *in situ*-synthesized **1**, which yielded NPs that were 11.0 ± 1.1 nm in diameter. These NPs were substantially smaller. To better understand the effects of LiBr on NP size, between 1 and 5 equivalents of LiBr were added to the solutions of $NiBr_2$(DME) before decomposition (Figure II-17). In all cases, the particles obtained were of diameters close to 3 nm. The absence of any trend prevented us from being able to draw any conclusions about the role of LiBr in the reaction.

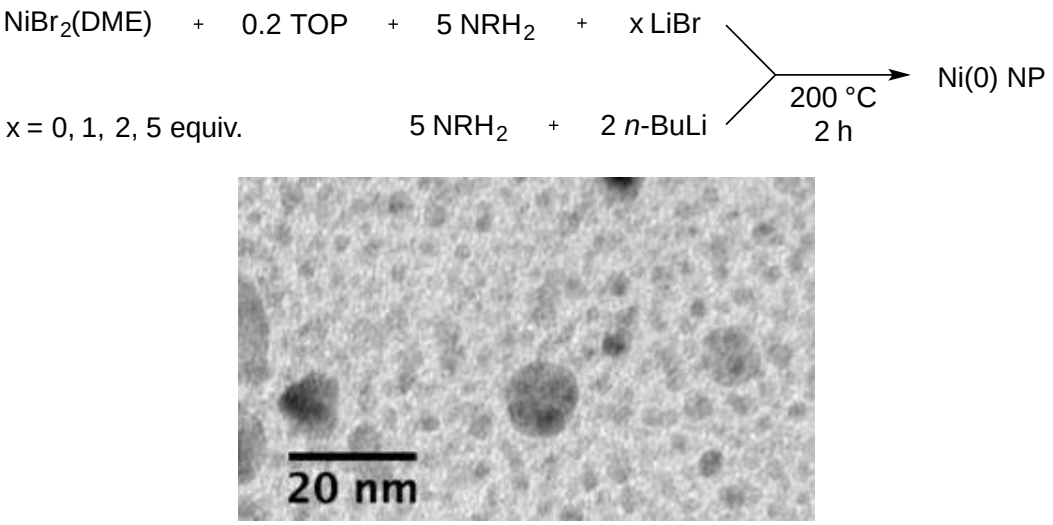

Figure II-17. Equation and TEM image of addition of 1 to 5 equiv. LiBr to solutions of $NiBr_2$(DME) before decomposition to Ni NPs, with representative TEM image. In all cases, TEM images looked nearly identical, and NPs were all of D ~ 3 ± 2 nm.

Noting the poor solubility of LiBr in oleylamine, and thus the inaccuracy of the stoichiometry of $NiBr_2$(DME) to LiBr, the addition of LiBr was reexamined using diphenyl ether as solvent (Figure II-18). The particles obtained using diphenyl ether (Ph_2O) as solvent, even with 0 equivalents of added LiBr, were smaller than those obtained from oleylamine (D = 4.6 ± 1.4 nm). It is possible that Ph_2O behaves as a surface ligand for Ni NPs, lowering the surface energy and thus limiting their size.

The particles obtained with greater amounts of free LiBr appeared to level off in size at a diameter of 3 nm. This suggested that the decomposition followed the same pathway as previously observed (*i.e.*, an aggregative mechanism involving the coalescence of smaller particles to form larger ones), but that the additional LiBr prevented the reaggregation of the smaller initial particles indicated by the crystalline zones, likely by behaving as surface ligands.

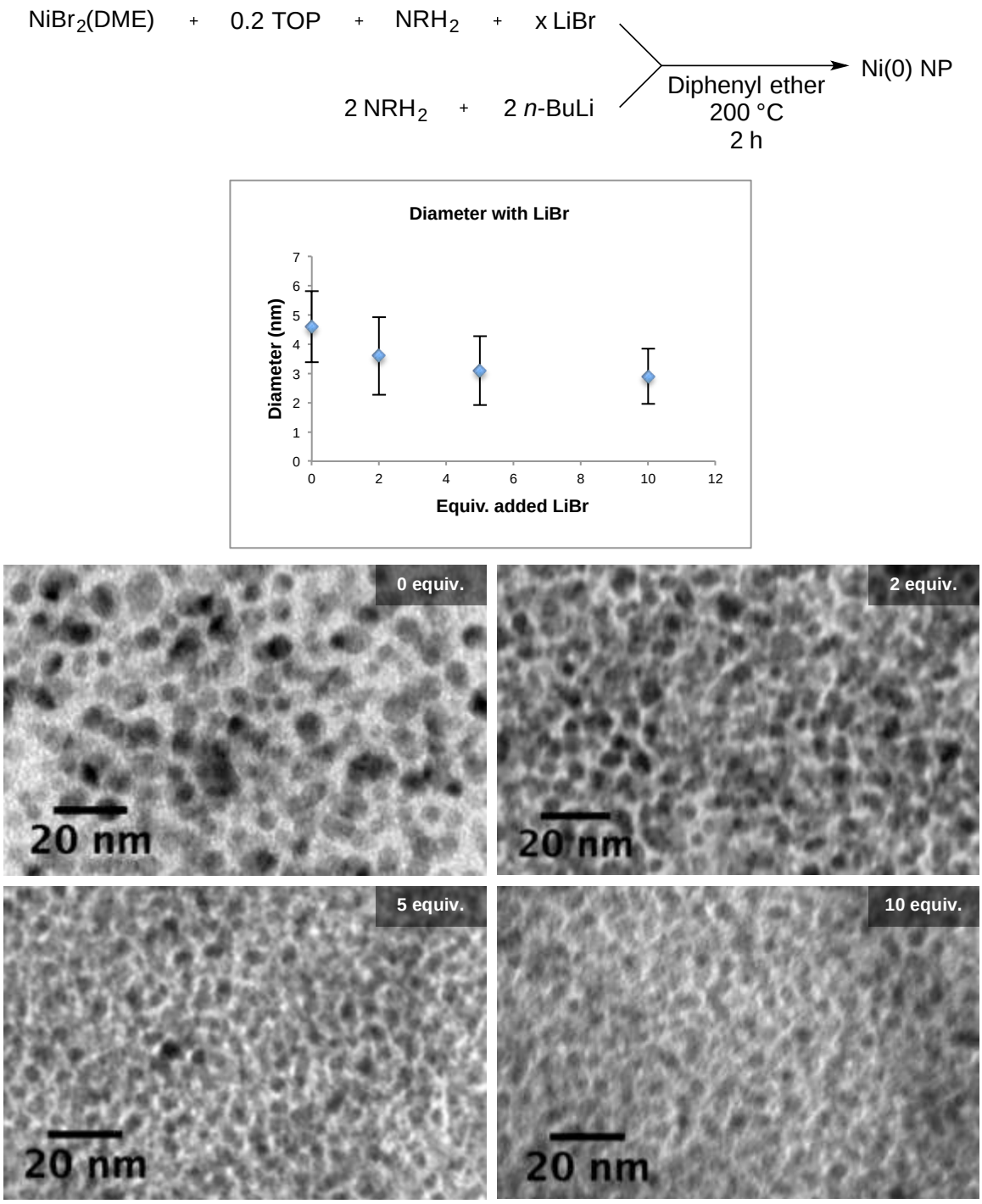

Figure II-18. Equation, summarizing graph, and TEM images of replacement of oleylamine as solvent by diphenyl ether; addition of 0 equiv. (D = 4.5 ± 1.2 nm), 2 equiv. (D = 3.6 ± 1.0 nm), 5 equiv. (D = 3.1 ± 1.0 nm), or 10 equiv. (D = 2.9 ± 0.9 nm) LiBr.

Unfortunately, it was not possible to examine the surfaces of the NPs using X-ray photoelectron spectroscopy (XPS) in order to ascertain the presence of bromide

surface ligands. However, the X-ray fluorescence is a good indication of its presence. The addition of LiBr to the system using isolated **1** does not appear to imitate the system using *in situ* or isolated **1**. This may be due to differing levels of solvation between LiBr synthesized *in situ vs.* added post facto. Nonetheless, the presence of the salt does affect the size and shape of the resulting NPs, whether by chemical or mechanical (*e.g.*, the movement of insoluble particles through the mixture or changes in viscosity) means.

8. Effect of oleylamine on nanoparticle size

In order to better evaluate the role of oleylamine, the number of equivalents of oleylamine with respect to the Ni precursor was varied from 2 to 14 equivalents (Figure II-19). To maintain a constant concentration, the total volume of the solution was balanced with octadecene (ODE). All other reaction parameters were kept the same (200 °C, 2 h, 0.2 equivalents of TOP). With two equivalents of oleylamine, we observe a low yield of NPs, as suggested by the colored supernatant after precipitation of particles, as well as by the small mass of NPs observed visually upon precipitation. TEM shows polydisperse particles. Increasing the amount of oleylamine resulted in larger particles with improved monodispersity and organization.

In contrast, Ni NPs obtained from the reduction of a $Ni(acac)_2$ precursor by amine (Scheme II-1) showed that an increase in the amount of oleylamine with respect to Ni(II) precursor led to an increase in the number of nucleation points, leading to smaller particles.[6] We propose that the different roles played by oleylamine in the different systems have led to these opposing effects. Oleylamine was the reducing agent in the $Ni(acac)_2$ system, so increasing the amount of oleylamine led to faster production of Ni(0), and consequently to more nucleation points. Meanwhile, in the present system, oleylamine is not the reducing agent; rather, the reducing agent is *oleylamide*. Instead, the neutral oleylamine acts as a better ligand for the starting Ni(II) than for the resulting Ni(0). The greater stability of the starting Ni(II) with increasing amounts of oleylamine thus appears to slow down nucleation and result in larger particles. This influence of oleylamine on size is most pronounced for six or fewer equivalents of oleylamine, with minimal change in size for increasing amounts.

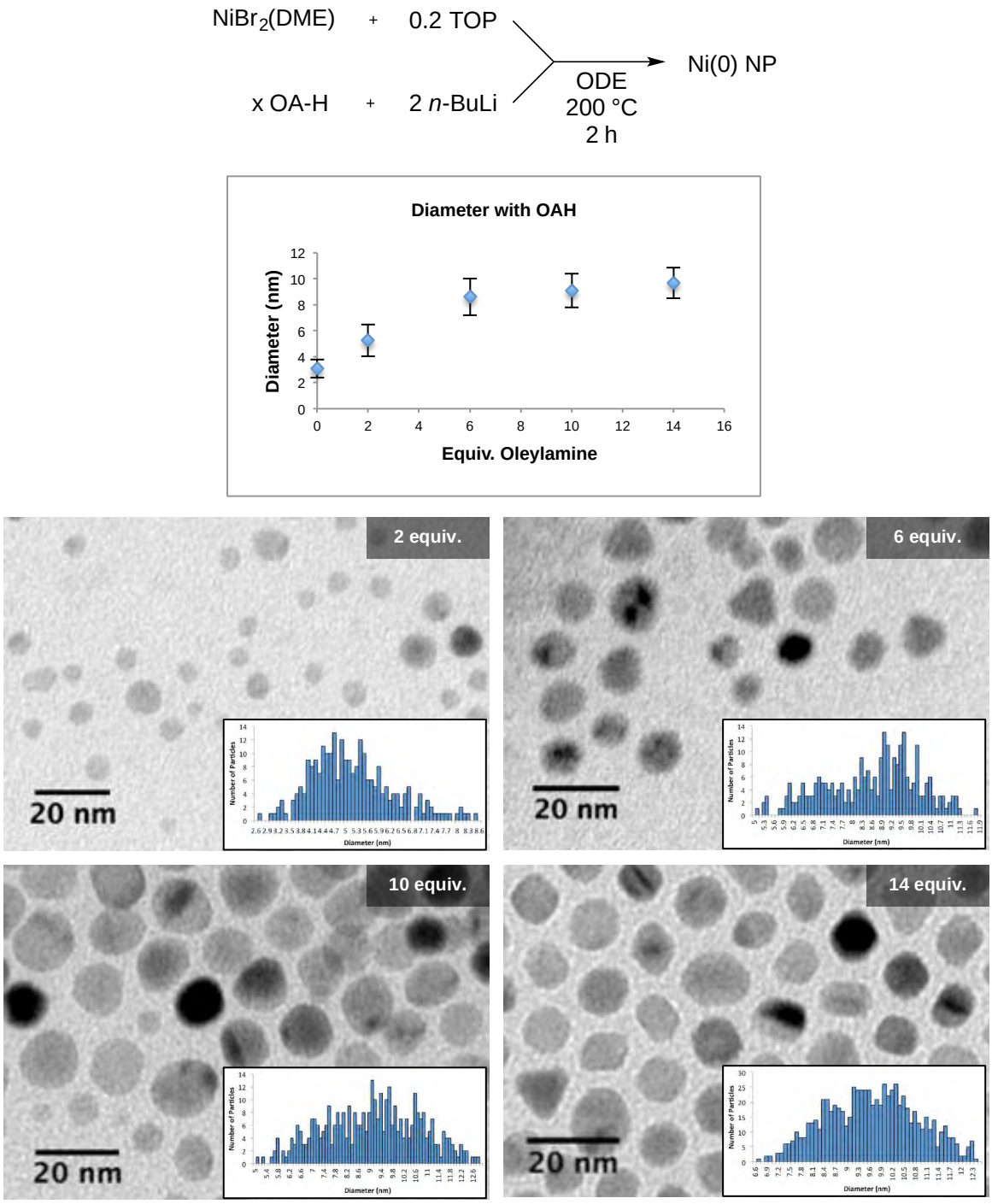

Figure II-19. Equation, summarizing graph, and TEM images of variation of equivalents of oleylamine with respect to $NiBr_2(DME)$. 2 equiv. (D = 5.3 ± 1.2 nm), 6 equiv. (D = 8.6 ± 1.4 nm), 10 equiv. (D = 9.1 ± 1.3 nm), and 14 equiv. (D = 9.7 ± 1.2 nm) oleylamine examined.

9. Solvent effects

In order to untangle the effects of the amine from those of the unsaturated bond, the oleylamine solvent used for NP synthesis previously (Figure II-4) was replaced by hexadecylamine (HDA)(Figure II-20). We expected the double bond of oleylamine to further stabilize the resulting NPs,[4,11] which would lead to an increase in NP size upon its absence. Instead, we see the opposite effect. Using hexadecylamine produced small, poorly defined particles of 2.8 ± 0.9 nm in diameter. This is contrary to the expected role of the unsaturated bond. We considered the possibility that the presumptive precursor nickel bis(hexadecylamide) was less stable than **1**, leading to the rapid formation of many nucleation points and resulting in smaller NPs.

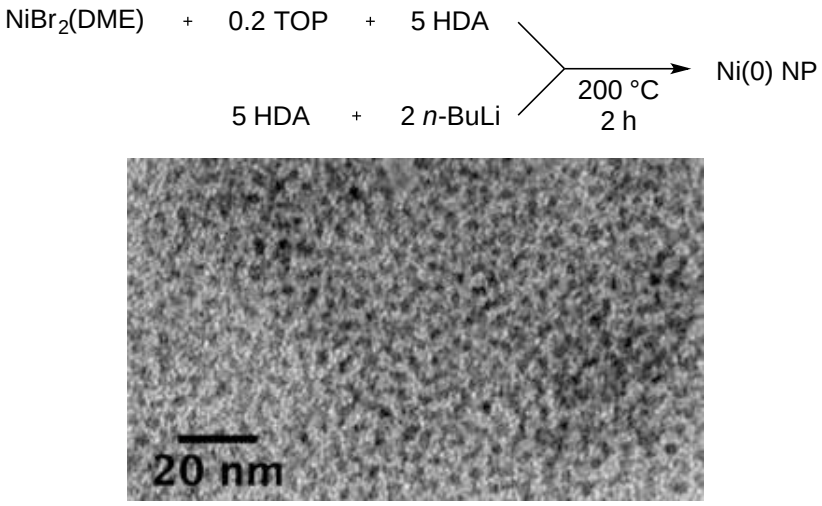

Figure II-20. Equation and TEM image of replacement of oleylamine by hexadecylamine (HDA) as solvent and as precursor to amide ligand (D = 2.8 ± 0.9 nm).

To test this hypothesis, oleylamine was used to form the nickel(II) diamide precursor, but hexadecylamine was once again used as solvent. We also hoped to glean information about the role of the amine moiety in solvent (*i.e.*, the amine other than the equivalent formed by β-H abstraction of one amide ligand by another). We thus employed hexadecene as solvent, in order to examine the role of the excess amine while retaining the double bond. Meanwhile, the use of hexadecane eliminated all possible stabilizing features (Figure II-21).

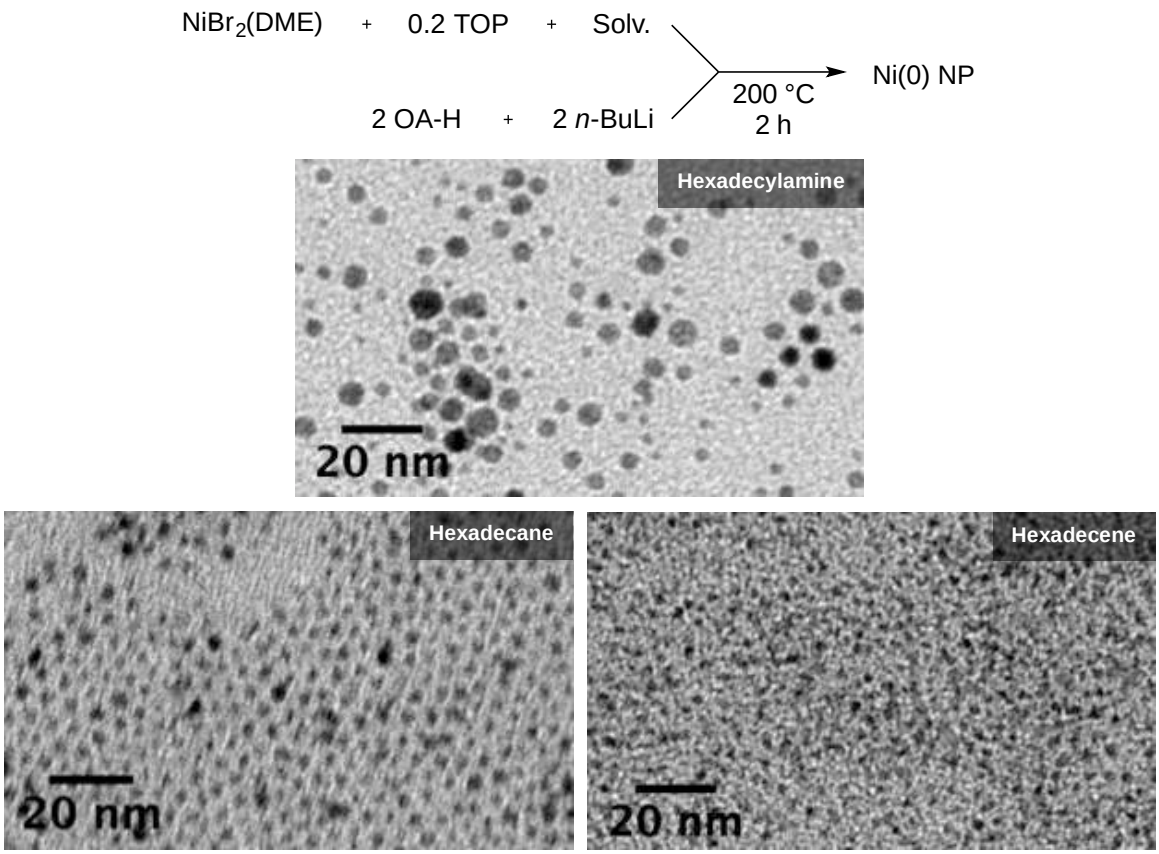

Figure II-21. Equation and TEM image of replacement of oleylamine as solvent by related solvents. Hexadecylamine (D = 5.1 ± 1.7 nm), hexadecene (D = 3.0 ± 0.4 nm), and hexadecane (D = 3.5 ± 0.7 nm) examined.

This set of experiments made clear that the combination of the amine moiety and the double bond led to much larger NPs, without providing a plausible reason. The use of hexadecylamine showed that the type of amide ligand in the nickel(II) precursor does indeed make a substantial difference to the resulting NPs. Comparing the two sets of NPs formed using hexadecylamine as solvent, using either nickel(II) dihexadecylamide as the precursor or using **1**, shows a difference in both size and size-dispersity by a factor of almost two.

Even when **1** is used as the precursor for the NPs, the absence of the double bond in the solvent makes a substantial difference in the size and size-dispersity. However, we must be careful in attributing all of the differences of nanoparticle size and size-dispersity to the existence or absence of a double bond. Small impurities in the solvent may well affect the results of the reaction, as has previously observed between different sources of TOP.[12]

Alternatively, the results observed in Figure II-20 may be due to differences in the premixing of reaction components. Because hexadecylamine is a solid at room temperature, the two separate components of the reaction were initially dissolved in benzene. After the two components were mixed together, the resulting solution was dried *in vacuo* before heating. These differences in set-up may have resulted in lingering benzene in the hexadecylamine conditions, despite extensive drying. The increased pre-mixing time may also result in ripening effects similar to those observed in section 6.

Another possibility is changing reaction volume. In each case, the stoichiometry between "solvent" and metal salt that was held constant; that is, eight equivalents of "solvent" were used to solubilize the reaction mixture. Although these differences are not large (790 µL for oleylamine vs. 703 µL for hexadecane, 688 µL for hexadecene, and 741 µL for hexadecylamine at 60 °C, above its melting point), they may account for some differences in the resulting particles.

Briefly, the slightly different solvents resulted in big differences in the resulting NPs. A combinatorial screening of all parameters might give a better idea of how each factor, particularly the amine moiety and the unsaturated bond, contributes to the NP size and size-dispersity. Without clearly understanding the molecular effects of each solvent, we may treat the parameter as a coarse means of controlling the size of the NPs.

10. DFT calculations: Mechanism of Ni(0) formation from Ni(II) precursor

DFT calculations yielded quantitative insight into the energetic cost of NP formation.[13] We specifically examined the chemical reduction of the $[Ni(NHR)_2]_n$ precursor into the initial Ni(0) monometallic species, which then form Ni(0) NPs by aggregation. The choice of functional used for DFT calculation, pseudo-potentials, and detailed parameters are described in the experimental section. Oleylamine was modeled by NH_2CH_3 to limit the computational cost, as it has been previously shown that larger chains (longer than three carbon units) do not significantly affect energy barriers.[14] The experiments described above show that the addition of RNH_2 to $[Ni(RNH)_2]_n$ followed by heating results in the formation of a monomeric species prior to reduction to Ni(0) NPs. We thus envisaged different pathways, starting from the following species: $Ni(NHCH_3)_2$, $Ni(NHCH_3)_2(NH_2CH_3)$, and

$Ni(NHCH_3)_2(NH_2CH_3)_2$. The pathway starting from the diamide complex $Ni(NHCH_3)_2$ is energetically more demanding than the pathway starting from $Ni(NHCH_3)_2(NH_2CH_3)$, and moreover, the former species is higher in energy than the latter. Meanwhile, the optimization of $Ni(NHCH_3)_2(CH_3NH_2)_2$ resulted in the decoordination of one equivalent of CH_3NH_2, showing the tricoordinate complex to be the most stable of the three possible starting species.

The optimized geometry for the tricoordinate complex $Ni(NHCH_3)_2(CH_3NH_2)$ is T-shaped at Ni, with the two amido CH_3NH ligands in *cis* position, as expected for two strong ligands demonstrating the trans-effect. This geometry is the most favorable for the transfer of a β-H of one amido to the other. Two such transfer pathways were calculated, labeled **I** and **II** (Scheme II-5). In pathway **I**, the H is transferred from the β-H of the amido that lies *cis* to the amine. TS_A is located 36.9 kcal/mol higher than the starting complex, and leads to a minimum at 24.0 kcal/mol, in which the imine is *cis* to both the amines. Pathway **II** is kinetically more favorable, as TS_B is located at 31.5 kcal/mol, 4.4 kcal/mol lower than TS_A. In TS_B, the H is transferred from the β-H of the amido *trans* to the amine.

This difference in energy between TS_B and TS_A may be rationalized by means of the differences in bond distances (Figure II-22). A key difference between the two transition states is the N1–Ni distance, which is much shorter in TS_B than in TS_A, a difference of 0.12 Å. This difference in length reflects he more amide-like character of N1, compared to the longer, amine-type N–Ni distances of N2 and N3. The shorter N1–Ni distance positions the β-H to form a more favorable five-membered ring, from which the hydrogen is transferred from C to N2.

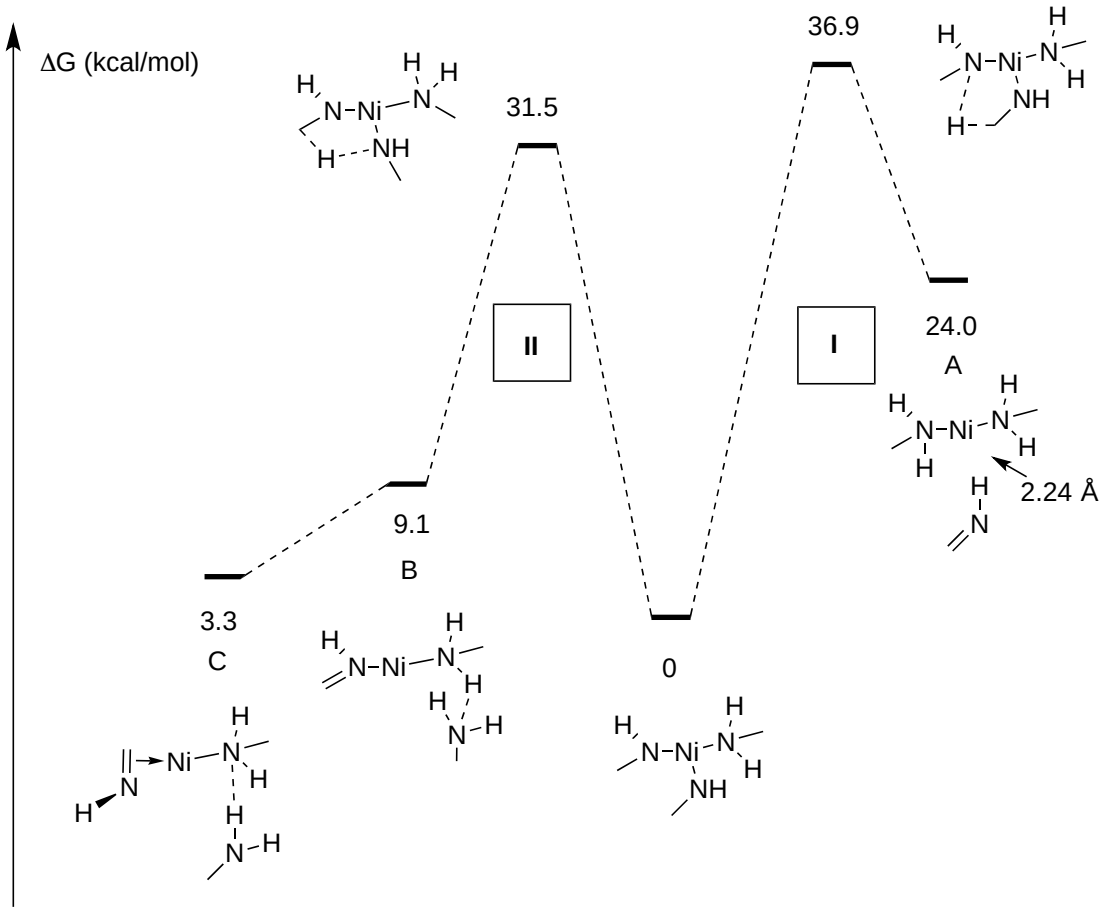

Scheme II-5. Possible pathways to Ni(0) formation. Pathway I lies to the right of the zero-point, and pathway II to the left. Density functional: M06L. Basis set: C, N: 6-31g*, H: 6-311+g**Ni: def2tzvp.

N1–Ni 1.779 Å
N2–Ni 1.953 Å
N3–Ni 1.986 Å

N1–Ni 1.899 Å
N2–Ni 1.923 Å
N3–Ni 1.891 Å

Figure II-22. Optimized GaussView models of transition states TS_A (right) and TS_B (left).

TS_B resolves to Ni(0) complex **B**, which is 9.1 kcal/mol higher in energy than the starting complex. This complex has several interesting features. First, the imine

ligand is bound to the Ni center via the N center. Secondly, the amine formed during the process is not coordinated to the Ni center, but rather forms a hydrogen bond with the coordinated amine. This complex then leads to a more stable Ni(0) species, C, that is 5.8 kcal/mol lower in energy compared to B, in which the imine is coordinated via the C=N π system. This coordination is consistent with the better stabilization of the Ni(0) d10 complex by metal back donation into the low lying π* system of the imine rather than by the simple donation of the lone pair of the imine N. These calculations show that the Ni(0) prefers the linear ML2 geometry to ML3, in which the imine and amine ligands are present. Nonetheless, the poorly stabilized 14-electron Ni(0) complex would undergo decomposition to Ni(0) NPs upon ligand dissociation at the reaction temperature. Overall, the mechanism proposed is in full agreement with experimental findings: fast reduction at 150 °C and the presence of two different ligands in the medium, allowing varied stabilization of the Ni(0) NPs. This mechanism is also in agreement with our initial hypothesis, which states that the nickel(II) diamide complexes would be efficient precursors for Ni(0) via intramolecular β-H transfer. This transfer provides a path for reduction without involvement of external reducing agents.

11. Extension to Fe and Co nanoparticles

In order to examine the generality of this nanoparticle synthesis method, we attempted to synthesize nanoparticles of Fe and Co. Fe NPs are of great interest because of their magnetic properties, catalytic utility, low toxicity, and low cost.[15a] The most successful current methods of Fe NP synthesis employ either the decomposition of the Fe(0) species iron(0) pentacarbonyl,[15] or the reduction of an isolated metal amide, iron(II) bis(trimethylsilylamide), under hydrogen pressure.[16] Carbonyl ligands are very tightly bound to the nanoparticles, while the $Fe[N(SiMe_3)_2]_2$ species lacks the β-hydrogen needed to follow the mechanism demonstrated above for nickel. Instead, $Fe[N(SiMe_3)_2]_2$ relies on hydrogen as the reducing agent.

The most effective methods of Fe NP synthesis from $Fe(CO)_5$ require the scale-limited and poorly reproducible hot injection method,[17] partly because of the low boiling point of the metal complex (103 °C). Furthermore, these syntheses are typically low yielding. The metastability of the metal complex leads to the

decomposition of the precursor to a variety of stable molecular metal clusters before NP synthesis.[15a] Moreover, the resulting nanoparticles, of 6 to 20 nm, bear the tightly bound CO ligands at the surface, which reduce the reactivity of the active surfaces for further use (*e.g.*, catalysis). This eliminates the big reactivity advantage nanoparticles have over bulk materials, despite the high surface area of nanoparticles. The use of the less tightly bound amine and phosphine ligands permits us to regain surface sites and reintroduces the possibility of high reactivity.

The synthesis of Fe NPs from $Fe[N(SiMe_3)_2]_2$ avoids these problems, and indeed results in the synthesis of highly ordered 3D superlattices of Fe nanocubes of 7-nm edges. However, the synthesis of the precursor is nontrivial, requiring a distillation step,[18] and the reaction uses hydrogen pressure over 48 h. We sought to develop a simpler method of Fe NP synthesis that would also avoid the problems arising from the decomposition of the carbonyl precursor.

Limited reaction condition optimization was performed, largely based on the results of optimization from the formation of Ni(0) NPs. An isolated iron(II) dioleylamide species did indeed result in Fe(0) NPs, of 5.2 ± 1.6 nm (Figure II-23). Changing various parameters, such as solvent and temperature, did not significantly improve monodispersity.

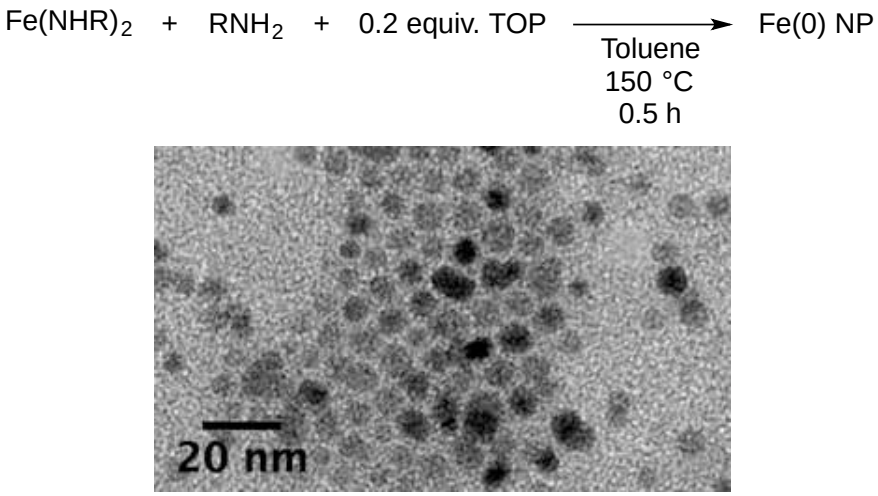

Figure II-23. Equation and TEM image of Fe(0) NPs from iron(II) dioleylamide (D = 5.2 ± 1.6 nm).

A literature survey of Co NP synthesis shows fewer examples of monodisperse particles. Co NPs are of increasing interest due to their activity in the electrochemical oxygen evolution reaction (OER) and their magnetism.[19a] Co(0)

particles have been most commonly obtained from the decomposition of dicobalt(0) octacarbonyl (< 10 nm),[19] or the reduction of cobalt(II) chloride using either sodium borohydride (10 – 20 nm) or hydrogen (gas-phase reduction, 50 – 78 nm).[20] The carbonyl precursor incurs many of the same problems described above for $Fe(CO)_5$, but non-carbonyl precursors typically fail to yield monodisperse particles. As in the case of Fe(0), an isolated cobalt(II) dioleylamide species was reduced to Co(0) NPs, of 4.7 ± 1.6 nm.

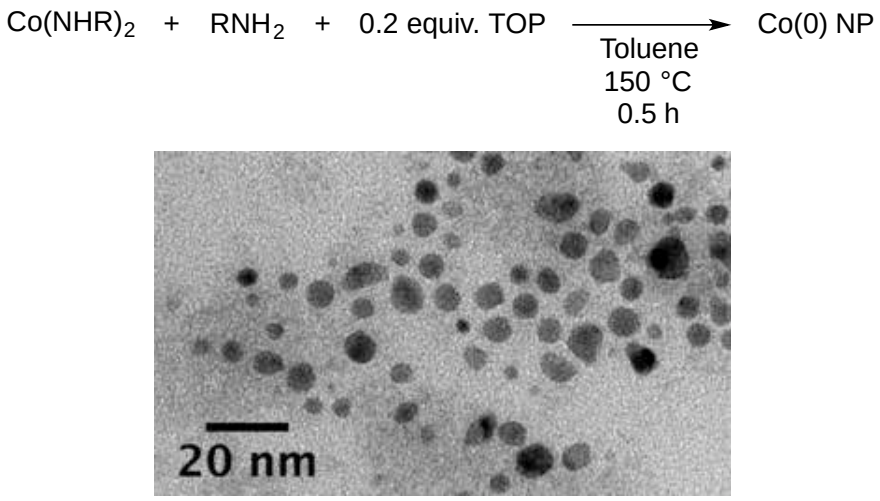

Figure II-24. Equation and TEM image of Co(0) NPs from cobalt(II) dioleylamide.

Employing the "two-pot" method used for Ni NP synthesis with the commercially available iron(II) bromide and cobalt(II) bromide resulted in quantitative conversion to NPs of 6.8 ± 0.8 nm for Fe and 4.5 ± 0.6 nm for Co (Figure II-25). The small size of these spherical, monodisperse particles, as well as the absence of carbonyl ligands, make them extremely promising for applications such as catalysis.

The use of a commercially available precursor, the presence of a solution-phase reducing agent, and the substantially shorter reaction time make this method of Fe NP synthesis much more accessible than that beginning from $Fe[N(SiMe_3)_2]_2$. The size-tunability observed in Ni may be extendable to Fe, which would result in particles suited for a greater variety of applications.

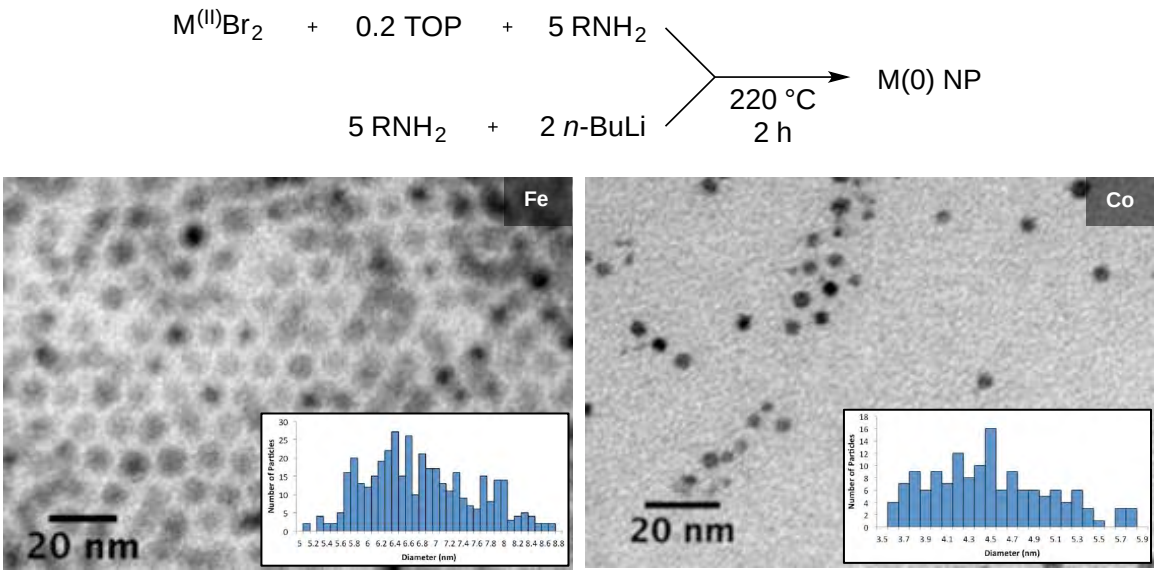

Figure II-25. Equation and TEM images of NPs obtained using "two-pot" method: Fe (D = 6.8 ± 0.8 nm) and Co (D = 4.5 ± 0.6 nm) NPs derived from MBr_2.

Similarly, the small size and relative monodispersity make these particles of Co promising for the high-value reactions for which Co NPs are prized. In the case of both metals, preliminary investigations suggest that the addition of TOP may result in size-tunability of the particles.

12. Catalysis with metal(0) nanoparticles

The synthesis of various metal(0) nanoparticles has been presented here with the goal of numerous applications. To that end, several preliminary reactions were attempted in order to show the utility of these nanoparticles for catalysis.

Molecular Ni(II) species have been shown to efficiently catalyze the hydrosilylation of alkenes. Tilley has shown the use of a monomeric, two-coordinate Ni(II) complex to catalyze the addition of a silane across the unsaturated bond of 1-octene (Scheme II-6).[21]

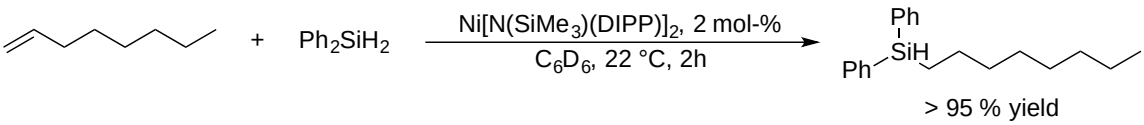

Scheme II-6. Hydrosilylation of 1-octene catalyzed by molecular nickel(II) bis[(trimethylsilyl)(diisopropylphenyl)amine].[21]

As a preliminary proof of concept, we examined the same reaction using the Ni NPs synthesized from **1** made *in situ* (Figure II-23). The Ni NPs require harsher conditions than the molecular nickel(II) catalyst (90 °C *vs.* 22 °C), but they perform the transformation quantitatively with half of the catalyst loading (1 % *vs.* 2 %, with respect to Ni). Further, the particles could be conveniently separated from the reaction by centrifugation. They could be reused at least once with no apparent loss of activity. To our knowledge, this is only the second example of the use of Ni(0) NPs for the catalytic hydrosilylation of alkenes. Indeed, the first example emerged in the literature in 2016, after the work shown in Scheme II-7 had already been carried out.[22]

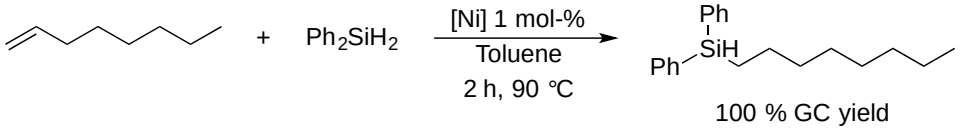

Scheme II-7. Hydrosilylation of 1-octene catalyzed by Ni NPs of D = 11.0 + 1.1 nm derived from *in situ*-synthesized **1**.

Another example of catalysis using the present Ni NPs is the hydrogenation of phenylacetylene. Previous work has shown that Ni NPs reduce phenylacetylene indiscriminately to ethylbenzene (Scheme II-8).[23]

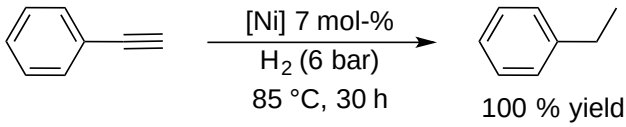

Scheme II-8. Reduction of phenylacetylene to ethylbenzene catalyzed by Ni NPs of 25 nm derived from $Ni(acac)_2$.[23]

Under milder conditions, using just 1 bar of H_2 instead of 6 bar, the Ni NPs synthesized from *in situ*-synthesized **1** selected predominantly for styrene production (Scheme II-9). By gas chromatography (GC), 89 % of the reduction product is styrene, while only 11 % of the fully hydrogenated ethylbenzene is obtained. Typically, this kind of product distribution is observed not with Ni(0) NPs, but with Ni_2P NPs, and to some extent, with $Ni_{3.5}P$ NPs.[23] The previously reported phosphorus-containing NPs display attenuated surface hydride adsorption. Phosphorus acts as a surface modifier, withdrawing electrons from Ni centers, and may also poison the surface by blocking unsaturated sites.[21] This suggests that the surface sites of the Ni NPs used in the present work also have poisoned surfaces,

despite not containing any phosphorus. The NPs used in the reaction demonstrated in Scheme II-9 contained oleylamine and TOP as surface ligands, as did those used in the present work, but the previous reaction mixture did not contain LiBr. We may thus postulate that the unsaturated surface sites are blocked by bromide ligands derived from the LiBr in solution.

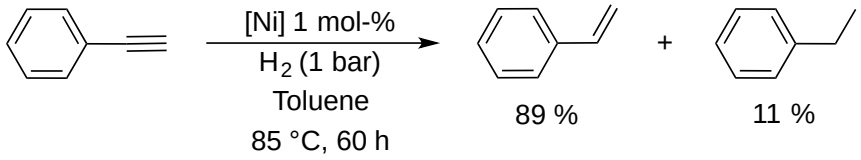

Scheme II-9. Reduction of phenylacetylene to a mixture of styrene and ethylbenzene catalyzed by Ni NPs of D = 11.0 + 1.1 nm derived from *in situ*-synthesized **1**.

A highly preliminary but potentially important example of catalysis using the Fe NPs synthesized in the present work involves the reduction of dinitrogen. The problem of nitrogen fixation is a notoriously difficult and vital one in the chemical literature.[24] Nishibayashi was able to achieve 25 equivalents tris(trimethylsilyl)amide from nitrogen using a $Fe(CO)_5$ catalyst with Na(0) and trimethylsilylchloride (Scheme II-10).[25]

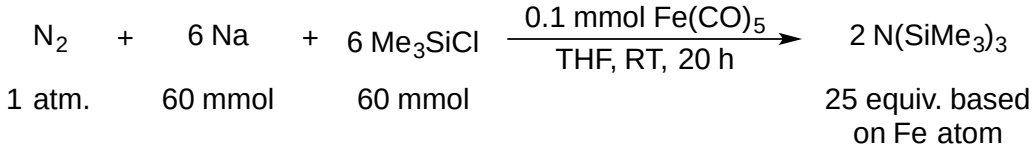

Scheme II-10. Reduction of N_2 to $N(TMS)_3$ using $Fe(CO)_5$.[25]

A similar reaction was attempted with the Fe NPs synthesized in the present work by the *in situ* formation of iron(II) dioleylamide (Scheme II-11). After three days in mild heat, a small amount of conversion to $N(TMS)_3$ was observed. Unfortunately, the system was not catalytic; indeed, a substoichiometric 44 % of $N(TMS)_3$ was obtained with respect to atoms of Fe. Although these results were very modest, the activity was promising, and merits further examination. To our knowledge, this is the first example of the reduction of N_2 using Fe(0) NPs. The experiment holds great promise for this highly desirable reaction.

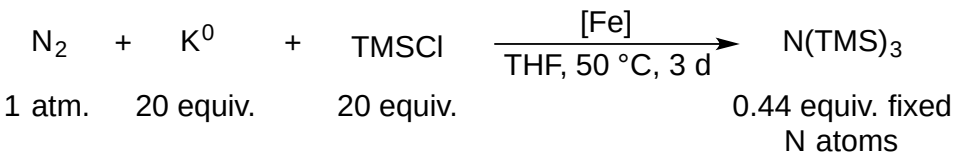

Scheme II-11. Reduction of N_2 to of $N(TMS)_3$ using Fe NPs derived from *in situ*-synthesized iron(II) dioleylamide. Equivalencies with respect to [Fe].

These results give a preliminary indication of the catalytic reactions that might be performed with the NPs described in this chapter. Although they are promising, room for improvement and expansion remains.

13. Conclusions

We demonstrated the synthesis of monodisperse metal(0) nanoparticles for Ni, Fe, and Co. This robust method crucially avoided the side production of water, preventing the formation of Fe and Co oxide particles. Ni was most thoroughly examined as the test case. The formation of Ni NPs was accomplished by thermally inducing the reduction of nickel(II) dioleylamide, which was formed from the commercially available $NiBr_2$(DME). This molecular precursor was either synthesized separately and isolated, or synthesized *in situ.* Calculations show that the reduction takes place by the abstraction of a β-H by one amide ligand from another, resulting in the formation of a Ni(0) amino-imino intermediate.

Both oleylamine and TOP acted as stabilizing ligands for the NPs, and TOP was used to tune the size of the resulting particles. The nickel(II) dioleylamide precursor polymerized in solution at room temperature, which resulted in differences between particles synthesized from isolated vs. *in situ*-formed precursor. This polymeric precursor depolymerized upon heating before undergoing reduction and forming Ni(0) nanoparticles.

The present work also performed preliminary investigations into the formation of Fe(0) and Co(0) NPs. The transformations that these different types of NPs can catalyze were also examined in a preliminary fashion, and the above results provide a promising debut for future work.

14. References

[1] Willis, A. L.; Chen, Z.; He, J.; Zhu, Y.; Turro, N. J.; O'Brien, S. *J. Nanomater.* **2007**, *14858*, 1–7. (b) Sun, S.; Zeng, H. *J. Am. Chem. Soc.* **2002**, No. 31, 8204–8205. (c) Nene, A. G.; Takahashi, M.; Somani, P. R. **2016**, 20–28.

[2] Carenco, Sophie; Boissiere, Cedric; Nicole, Lionel; Sanchez, Clement; le Floch, Pascal; Mézailles, Nicolas. *Chem. Mater.* **2010**, 22(4), 1340–1349.

[3] Mott, D.; Galkowski, J.; Wang, L.; Luo, J.; Zhong, C. J. *Langmuir* **2007**, *23* (10), 5740–5745.

[4] Mourdikoudis, S.; Liz-marzan, L. M. *Chem. Mater.* **2013**, *25* (9), 1465–1476.

[5] M.-J. Casanove, P. Lecante, E. Snoeck, A. Mosset, C. Roucau. *Journal de Physique III, EDP Sciences*, **1997**, *7* (3), 505–515.

[6] Thanh, N. T. K.; Maclean, N.; Mahiddine, S. *Chem. Rev.* **2014**, *114* (15), 7610–7630.

[7] (a) Mohamed, M. B.; Wang, Z. L.; El-Sayed, M. *J. Phys. Chem. A* **1999**, *103* (49), 10255–10259. (b) Jiang, X. C.; Chen, W. M.; Chen, C. Y.; Xiong, S. X.; Yu, A. B. *Nanoscale Res. Lett.* **2011**, *6* (1), 1–9. (c) Lee, S.; Song, D.; Kim, D.; Lee, J.; Kim, S.; Park, I. Y.; Choi, Y. D. *Mater. Lett.* **2004**, *58* (3–4), 342–346.

[8] Lipschutz, M. I.; Tilley, T. D. *Chem. Commun. (Camb).* **2012**, *48* (57), 7146–7148. (b) Hope, H.; Olmstead, M. M.; Murray, B. D.; Power, P. P. *J. Am. Chem. Soc.* **1985**, *107* (3), 712–713. (c) Faust, M.; Bryan, A. M.; Mansikkamäki, A.; Vasko, P.; Olmstead, M. M.; Tuononen, H. M.; Grandjean, F.; Long, G. J.; Power, P. P. *Angew. Chem. Int. Ed.* **2015**, *54* (44), 12914–12917.

[9] Cohen, Y.; Avram, L.; Frish, L. *Angew. Chem. Int. Ed.* **2005**, *44* (4), 520–554.

[10] (a) Tang, B.; Xu, S.; An, J.; Zhao, B.; Xu, W.; Lombardi, J. R. *Phys. Chem. Chem. Phys.* **2009**, *11* (44), 10286–10292. (b) Zhang, Z.; Li, H.; Zhang, F.; Wu, Y.; Guo, Z.; Zhou, L.; Li, J. *Langmuir* **2014**, *30* (10), 2648–2659.

[11] Yanyun, M.; Zeng, J.; Li, W.; McKiernan, M.; Xie, Z.; Xia, Y. *Adv. Mater.* **2010**, *22* (17), 1930–1934.

[12] Carenco, S. Doctoral Dissertation, l'Université Pierre et Marie Curie, **2011**.

[13] Calculations performed by N. Mézailles.

[14] Carenco, S., Labouille, S., Bouchonnet, S., Boissière, C., Le Goff, X.-F., Sanchez, C., Mézailles, N. *Chem. Eur. J.*, **2012**, *18*(44), 14165–73.

[15] (a) Huber, D. L. *Small* **2005**, *1* (5), 482–501. (b) Farrell, D.; Majetich, S. A.; Wilcoxon, J. P. *J. Phys. Chem.* **2003**, *107* (40,2003), 11022–11030. (c) Chen, Y. X.; Chen, S. P.; Zhou, Z. Y.; Tian, N.; Jiang, Y. X.; Sun, S. G.; Ding, Y.; Zhong, L. W. *J. Am. Chem. Soc.* **2009**, *131* (31), 10860–10862. (d) Carenco, S.; Hu, Y.; Florea, I.; Ersen, O.; Boissière, C.; Mézailles, N.; Sanchez, C. *Chem. Mater.* **2012**, *24* (21), 4134–4145.

[16] Chaudret, B.; Amiens, C.; Renaud, P.; Fejes, P. *Science* **2004**, *303*, 821–823.

[17] (a) Henglein, A. *J. Phys. Chem.* **1982**, *86*(13), 2291−2293. (b) Rossetti, R.; Hull, R.; Gibson, J. M.; Brus, L. E. *J. Chem. Phys.* **1985**, *82*(1), 552−559. (c) Murray, C. B.; Norris, D. J.; Bawendi, M. G. *J. Am. Chem. Soc.* **1993**, *115*(19), 8706−8715. (d) Park, J.; Joo, J.; Kwon, S. G.; Jang, Y.; Hyeon, T. *Angew. Chem., Int. Ed.* **2007**, *46*(25), 4630−4660. (e) Van Embden, J.; Chesman, A. S. R.; Jasieniak, J. J. *Chem. Mater.* **2015**, *27* (7), 2246–2285.

[18] Andersen, R.; Faegri, K.; Green, J. C.; Haaland, A.; Lappert, M. F.; Leung, W. P.; Rypdal, K. *Inorg. Chem.* **1988**, *27* (10), 1782–1786.

[19] (a) Wu, L.; Li, Q.; Wu, C. H.; Zhu, H.; Mendoza-Garcia, A.; Shen, B.; Guo, J.; Sun, S. *J. Am. Chem. Soc.* **2015**, *137* (22), 7071–7074. (b) Michalek, F.; Lagunas, A.; Jimeno, C.; Pericas, M. A. *J. Mater. Chem.* **2008**, *18* (39), 4692–4697. (c) Yang, H. T.; Su, Y. K.; Shen, C. M.; Yang, T. Z.; Gao, H. J. *Surf. Interface Anal.* **2004**, *36* (2), 155–160. (d) Schällibaum, J.; Dalla Torre, F. H.; Caseri, W. R.; Löffler, J. F. *Nanoscale* **2009**, *1* (3), 374–381. (e) Hess, P. H.; Parker, P. H. *J. Appl. Polym. Sci.* **1966**, *10*, 1915–1927. (f) Zacharaki, E.; Kalyva, M.; Fjellvåg, H.; Sjåstad, A. O. *Chem. Cent. J.* **2016**, *10*, 10–11.

[20] (a) Jang, H. D.; Hwang, D. W.; Kim, D. P.; Kim, H. C.; Lee, B. Y.; Jeong, I. B. *Mater. Res. Bull.* **2004**, *39* (1), 63–70.(b) Liang, X.; Zhao, L. *RSC Adv.* **2012**, *2* (13), 5485–5487.

[21] Lipschutz, M. I.; Tilley, T. D. *Chem. Commun.* **2012**, *48* (57), 7146–7148.

[22] Buslov, I.; Song, F.; Hu, X. *Angew. Chemie Int. Ed.* **2016**, *55*, 12295–12299.

[23] Carenco, S.; Leyva-Pérez, A.; Concepción, P.; Boissière, C.; Mézailles, N.; Sanchez, C.; Corma, A. *Nano Today* **2012**, *7* (1), 21–28.

[24] Yang, Z.; Ho, B. M.; Lukoyanov, D.; Yang, Z.; Dean, D. R.; Seefeldt, L. C. *Chem. Rev.* **2014**, *114* (8), 4041–4062.

[25] Yuki, M.; Tanaka, H.; Sasaki, K.; Miyake, Y.; Yoshizawa, K.; Nishibayashi, Y. *Nat. Commun.* **2012**, *3:1254*, 1–6.

15. Experimental Details

General considerations

All reactions were routinely performed under an inert atmosphere of argon or nitrogen using standard Schlenk and glovebox techniques and dry deoxygenated solvents. Solvents were obtained from an MBraun Solvent Purifying system SPS 800. Oleylamine (OA, Aldrich, 98 %) and 1-octadecene (ODE, Aldrich, 90 %) were dried *in vacuo* for 1 h at 130 °C and taken into the glovebox for use. Lithium bromide (Aldrich, ≥ 99 %) was dried *in vacuo* overnight at 240 °C and taken into the glovebox for use. Nickel(II) bromide ethylene glycol dimethyl ether complex ($NiBr_2$(DME), Aldrich, 97 %), iron(II) bromide (Aldrich, 98 %), cobalt(II) bromide (Aldrich 99 %), *n*-butyllithium (Aldrich, 2.5 M in hexane), trioctylphosphine (TOP, Cytec), and deuterated THF and toluene (Aldrich, ≥ 99.5 atom % D) were used as received.

Synthesis of Precursor

Synthesis of nickel(II) dioleylamide 1.

Oleylamine (10.84 mL, 31.84 mmol) was dissolved in 10 mL pentane and chilled on the Schlenk line in an ice water bath. To this, 2.5 M *n*-BuLi in hexanes (12.7 mL, 31.84 mmol) was added slowly. The bath was removed. The solution was warmed to room temperature and stirred for three hours. It was dried *in vacuo* to a yellow foam. This was redissolved in 10 mL toluene. $NiBr_2$(DME) (5.18 g, 16.8 mmol) was added, and the resulting dark brownish purple solution was stirred at room temperature overnight. It was dried *in vacuo* and redissolved in 20 mL pentane. The mixture was stirred for one hour, and then the insoluble lithium bromide was permitted to settle. The supernatant was filtered and dried in *vacuo*. The nuclear magnetic resonance spectrum was recorded on a Bruker AC-300 SY spectrometer operating at 300.13 MHz for ^{1}H. ^{1}H NMR (300.1 MHz, toluene-*d8*): δ = 0.9 – 2.0 ppm (m, $Ni[N(H)C_8\mathbf{H}_{16}CH{=}CHC_8\mathbf{H}_{16}]_2$), δ = 2.0 – 2.5 ppm (m, $Ni[N(\mathbf{H})C_8H_{16}CH{=}CHC_8H_{16}]_2$), δ = 5.3 – 5.7 ppm (m, $Ni[N(H)C_8H_{16}C\mathbf{H}{=}C\mathbf{H}C_8H_{16}]_2$). An elemental analysis corresponded with the desired product. Expected: % C: 73.1, % H: 12.3, % N: 4.7. Found: % C: 73.4 %, % H: 11.9, % N: 4.9.

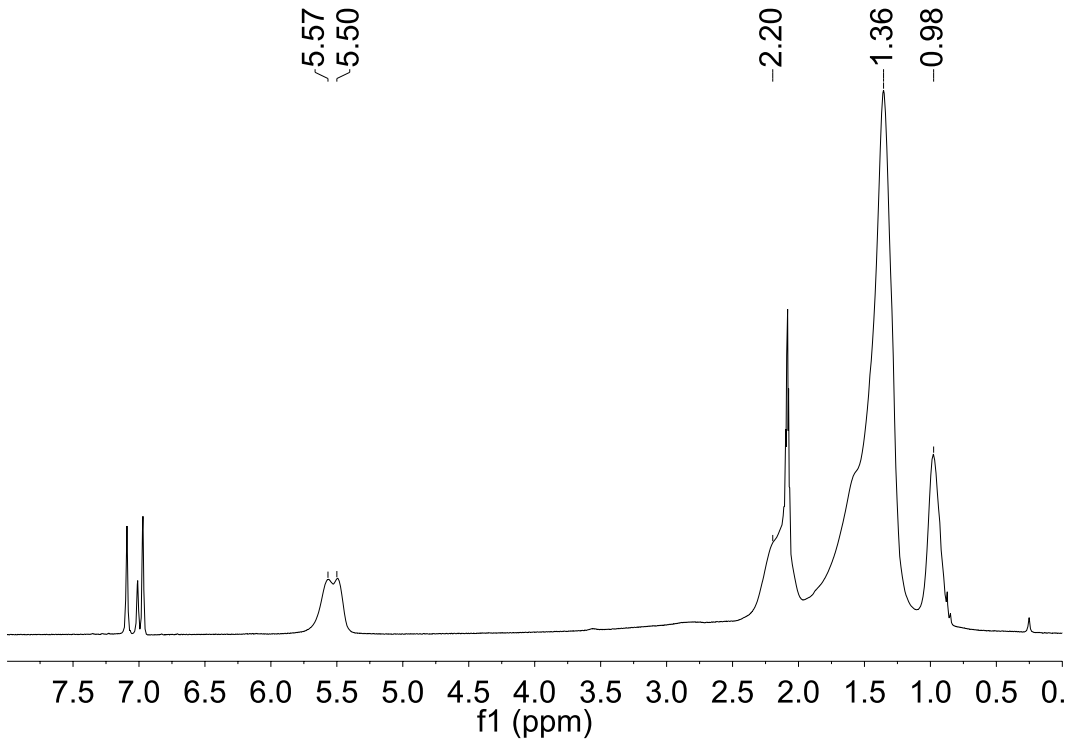

Figure Exp2.1: ^{1}H NMR spectrum of nickel(II) dioleylamide in toluene-d_8.

The broad nature of the peaks, particularly the two sets of peaks observed around 5.5 ppm, are indicative of the oligomeric nature of the precursor.

Analysis of TEM images

TEM samples were prepared by depositing a drop of a pentane solution of NPs on a copper grid. The images were recorded on a JEOL JEM 1400 TEM. EDX was performed on a JEOL JEM-ARM-200F.

TEM images were analyzed using ImageJ software. Areas of NPs were collected and the diameter was determined by assuming that the NPs are spherical. The analysis of particles of < 2 nm in diameter Statistical analyses were performed using Microsoft Excel, using the STDEV.S function on sorted frequencies of diameters.

Synthesis of Nanoparticles

The procedures outlined below were repeated at least twice to verify reproducibility.

1. Synthesis of nickel(0) nanoparticles using isolated 3.

In the most basic reaction shown in Figure II-1 of the text, **1** (59.2 mg, 0.1 mmol) was dissolved in 1 mL toluene in a Schlenk flask with a magnetic stir bar. This mixture was heated at 150 °C for 0.5 h on a hot plate in a silicone oil bath. The flask was cooled to room temperature by being plunged immediately into a beaker of tap water. The particles were precipitated by addition of 4 mL dry ethanol, and the mixture was centrifuged. The supernatant was removed by pipette, and the NPs were redispersed in pentane.

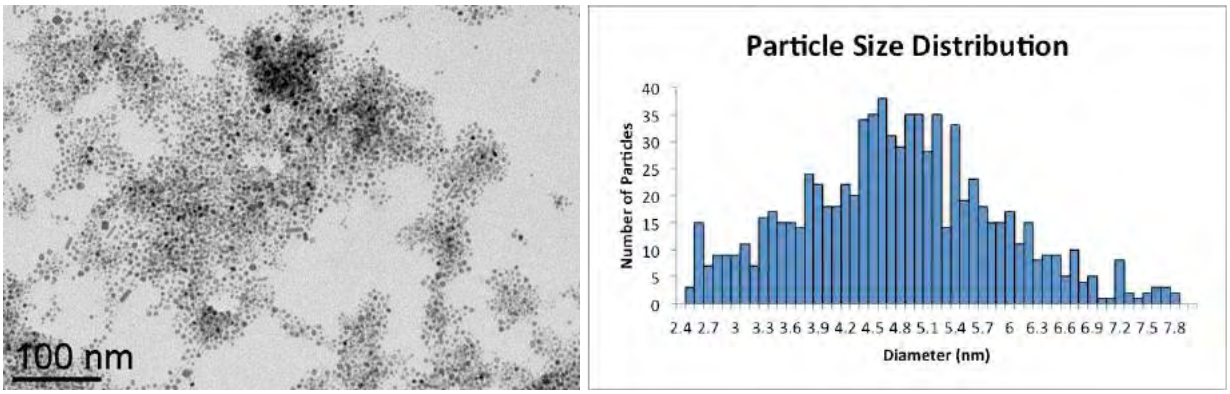

Figure Exp2.2: TEM image of Ni NPs synthesized from isolated **1** decomposed in toluene at 150 °C and corresponding size distribution.

In the reaction shown in Figure II-2 of the text, which produced a bimodal distribution of particles, one equivalent oleylamine (33.0 µL, 0.1 mmol) was also added before heating.

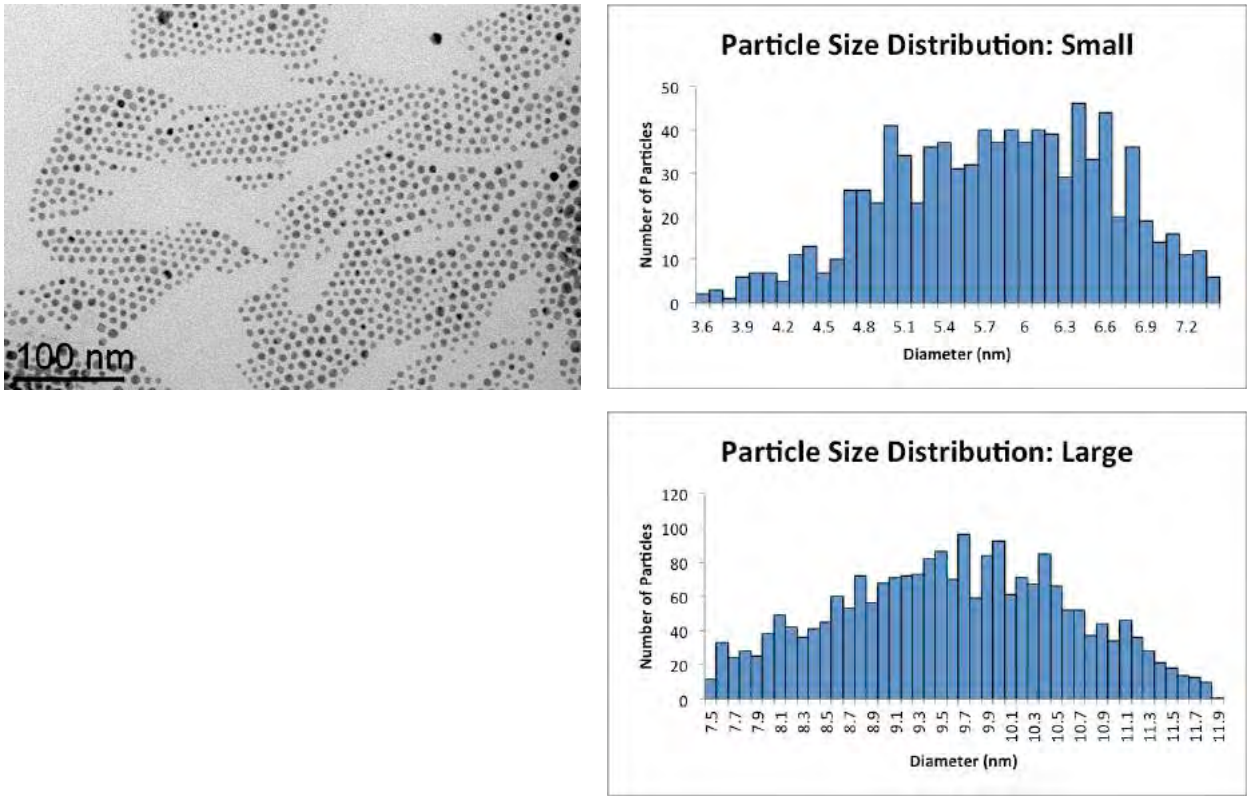

Figure Exp2.3: TEM image of Ni NPs synthesized from isolated **1** decomposed in toluene at 150 °C in the presence of 1 free equiv. oleylamine and corresponding size distribution, separated into small and large particles to better highlight the bimodal nature of the resulting particles.

2. Effect of TOP on particle size

In the series of reactions shown in Figure II-3 of the text, which demonstrated the indirect correlation between the amount of TOP and the size of the resulting particles, **1** (59.2 mg, 0.1 mmol) was dissolved in toluene in a Schlenk flask with a magnetic stir bar, along with oleylamine (33.0 µL, 0.1 mmol) and TOP. The reactions contained (a) 0.2, (b) 5, (c) 10, or (d) 15 equivalents TOP [(a) 8.9 µL, 0.02 mmol; (a) 223 µL, 0.5 mmol; (a) 446 µL, 1.0 mmol; (a) 669 µL, 1.5 mmol]. Correspondingly, the reactions held (a) 991 µL, (b) 777 µL, (c) 554 µL, or (d) 331 µL toluene, bringing the total volume of each solution to roughly 1 mL. Each of the four reactions was then heated at 150 °C for 0.5 h. As before, they were cooled to room temperature by being plunged immediately into a beaker of tap water. The particles were precipitated by addition of 4 mL dry ethanol to each flask, and the mixtures were centrifuged. The supernatants were removed by pipette, and the NPs were redispersed in pentane.

In the cases of 0.2, 2, and 5 equivalents of added TOP, some small nanoparticles were obtained as well. The small particles can be separated from the large ones by employing size-selective precipitation. Instead of using 4 mL dry ethanol to precipitate the NPs, just 1 mL was used at first, resulting in the incomplete precipitation of the particles and favoring the precipitation of the larger NPs. The resulting precipitate was then rewashed with 4 mL fresh, dry ethanol. This method also results in the loss of some small, unquantified amount of large NPs.

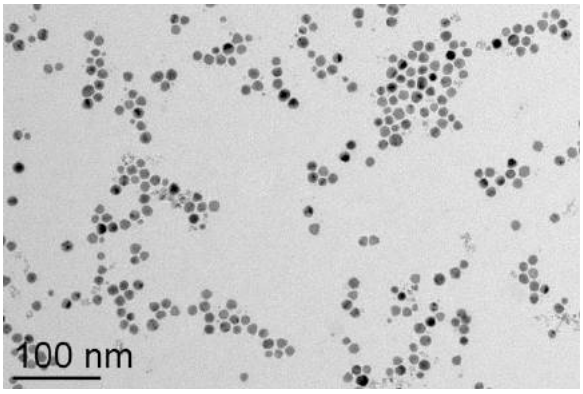

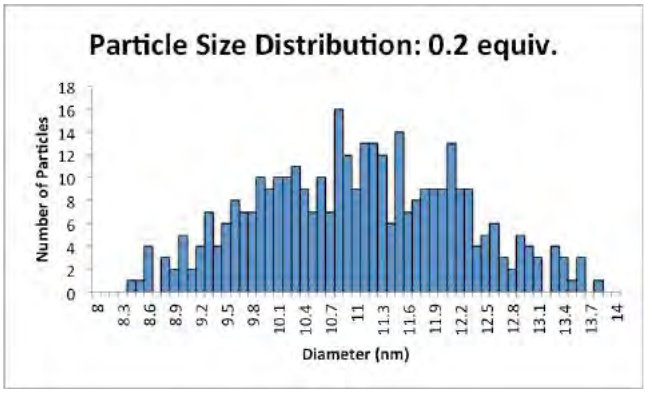

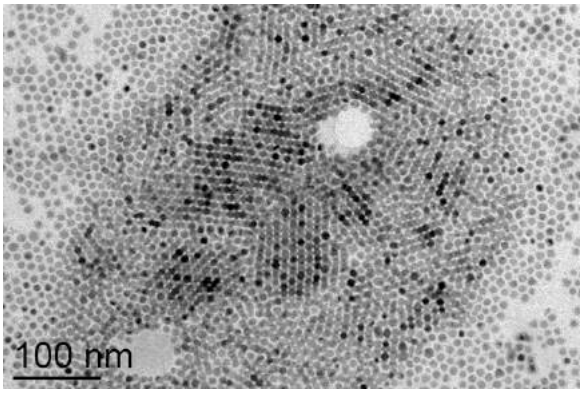

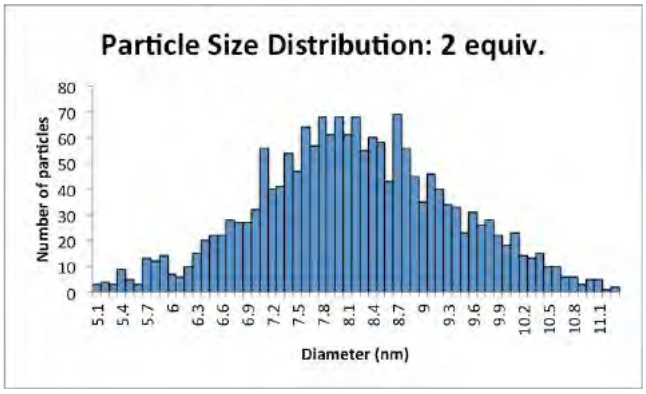

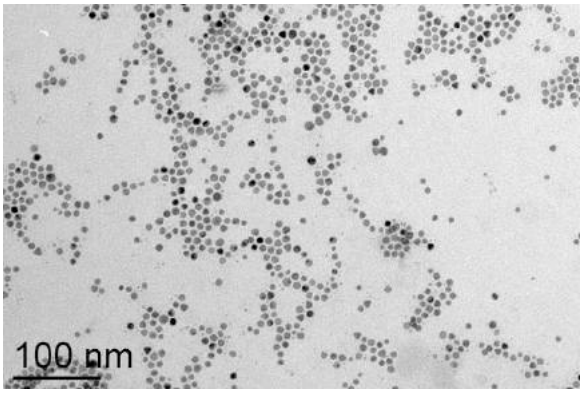

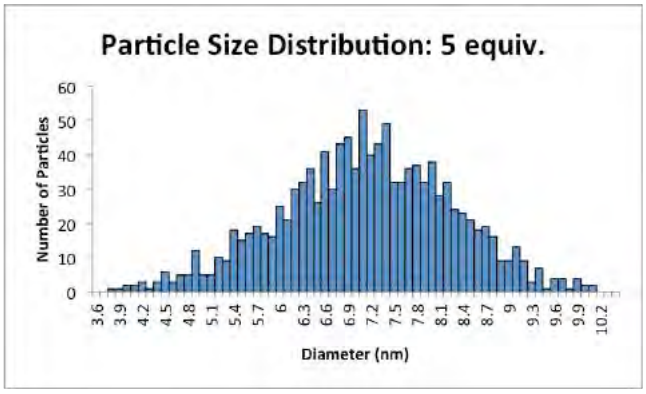

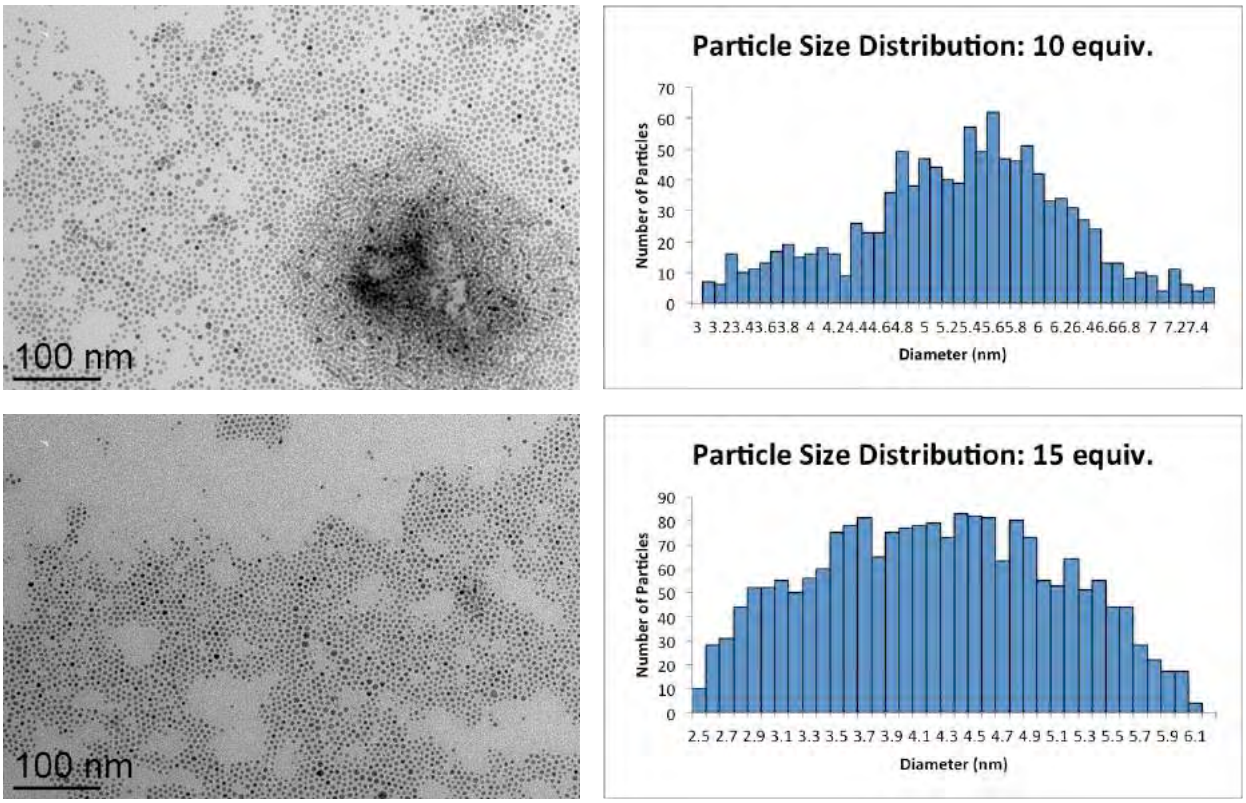

Figure Exp2.4: TEM images of Ni NPs synthesized from isolated **1** decomposed in toluene at 150 °C in the presence of 1 equiv. free oleylamine and 0.2, 2, 5, 10, and 15 equiv. TOP, and corresponding size distributions.

3. Synthesis of nickel(0) nanoparticles using in situ-synthesized 1.

In the most direct analogue to the nanoparticles seen in Figure II-3 of the text, in which isolated **1** was decomposed in toluene in the presence of 0.2 equiv. TOP at 150 °C, the same reaction was undertaken with the *in situ* formation of the bis(amide) complex. In this reaction, $NiBr_2$(DME) (92.6 mg, 0.3 mmol), oleylamine (98.7 µL, 0.3 mmol), TOP (26.8 µL, 0.06 mmol), and toluene (395 µL) were added to a Schlenk flask with a magnetic stir bar. A 5-mL scintillation vial with a magnetic stir bar was charged with oleylamine (197 µL, 0.6 mmol), *n*-BuLi (240 µL, 0.6 mmol), and toluene (297 µL). After 15 minutes of stirring, the solution in the scintillation vial was transferred via pipette to the Schlenk flask containing the nickel mixture. The resulting reddish mixture was heated at 150 °C for 0.5 h. It was cooled, precipitated, and redispersed using the same procedure outlined above. This reaction, which is the closest possible analogue to the procedure followed for the NPs observed in Figure II-3, yielded very different NPs.

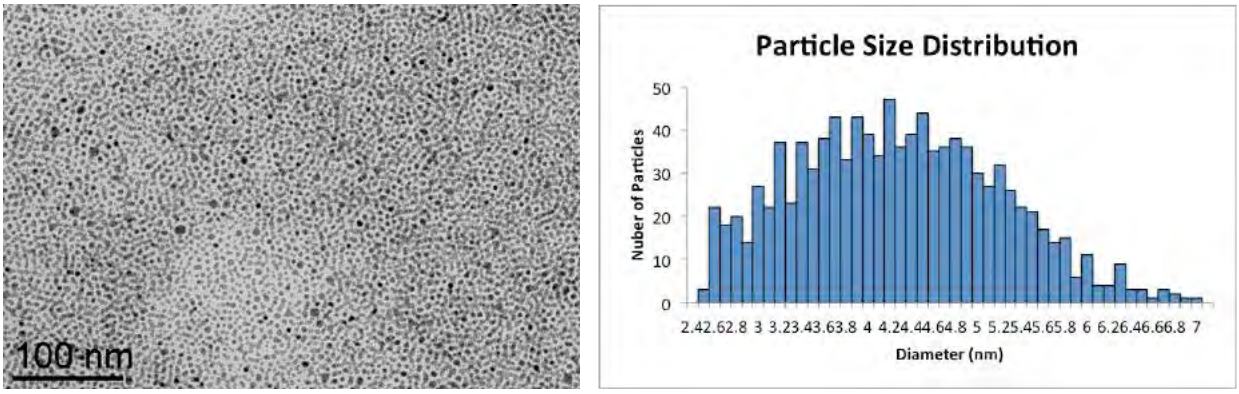

Figure Exp2.5: TEM image of Ni NPs synthesized from *in situ*-synthesized **1** decomposed in toluene at 150 °C in the presence of 1 equiv. free oleylamine and 0.2 equiv. TOP, and corresponding size distribution.

In the reaction shown in Figure II-4 of the text, $NiBr_2$(DME) (92.6 mg, 0.3 mmol), oleylamine (494 µL, 1.5 mmol), and TOP (26.8 µL, 0.06 mmol) were added to a Schlenk flask with a magnetic stir bar. A 5-mL scintillation vial with a magnetic stir bar was charged with oleylamine (494 µL, 1.5 mmol) and *n*-BuLi (240 µL, 0.6 mmol). After 15 minutes of stirring, the viscous, yellow solution in the scintillation vial was transferred via pipette to the Schlenk flask containing the nickel mixture. The resulting reddish mixture was heated at 200 °C for 2 h. It was cooled, precipitated, and redispersed using the same procedure outlined above.

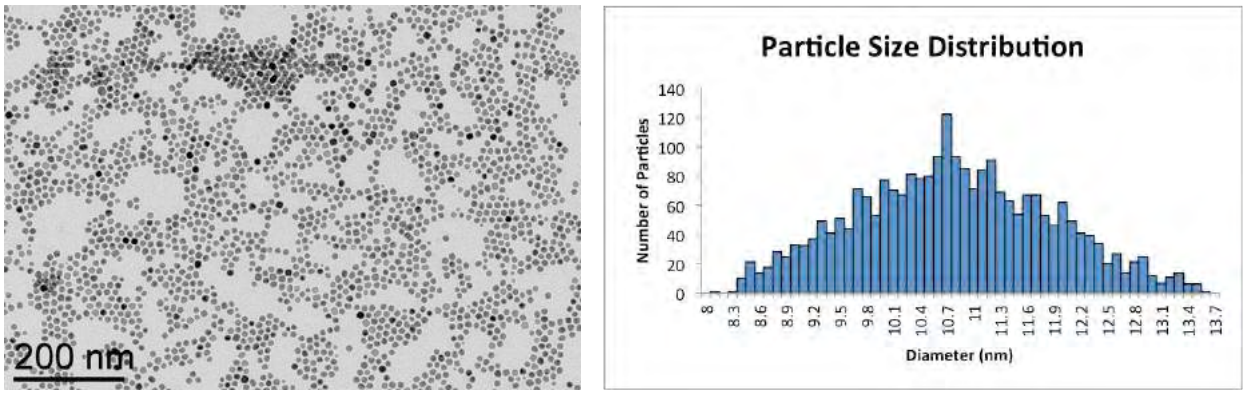

Figure Exp2.6: TEM image of Ni NPs synthesized from *in situ*-synthesized **1** decomposed in oleylamine at 200 °C in the presence of 0.2 equiv. TOP for 2 h, and corresponding size distribution.

This same reaction was stopped after 10 minutes to result in the particles seen in Figure II-7.

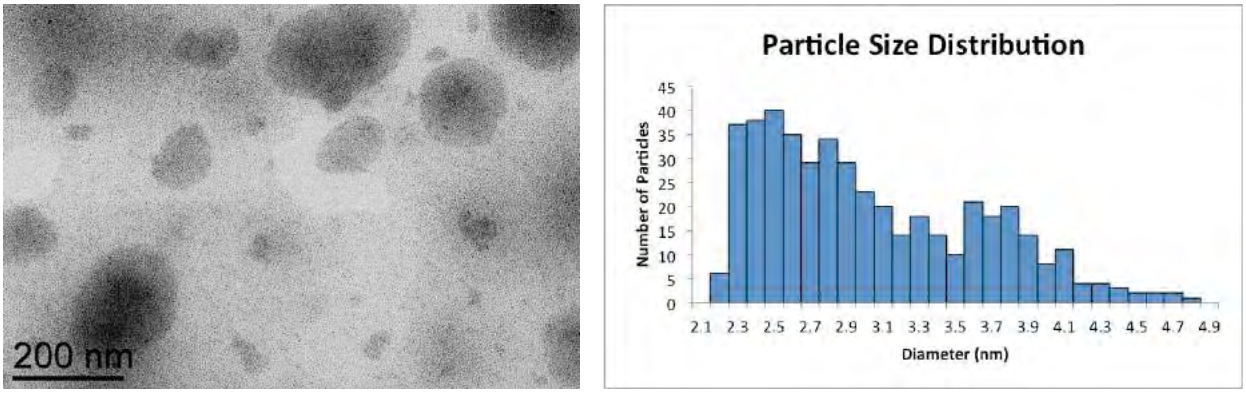

Figure Exp2.7: TEM image of Ni NPs synthesized from *in situ*-synthesized **1** decomposed in oleylamine at 200 °C in the presence of 0.2 equiv. TOP after 10 min., and corresponding size distribution.

The above reaction was also repeated after having dried the solution *in vacuo* to eliminate residual hexanes from the solution of *n*-BuLi. No difference was observed in the resulting TEM images from this drying step.

4. Effect of temperature on particle size

In the series of reactions summarized in Figure II-8, which demonstrated the direct correlation between temperature and the size of the resulting particles, $NiBr_2$(DME) (92.6 mg, 0.3 mmol), oleylamine (494 µL, 1.5 mmol), and TOP (26.8 µL, 0.06 mmol) were added to a Schlenk flask with a magnetic stir bar. A 5-mL scintillation vial with a magnetic stir bar was charged with oleylamine (494 µL, 1.5 mmol) and *n*-BuLi (240 µL, 0.6 mmol). After 15 minutes of stirring, the viscous, yellow solution in the scintillation vial was transferred via pipette to the Schlenk flask containing the nickel mixture. The resulting reddish mixture was heated at either 100 °C or 150 °C for 2 h. It was cooled, precipitated, and redispersed using the same procedure outlined above.

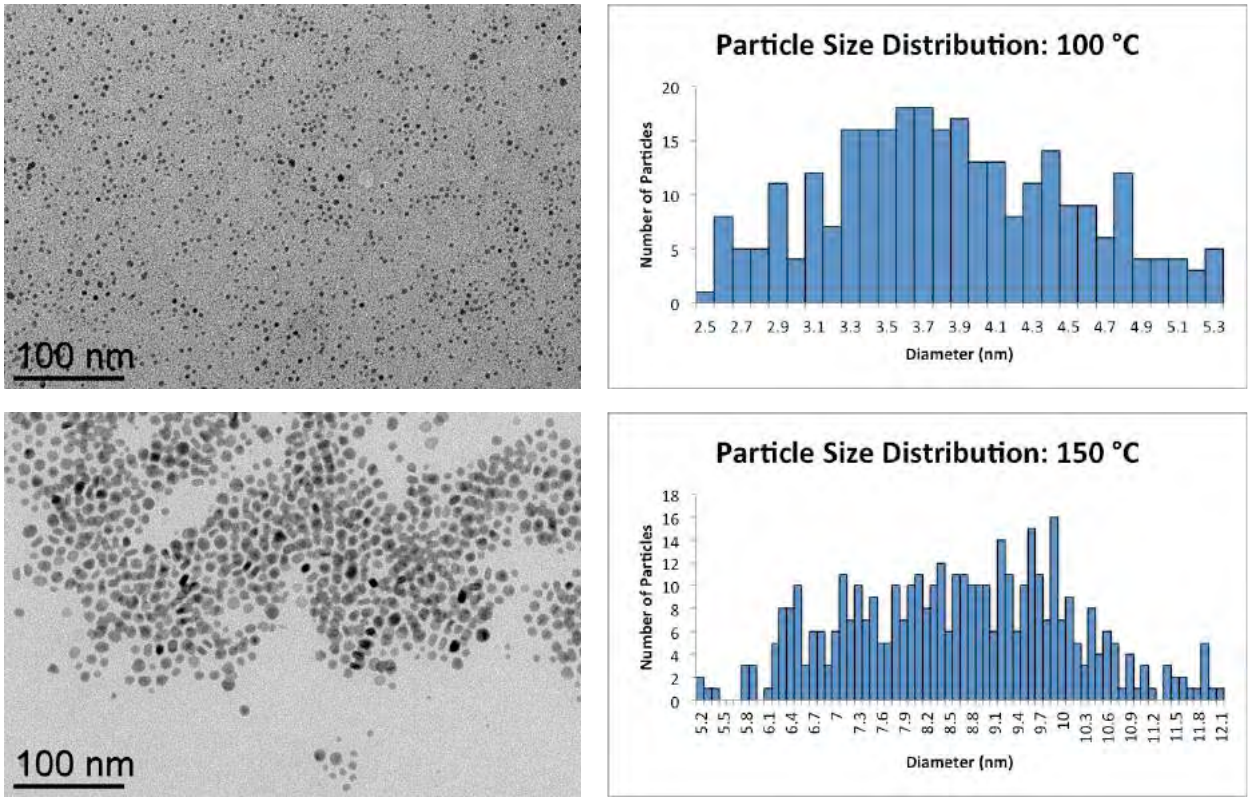

Figure Exp2.8: TEM images of Ni NPs synthesized from *in situ*-synthesized **1** decomposed in oleylamine at either 100 °C or 150 °C in the presence of 0.2 equiv. TOP after 2 h, and corresponding size distributions.

5. Effect of precursor polymer size on nanoparticles

Figure II-11 of the text shows NPs obtained using nearly identical procedures starting from isolated *vs. in situ*-synthesized nickel(II) dioleylamide. NPs from isolated **1** were obtained using the procedure indicated above for Figure Exp2.3. Parallel NPs were obtained from *in situ*-synthesized **1** as follows: $NiBr_2$(DME) (30.9 mg, 0.1 mmol), oleylamine (33.0 µL, 0.1 mmol), and 0.5 mL toluene were added to a Schlenk flask with a magnetic stir bar. A 5-mL scintillation vial with a magnetic stir bar was charged with oleylamine (65.9 µL, 0.2 mmol), *n*-BuLi (80 µL, 0.2 mmol), and 0.35 mL toluene. After 15 minutes of stirring, the solution in the scintillation vial was transferred via pipette to the Schlenk flask containing the nickel mixture. The resulting reddish mixture was stirred at room temperature for 16 h. It was then heated at 150 °C for 0.5 h, and cooled by being plunged immediately into a beaker of tap water. Both sets of particles were precipitated and redispersed using the same procedure outlined above.

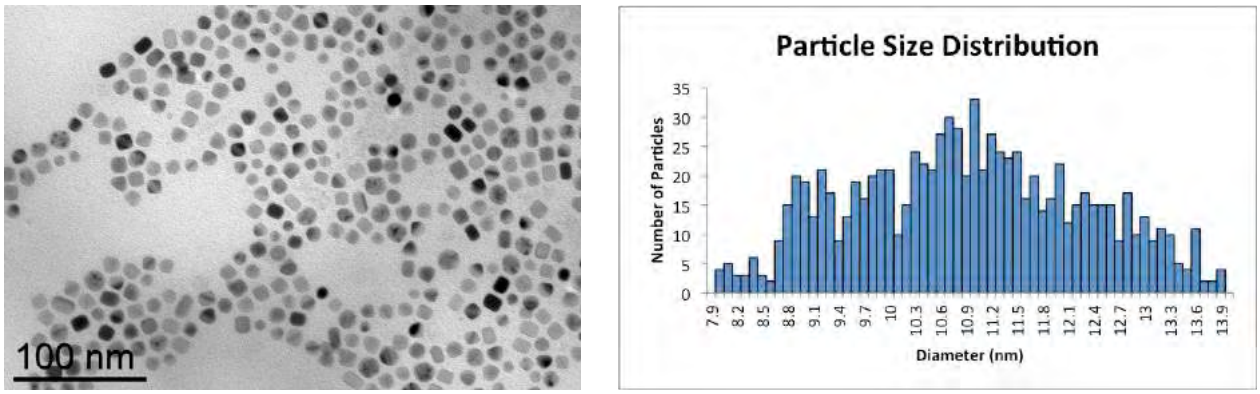

Figure Exp2.9: TEM image of Ni NPs synthesized from *in situ*-synthesized **1** decomposed in oleylamine at 150 °C for 0.5 h after 16 h resting of the precursor solution, and corresponding size distribution.

For comparison, the same procedure was repeated without solution resting, as shown in Figure II-12. $NiBr_2$(DME) (30.9 mg, 0.1 mmol), oleylamine (33.0 µL, 0.1 mmol), and 0.5 mL toluene were added to a Schlenk flask with a magnetic stir bar. A 5-mL scintillation vial with a magnetic stir bar was charged with oleylamine (65.9 µL, 0.2 mmol), *n*-BuLi (80 µL, 0.2 mmol), and 0.35 mL toluene. After 15 minutes of stirring, the viscous, yellow solution in the scintillation vial was transferred via pipette to the Schlenk flask containing the nickel mixture. The resulting reddish mixture was immediately heated at 150 °C for 0.5 h, cooled by being plunged immediately into a beaker of tap water, and precipitated and redispersed using the procedure outlined above.

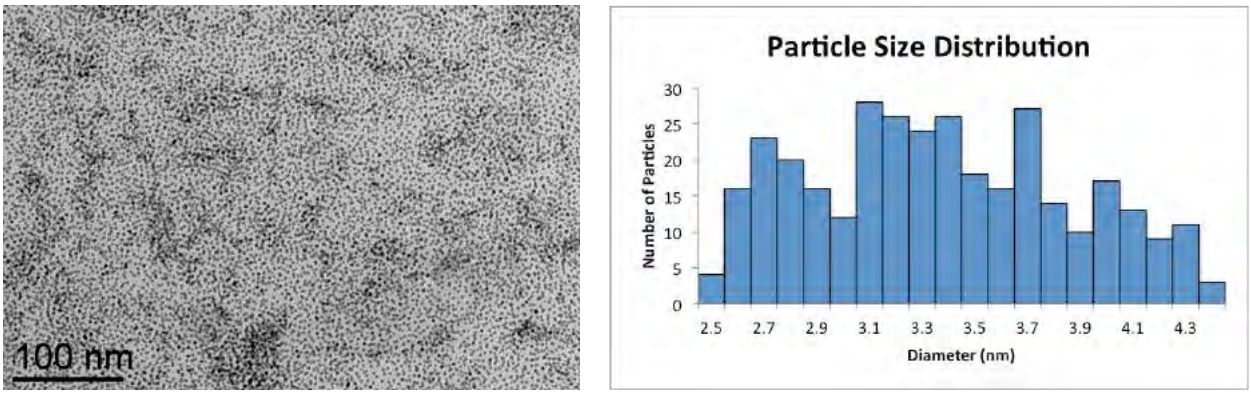

Figure Exp2.10: TEM image of Ni NPs synthesized from *in situ*-synthesized **1** decomposed in oleylamine at 150 °C for 0.5 h without resting, and corresponding size distribution.

Figure II-13 of the text also shows NPs obtained using nearly identical procedures starting from isolated *vs. in situ*-synthesized nickel(II) dioleylamide. NPs from isolated **1** were

obtained using the procedure as follows: **1** (177.6 mg, 0.3 mmol) was dissolved in oleylamine (790 µL, 2.4 mmol) in a Schlenk flask with a magnetic stir bar. It was then heated at 200 °C for 2 h, cooled by being plunged immediately into a beaker of tap water, and precipitated and redispersed using the procedure outlined above.

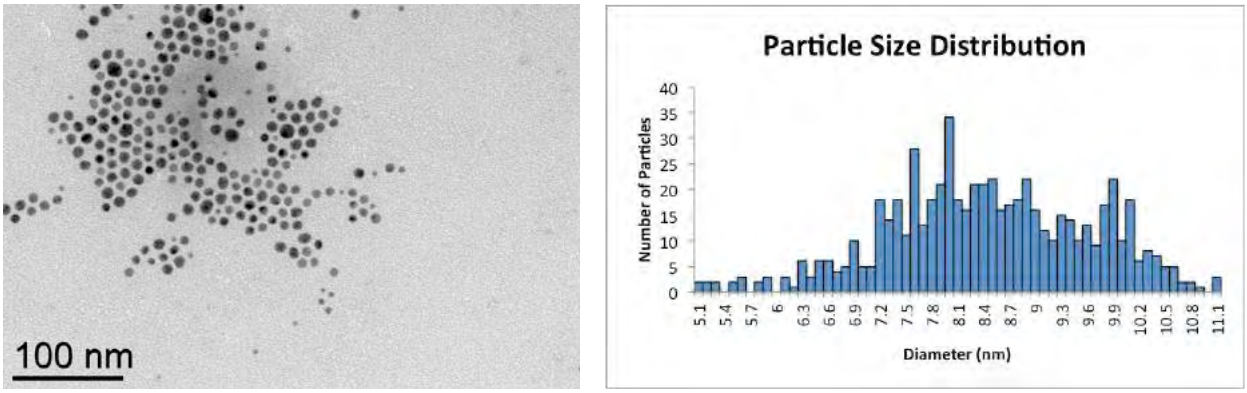

Figure Exp2.11: TEM image of Ni NPs synthesized from isolated **1** decomposed in oleylamine at 200 °C for 2 h, and corresponding size distribution.

In a parallel reaction, NPs were obtained from *in situ*-synthesized **1** as follows: $NiBr_2$(DME) (92.6 mg, 0.3 mmol), oleylamine (98.7 µL, 0.3 mmol), and 0.5 mL benzene were added to a Schlenk flask with a magnetic stir bar. A 5-mL scintillation vial with a magnetic stir bar was charged with oleylamine (197 µL, 0.6 mmol), *n*-BuLi (240 µL, 0.6 mmol), and 0.5 mL benzene. After 15 minutes of stirring, the solution in the scintillation vial was transferred via pipette to the Schlenk flask containing the nickel mixture. The resulting mixture was stirred at room temperature for 16 h. It was then dried *in vacuo* and resuspended in oleylamine (691 µL, 2.1 mmol). After heating at 200 °C for 2 h, it was cooled by being plunged immediately into a beaker of tap water, and precipitated and redispersed using the procedure outlined above.

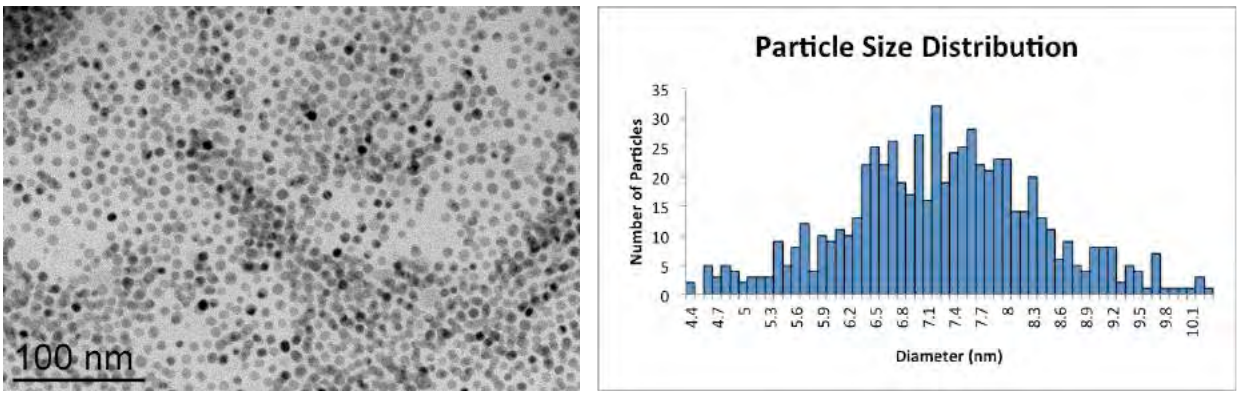

Figure Exp2.12: TEM image of Ni NPs synthesized from *in situ*-synthesized, aged **1** decomposed in oleylamine at 200 °C for 2 h, and corresponding size distribution.

6. Effect of lithium bromide (LiBr) on nanoparticle size and shape

In order to further close the gap between the apparent synthetic methods of NP synthesis from isolated *vs. in situ*-synthesized **1**, the addition of LiBr to a solution of isolated **1** was examined in Figure II-16 of the text. **1** (177.6 mg, 0.3 mmol), TOP (26.8 µL, 0.06 mmol), and LiBr (52.1 mg, 0.6 mmol) were suspended in oleylamine (790 µL, 2.4 mmol) in a Schlenk flask with a magnetic stir bar. It was then heated at 200 °C for 2 h, cooled by being plunged immediately into a beaker of tap water, and precipitated and redispersed using the procedure outlined above.

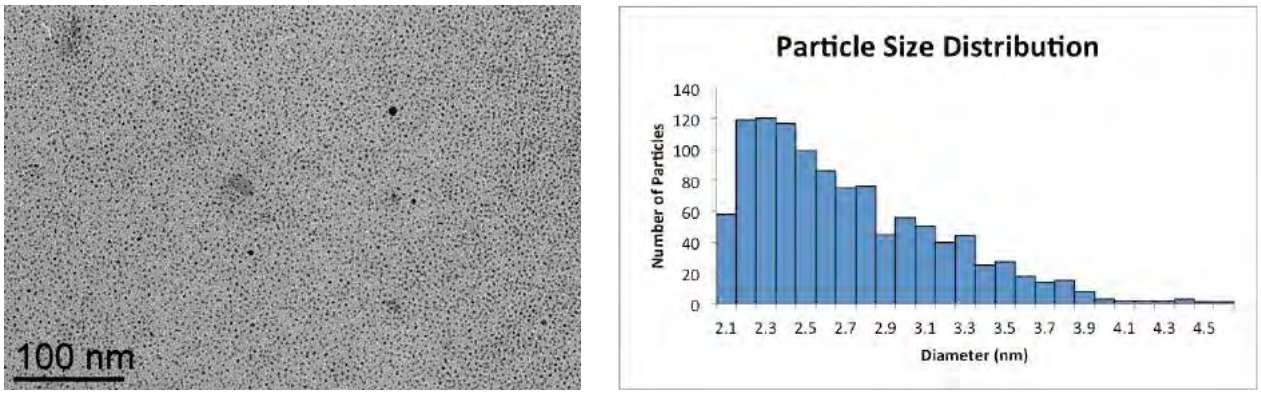

Figure Exp2.13: TEM image of Ni NPs synthesized from isolated **1** decomposed in oleylamine at 200 °C for 2 h in the presence of TOP and LiBr, and corresponding size distribution.

In order to better understand the role of LiBr in the formation and size of the NPs, different amounts of LiBr were added to in situ-synthesized **1**, as shown in Figure II-17. NiBr2(DME) (92.6 mg, 0.3 mmol), TOP (26.8 µL, 0.06 mmol), and 1, 2, or 5 equiv. LiBr (26.1 mg, 0.3 mmol; 52.1 mg, 0.6 mmol; 130.3 mg, 1.5 mmol; or 260.5 mg, 3.0 mmol) were suspended in oleylamine (494 µL, 1.5 mmol) in a Schlenk flask with a magnetic stir bar. A 5-mL scintillation vial with a magnetic stir bar was charged with oleylamine (494 µL, 1.5 mmol) and *n*-BuLi (240 µL, 0.6 mmol). After 15 minutes of stirring, the solution in the scintillation vial was transferred via pipette to the Schlenkflask containing the nickel mixture. The resulting mixtures were heated at 200 °C for 2 h. They were cooled, precipitated, and redispersed using the same procedure outlined above. D (1 equiv.) = 3.3 ± 1.3 nm; D (2 equiv.) = 2.9 ± 1.2 nm; D (5 equiv.) = 3.3 ± 0.9 nm.

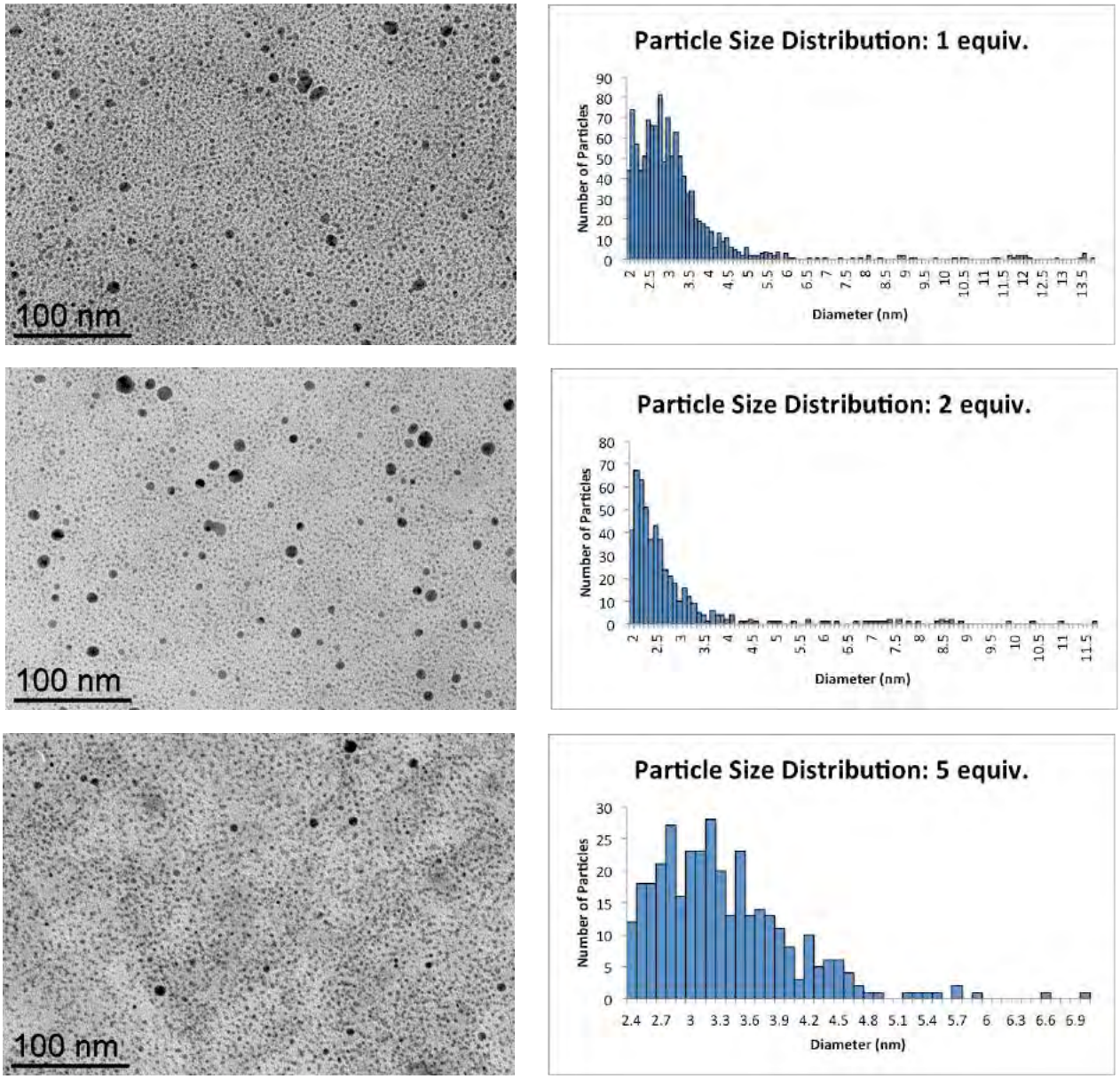

Figure Exp2.14: TEM images of Ni NPs synthesized from *in situ*-synthesized **1** decomposed in oleylamine at 200 °C for 2 h in the presence of TOP and 1, 2, or 5 equiv. LiBr, and corresponding size distributions.

To increase the solubility of LiBr in the reaction mixture, oleylamine was replaced by diphenyl ether as solvent, as demonstrated in Figure II-18. $NiBr_2$(DME) (92.6 mg, 0.3 mmol), TOP (26.8 µL, 0.06 mmol), 0, 2, 5, or 10 equiv. LiBr (0; 52.1 mg, 0.6 mmol; 130.3 mg, 1.5 mmol; or 260.5 mg, 3.0 mmol), and oleylamine (98.7 µL, 0.3 mmol) were suspended in diphenyl ether (395 µL) in a Schlenk flask with a magnetic stir bar. A 5-mL scintillation vial with a magnetic stir bar was charged with oleylamine (197 µL, 0.6 mmol), *n*-BuLi (240 µL, 0.6 mmol), and diphenyl ether (296 µL). After 15 minutes of stirring, the solution in the

scintillation vial was transferred via pipette to the Schlenk flask containing the nickel mixture. The resulting mixtures were heated at 200 °C for 2 h. They were cooled, precipitated, and redispersed using the same procedure outlined above.

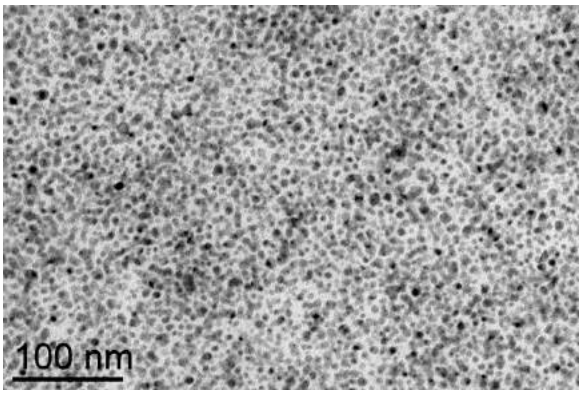

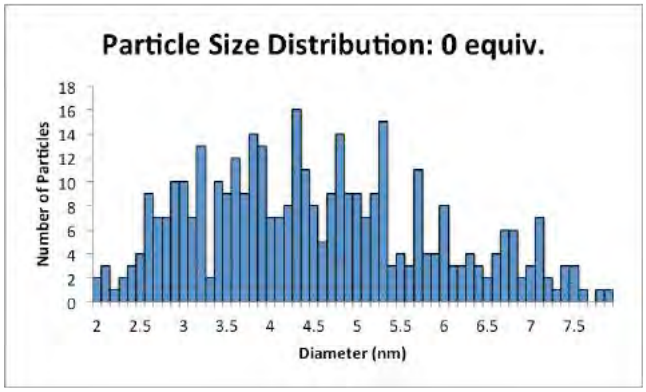

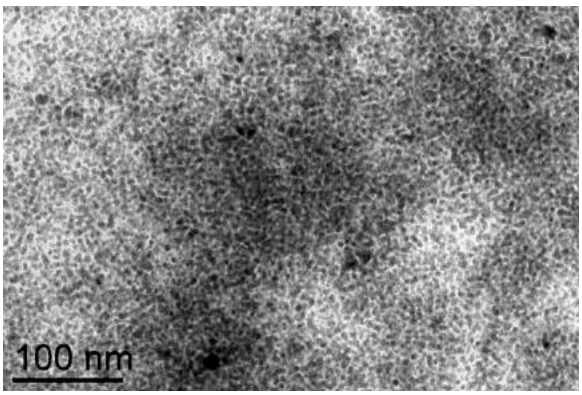

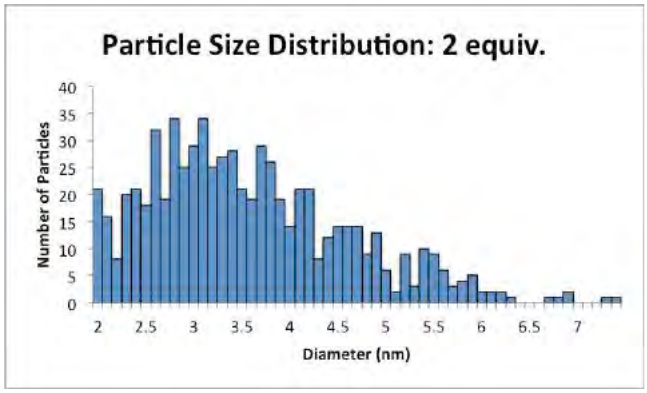

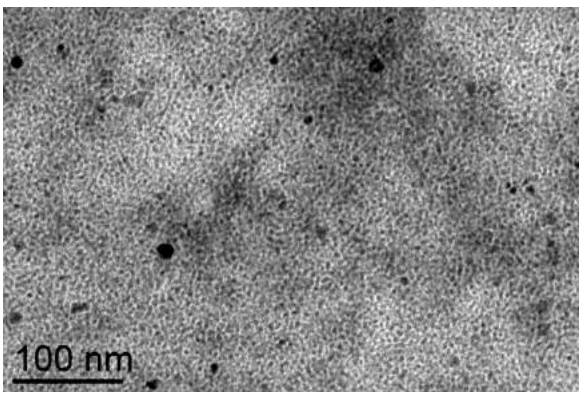

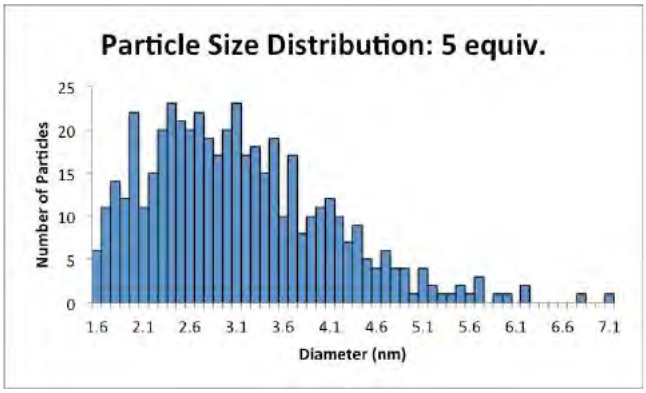

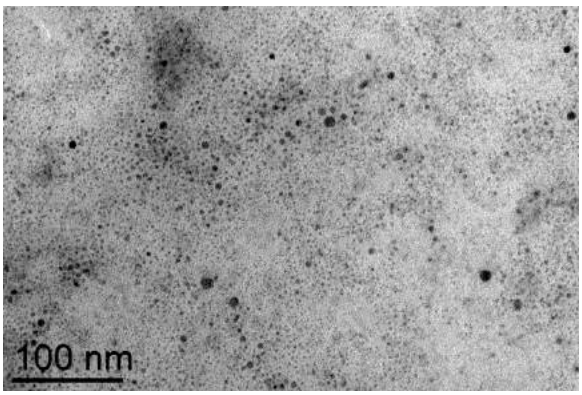

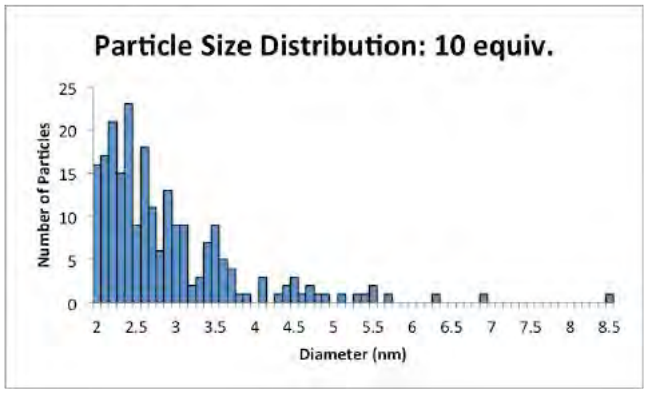

Figure Exp2.15: TEM images of Ni NPs synthesized from *in situ*-synthesized **1** decomposed in diphenyl ether at 200 °C for 2 h in the presence of TOP and 0, 2, or 5, 10 equiv. LiBr, and corresponding size distributions.

7. Effect of oleylamine on particle size

In the series of reactions shown in Figure II-19, which demonstrated the direct correlation between the amount of oleylamine and the size of the resulting particles, products were initially added either to a Schlenk flask or to a vial, in the quantities listed in the following table under either "Flask" or "Vial." $NiBr_2$(DME) (46.3 mg, 0.15 mmol), TOP (13.4 µL, 0.03 mmol), oleylamine (Flask), and ODE (Flask) were added to a Schlenk flask. A 5-mL scintillation vial was charged with at least 2 equiv. oleylamine (Vial), *n*-BuLi (120 µL, 0.3 mmol), and ODE (Vial). The same procedure outlined above (15 minutes of independent stirring, pipette transfer from vial to Schlenk flask, heating at 200 °C for 2 h) was followed for each reaction. Below are the quantities of oleylamine and ODE in each reaction.

Table Exp2.1. Quantities of oleylamine or octadecene (ODE) added in each reaction

Equiv. Oleylamine	Amount Oleylamine (Flask), µL	Amount Oleylamine (Vial), µL	Amount ODE (Flask), µL	Amount ODE (Vial), µL
2	0	98.7	451	451
6	148	148	352	352
10	247	247	253	253
14	346	345	155	155

Each reaction was cooled, precipitated, and redispersed using the same procedure outlined above.

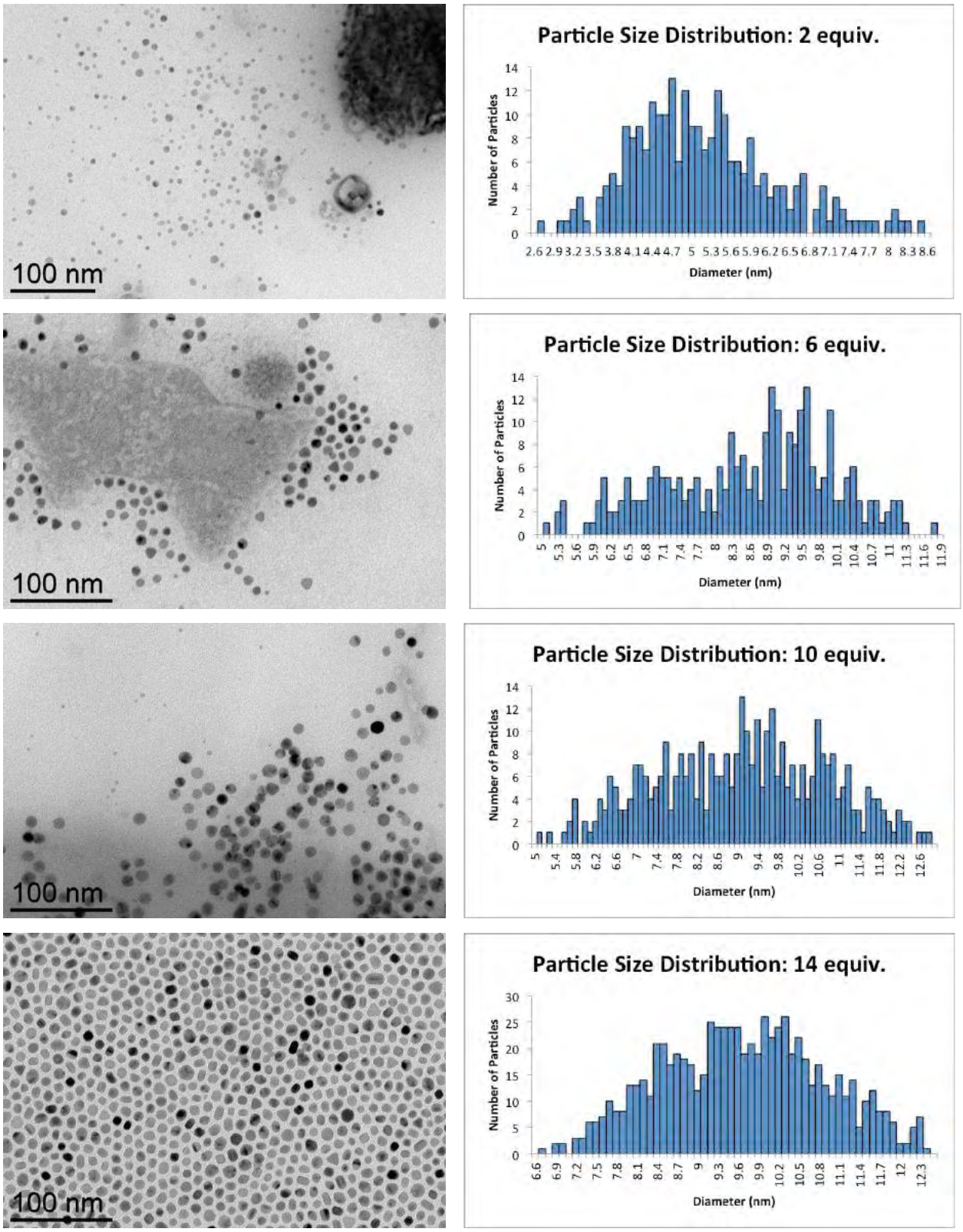

Figure Exp2.16: TEM images of Ni NPs synthesized from *in situ*-synthesized **1** decomposed in octadecylamine at 200 °C for 2 h in the presence of TOP and 2, 6, 10, or 14 equiv. oleylamine, and corresponding size distributions.

8. Solvent effects

Figure II-20 replaced oleylamine with hexadecylamine as solvent and amide ligand in order to examine the effect of the double bond. $NiBr_2$(DME) (92.6 mg, 0.3 mmol), hexadecylamine (362.2 mg, 1.5 mmol), and TOP (26.8 µL, 0.06 mmol) were added to a Schlenk flask with a magnetic stir bar with 0.5 mL benzene. A 5-mL scintillation vial with a magnetic stir bar was charged with hexadecylamine (362.2 mg, 1.5 mmol) and *n*-BuLi (240 µL, 0.6 mmol) with 0.5 mL benzene. After 15 minutes of stirring, the solution in the scintillation vial was transferred via pipette to the Schlenk flask containing the nickel mixture. The resulting mixture was dried *in vacuo* and heated at 200 °C for 2 h. It was cooled by being plunged immediately into a beaker of tap water, and precipitated and redispersed using the procedure outlined above.

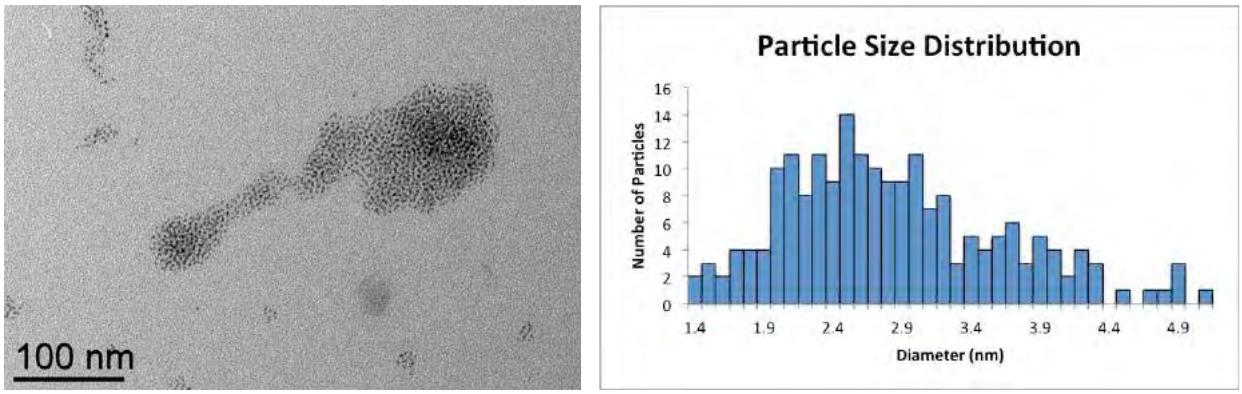

Figure Exp2.17: TEM images of Ni NPs synthesized by replacing all oleylamine with hexadecylamine, decomposed at 200 °C for 2 in the presence of TOP, and corresponding size distributions.

Figure II-21 retains the use of **1** as the organometallic precursor, but replaces the oleylamine as solvent by hexadecylamine, hexadecane, and hexadecene.

$NiBr_2$(DME) (92.6 mg, 0.3 mmol), TOP (26.8 µL, 0.06 mmol), and hexadecylamine (579.5 mg, 2.4 mmol) were suspended in 0.5 mL benzene in a Schlenk flask with a magnetic stir bar. A 5-mL scintillation vial with a magnetic stir bar was charged with oleylamine (197 µL, 0.6 mmol), *n*-BuLi (240 µL, 0.6 mmol), and 0.5 mL benzene. After 15 minutes of stirring, the solution in the scintillation vial was transferred via pipette to the Schlenk flask containing the nickel mixture. The

resulting mixture was dried *in vacuo* and heated at 200 °C for 2 h. It was cooled by being plunged immediately into a beaker of tap water, and precipitated and redispersed using the procedure outlined above.

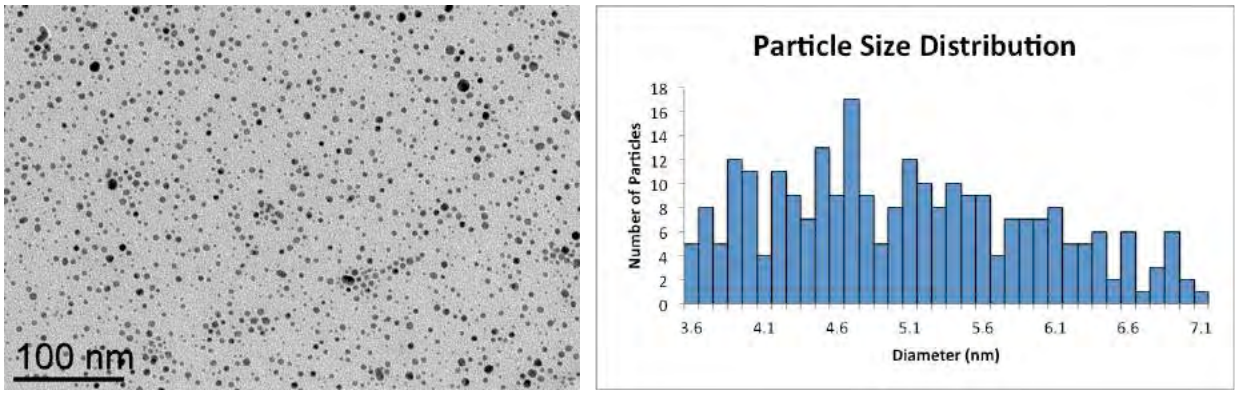

Figure Exp2.18: TEM images of Ni NPs synthesized from *in situ*-synthesized **1** decomposed in hexadecylamine at 200 °C for 2 h in the presence of TOP, and corresponding size distributions.

$NiBr_2$(DME) (92.6 mg, 0.3 mmol) and TOP (26.8 µL, 0.06 mmol) were suspended in and hexadecene (344 µL, 1.2 mmol) in a Schlenk flask with a magnetic stir bar. A 5-mL scintillation vial with a magnetic stir bar was charged with oleylamine (197 µL, 0.6 mmol), *n*-BuLi (240 µL, 0.6 mmol), and hexadecene (344 µL, 1.2 mmol). After 15 minutes of stirring, the solution in the scintillation vial was transferred via pipette to the Schlenk flask containing the nickel mixture. The resulting mixture was heated at 200 °C for 2 h. It was cooled by being plunged immediately into a beaker of tap water, and precipitated and redispersed.

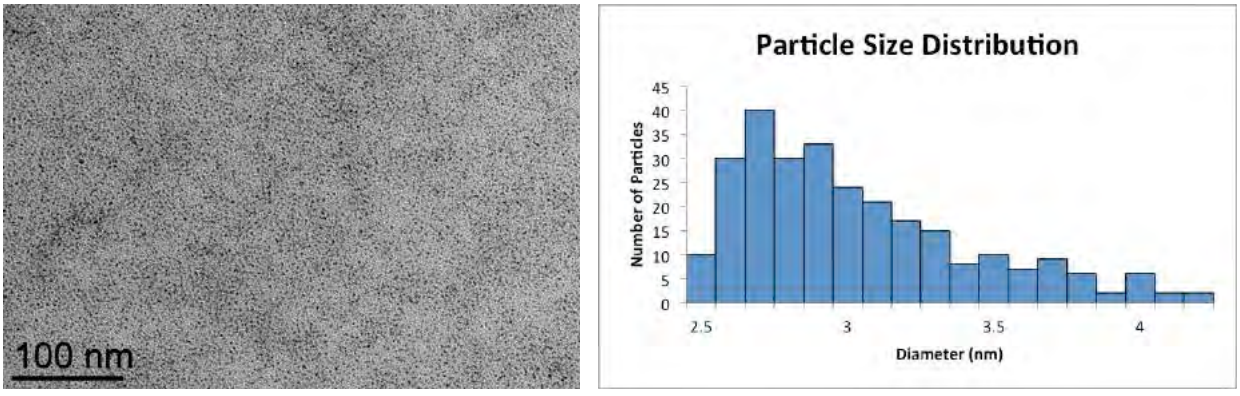

Figure Exp2.19: TEM images of Ni NPs synthesized from *in situ*-synthesized **1** decomposed in hexadecene at 200 °C for 2 h in the presence of TOP, and corresponding size distributions.

An identical reaction was performed using hexadecane (twice 352 µL, 1.2 mmol) instead of hexadecene.

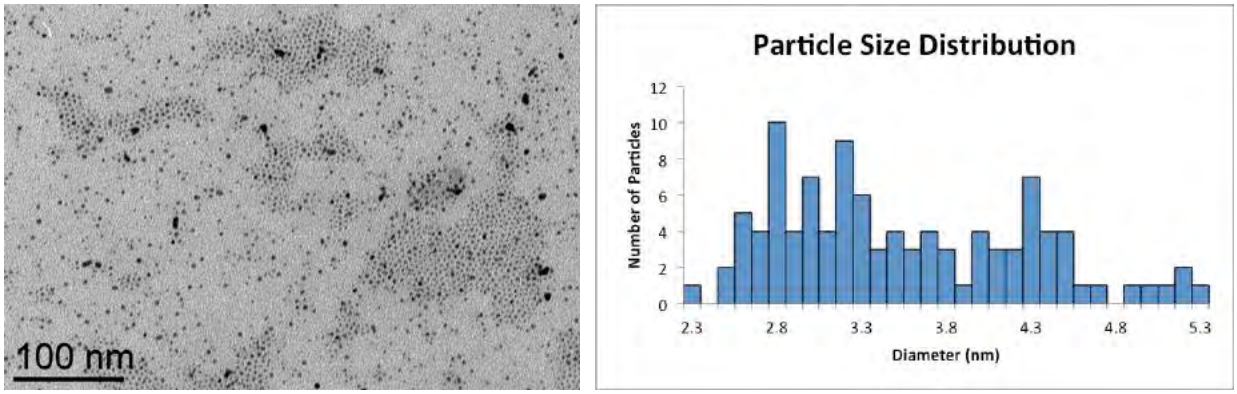

Figure Exp2.20: TEM images of Ni NPs synthesized from *in situ*-synthesized **1** decomposed in hexadecane at 200 °C for 2 h in the presence of TOP, and corresponding size distributions.

9. Unoptimized iron(0) and cobalt(0) nanoparticles from isolated M(II) bis(oleylamide)

Following the guide of Ni(0) NP formation, some optimization was explored in the formation of Fe(0) and Co(0) NPs. As in the case of Ni(0), both the iron(II) and cobalt(II) bis(oleylamide) species were synthesized following the same procedure outlined above for the formation of nickel(II) bis(oleylamide), replacing $NiBr_2$(DME) was replaced by $FeBr_2$ or $CoBr_2$. The same reaction set-up was used as those that produced particles of 11.0 ± 1.2 nm in the case of Ni(0) (Figure II-3), as shown in Figure II-24. Iron(II) dioleylamide (58.9 mg, 0.1 mmol) or cobalt(II) dioleylamide (59.2 mg, 0.1 mmol), oleylamine (33.0 µL, 0.1 mmol), and TOP (8.9 µL, 0.02 mmol) were dissolved in 1 mL toluene in a Schlenk flask with a magnetic stir bar. These mixtures were heated at 150 °C for 0.5 h on a hot plate in a silicone oil bath. They were cooled by being plunged immediately into a beaker of tap water, and precipitated and redispersed, with the replacement of ethanol as precipitation solvent by acetone.

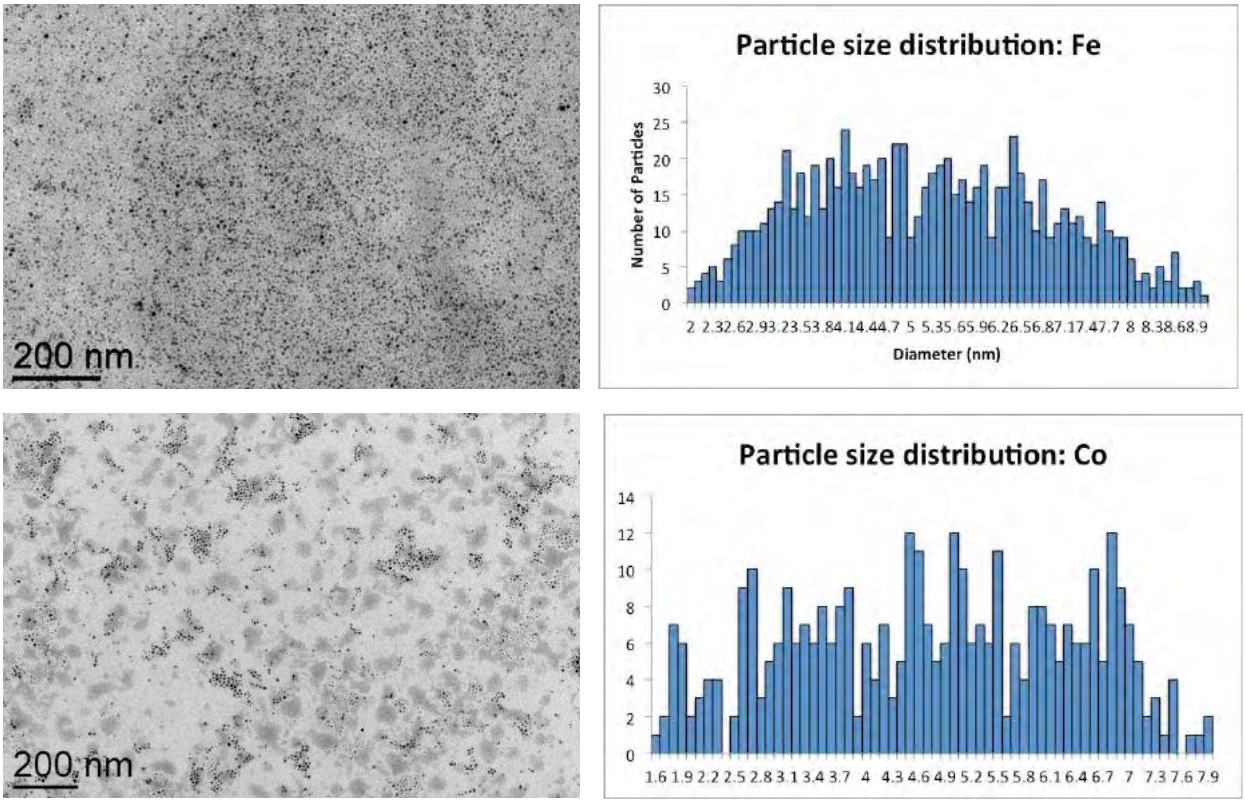

Figure Exp2.21: TEM images of Fe or Co NPs synthesized from isolated iron(II) or cobalt(II) dioleylamide decomposed in toluene at 150 °C for 0.5 h in the presence of oleylamine and TOP, and corresponding size distributions.

Various optimization procedures were attempted, including variation of equivalents of oleylamine and TOP, changing solvent from toluene to oleylamine or octadecene, increasing the temperature or time of the reaction, and changing the reducing agent from oleylamide to *n*-BuLi or KC_8.

10. Synthesis of iron(0) and cobalt(0) nanoparticles from in situ-synthesized M(II) bis(oleylamide)

In the reactions shown in Figure II-25, MBr_2 ($FeBr_2$: 64.7 mg; $CoBr_2$: 65.6 mg, 0.3 mmol), oleylamine (494 µL, 1.5 mmol), and TOP (26.8 µL, 0.06 mmol) were added to a Schlenk flask with a magnetic stir bar. A 5-mL scintillation vial with a magnetic stir bar was charged with oleylamine (494 µL, 1.5 mmol) and *n*-BuLi (240 µL, 0.6 mmol). After 15 minutes of stirring, the solution in the scintillation vial was transferred via pipette to the Schlenk flask containing the nickel mixture. The resulting mixture was heated at 220 °C for 2 h. It was cooled, precipitated, and redispersed using the same procedure outlined above, with the replacement of ethanol as precipitation solvent by acetone.

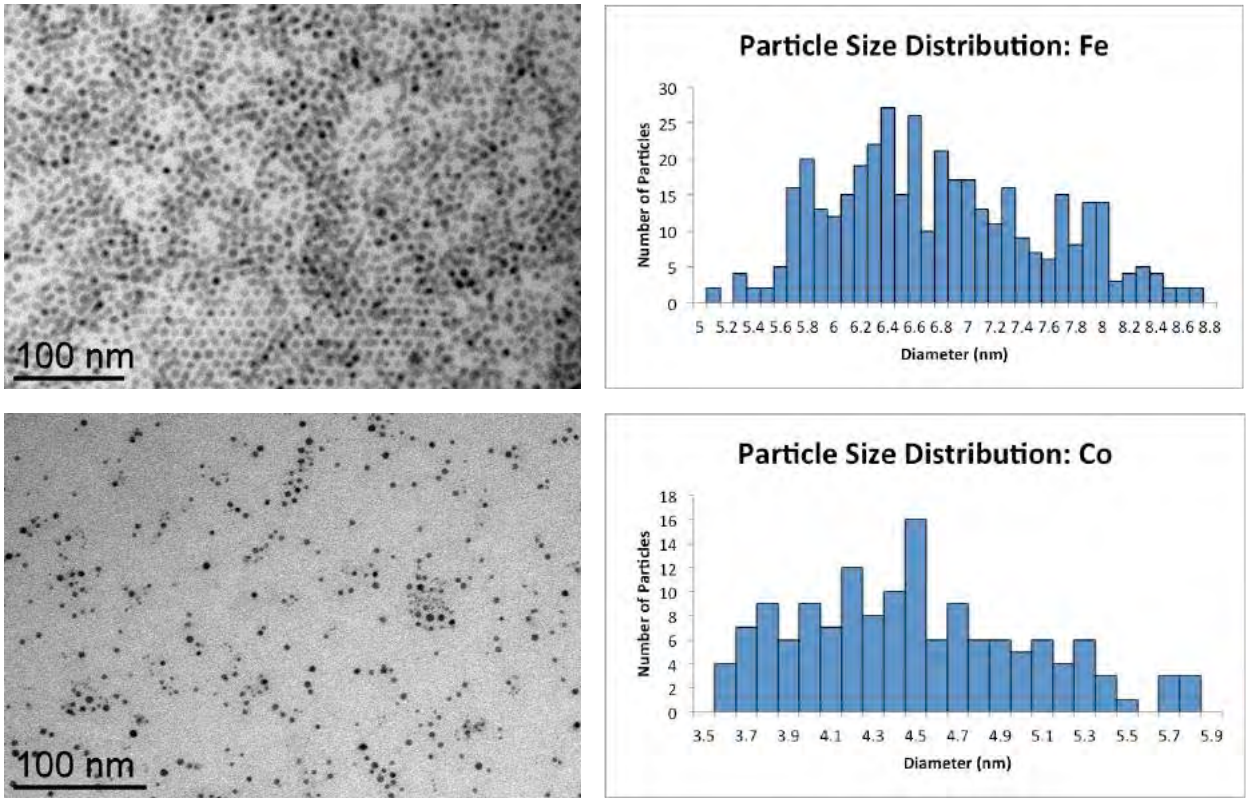

Figure Exp2.22: TEM images of Fe or Co NPs synthesized from *in situ*-synthesized iron(II) or cobalt(II) dioleylamide decomposed in oleylamine at 220 °C for 2 h in the presence of TOP, and corresponding size distributions.

11. Catalysis using metal(0) nanoparticles

Scheme II-6 shows the catalytic hydrosilylation of 1-octene by Ni(0) NPs of 11.0 ± 1.1 nm diameter (those shown in Figure II-4). Using 0.01 equiv. $NiBr_2$(DME) (30.9 mg, 0.1 mmol), Ni(0) NPs were isolated by precipitation from ethanol as described above and dried *in vacuo* overnight. To these isolated particles was added 1-octene (1.73 mL, 11.0 mmol), diphenylsilane (1.85 mL, 10.0 mmol), and 5 mL toluene. This mixture was heated for 2 h at 90 °C to result in quantitative conversion to (*n*-octyl)diphenylsilane. Yield was examined using GCMS using a bromobenzene internal standard.

These same nanoparticles were used for the reaction shown in Scheme II-8, in which Ni(0) NPs of 11.0 ± 1.1 nm diameter were used to reduce phenylacetylene. Using 0.01 equiv. $NiBr_2$(DME) (30.9 mg, 0.1 mmol), Ni(0) NPs were isolated by precipitation from ethanol as described above and dried *in vacuo* overnight. To these isolated particles was added phenylacetylene (1.10 mL, 10.0 mmol) and 5 mL toluene. This mixture was frozen in liquid nitrogen, degassed twice, and then put under 1 bar H_2. The mixture was heated to 85 °C over 60 h. GCMS showed a ratio of styrene to ethylbenzene of 89:11.

Similarly, the Fe(0) NPs shown in Figure II-25 were used to catalyze the reduction of nitrogen. Using $FeBr_2$ (53.9 mg, 0.25 mmol), Fe(0) NPs were isolated by precipitation from acetone as described above and dried *in vacuo* overnight. To these isolated particles was added potassium(0) (195 mg, 5.0 mmol), trimethylsilylchloride (635 µL, 5.0 mmol), and 3 mL THF. The Schlenk flask was prepared in a glovebox that was under nitrogen atmosphere, and thus the solution was under 1 bar N_2. It was heated at 50 °C for 80 h. Quantity of $N(TMS)_3$ titrated using indophenol method (hydrolysis using sulfuric acid, followed by addition of buffer, phenol, and sodium hypochlorite in water, and consequent examination by UV-Vis spectroscopy). This method shows a yield of 0.11 mmol $N(TMS)_3$ (44 % with respect to [Fe]).

Diffusion-ordered NMR spectroscopy (^{1}H DOSY NMR)

DOSY NMR spectra were recorded on a Bruker Avance 500 spectrometer equipped with a 5 mm triple resonance inverse Z-gradient probe (TBI ^{1}H, ^{31}P, BB).

The hydrodynamic radius r_H of a species in solution was obtained using the equation:

$$r_H = \frac{k_B T}{6\pi\eta D}$$

where D = diffusion coefficient (m^2/s), k_B = Boltzmann constant (1.38E-23 J/K), T = temperature (293 K), and η = viscosity (0.56E-3 Pa•s for toluene, 0.48E-3 Pa•s for THF).

The diffusion coefficients indicated on the spectra below are in cm^2/s, rather than in the m^2/s required for the equation described above.

Preparation of samples

Procedure for Figure II-9a: A 5-mL scintillation vial with a magnetic stir bar was charged with **1** (19.2 mg, 0.03 mmol) and 0.75mL toluene-d_8.

Procedure for Figure II-9b: A 5-mL scintillation vial with a magnetic stir bar was charged with $NiBr_2$(DME) (10 mg, 0.03 mmol) and 0.3 mL toluene-d_8. A second 5-mL scintillation vial with a magnetic stir bar was charged with oleylamine (21.4 µL, 0.06 mmol), *n*-BuLi (26.0 µL, 0.06 mmol), and 0.45 mL toluene-d_8. After 15 minutes of stirring, the oleylamide salt solution was transferred via pipette to the vial containing the nickel(II) salt. The resulting mixture was stirred briefly before being transferred to a J-Young NMR tube.

Procedure for Figure II-9c: The NMR sample from 9b was maintained at room temperature for three days before a new spectrum was obtained.

Procedure for Figure II-9d: The NMR sample from 9c was heated at 150 °C for five minutes before a new spectrum was obtained.

Heating the sample shown in Figure II-9a for five minutes at 150 °C resulted in a similar spectrum to that shown in Figure II-9d. Here, the diffusion coefficients indicate particles of 1.1 nm and 2.5 nm in radius, based on the peaks indicated at 5.51 – 5.56 ppm.

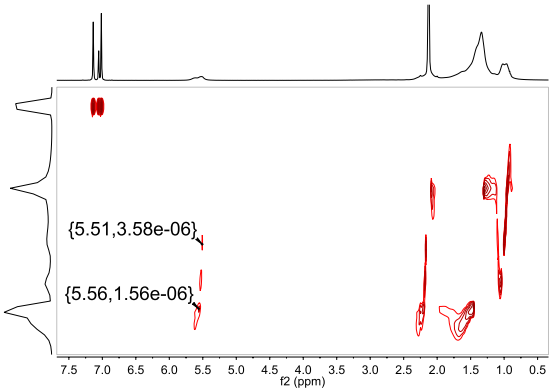

Figure Exp2.23: DOSY NMR spectrum of isolated **1** after 5 min. heating at 150 °C.

In order to better reproduce the reaction conditions, a spectrum was obtained with eight free equivalents of oleylamine in solution, as shown in Figure II-10. A 5-mL scintillation vial with a magnetic stir bar was charged with $NiBr_2$(DME) (10 mg, 0.03 mmol), oleylamine (53.5 µL, 0.15 mmol), and 0.3 mL toluene-d_8. A second 5-mL scintillation vial with a magnetic stir bar was charged with oleylamine (53.5 µL, 0.15 mmol), *n*-BuLi (26.0 µL, 0.06 mmol), and 0.343 mL toluene-d_8. After 15 minutes of stirring, the oleylamide salt solution was transferred via pipette to the vial containing the nickel(II) salt. The resulting mixture was stirred briefly before being transferred to a J-Young NMR tube. After three days, the diffusion coefficients indicated free oleylamine (δ = 5.47 ppm, r = 0.6 nm) and particles of 2.2 nm in radius (δ = 5.51 ppm).

An examination of bonding mode (bridging amines *vs.* alkenes) was performed by taking DOSY NMR spectra of $NiBr_2$(DME) mixed with lithium dihexadecylamide. A 5-mL scintillation vial with a magnetic stir bar was charged with $NiBr_2$(DME) (10 mg, 0.03 mmol), hexadecylamine (36.2 mg, 0.15 mmol), and 0.3 mL toluene-d_8. A second 5-mL scintillation vial with a magnetic stir bar was charged with hexadecylamine (36.2 mg,0.15 mmol), *n*-BuLi (26.0 µL, 0.06 mmol), and 0.45 mL toluene-d_8. After 15 minutes of stirring, the hexadecylamide salt solution was transferred via pipette to the vial containing the nickel(II) salt. The resulting mixture was stirred briefly before being transferred to a J-Young NMR tube. After 30 minutes, the diffusion coefficients indicated oligomers of 0.5 nm in radius (δ = 1.66 ppm). After three days, the diffusion coefficients indicated oligomers of 3.4 nm in radius (δ = 1.64 ppm).

X-Ray Powder Diffraction (XRD)

X-Ray powder diffractograms were recorded on a PANalytical X'Pert Pro θ using a Cu source (wavelength: 1.5418 Å) and a linear X'Celerator detector. The diffractometer was used in Bragg-Brentano configuration with Soller front slits (0.04 rad) and divergence slits coupled with a filter to insure a constant length of irradiation of 10 mm. Data were recorded with 2θ between 2 and 90° (step: 0.016°, 1000 s per step). Samples were deposited on a Si holder.

Particles obtained from the method displayed in Figure II-4 were washed thrice with ethanol and dried *in vacuo.* The sufficiently large particle size of 11.0 nm seemed conducive to XRD, but as shown in Figure II-5, the peaks were too small and broad to perform an adequate Scherrer analysis, suggesting a small crystallite size.

Pattern List

Visible	Ref.Code	Score	Compound Name	Displ.[°2 θ]	Scale Fac.	Chem. Formula
*	96-901-2969	1	Nickel	0,000	0,094	Ni4.00

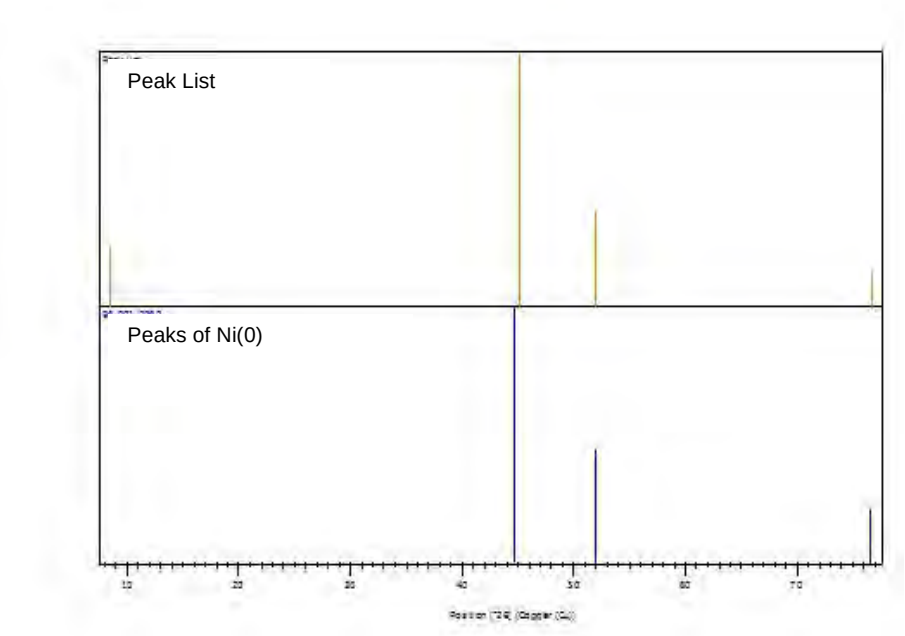

Figure Exp2.24: Comparison of peaks obtained from sample of Ni(0) NPs with theoretical pattern.

As a result, we turned to a method better adapted for small crystalline zones: WAXS.

Wide-Angle X-Ray Scattering (WAXS)

Wide-angle X-ray scattering (WAXS) measurements were performed on a laboratory prototype at the Centre d'Elaboration de Matériaux et d'Etudes Structurales (CEMES). The machine has been optimized for the study of amorphous and nanocrystalline materials. It uses molybdenum radiation (0.071069 nm) monochromatized by a graphite crystal, and a low-noise solid-state detector. The instrument was used for these studies at a power of 1 kW, and each measurement lasted 15 – 20 h. WAXS was also used to obtain a radial distribution function and X-ray fluorescence, as shown in Figures II-6 and II-15.

Computational methods

Geometry optimizations and transition state calculations were performed using the Gaussian09. The M06L exchange-correlation functional was employed with a def2tzvp basis set on Ni, 6-311+g** on H, and 6-31g* on C and N. A full frequency calculation was performed on each structure to establish true minima, or maxima for transition states. Computed energies were corrected for thermal free energies. Structural models were generated from GaussView 03.

The two likely transition states for β-H transfer were calculated:

TS_B:
CHN2 142.56
N3NiN1 166.73
N2NiN1 88.97
N2NiN3 103.54
N1–Ni 1.779
N2–Ni 1.953
N3–Ni 1.986

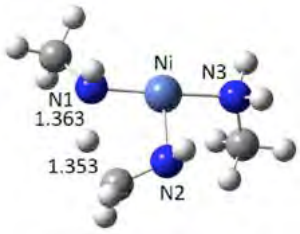

TS_A:
CHN1 142.10
N3NiN1 174.71
N2NiN1 87.95
N2NiN3 96.55
N1–Ni 1.899
N2–Ni 1.923
N3–Ni 1.891

As was the starting complex:

N3NiN1 162.96
N2NiN1 110.30
N2NiN3 86.7
N1–Ni 1.758
N2–Ni 1.852
N3–Ni 1.987

Figure Exp2.25: Calculated configurations of two possible transition states and starting complex.

Chapter III: Synthesis of metal phosphide nanoparticles using white phosphorus

1. History and overview of nickel phosphide nanoparticles

Metal phosphide (M_xP_y) nanoparticles are interesting for a variety of applications, including catalysis, batteries, and electrocatalysis.[1] In particular, nickel phosphide in the form of Ni_2P demonstrates a diverse set of uses. Our work on synthesizing Ni(0) nanoparticles (NPs) (see Chapter II), combined with previous work in the group on the formation of Ni_2P NPs from Ni NPs,[2] encouraged us to investigate whether we could develop a mild, water-free synthesis of Ni_2P NPs from the present particles.

Ni_2P was first synthesized by Bertrand Pelletier in the late 18th century.[3] Its structure is comprised of interleaved planes of Ni_3P and Ni_3P_2. The average stoichiometry of these layers is thus Ni_2P (Figure III-1).[4] Ni–Ni bonds in Ni_2P are only slightly longer than those in Ni(0) fcc, with Ni–P distances between 2.2 – 2.5 Å. The overall structure is therefore densely packed.

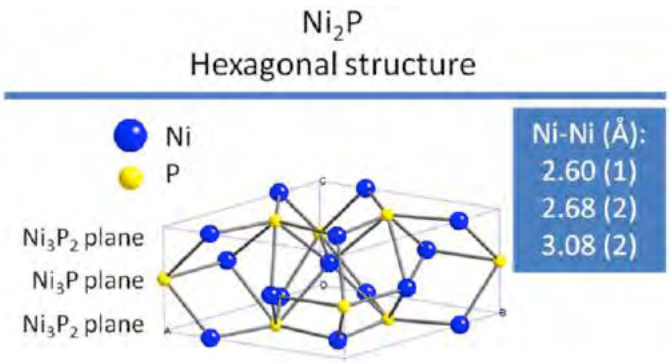

Figure III-1. Crystal structure of Ni_2P.[4]

Electron delocalization in metal phosphides generally decreases with increasing amounts of P. Strong overlap between the orbitals of phosphorus and metal allows significant electron back donation from the metal to the phosphorus, leading to a reduction of electron density at the metal. These properties cause Ni_2P NPs to demonstrate very different reactivity from Ni(0) NPs. For example, unlike pure metals, which are conductors, many metal phosphides, such as Ni_2P, are semiconductors.[5]

These semiconducting properties permit their use in a wide variety of applications. Ni_2P and other transition metal phosphide semiconductor NPs have been used as anode materials for photoelectrochemical solar cells and solar chargeable

batteries.[6] Ni_2P is not only inexpensive compared to semiconductors such as InP or GaP, but it is also chemically stable in acid and alkali media. Its band gap (1.0 eV) permits excitation by the majority of the solar spectrum (between 1.0 and 1.9 eV). Although it is less efficient than other semiconductors like InP or GaP, it is more stable, resisting chemical, electrochemical, and photoelectrochemical decomposition in solution.

Ni_2P NPs have also been examined as an anode material for lithium batteries because of their ability to insert a large number of Li atoms per lattice unit.[7] Bulk Ni_2P alone demonstrates no electrochemical activity, as it is not a conductive material. Upon mixing with a conductive additive such as carbon, its capacity can be increased to ~500 mAh/g. Unfortunately, Ni_2P undergoes a partially reversible reaction with Li, limiting its application as an anode material in electrochemical cells. Carbon-free Ni_2P NPs are inactive towards Li, but a calcination step results in a conductive carbon coating that improves the mechanical integrity of the electrode and creates a lithium-permeable network. The carbon-coated Ni_2P NPs show a reversible capacity of ~200 mAh/g, and are able to insert up to 3 Li per lattice unit. Furthermore, while bulk Ni_2P capacity collapses after a few cycles, Ni_2P NPs with a carbon shell show much better retention. Thus, Ni_2P/C NPs have improved electrochemical properties compared to bulk Ni_2P/C, providing a somewhat reversible means of Li insertion.

Ni_2P has also been used in a large variety of catalytic roles. In one highly industrially relevant process, Ni_2P is widely used to catalyze the hydrodesulfurization (HDS) and hydrodenitrogenation (HDN) of petroleum feedstocks.[8] These are key processes needed to ensure clean fuel use for transportation. Organosulfur compounds can poison the catalysts that process these feedstocks.[9] They can also be oxidized to SO_2 during the combustion process. Legislation thus demands that levels of sulfur in petroleum feedstocks, in the form of thiols, thiophenes, and organic sulfides, be below 10 ppm. Similarly, organonitrogen compounds such as pyridine that are found in feedstocks produce NO_x pollutants during combustion. Metal phosphides, and particularly Ni_2P, are able to take up sulfur or nitrogen atoms during the process of HDS or HDN without permitting the S or N to permeate the particles. In fact, surface-treating Ni_2P by H_2S was found to augment HDS activity.[9d]

Many metal phosphide nanoparticles such as Ni_2P, CoP, and Fe_2P are highly active hydrogen evolution catalysts, producing H_2 from water (Scheme III-1).[10] The

mechanisms of the hydrogen evolution reaction (HER) and HDS are similar. Both mechanisms require the catalyst to bind H_2. Further, Ni_2P produces H_2 via the water-gas shift reaction, which combines carbon monoxide and water to form hydrogen and carbon dioxide (Scheme III-1).[11] It also reportedly bears a structural and electronic resemblance to [NiFe] hydrogenase, a highly active biological HER catalyst.[12] Indeed, Ni_2P NPs have among the highest HER activity of any non-noble metal electrocatalyst.[13] They produce H_2 from H_2O in nearly quantitative faradaic yield. Moreover, they are thermostable and stable in aqueous media.

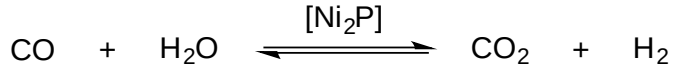

Scheme III-1. Ni_2P-catalyzed water-gas shift reaction, producing H_2.

Ni_2P can catalyze not only the HER, but also the oxygen evolution reaction (OER), the other half of the water splitting reaction (Scheme III-2).[14] Few catalysts can catalyze both the HER and OER in the same media. The ability to split water electrochemically into both hydrogen and oxygen may lead to a method of solar energy storage. Under the catalytic conditions, Ni_2P forms a core-shell Ni_2P/NiO_x species that produces a high current density at a low overpotential, making it among the most active of non-precious metal OER catalysts.

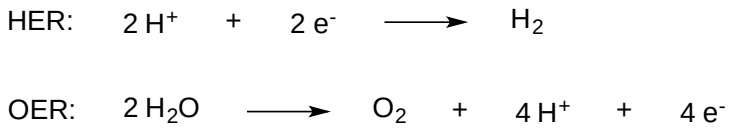

Scheme III-2. Hydrogen and oxygen evolution reactions.

Ni_2P NPs have also been used as a cocatalyst with Pd NPs for the anodic reaction in a direct formic acid fuel cell.[15] These fuel cells, which typically employ Pd catalysts, are a promising energy conversion system. The use of Ni_2P cocatalysts augmented the power density of the fuel cell by 3.5 times that of the commercial Pd anode catalyst alone. In a direct formic acid fuel cell, formic acid is oxidized by oxygen to carbon dioxide and water (Scheme III-3). The joint Pd-Ni_2P cocatalyst system performed the anodic reaction, in which formic acid is oxidized to CO_2. The hybrid catalyst system yielded both higher power density and discharge stability than many state-of-the-art catalysts.

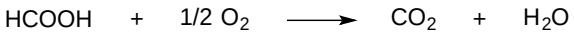

Scheme III-3. Net reaction in direct formic acid fuel cell.

In addition, Ni_2P NPs can catalyze various hydrogenation reactions. Ni_2P NPs exhibit H_2 activation and incorporation in a manner that resembles noble metal catalysts more closely than it resembles Ni(0) NPs.[16] For example, the hydrodeoxygenation of acetic acid to form methane, carbon monoxide, and water using Ni_2P NPs has been reported (Scheme III-4).[6]

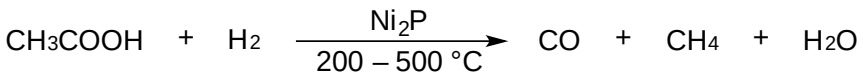

Scheme III-4. Hydrodeoxygenation of acetic acid.

Ni_2P NPs supported on silica have also been found to hydrogenate naphthalene (Scheme III-5).[17] Polycyclic aromatic hydrocarbons (PAHs) such as naphthalene in transportation fuels contribute to the formation of environmentally harmful emissions, and their removal improves fuel quality. Moreover, the cycloalkane products that result from the reduction of such PAHs are considered ideal components of jet fuel. Thus, the ability to convert naphthalene into decalin represents the conversion from harmful impurities in transportation fuels to ideal feed oils for jet fuels. Using Ni_2P NPs on silica, up to 92 % selectivity is observed for the hydrogenation of naphthalene to decalin.

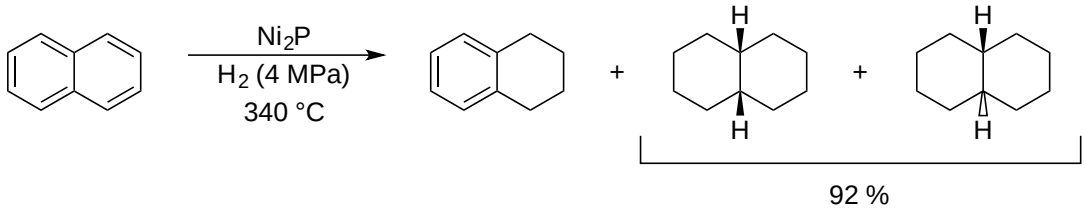

Scheme III-5. Hydrogenation of naphthalene to decalin with high selectivity.

Ni_2P NPs have been found to catalyze the selective reduction of phenylacetylene to predominantly styrene (Scheme III-6).[18] This kind of selective reduction is a major challenge, and Ni(0) NPs reduce phenylacetylene exclusively to ethylbenzene under hydrogen (Chapter I). This attenuation of the hydrogenation activity of Ni_2P has been attributed to the electron-withdrawing effect of phosphorus on nickel.

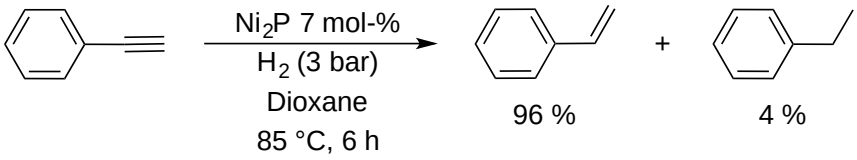

Scheme III-6. Partial hydrogenation of phenylacetylene to predominantly styrene.

2. Literature syntheses of Ni_2P

Due to their importance in numerous chemical applications, many synthetic methods have been developed for Ni_2P NPs. These methods can be categorized by their phosphorus source (Scheme III-7).

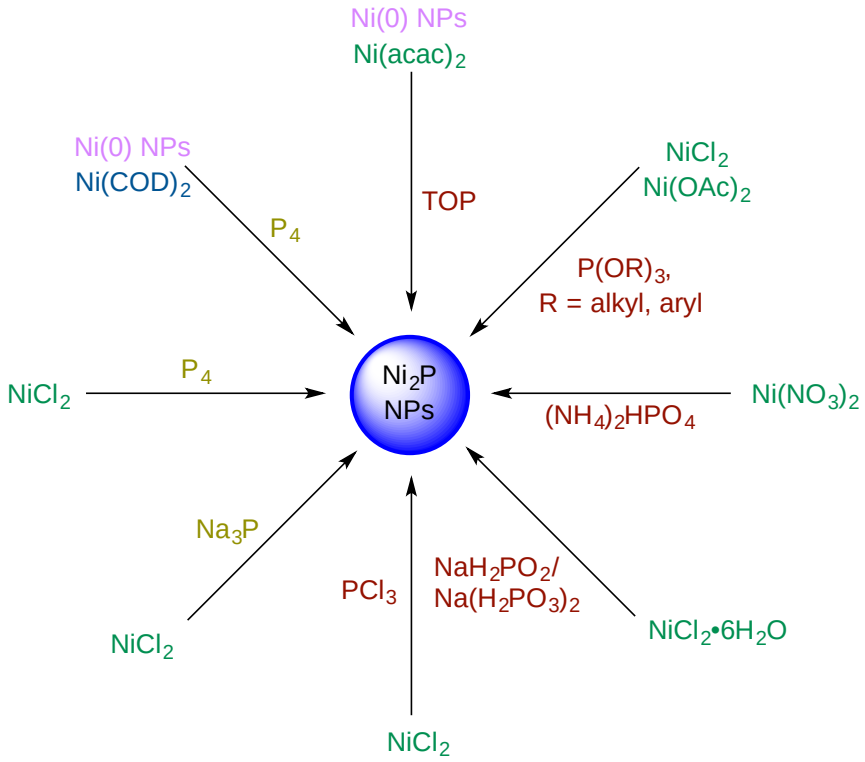

Scheme III-7. Summary of metal precursors and phosphorus sources for formation of Ni_2P NPs.

One method of Ni_2P NP synthesis employs trioctylphosphine (TOP). Pre-synthesized Ni(0) NPs were redispersed in excess TOP, then injected at 290 °C into octyl ether before being reacted at 300 °C for 2 h.[19] This resulted in particles of 5.6 nm in diameter. Alternatively, pre-synthesized Ni(0) NPs were redispersed in 1-octadecene with the aid of sonication, then mixed with excess TOP and oleylamine. This mixture was heated at 320 °C for 1 h to result in hollow particles of 5 – 15 nm.[20]

Ni_2P NPs could also be obtained directly from a Ni(II) precursor without first synthesizing Ni(0) NPs.[15] Nickel(II) acetylacetonate [$Ni(acac)_2$] was heated in 1-octadecene, oleylamine, and TOP at 320 °C for 2 h to form Ni_2P NPs of 17 nm. The advantage of such reactions is that TOP may serve not only as phosphorus source, but also as solvent and as stabilizing ligand for the resulting nanoparticles. However, high temperatures are necessary to induce the decomposition of the phosphine, and there is little control over the stoichiometry of nickel to phosphorus. At more moderate temperatures, such as those used in Chapter II for the synthesis of Ni(0) NPs in the present work, TOP does not decompose and thus serves simply as a surface ligand rather than a source of P.

A second method uses phosphate as the phosphorus source.[9c] Aqueous ammonia phosphate [$(NH_4)_2HPO_4$] was aged with nickel(II) nitrate hexahydrate and citric acid overnight at 90 °C, dried in an oven at 124 °C, and was then calcined at 500 °C for 5 h. It was then reduced under H_2 before being passivated in 1 % O_2 to finally result in 20-nm-diameter Ni_2P NPs.

Other particles use sodium hypophosphite [$Na(H_2PO_2)$] as the P source.[21] A mixture of sodium hypophosphite and nickel chloride hexahydrate was mechanically ground together, then heated in a tube furnace at 250 °C under continuous nitrogen flow, resulting in polydisperse Ni_2P NPs between 10 – 50 nm. In a very similar reaction, sodium hypophosphite was replaced by sodium dihydrogenphosphite [$Na(H_2PO_3)$]. The hypophosphite and dihydrogenphosphite were found to initially produce phosphine (PH_3), which could then reduce the nickel(II) species.

PCl_3 can also be used as the P source.[22] It was reacted with anhydrous $NiCl_2$ and sodium in benzene at 330 °C over 20 h in an autoclave to result in 80-nm NPs. The flammable, pyrophoric, and toxic reagent PH_3 has also been used with nickel sources such as nickel(II) nitrate hexahydrate, nickel(II) acetate tetrahydrate, and ammonia nickel(II) nitrilotriacetate.[9a] These metal salts were used to impregnate a silica surface, which was then dried at 100 °C for 12 h. After reduction under H_2, the nickel/silica surfaces were calcined in a 10 % mixture of PH_3 in H_2 at 250 °C for 2 h before being passivated in 1 % O_2 to give Ni_2P NPs of 5 – 30 nm.

$P(OR)_3$ (R = alkyl or aryl) has also be used as a phosphorus source.[23] In the presence of oleylamine, it reacts with nickel(II) chloride or nickel(II) acetate in octadecene at 275 °C to form Ni_2P NPs. By changing the reaction parameters

(particularly the identity of the organophosphite precursor), these same components can be used to form $Ni_{12}P_5$ instead.

Another synthesis of Ni_2P employs Na_3P as the phosphorus source.[24] Na_3P was added to anhydrous $NiCl_2$ and toluene in an autoclave, which was maintained at 150 °C for 8 h to produce particles of 10 nm. This Na_3P species was made by the reduction of white phosphorus (P_4) by Na(0). Because it was a more active phosphorus source than those previously described, it could be heated at lower temperature than the above reactions.

In order to eliminate this additional step of forming Na_3P, P_4 is also used directly as the phosphorus source. Nickel(II) chloride hexahydrate was mixed with P_4 in aqueous ammonia at 160 °C for 12 h to result in Ni_2P NPs of 28 nm.[25] By changing the solvent from aqueous ammonia to ethylenediamine and lowering the temperature to 80 – 140 °C, particles of 50 nm could be obtained.[26] However, a qualitative examination of transmission electron microscopy (TEM) images of these particles quickly emphasized the need for improvements in the size-dispersity of the particles, which were not listed in the cited articles. Previous work in our group also used P_4 as an active phosphorus source, and greatly improved upon the size-dispersity and reaction time demonstrated in the above reports.[2,27]

Most simply, Ni_2P NPs could be obtained by direct addition of stoichiometric P_4 to nickel(0) bis(cyclooctadiene), which immediately resulted in an amorphous black solid.[2] Upon heating in trioctylphosphine oxide, this amorphous solid formed crystalline Ni_2P. Alternatively, Ni(0) NPs could be treated with stoichiometric amounts of P_4 at up to 220 °C h to obtain crystalline particles of Ni_2P of 4.8 – 25 nm or 50 – 80 nm, depending on the surface ligands and reaction conditions.

Interestingly, while simple Ni_2P nanoparticles were formed from Ni(0) and stoichiometric white phosphorus, Ni(0) nanoparticles heated in the presence of white phosphorus in a ratio of 1:3 phosphorus:nickel were found to form core-shell structures. The structures were composed of Ni_2P cores with a shell of Ni(0), instead of homogeneous Ni_3P.[28] Using an excess of phosphorus also still resulted in the formation of Ni_2P, with leftover P_4 remaining in solution.

We hoped to use a similar procedure of adding stoichiometric P_4 to convert the Ni(0) NPs reported in Chapter II to Ni_2P NPs. It was not clear that the same procedures used for previously synthesized Ni NPs would work in this case. We showed in Chapter II that the properties of Ni NPs derived from a $Ni(acac)_2$ complex

were not the same as those we obtained from a nickel(II) dioleylamide precursor. Specifically, we showed that while Ni NPs from $Ni(acac)_2$ catalyzed the full reduction of phenylacetylene to ethylbenzene,[29] Ni NPs from $1/n[Ni(oleylamide)_2]_n$ are able to catalyze the partial reduction of phenylacetylene to predominantly styrene in a ratio of 89:11 styrene:ethylbenzene. This demonstrates the attenuation of surface hydrogen adsorption on the surface of the Ni(0) NPs thus produced. Phosphorus in Ni_2P NPs is understood to draw electron density away from the Ni centers and to block unsaturated Ni(0) sites, thus resulting in more gentle hydrogenation behavior. The surface ligands on the Ni NPs synthesized in Chapter II, however, appeared to have blocked surface sites even without phosphorus present inside the particles. Thus, it was unclear whether the same procedures used previously to convert Ni NPs to Ni_2P NPs would work in this case.

3. Present synthesis of Ni_2P

Despite the different surface properties of the present Ni(0) NPs *vs.* those synthesized previously, we attempted to form Ni_2P NPs from Ni(0) NPs made from *in situ*-synthesized nickel(II) dioleylamide (see Chapter II for details on Ni(0) NP synthesis). As previously observed, simply heating either the isolated or unpurified nanoparticles in the presence of P_4 and oleylamine resulted in the stoichiometric formation of Ni_2P NPs (Figure III-2).

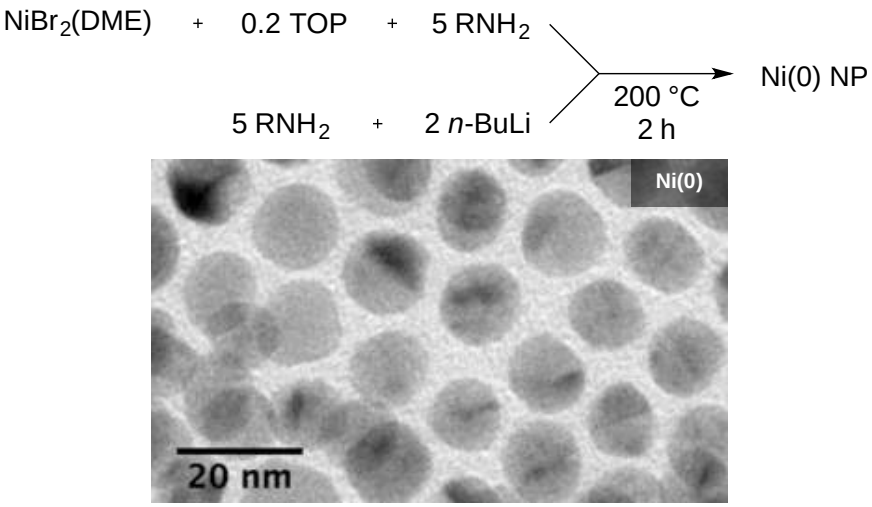

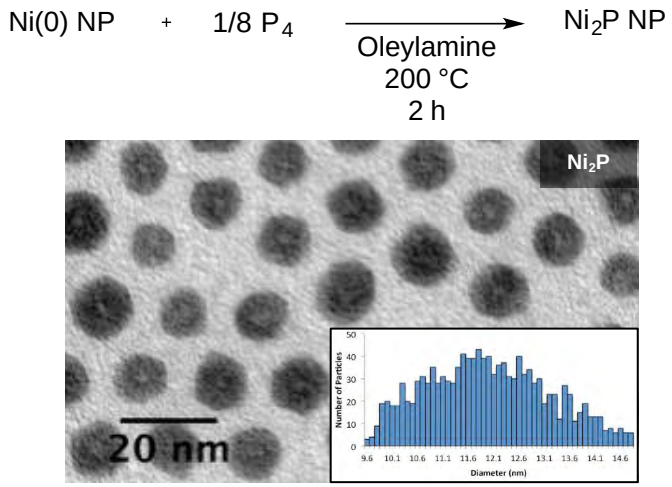

Figure III-2. Equations and TEM images of the formation of Ni_2P NPs (bottom, D = 12.0 ± 1.1 nm) from isolated Ni(0) NPs (top, D = 11.0 ± 1.1 nm).

X-ray diffraction (XRD) yielded little information on the structure of the Ni_2P NPs, suggesting the product to be amorphous, or comprised of very small crystals. This latter possibility was eliminated by wide-angle X-ray scattering (WAXS), which is able to analyze small crystalline zones. WAXS suggested that the phosphorus incorporation resulted in the corrosive amorphization of the particles, beginning at the surface and working its way to the center (Figure III-3). A series of diffractograms over two hours showed the progressive loss of crystallinity.

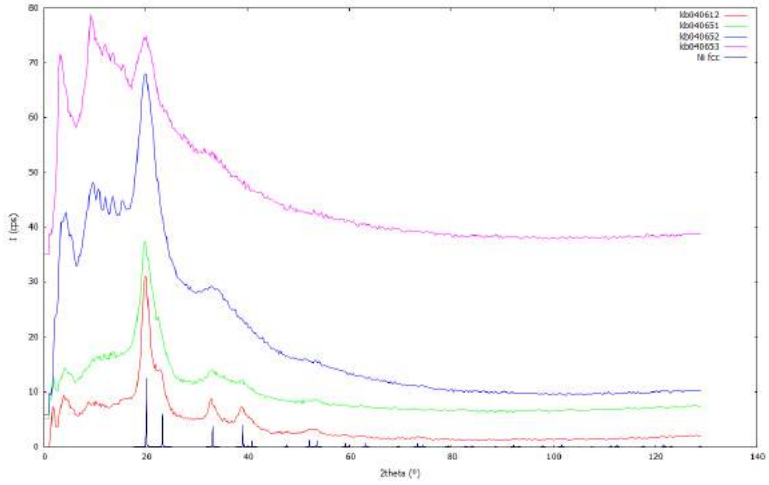

Figure III-3. WAXS diffractogram showing increasing amorphization of Ni(0) NPs upon addition of P_4 and consequent heating. Bottom-most blue line diagram: Ni(0)

fcc. From top to bottom: diffractogram after 0 (red), 5 (green), 30 (blue), and 120 (purple) minutes of heating of Ni(0) NPs with P_4.

We thus used ^{31}P NMR to monitor consumption of P_4, using triphenylphosphine as an internal standard. We saw complete consumption of P_4 after 60 minutes of heating (Figure III-4).

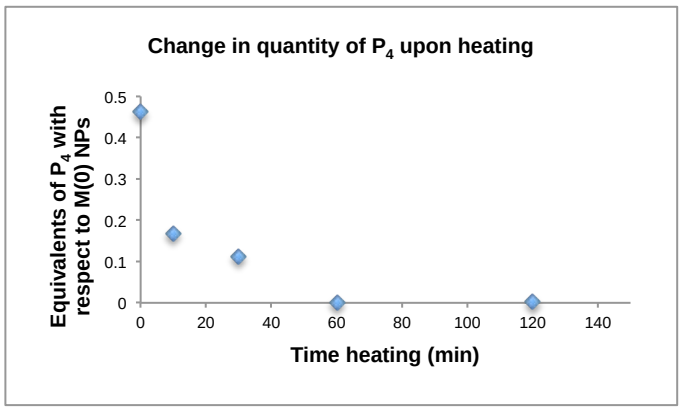

Figure III-4. Plot of consumption of P_4 over time, upon heating with Ni(0) NPs. Amount of P_4 remaining measured using ^{31}P NMR spectroscopy, with respect to triphenylphosphine internal standard.

The TEM images of the resulting particles showed significant morphological changes. They demonstrated a slight increase in size and had hollow centers. The hollowness might be indicative of the nanoscale Kirkendall effect, in which the outward diffusion of Ni occurs faster than the inward diffusion of P, resulting in empty centers.[30] Heating the particles under the same conditions in the absence of P_4 did not result in such conformational changes, confirming that they were a result of reaction with P_4.

Heating the Ni_2P particles under argon at 200 °C for four hours appeared to induce a crystallizing/ripening effect, resulting in an X-ray diffractogram with peaks corresponding to Ni_2P (Figure III-5). Scherrer analysis of the peak widths indicated particle diameters of about 20 nm. Unfortunately, the particles could not be resuspended in pentane, toluene, or oleylamine in order to obtain a TEM image.

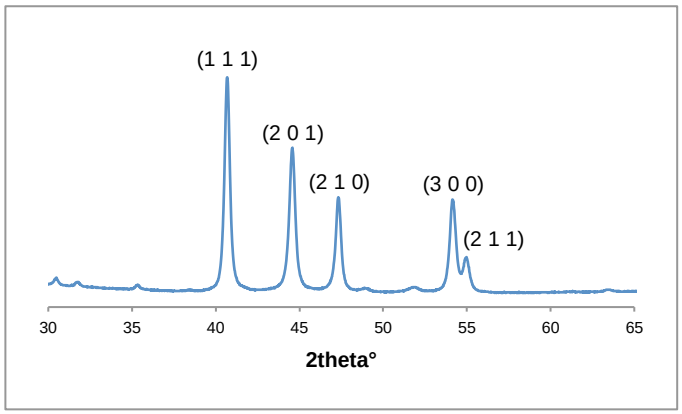

Figure III-5. XRD pattern of crystalline Ni_2P NPs upon annealing of amorphous particles under Ar for 4 h.

In order to better understand the mechanism of P_4 reactivity with Ni(0), the evolution of the particles was observed over time (Figure III-6). The Ni(0) NPs of 11 nm in diameter were found to be composed of crystalline zones of 3 nm (see Chapter II). Upon reaction with P_4, we initially observed digestion of the 11-nm particles down to their 3-nm crystalline zones. This was followed by the coalescence of these smaller particles into bigger ones, which equilibrated to the final, more monodisperse particles seen after two hours.

In a second examination of the same principle, the formation of the Ni_2P NPs was observed with substoichiometric (0.5 equivalents) and excess (15 equivalents) TOP (Figure III-7). A substoichiometric quantity appeared to arrest the recoalescence of some particles after digestion to monocrystalline forms, while others, presumably those not stabilized by TOP, were permitted to aggregate as expected. The presence of an excess of TOP, however, resulted exclusively in smaller particles.

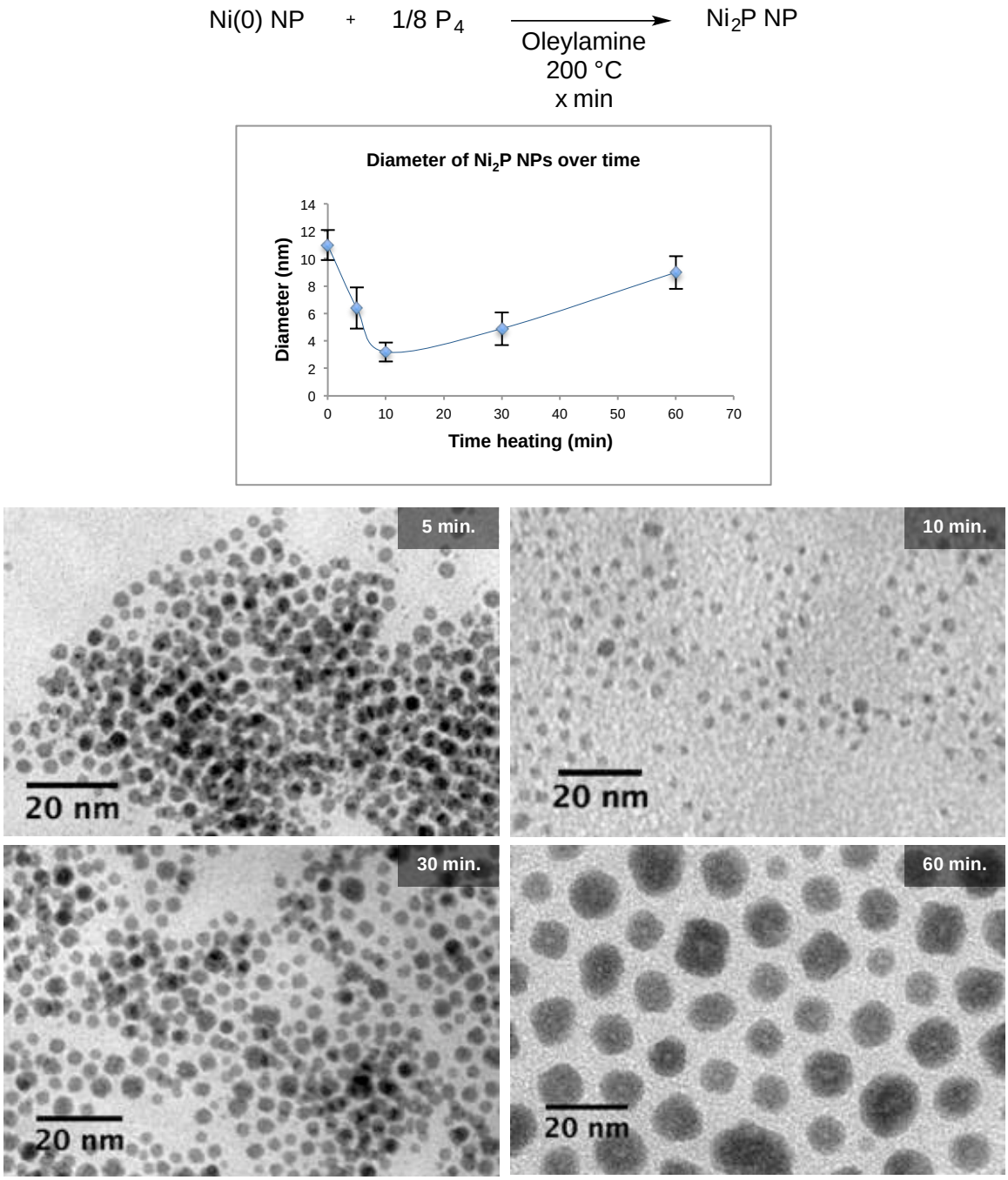

Figure III-6. Equation, summarizing graph, and TEM images of the evolution of Ni_2P particles over time. Left: TEM images of particles after heating for 5 min. (D = 6.4 ± 1.5 nm), 10 min. (D = 3.2 ± 0.7 nm), 30 min. (D = 4.9 ± 1.2 nm), and 60 min. (D = 9.0 ± 1.2 nm). Right: Plot of diameters over time, to show general size reduction and consequent growth. Line drawn through points to serve as guide to the eye.

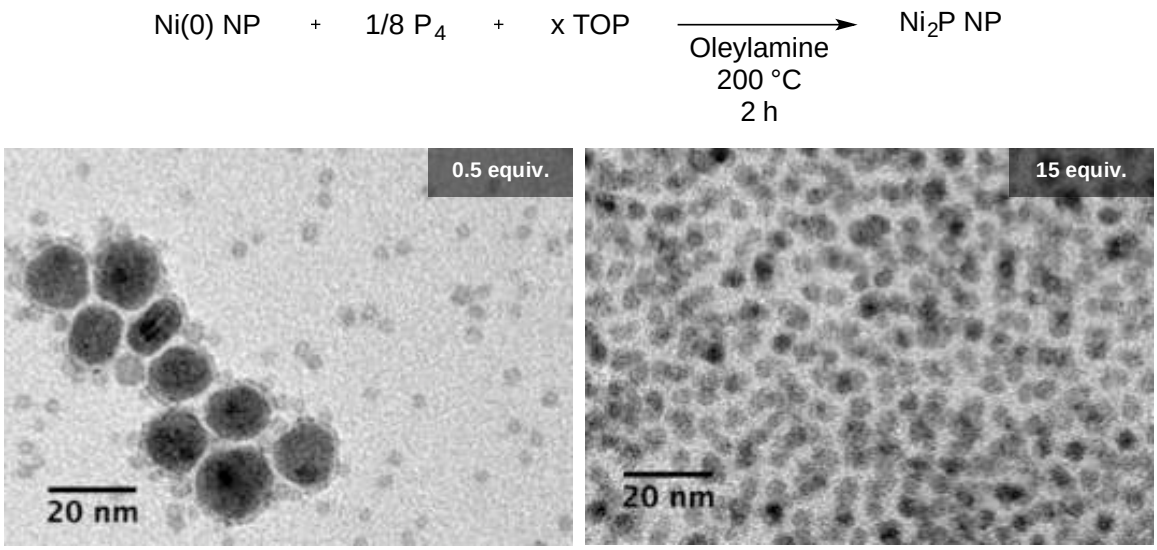

Figure III-7. Equation and TEM images of the formation of Ni_2P particles in the presence of 0.5 equiv. (D = 3.3 ± 0.6 nm or 11.6 ± 1.1 nm) and 15 equiv. (D = 4.2 ± 0.8 nm) TOP.

Halting the addition of P_4 to Ni(0) NPs in the presence of 15 equivalents of TOP reveals the formation of flower-like collections of particles (Figure III-8). They show the disaggregation of the initial Ni(0) NPs along grain boundaries between crystalline zones. We may postulate that grain boundaries act as a pathway for the diffusion of P into Ni(0) NPs, as they were seen to do at high temperature in previous work.[28] Once broken up by P insertion, the excess TOP in solution stabilized the particle surfaces and prevented reaggregation. Over time, with longer heating, the separated particles were able to redistribute in solution to form the completely disaggregated smaller particles seen in Figure III-6.

The timed study and the examination of the addition of TOP suggest that the addition of P_4 to Ni(0) NPs does not undergo a diffusion mechanism, as we might have supposed from the hollow centers. Instead, it undergoes digestion along grain boundaries, followed by reaggregation due to high surface energies. This is in contrast to the previous system studied in the group,[28] in which Ni(0) NPs appeared to follow a "templating" mechanism. In this mechanism, P_4 reacted with the surface of the Ni(0) NPs before diffusing into the NP, rather than reacting along grain boundaries, as it did in the present case.

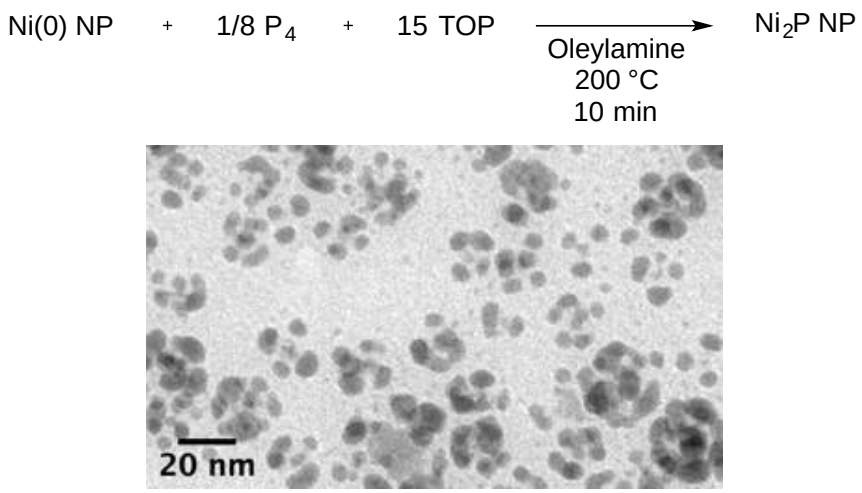

Figure III-8. Equations and TEM images of the disaggregation of Ni(0) NPs with P_4 in the presence of 15 equiv. TOP (individual particles: D = 4.6 ± 1.3 nm; overall flower-like clusters: D = 25 – 30 nm, with too few particles for reliable statistical analysis).

The amount of added P_4 was varied between 0.25 equivalents P per Ni to 1 equivalent P per Ni, in order to examine whether we could form Ni_3P or NiP_2. However, crystalline particles were not obtained, and thus the identities of the products could not be ascertained. Nonetheless, when 1:1 P:Ni were heated together, roughly 0.5 equivalents of P_4 remained after several hours of heating at 200 °C. This suggested that excess amounts of phosphorus still produced exclusively Ni_2P, as was previously observed.[28] Post-synthetic annealing might result again in the formation of crystalline NPs, which would permit the use of XRD to evaluate the identity of the product.

4. Extension to syntheses of Fe_2P and Co_2P

These reactions were extended to iron and cobalt NPs. Fe(0) and Co(0) NPs were prepared from *in situ*-synthesized iron(II) and cobalt(II) dioleylamide (Figure III-9). These NPs were reacted with P_4 to form their corresponding phosphides. In each case, the consumption of 0.5 equivalents of phosphorus by ^{31}P NMR spectroscopy suggests the formation of M_2P NPs (M = Fe, Co).

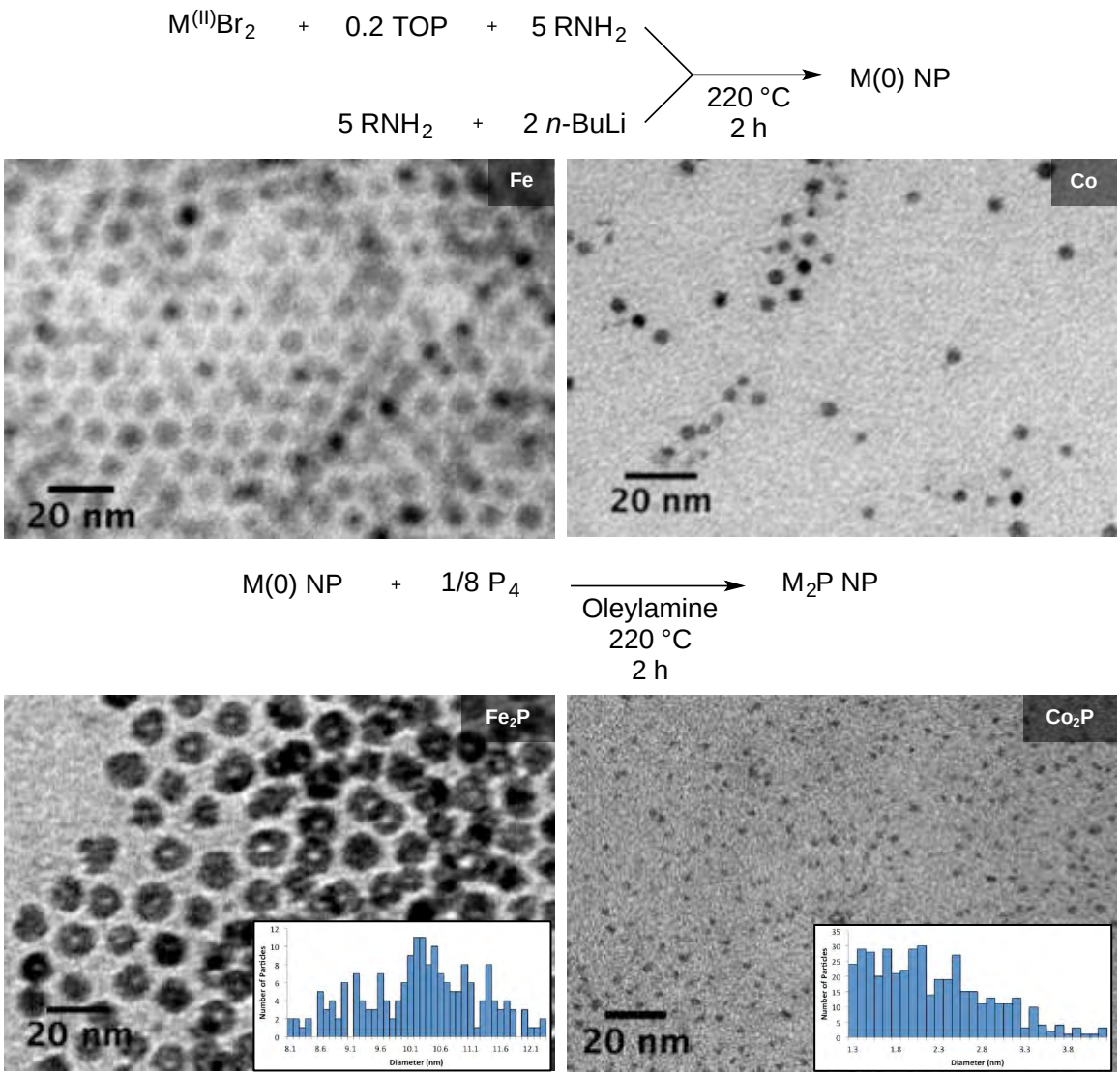

Figure III-9. Equations and TEM images of the formation of M_2P NPs; schemes on left and corresponding TEM images on right. Top: Synthesis of M(0) NPs (Fe(0) of D = 6.8 ± 0.8 nm, Co of D = 4.5 ± 0.6 nm). Bottom: Synthesis of M_2P NPs from isolated M(0) NPs (Fe_2P of D = 10.3 ± 1.0 nm, Co_2P of D = 1.8 ± 0.9 nm).

Interestingly, all three metal phosphide NPs synthesized (Ni, Fe, and Co) had hollow centers, though this is difficult to see in the above TEM image of small Co_2P NPs. Again, the samples of Fe(0) and Co(0) NPs were heated in the absence of P_4 under otherwise identical conditions, and no such conformational change was seen.

Once again, the particles were too amorphous to yield clear XRD peaks, and the incorporation of phosphorus was evaluated by ^{31}P NMR. Again, 0.25, 0.5, and 1

equivalents of P were added per equivalent of M(0). In all cases, the use of 1:1 P:M resulted in about 0.5 equivalents of unreacted P_4 after 2 h of heating.

These preliminary results of the formation of metal phosphide NPs using the Ni(0), Fe(0), and Co(0) NPs synthesized in Chapter II require further analysis to definitively confirm their identity, particularly in the form of XRD or WAXS. The only methods of evaluation we have heretofore employed, particularly for the putative Fe_2P and Co_2P, are the disappearance of P_4 without the appearance of any new peaks by ^{31}P NMR, and circumstantial evidence like the morphological changes induced by P_4. Post-reaction annealing is hoped to induce crystallization in the putative Fe_2P and Co_2P NPs, as it did for Ni_2P. The mechanism of particle ripening during annealing also needs to be examined.

Nonetheless, these results show that P_4 may be used as a highly reactive source of phosphorus for the formation of M_2P NPs, using M(0) NPs synthesized from commercially available metal(II) bromide salts. Mechanistic studies indicate a digestive mechanism of P_4 incorporation into the metals, followed by a reaggregation of smaller particles. Importantly, taken in conjunction with previous work, this study underlines that the mechanism of reaction is highly dependent on the ligand system stabilizing the precursor M(0) NPs. The above work is a promising foundation for a facile, robust synthesis of an important class of NPs.

5. References

[1] (a) Callejas, J. F.; Read, C. G.; Woske, C. W.; Lewis, N. S.; Schaak, R. E. *Chem. Mater.* **2016**, *28* (17), 6017–6044. (b) Carenco, S.; Portehault, D.; Boissière, C.; Mézailles, N.; Sanchez, C. *Chem. Rev.* **2013**, *113* (10), 7981–8065. (c) Eric J. Popczun, James R. McKone, Carlos G. Read, Adam J. Biacchi, Alex M. Wiltrout, Nathan S. Lewis, and Raymond E. Schaak. *J. Am. Chem. Soc.* **2013** *135* (25), 9267-9270

[2] Carenco, S.; Resa, I.; Le Goff, X.; Le Floch, P.; Mézailles, N. *Chem. Commun. (Camb).* **2008**, No. 22, 2568–2570.

[3] Pelletier, B.; Pelletier, C.; Sédillot, J. *Chez Croullerois: Paris*, **1798**, *2*, 42.

[4] (a) Carenco, S.; Portehault, D.; Boissière, C.; Mézailles, N.; Sanchez, C. *Chem. Rev.* **2013**, *113* (10), 7981–8065. (b) Oyama, S. T.; Gott, T.; Zhao, H.; Lee, Y. K. *Catal. Today* **2009**, *143* (1–2), 94–107. (c) Kanama, D.; Oyama, S. T.; Otani, S.; Cox, D. F. *Surf. Sci.* **2004**, *552* (1–3), 8–16.

[5] Sharon, M.; Tamizhmani, G. *J. Mater. Sci.* **1986**, *21* (6), 2193–2201.

[6] Sharon, M.; Tamizhmani, G.; Levy-Clement, C.; Rioux, J. *Sol. Cells* **1989**, *26*, 303–312.

[7] Carenco, S.; Surcin, C.; Morcrette, M.; Larcher, D.; Mézailles, N.; Boissière, C.; Sanchez, C. *Chem. Mater.* **2012**, *24* (4), 688–697.

[8] (a) Oyama, S. T.; Wang, X.; Lee, Y. K.; Chun, W. J. *J. Catal.* **2004**, *221* (2), 263–273. (b) Senevirathne, K.; Burns, A. W.; Bussell, M. E.; Brock, S. L. *Adv. Funct. Mater.* **2007**, *17* (18), 3933–3939.

[9] Yang, S.; Liang, C.; Prins, R. *J. Catal.* **2006**, *237* (1), 118–130. (b) Fuks, D.; Vingurt, D.; Landau, M. V.; Herskowitz, M. *J. Phys. Chem. C* **2010**, *114* (31), 13313–13321. (c) Wang, R.; Smith, K. J. *Appl. Catal. A Gen.* **2009**, *361* (1–2), 18–25. (d) Duan, X.; Teng, Y.; Wang, A.; Kogan, V. M.; Li, X.; Wang, Y. *J. Catal.* **2009**, *261* (2), 232–240.

[10] Callejas, J. F.; Read, C. G.; Woske, C. W.; Lewis, N. S.; Schaak, R. E. *Chem. Mater.* **2016**, *28*(17), 6017–6044.

[11] Liu, P.; Rodriguez, J. A.; Takahashi, Y.; Nakamura, K. *J. Catal.* **2009**, *262* (2), 294–303.

[12] Liu, P.; Rodriguez, J. A. *J. Am. Chem. Soc.* **2005**, *127* (1), 14871–14878.

[13] Popczun, E. J.; McKone, J. R.; Read, C. G.; Biacchi, A. J.; Wiltrout, A. M.; Lewis, N. S.; Schaak, R. E. *J. Am. Chem. Soc.* **2013**, *135* (25), 9267–9270.

[14] Stern, L.-A.; Feng, L.; Song, F.; Hu, X. *Energy Environ. Sci.* **2015**, *8*, 2347–2351.

[15] Chang, J.; Feng, L.; Liu, C.; Xing, W.; Hu, X. *Angew. Chem. Int. Ed.* **2014**, *53* (1), 122–126.

[16] Habas, S. E.; Baddour, F. G.; Ruddy, D. A.; Nash, C. P.; Wang, J.; Pan, M.; Hensley, J. E.; Schaidle, J. A. *Chem. Mater.* **2015**, *27* (22), 7580–7592.

[17] Zhang, X.; Zhang, Q.; Guan, J.; He, D.; Hu, H.; Liang, C. *Asia-Pac. J. Chem. Eng.* **2009**, *4*, 574–580.

[18] (a) Carenco, S.; Leyva-Pérez, A.; Concepción, P.; Boissière, C.; Mézailles, N.; Sanchez, C.; Corma, A. *Nano Today* **2012**, *7* (1), 21–28. (b) Chen, Y.; Li, C.; Zhou, J.; Zhang, S.; Rao, D.; He, S.; Wei, M.; Evans, D. G.; Duan, X. *ACS Catal.* **2015**, *5* (10), 5756–5765.

[19] Henkes, A. E.; Vasquez, Y.; Schaak, R. E. *J. Am. Chem. Soc.* **2007**, *129* (7), 1896–1897.

[20] Chiang, R. K.; Chiang, R. T. *Inorg. Chem.* **2007**, *46* (2), 369–371.
[21] Feng, L.; Vrubel, H.; Bensimon, M.; Hu, X. *Phys. Chem. Chem. Phys.* **2014**, *16* (13), 5917–5921.
[22] Lü, B.; Bai, Y. J.; Feng, X.; Zhao, Y. R.; Yang, J.; Chi, J. R. *J. Cryst. Growth* **2004**, *260* (1-2), 115–117.
[23] Men, L.; White, M. A.; Andaraarachchi, H.; Rosales, B. A.; Vela, J. *Chem. Mater.* **2016**, *ASAP*.
[24] Qian, X. F.; Zhang, X. M.; Wang, C.; Wang, W. Z.; Qian, Y. T. *Mater. Res. Bull.* **1998**, *33* (5), 669–672.
[25] Su, H. L.; Xie, Y.; Li, B.; Liu, X. M.; Qian, Y. T. *Solid State Ionics* **1999**, *122*, 157–160.
[26] Xie, Y.; Su, H. L.; Qian, X. F.; Liu, X. M.; Qian, Y. T. *J. Solid State Chem.* **2000**, *149*, 88–91.
[27] Carenco, S.; Hu, Y.; Florea, I.; Ersen, O.; Boissière, C.; Mézailles, N.; Sanchez, C. *Chem. Mater.* **2012**, *24* (21), 4134–4145.
[28] Carenco, S.; Goff, X. F. Le; Shi, J.; Roiban, L.; Ersen, O.; Mézailles, N. *Chem. Mater.* **2011**, *23*, 2270–2277.
[29] Carenco, S.; Leyva-Pérez, A.; Concepción, P.; Boissière, C.; Mézailles, N.; Sanchez, C.; Corma, A. *Nano Today* **2012**, *7* (1), 21–28.
[30] Yin, Y.; Rioux, R. M.; Erdonmez, C. K.; Hughes, S.; Somorjai, G. A.; Alivisatos, A. P. *Science.* **2004**, *304* (5671), 711–714.

6. Experimental Details

General considerations

General considerations may be taken from the experimental section of Chapter II. TEM images were also analyzed in the same way as described in that section. X-ray diffractometry

Synthesis of Nanoparticles

The procedures outlined below were repeated at least twice to verify reproducibility.

1. Synthesis of Ni_2P nanoparticles.

Ni_2P NPs were obtained from Ni(0) NPs prepared from $NiBr_2$(DME) by the *in situ* formation of nickel(II) dioleylamide, as described in Chapter II. These Ni(0) NPs of D = 11.0 ± 1.1 nm were isolated via precipitation by ethanol and drying *in vacuo*. Stoichiometries were calculated with respect to the starting amount of $NiBr_2$(DME). All of the Ni(0) NPs obtained from 0.3 mmol $NiBr_2$(DME) (92.6 mg) were resuspended in 0.5 mL oleylamine. A solution of 0.56 M P_4 in toluene (0.27 mL, 0.15 mmol with respect to P) was added to the suspension. The mixture was heated at 200 °C for 2 h. It was cooled, precipitated, and redispersed using the same procedure outlined in Chapter II.

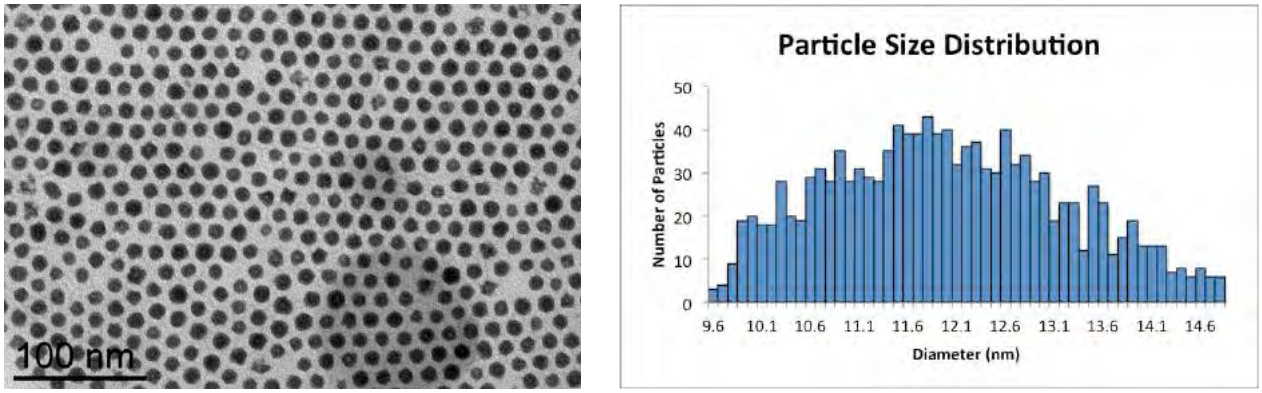

Figure Exp3.1: TEM image of Ni_2P NPs synthesized from isolated Ni(0) NPs with stoichiometric P_4, in oleylamine at 200 °C for 2 h, and corresponding size distribution.

This reaction was also repeated after having dried the solution *in vacuo* to eliminate residual toluene from the solution of P_4. No difference was observed in the resulting TEM images from this drying step.

This reaction was also run to shorter time periods, being stopped and plunged into a bath of water at room temperature after 5, 10, 30, and 60 minutes of reaction time (rather than the full 2 h), to obtain Figure III-6.

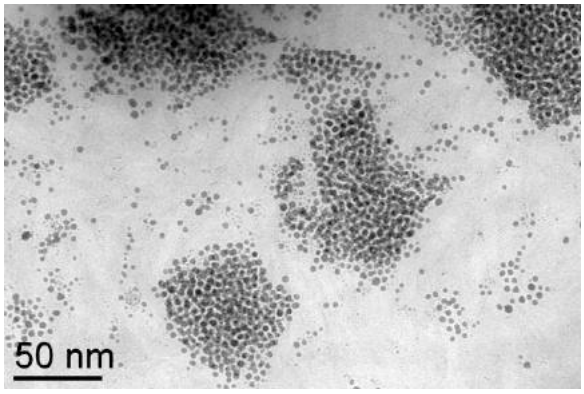

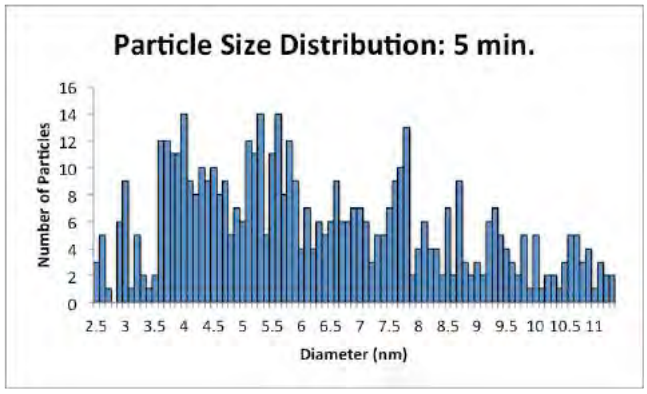

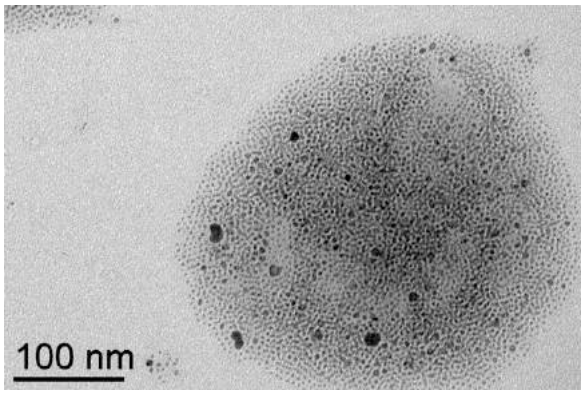

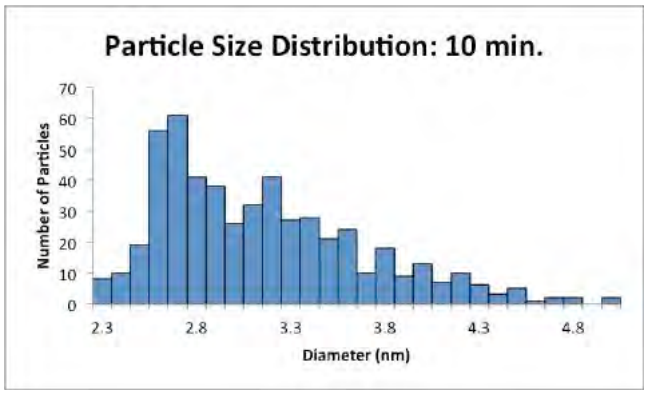

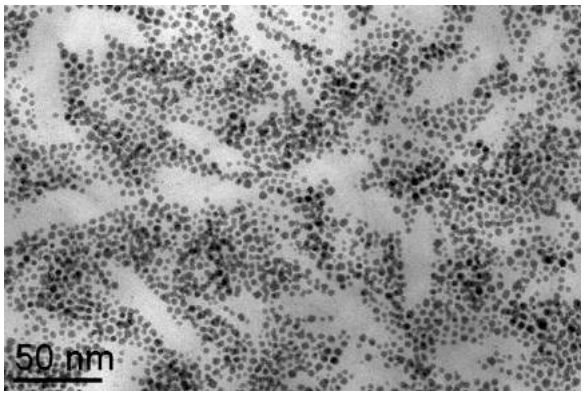

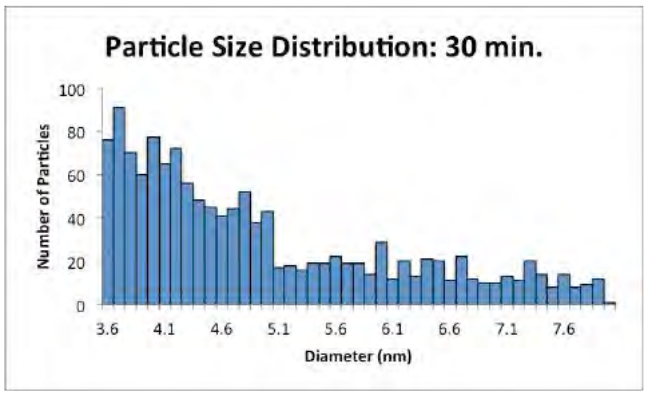

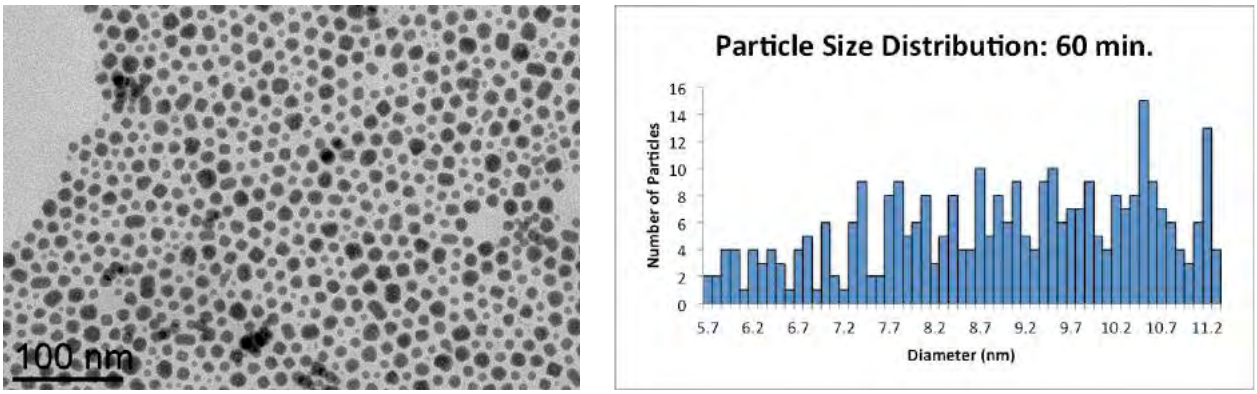

Figure Exp3.2: TEM images of Ni_2P NPs synthesized from isolated Ni(0) NPs with stoichiometric P_4, in oleylamine at 200 °C for 5, 10, 30, or 60 min., and corresponding size distributions.

The reaction was repeated with 0.5 or 15 equivalents of added TOP. All of the Ni(0) NPs obtained from 0.3 mmol $NiBr_2$(DME) (92.6 mg) were resuspended in 0.5 mL oleylamine and TOP (67.0 μL, 0.15 mmol; or, 2.0 mL, 4.5 mmol). A solution of 0.56 M P_4 in toluene (0.27 mL, 0.15 mmol with respect to P) was added to the suspension. The mixtures were heated at 200 °C for 2 h. They were cooled, precipitated, and redispersed using the same procedure outlined previously.

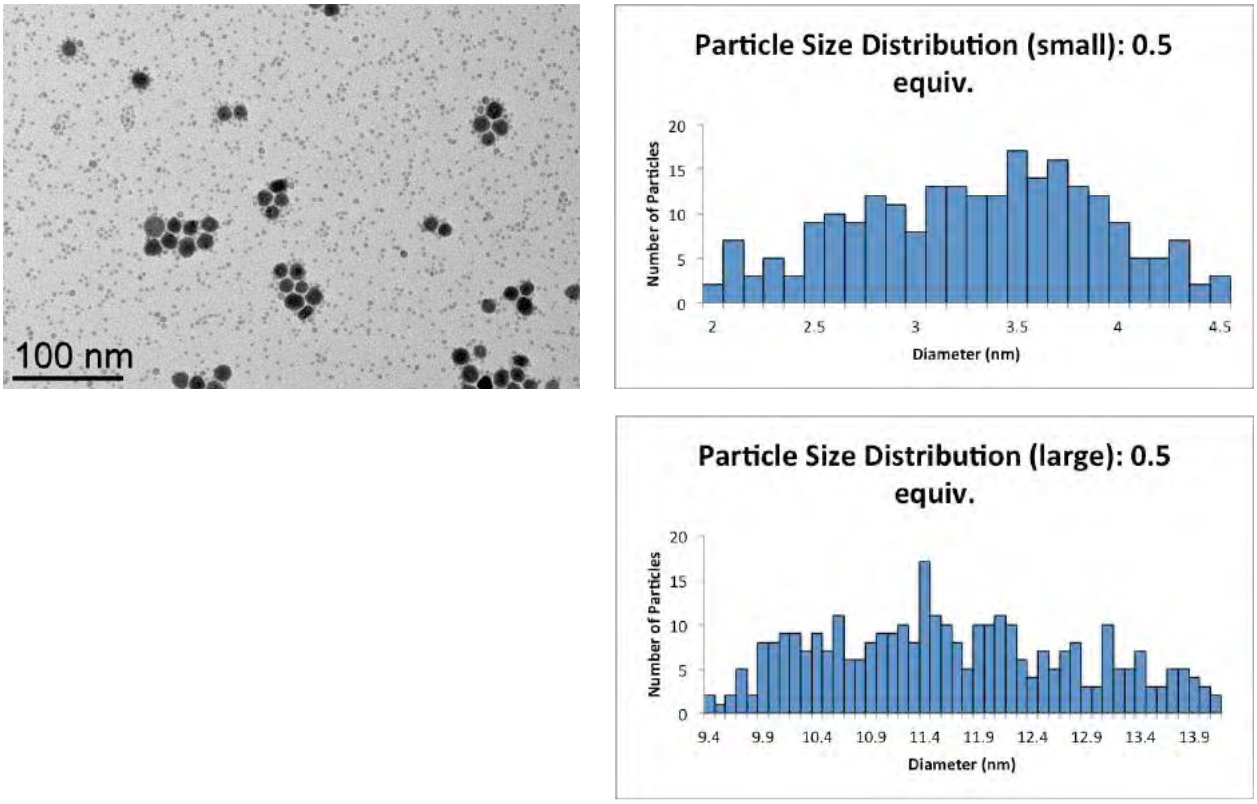

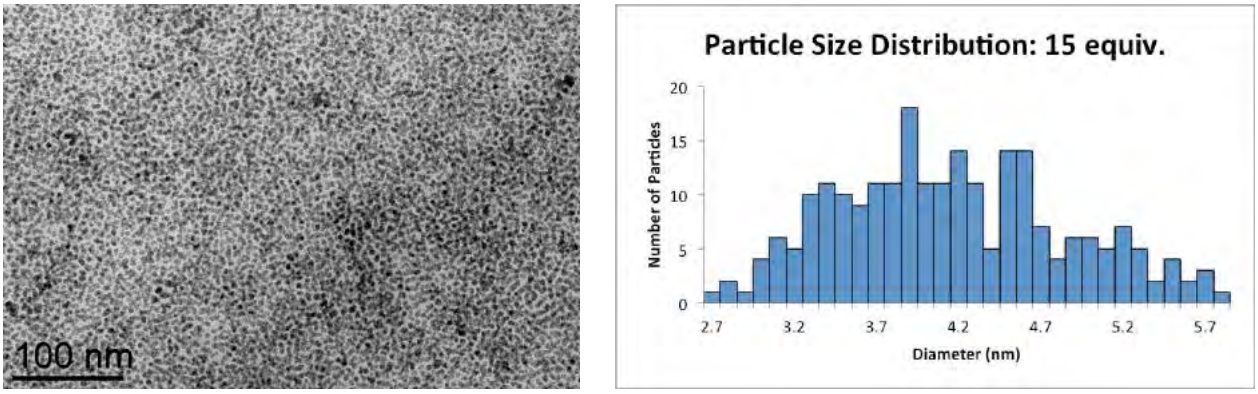

Figure Exp3.3: TEM images of Ni_2P NPs synthesized from isolated Ni(0) NPs with stoichiometric P_4 and 0.5 or 15 equiv. TOP, in oleylamine at 200 °C for 2 h, and corresponding size distributions.

The reaction using 15 equiv. TOP was stopped after just 10 minutes.

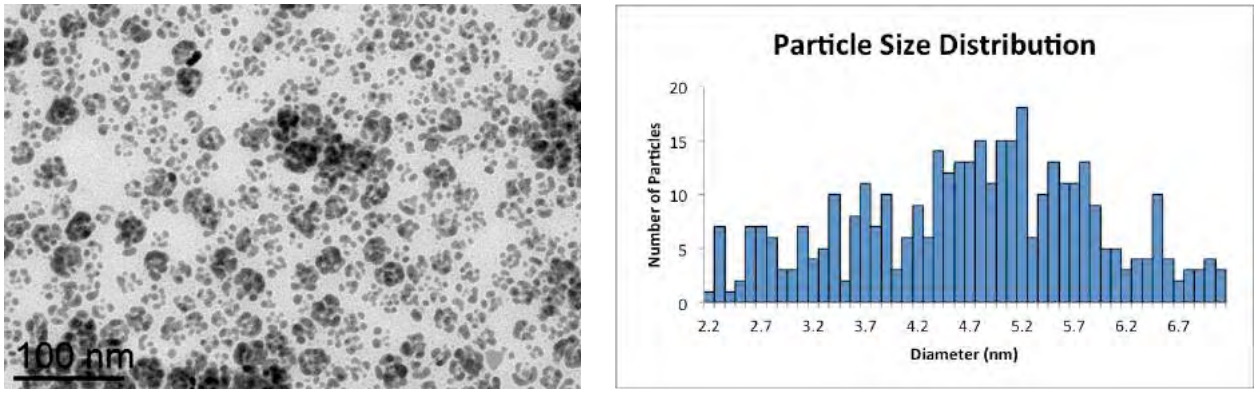

Figure Exp3.4: TEM image of Ni_2P NPs synthesized from isolated Ni(0) NPs with stoichiometric P_4 and 15 equiv. TOP, in oleylamine at 200 °C for 10 min., and corresponding size distribution.

2. Synthesis of iron and cobalt phosphide nanoparticles from M(0) nanoparticles

In the reactions shown in Figure III-9, putative M_2P NPs (M = Fe, Co) were obtained from the stoichiometric addition of P_4 to M(0) NPs prepared from MBr_2 by the *in situ* formation of metal(II) dioleylamide, as described in Chapter II. These M(0) NPs of D = 6.8 ± 0.8 nm for Fe(0) and D = 1.8 ± 0.9 nm for Co(0) were isolated via precipitation by ethanol and drying *in vacuo*. Stoichiometries were calculated with respect to the starting amount of $NiBr_2$(DME). All of the M(0) NPs obtained from 0.3 mmol MBr_2 ($FeBr_2$: 64.7 mg; $CoBr_2$: 65.6 mg) were resuspended in 0.5 mL

oleylamine. A solution of 0.56 M P_4 in toluene (0.27 mL, 0.15 mmol with respect to P) was added to the suspension. The mixture was heated at 200 °C for 2 h. It was cooled, precipitated, and redispersed using the same procedure outlined previously, with the replacement of ethanol as precipitation solvent by acetone.

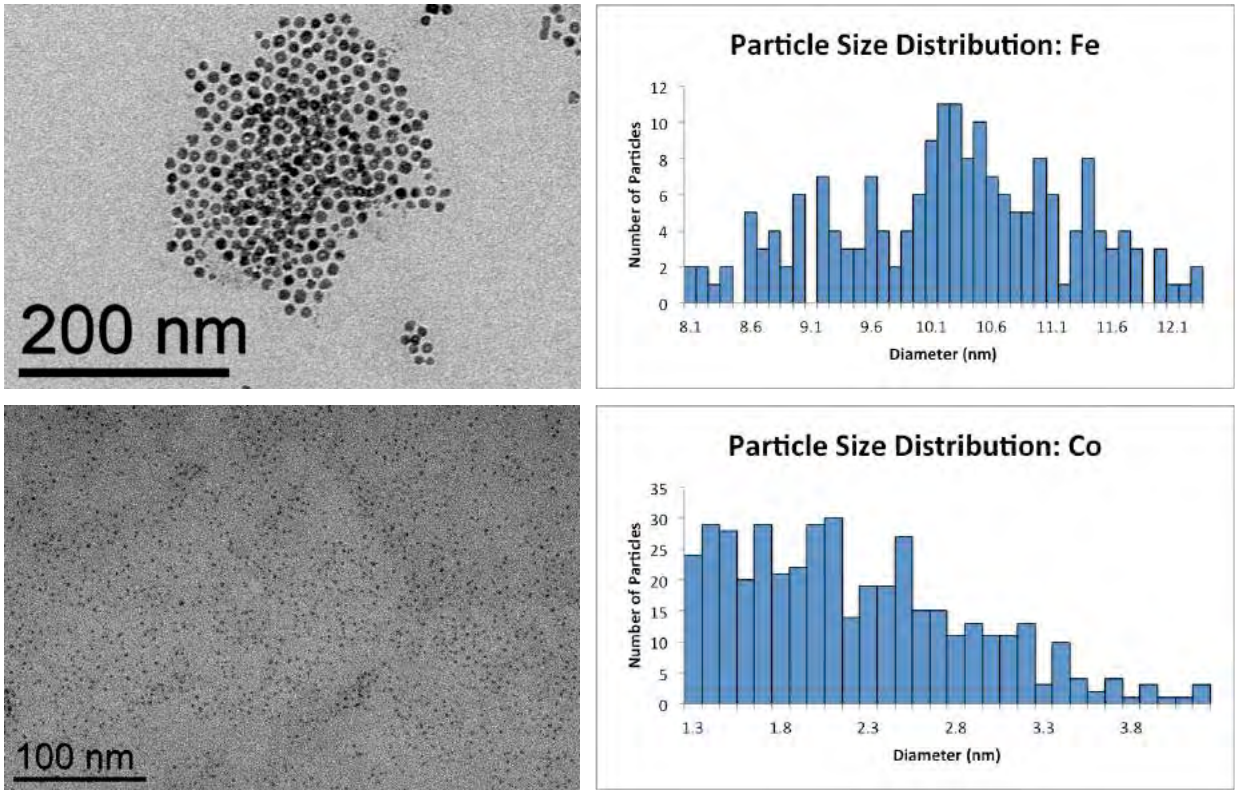

Figure Exp3.5: TEM images of putative M_2P NPs (M = Fe, Co) synthesized from isolated M(0) NPs with stoichiometric P_4, in oleylamine at 200 °C for 2 h, and corresponding size distributions.

^{31}P Nuclear Magnetic Resonance (NMR) Spectroscopy

^{31}P NMR spectra were recorded on a Bruker AC-300 SY spectrometer operating at 121.4 MHz for ^{31}P. Integrations were performed with respect to triphenylphosphine internal standard.

Stoichiometries of Ni:P were calculated with respect to the starting amount of $NiBr_2$(DME). All of the Ni(0) NPs obtained from a previous reaction (0.3 mmol $NiBr_2$(DME), 92.6 mg) were resuspended in 0.5 mL oleylamine in a Schlenk flask. A solution of 0.56 M P_4 in toluene (0.27 mL, 0.15 mmol with respect to P) was added to the suspension. The mixture was heated at 200 °C for 0, 5, 30, 60, or 120. Each sample was transferred to a J-Young tube containing triphenylphosphine (0.1 mmol, 26.2 mg). Each NMR was obtained over 64 scans, with a d1 = 60 sec.

X-Ray Powder Diffraction (XRD) and Wide-Angle X-Ray Scattering (WAXS)

XRD and WAXS measurements were performed as described in the experimental section of Chapter II. Crystallite sizes were calculated from XRD using the Scherrer Calculator tool of the Highscore software.

Scherrer formula:

Crystallite size (average) = $k * \lambda / (B_{size} \cos \theta)$

With:

- $B_{size} = B_{obs} - B_{std}$
- B_{obs} = FWHM of the sample
- B_{std} = FWHM of a standard (LaB_6)
- $k = 0.9$ (spherical approximation)
- $\lambda = 1.5418$ Å

Particles obtained from the method displayed in Figure III-5 were washed thrice with ethanol and dried *in vacuo.*

In a complement to Figure III-4, in which WAXS shows the increasing amorphization of the Ni(0) during heating with P_4, the plot of the radial distribution function shows diminishing crystalline zones. A series of parallel reactions were set up. In each, all of the Ni(0) NPs obtained from 0.3 mmol $NiBr_2$(DME) (92.6 mg) were resuspended in 0.5 mL oleylamine. A solution of 0.56 M P_4 in toluene (0.27 mL, 0.15 mmol with respect to P) was added to the suspension. The mixture was heated at 200 °C for 0 (red), 5 (green), 30 (blue), or 120 (purple) min. It was cooled, precipitated, and redispersed using the same procedure described previously.

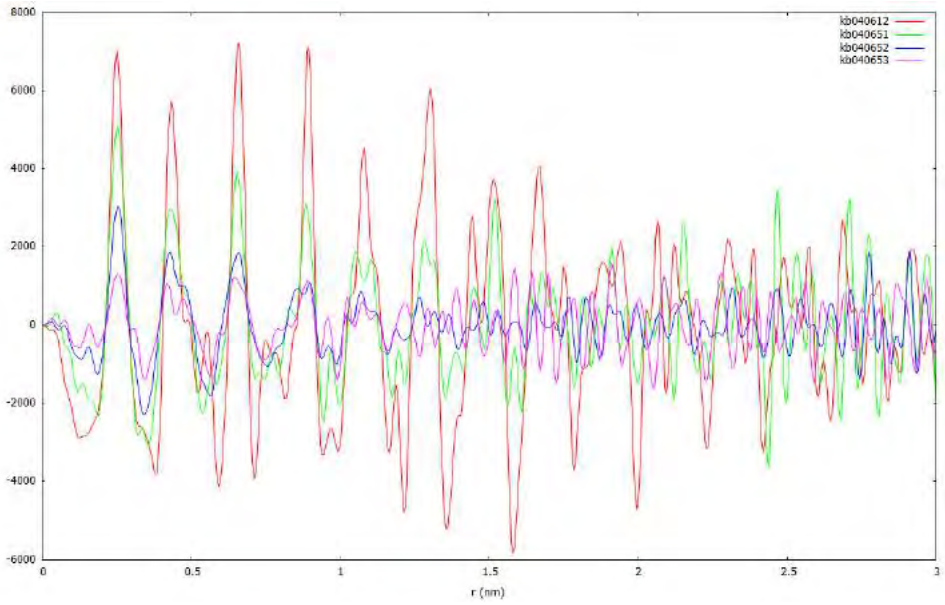

Figure 3.5: Radial distribution function plot of amorphization of Ni(0) NPs upon heating with P_4.

Chapter IV: Literature use of white phosphorus to synthesize organophosphines

1. History of phosphorus chemistry

Phosphorus is a key component of life.[1] In the form of phosphates, or PO_4^{3-}, it is found in DNA, RNA, ATP, and cell membranes. The average adult human body contains about 0.5 kg phosphorus, primarily in the bones and teeth,[2] and a well-fed adult consumes and excretes 1 – 3 g phosphorus per day. Bone ash and fossils are rich in phosphates, leading farmers from thousands of years ago to lay calcined bones and guano on their fields as natural fertilizers.[3] The modern understanding of phosphate fertilizers came from the 19th century, when the theory of phosphorus uptake in plants from soil was first developed. Today, 90 % of phosphorus-containing chemical synthesis is for the production of fertilizers. Most of the remaining 10 % is reduced to elemental phosphorus.

Elemental phosphorus exists in the form of several allotropes, among them the highly stable, unreactive, and less common violet and black allotropes, and the somewhat unreactive, polymeric, and poorly understood red phosphorus.[4] The most reactive allotrope of elemental phosphorus is the tetrahedral white phosphorus (P_4) (Figure IV-1).

Figure IV-1. White phosphorus (P_4), in its structural formula (left) and in its physical form (right).

The ubiquity of phosphorus in organic matter led to the initial isolation of P_4 from urine. In 1669, Hennig Brand first isolated P_4 during his search for the philosopher's stone by drying urine and heating the residue in the absence of air.[5] The resulting white, waxy substance he obtained glowed in the dark, leading him to name it *phosphorus*, or "bearer of light." He required 1100 L urine to produce 60 g P_4.

In the 18th century, the principal source of P_4 shifted from urine to bone ash. By the 19th century, P_4 was mainly derived from bird and bat guano mined from tropical islands. Today it is obtained from phosphate rock, which is largely comprised of animal remains and excrement. Its increased accessibility led to its increased use and misuse.

In the 19th century, P_4 was first commercially produced for match industry. The quotidian usage of this highly poisonous and flammable product led to many accidental poisonings, as well as its misuse for murders and suicides.[6] Match factory workers often developed sever necrosis in their jawbones from phosphorus deposition. During World War I, P_4 was used in incendiaries, smoke screens, and tracer bullets.[7] Its use during World War II included large-scale bombs.

Today, the industrial and laboratory use of P_4 is highly regulated. Its high reactivity renders it useful for chemical manipulation, and it is a well-behaved and relatively safe reagent when used under air-free conditions in 0.5 – 1 M solutions in toluene. It is thus a valuable tool for phosphorus chemistry, meriting a closer examination of its properties.

2. Modern production of white phosphorus and phosphorus products

P_4 is a waxy, white, light-sensitive solid that is industrially produced from the reduction of mined phosphate rock on the scale of 900,000 tonnes/y.[8] This rock, comprised primarily of calcium phosphate, is heated at high temperature in the presence of sand and refined coal to produce vaporized P_4 (Scheme IV-1). The vapor is then condensed into a white powder under water to prevent air oxidation.

Industrially, white phosphorus is a key intermediate to more valuable products. It is chlorinated to PCl_3 or reacted with aqueous KOH to yield mixtures of potassium hypophosphite (KH_2PO_2) and PH_3. These products are all subsequently used in various processes, such as the use of hypophosphites for electroless nickel-plating.[9]

Of note are the formations of PH_3 and PCl_3, the two precursors most relevant to the synthesis of organophosphines. The formation of each equivalent of PH_3 from P_4 requires the coproduction of a much greater amount of phosphorus-containing byproduct, while the formation of PCl_3 requires six equivalents of toxic chlorine gas per P_4 precursor. Nonetheless, PH_3 and PCl_3 are common precursors for the formation of organophosphines.

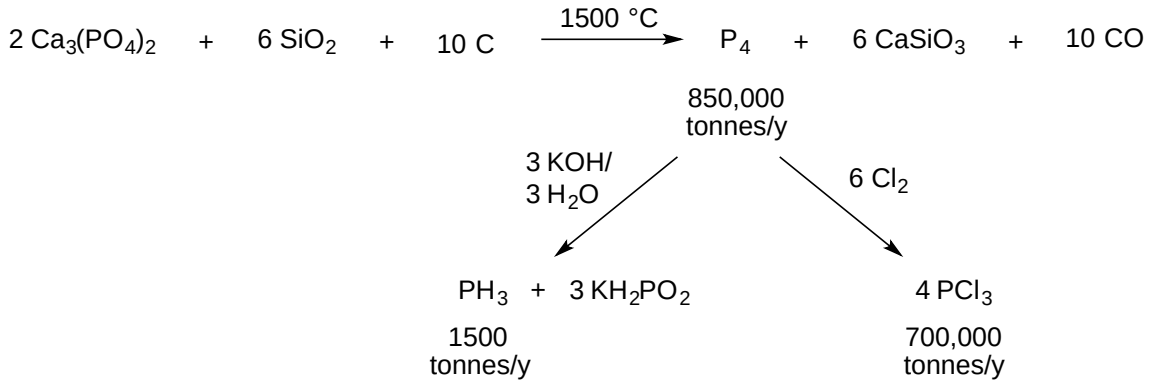

Scheme IV-1. Commercial synthesis of P_4 and consequent production of industrially important phosphorus products.

3. Synthesis of organophosphines from PCl_3 and PH_3

Organophosphines, which are widely used in both chemistry and biology, are the most important class of phosphorus-containing molecules in the laboratory. Organophosphines and their oxides are highly biologically active.[10,11] In the chemistry laboratory, organophosphines are powerful ligands for organometallic catalysis.[12] The trigonal pyramidal molecular geometry of organophosphines provides the metal center with a cone of steric protection. The stability they impart on the metal center through σ donation and π back-donation, in addition to their lability, permits the metal center to perform diverse reactions. Their high barrier to amine-like inversion (132 kJ/mol) permits them to exhibit pseudo-chirality.[13]

Most syntheses of organophosphines employ PCl_3 or PH_3 as the starting material. Their uses have both advantages and drawbacks.[14] For example, PH_3 only produces tertiary organophosphines in reaction with straight-chain alkenes. It is also difficult to use, since it is a deadly gas. The high reactivity of the volatile, air-sensitive, and pyrophoric PH_3 that makes it useful also makes it undesirable for laboratory use. PCl_3, meanwhile, results in the coproduction of chloride salts. Nonetheless, PCl_3 and PH_3 serve widely as precursors to organophosphine compounds, in the laboratory and industrially, respectively.

PCl_3 also serves commercially as a precursor to such products as PCl_5, $POCl_3$, and $PSCl_3$, which are used as herbicides, insecticides, plasticizers, oil additives, and flame-retardants. However, the use of halogenated agents for these applications results in the release of halides into the environment. Using organophosphines in the

same roles permits the avoidance of persistent chlorinated hydrocarbons in the environment.

PCl_3 behaves both as an electrophile and a weak nucleophile. As an electrophile, chloride serves as an effective leaving group. For example, PCl_3 reacts with ethanol to form $P(OEt)_3$ in the presence of a base (Scheme IV-2),[15] which is used as a soft ligand for metals such as Ni(0), Pd(0), and Pt(0).[16] Similarly, in the presence of a Lewis acid such as $AlCl_3$, PCl_3 undergoes electrophilic aromatic substitution to result in halophosphine compounds (Scheme IV-2). Halophosphines, which are highly reactive, are more interesting as intermediates than as final products. They can be reduced by reagents such as $LiAlH_4$ to produce primary phosphines.

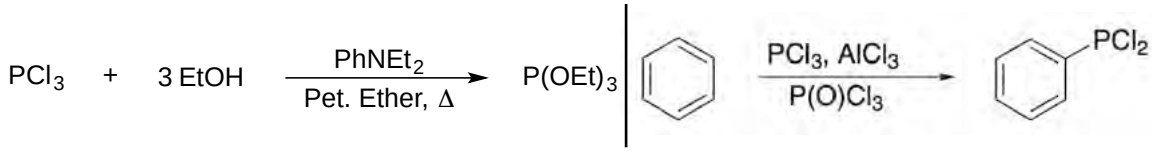

Scheme IV-2. Electrophilic behavior of PCl_3. Left: Base-catalyzed formation of phosphite. Right: Lewis acid-catalyzed electrophilic aromatic substitution.

The formal lone pair on PCl_3 permits it to behave as a weak nucleophile, resulting in adducts with strong Lewis acids such as BBr_3.[17] It also serves as a chlorinating agent, and, as mentioned above, as a starting material for the formation of organophosphorus compounds.[18] When reacted with Grignard reagents, PCl_3 produces tertiary organophosphines (Scheme IV-3).

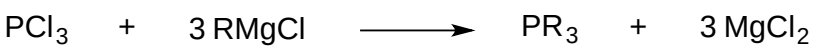

R = phenyl, cyclohexyl, butyl, octyl, tolyl

Scheme IV-3. Nucleophilic reaction of PCl_3 with Grignard reagents.

In the presence of metallic sodium, PCl_3 also reacts with aryl halides to produce triarylphosphine (Scheme IV-4).

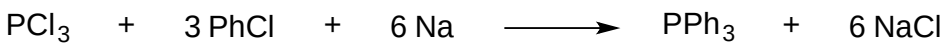

Scheme IV-4. Nucleophilic reaction of PCl_3 with phenyl chloride in presence of Na(0) to form tertiary organophosphines.

The toxic and flammable PH_3 is commonly used as a fumigant and dopant for semiconductors, but it is also used industrially as a precursor for organophosphorus compounds. The gaseous and very toxic PH_3 can be difficult to use, especially in laboratory settings, rendering it a challenging starting material for organophosphine synthesis.

To form organophosphines, aldehydes or alkenes are typically added to the P–H bond.[19] The radical-induced addition of internal alkenes to PH_3 has been shown to produce primary and secondary phosphines with high selectivity, particularly with cyclic alkenes (Scheme IV-5). This addition may also be catalyzed by acid for terminal alkenes. Meanwhile, the use of a terminal alkene with a radical initiator results in the formation of tertiary organophosphines.

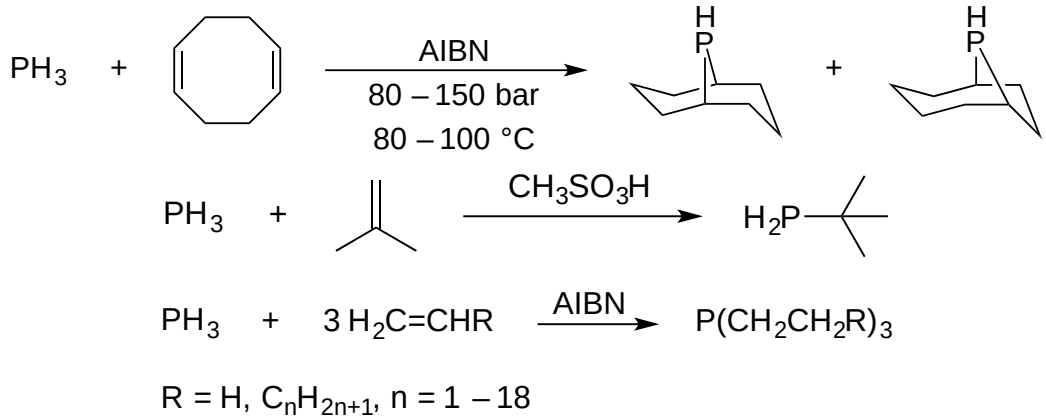

Scheme IV-5. Examples of alkene addition to PH_3. Top: radical-induced addition of cyclooctadiene to PH_3 using azobisisobutyronitrile (AIBN) as initiator. Middle: acid-catalyzed addition of isobutene to PH_3. Bottom: tertiary addition of terminal to PH_3 using radical initiation.

Ideally, a facile method for the production of organophosphines could be developed without requiring the toxic and pyrophoric reagent PH_3, or without the coproduction of chlorinated waste from PCl_3. Because both of these products come from elemental phosphorus, we hoped to develop a better route to organophosphorus compounds directly from an elemental precursor.

4. Properties and reactivity of white phosphorus

The tetrahedral P_4 is the least dense and most reactive allotrope of phosphorus,

and is flammable and pyrophoric. P_4 molecules are arranged in either the α or β crystalline forms.[20] The α form, which is more stable at room temperature, has a cubic crystal structure, which transforms to the hexagonal β form at –78 °C. P_4 exists in this tetrahedral form up to a temperature of 800 °C, at which point it decomposes to P_2.

Each P atom of P_4 formally bears a lone pair, and thus a superficial examination of the molecule might suggest it to be nucleophilic. However, its molecular orbital (MO) diagram reveals that the lone pairs do not lie in the highest occupied molecular orbital (HOMO) of the molecule (Figure IV-2).[21] Instead, the HOMO of P_4 lies on the P–P bonds, and are low-lying and poorly nucleophilic. Taken in conjunction with the low-lying lowest unoccupied molecular orbitals (LUMO) of P_4, we discover that P_4 is in fact electrophilic.

However, the P-centered lone pairs may be used to coordinate transition metal fragments or main group elements. Starting as far back as 1979, there are literature reports of P_4 coordinating to metal complexes (Scheme IV-6).[22] Sacconi's η^1-P_4 Ni(0) complex was the first to demonstrate an intact, vertex-coordinated P_4. Following this report, complexes with metal centers including W(0), Re(I), Fe(I), and Ru(I) were reported.

More recently, side-on coordination of P_4 has been accomplished in complexes of Ag(I), Cu(I), and Au(I). This may be seen as the first step of an oxidative addition of P_4 into the metal center. The side-on coordination of P_4 elongates the coordinating P–P bond, and may lead to the formal reduction of the tetrahedron to a P_4^{2-} unit. Indeed, Rh(III) complexes bearing this P_4^{2-} ligand have been synthesized by Ginsberg.

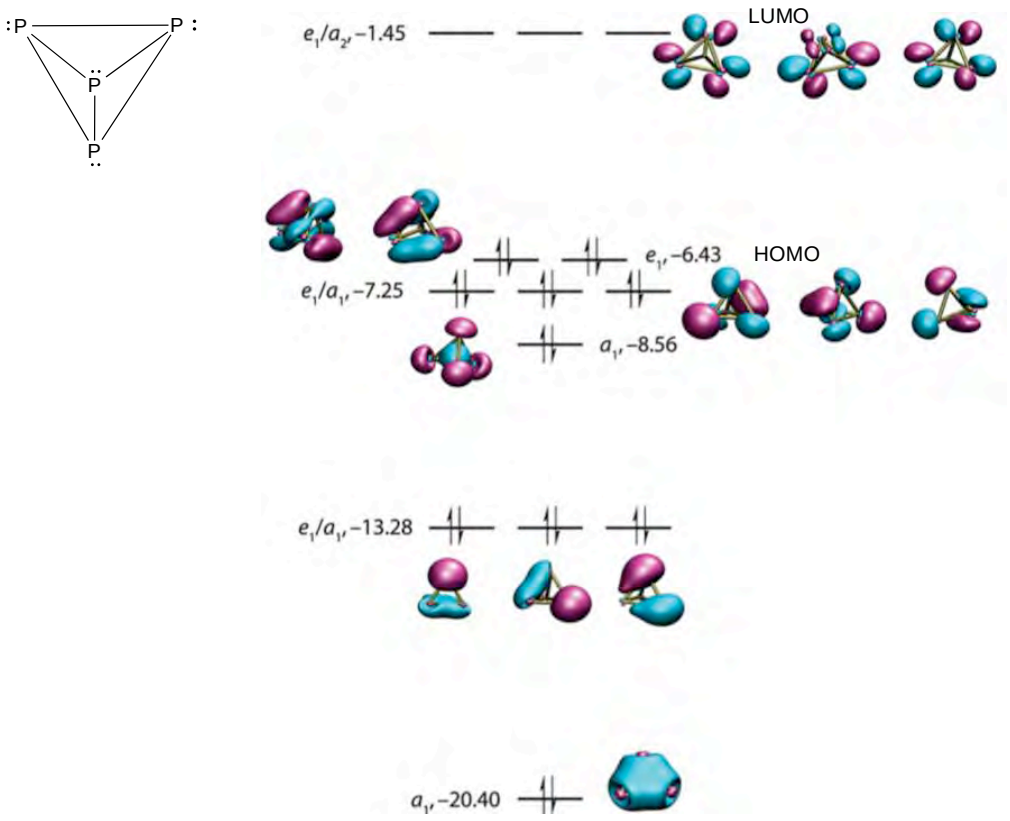

Figure IV-2. Molecular orbital diagram of P_4, with labeled HOMO and LUMO.[21] DFT: OLYP, QZ4P (eV).

We thus see that mild functionalization of P_4 to organophosphine derivatives has been pursued for many years, largely using metal centers to control its activity. Carefully designed, unsaturated transition metal complexes, typically featuring bulky and strongly electron donating ligands, allow both coordination of P_4 and/or insertion into one P–P bond prior to functionalization by hydrides or organic nucleophiles.[23] While these modes of coordination are interesting as conceptual proof of P_4 activation, they do not render the phosphorus atoms in the tetrahedron any more practically useful.

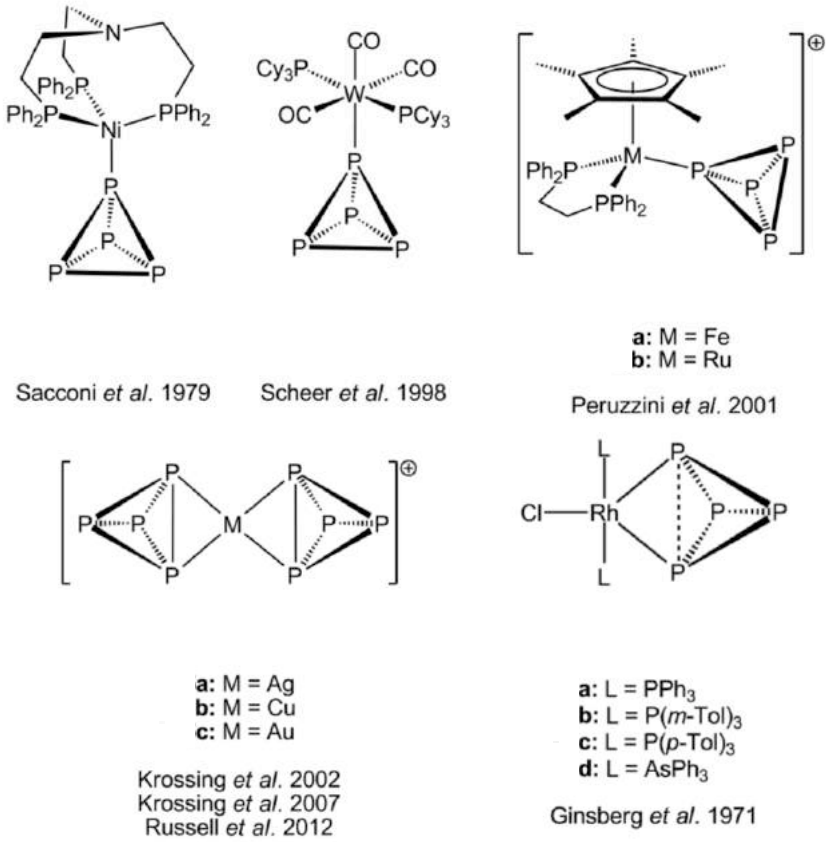

Scheme IV-6. Coordination of P_4 to metal complexes.[22a]

The high reactivity of P_4 makes it difficult to control, and thus its practical chemistry is not well developed. Chemistry trying to exploit the electrophilic nature of P_4 stretches back over 50 years. Early examples of the addition of small anions onto P_4 produce just a small yield of phosphine, along with a large quantity of polyphosphide (Scheme IV-7).[24] This shows that the addition of a nucleophile to white phosphorus converts the P_4 moiety from an electrophile into a nucleophile. This new P_4 nucleophile then reacts with neutral P_4 in an uncontrolled fashion to produce complex mixtures of phosphorus oligomers. The competitive mechanisms of this fragmentation process are poorly understood.

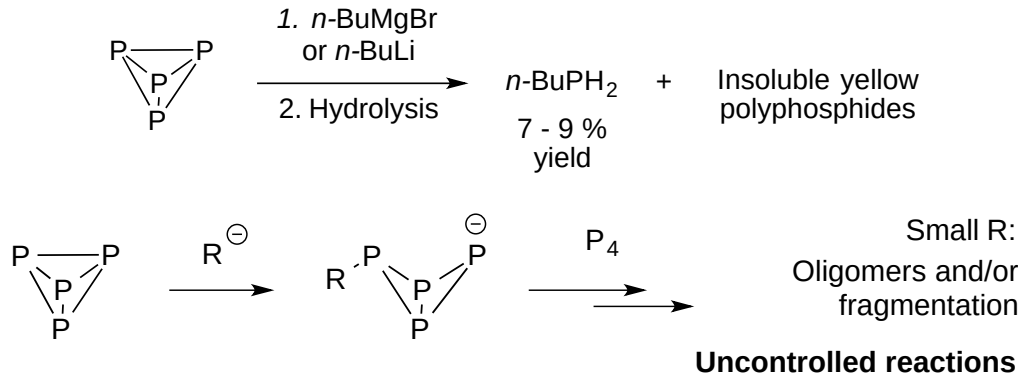

Scheme IV-7. Uncontrolled fragmentation of P_4 upon reaction with small organometallic carbanions.

Similarly, Baudler performed the reduction of P_4 with sodium/potassium naphthalenide.[25] In the presence of rogue protons presumably scavenged from solvent, she obtained just 4 % identifiable product of $(Na/K)HP_4$, while as in the previous case, the bulk of the phosphorus resulted in polyphosphides (Scheme IV-8).

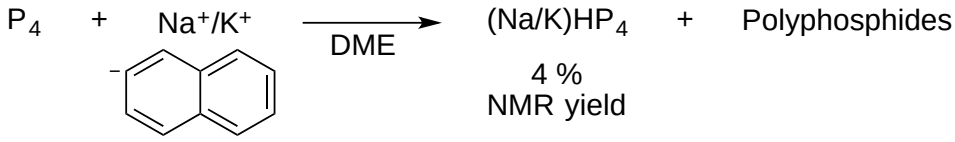

Scheme IV-8. Reduction of P_4 by naphthalenide.

A summary of the coordination modes of P_4 and its consequent degradation is represented below (Scheme IV-9). The tetrahedron (A) may bind to the metal either via the lone pair on the P atom, or via a P–P bond. Once the tetrahedron has been opened to a butterfly conformation, the butterfly may either chelate a metal in a bidentate fashion (B), or may serve as a bridging ligand (C). From there, the central P–P bond may break to form a square planar conformation (D). This can then linearize (G), and then break down into P_2 fragments that again bond via the P–P bond or via the P atoms themselves (I). Alternatively, an outer P–P bond of the butterfly conformation can break (F), whereupon a second outer P–P bond breakage would lead to a highly branched P_4 species (H). These downstream phosphorus products could then recombine in various ways to form oligomers.

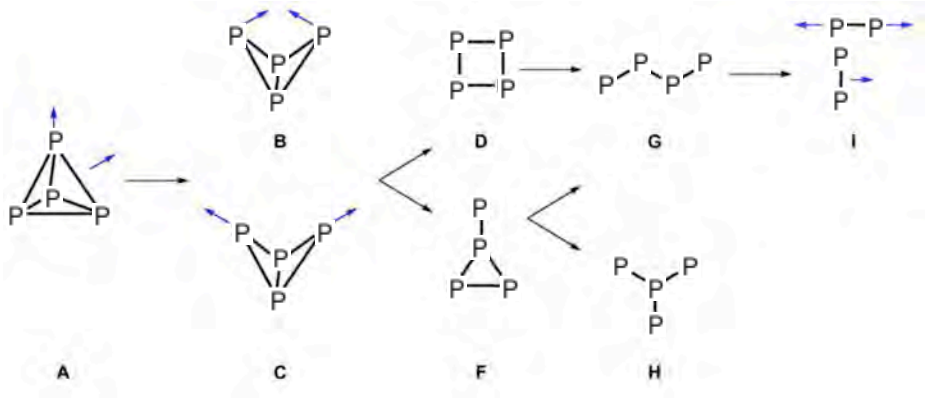

Scheme IV-9. Coordination modes and degradation of P_4.[22a]

To avoid this kind of uncontrolled reactivity, P_4 activation research has turned to bulky reagents that protect the open P_4 butterfly from further reactions. Scherer applied the idea of bulk to form a bimetallic Fe(II) complex with a bridging P_4 butterfly, demonstrating the ability of metals to open the P_4 tetrahedron (Scheme IV-10).[26]

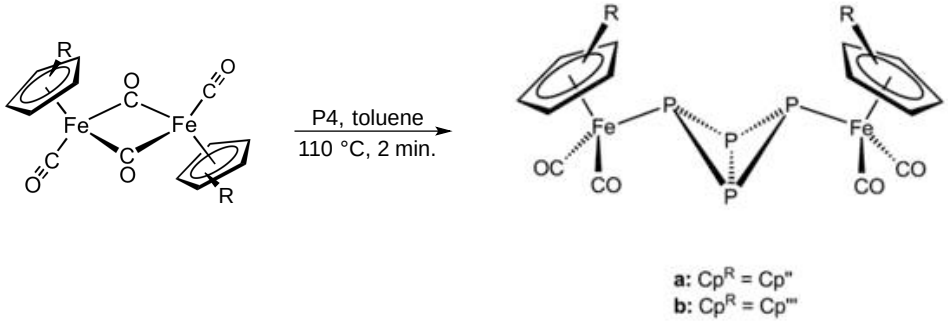

Scheme IV-10. Trapping of P_4 butterfly by bulky Fe complexes.[26]

Lammertsma used bulky aryl nucleophiles and Lewis acids to functionalize white phosphorus into phosphorus-containing organic compounds (Scheme IV-11).[27] These bulky substituents prevent the four trapped phosphorus atoms from reacting with P_4 remaining in solution. This thus serves as a stable model for an intermediate in P_4 activation mechanisms.

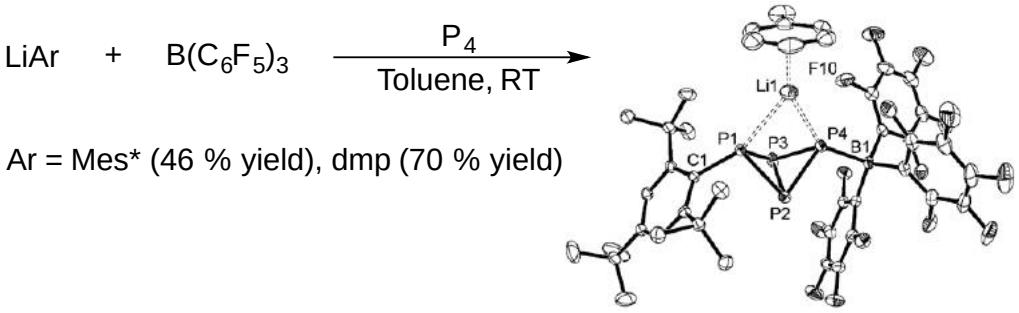

Scheme IV-11. Trapping of P_4 butterfly with bulky ligands after nucleophilic attack.[27]

Scheer adapted the same principle to use large radicals to form C–P bonds, once again trapping white phosphorus in the butterfly configuration (Scheme IV-12).[28]

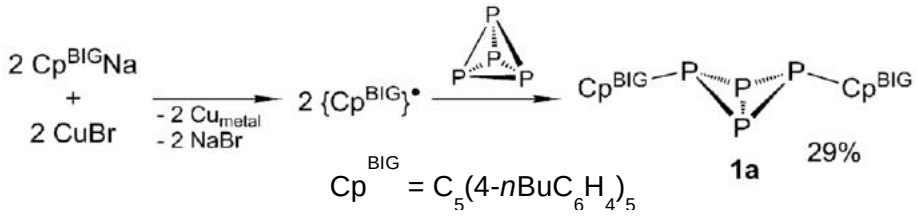

Scheme IV-12. Tetrahedron opening and subsequent trapping of P4 butterfly with bulky radicals.[28]

Arnold's use of bulky complexes, however, led to a square planar, cyclo-P_4 sandwich complex (Scheme IV-13).[29] This configuration of P_4 may be seen as a model for a different high-energy intermediate in P_4 activation mechanisms.

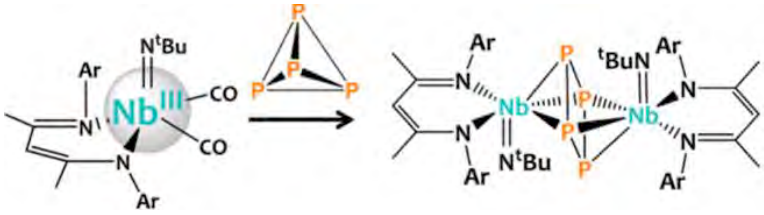

Scheme IV-13. Trapping of square planar P_4 by bulky Nb complexes.[29]

Finally, Bertrand has used various neutral N-heterocyclic carbenes (NHCs) to perform the addition of a neutral nucleophile to P_4.[30] In one example of his extensive work on P_4 activation, two bulky NHC ligands were use to open the P_4 tetrahedron and eventually form a novel P_{12} cluster in high yield (Scheme IV-14).

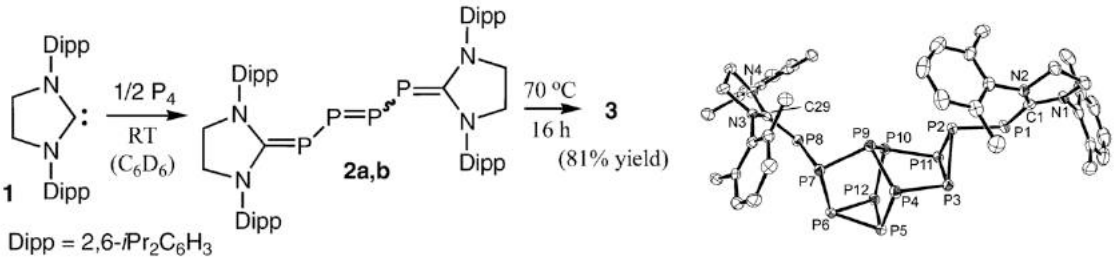

Scheme IV-14. Trapping and opening of P_4 by bulky NHC ligands, followed by formation of P_{12} cluster.[30]

These examples demonstrate the ability of bulky reactants to activate P_4 in a controlled fashion. However, the attendant bulk of the ligands diminishes their consequent utility.

One of the few examples of the molecular conversion of P_4 into a useful product is by Peruzzini (Scheme IV-15).[31] He proposed the coordination of P_4 to open coordination sites in Rh and Ir complexes, followed by oxidative addition. Consequent insertion of a hydride into the M–P bond, followed by reaction with H_2, resulted in the formation of one equivalent of PH_3 per molecule of white phosphorus. While this is a beautiful demonstration of the ability of a metal to reduce P_4 within its coordination sphere, this process ultimately produces just one equivalent of useful phosphorus per four P atoms in the starting tetrahedron. Further, the method uses expensive transition metals, thus making it a highly cost-ineffective process.

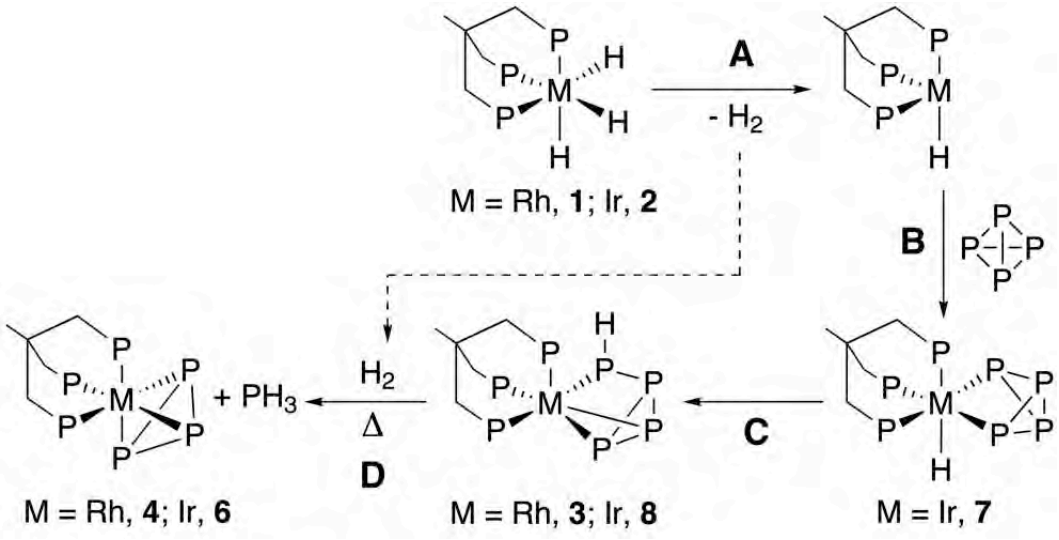

Scheme IV-15. Controlled reduction of P_4 to PH_3 using Rh or Ir.[31]

5. Goals of the present work

The previous section outlines the potential of P_4 functionalization to products other than PH_3 or PCl_3, though the products are by and large synthetic dead ends. We see that the use of small nucleophiles results in uncontrolled reactivity. The use of bulky reagents, such as anions, radicals, or neutral carbenes, appears to be necessary to induce the selective, controlled activation of white phosphorus over otherwise favorable fragmentation. However, the resulting phosphorus atoms have little interesting consequent reactivity.

Our goal was to convert P_4 into synthetically useful products. We sought a compromise between the utility of a reaction between P_4 and small nucleophiles, and the stability and selectivity of its reaction with bulky, highly specialized nucleophiles. In terms of synthetic potential, it is desirable to break all of the P–P bonds in P_4 in favor of generating "P–A" bonds. Among these "P–A" bonds are P–H bonds, which possess a very rich chemistry.

The use of a transition metal hydride to form PH_3 (Scheme IV-15) appears to be one of the only examples in the literature of the reduction of P_4 by hydrides. However, the use of an expensive transition metal and the consequent conversion of just one of the four P atoms per equivalent of P_4 showed us that there is much room for improvement. We sought to perform similar insertions of hydrides into white phosphorus while using all of the atoms in P_4, and to do so using exclusively main

group elements.

For this synthetic strategy to be successful, a major challenge is avoiding the formation of polyphosphides via reaction between the newly formed P–H anionic moiety and the electrophilic P_4 starting material. One of the most desirable targets is the phosphanide anion (MPH_2), which has been abundantly explored in the literature.[32] Current methods of MPH_2 synthesis are nontrivial, such as the addition of a strong base to PH_3 in liquid ammonia (Scheme IV-16a), the reduction of red phosphorus to PM_3 in liquid ammonia/DME followed by selective double protonation (Scheme IV-16b), the addition of M(0) to red phosphorus in liquid ammonia (Scheme IV-16c), or proton transfer from PH_3 to an amide (Scheme IV-16d).

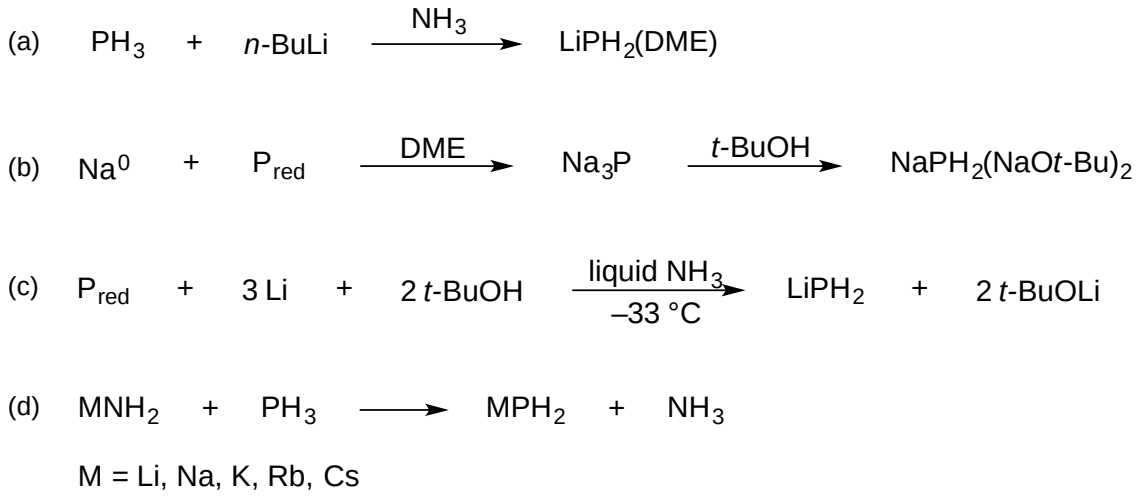

Scheme IV-16. (a) Formation of $LiPH_2$ species by lithiation of phosphine;[32d] (b) formation of $NaPH_2$ species by reduction of red phosphorus, followed by coordination of butoxide;[32e] (c) formation of $LiPH_2$ species by reduction of red phosphorus in liquid ammonia;[32f] and (d) formation of MPH_2 species by proton transfer from phosphine to amide.[32g]

We sought instead a simple synthetic method to convert P_4 directly to a phosphanide, hoping in particular to form a stable source of labile P–H bonds. We did so using only main group reagents, and were able to limit the fragmentation and oligomerization of P_4 in the reaction medium. This was accomplished not with bulky reagents that would then render the phosphanide a reactive dead end, but rather by using stabilizing borane adducts. The reactivity of this stabilized phosphanide species was examined, particularly towards the formation of organophosphines.

6. References

[1] Butusov, M.; Jernelöv, A. *Phosphorus: An Element that could have been called Lucifer* **2013**, *9*, 13–18.

[2] Bernhardt, Nancy E.; Kasko, Artur M. *Nutrition for the Middle Aged and Elderly* **2008**, 171–171. Southport: Nova Science Publishers, Inc. ISBN 1-60456-146-7.

[3] Kongshaug, G.; Brentnall, B.; Chaney, K.; Gregersen, J.-H.; Stokka, P.; Persson, B.; Kolmeijer, N.; Arne, C.; Legard, T.; Munk, H.; Skauli, O. *Ullmann's Encycl. Ind. Chem.* John Wiley & Sons **2012**, *26*, 633–677. ISBN: 9783527306732.

[4] (a) Cotton, F. A.; Wilkinson, G. *Advanced Inorganic Chemistry, Fifth Ed.* New York: John Wiley & Sons **1988**, 386–386. (b) Roth, W. L.; DeWitt, T. W.; Smith, A. J. *J. Am. Chem. Soc.* **1947**, *69* (11), 2881–2885.

[5] Diskowski, H.; Hoffman, T. *Ullmann's Encycl. Ind. Chem.* John Wiley & Sons **2012**, *26*, 725–745. ISBN: 9783527306732.

[6] Emsley, John. *The Shocking History of Phosphorus* **2000**, London: Macmillan. ISBN 0-330-39005-8.

[7] Threlfall, R. E. *The Story of 100 years of Phosphorus Making: 1851–1951* Oldbury: Albright & Wilson Ltd. **1951**, 167–185.

[8] Shriver, Atkins. *Inorganic Chemistry, Fifth Ed*. New York: W. H. Freeman and Company **2010**, 379–379.

[9] Abrantes, L. M.; Correia, J. P. *J. Electrochem. Soc.* **1994**, *141* (9), 2356–2360.

[10] Bonner, M. R.; Coble, J.; Blair, A.; Beane Freeman, L. E.; Hoppin, J. A.; Sandler, D. P.; Alavanja, M. C. R. *Am. J. Epidemiol.* **2007**, *166* (9), 1023–1034.

[11] Wishart, D. S.; Knox, C.; Guo, A. C.; Shrivastava, S.; Hassanali, M.; Stothard, P.; Chang, Z.; Woolsey, J. *Nucleic Acids Res.* **2006**, 34 (Database issue), D668–D672.

[12] Downing, J. H.; Smith, M. B. *Compr. Coord. Chem. II* **2004**, *1*, 253–296.

[13] Kölmel, C.; Ochsenfeld, C.; Ahlrichs, R. *Theor. Chim. Acta* **1992**, *82* (3–4), 271–284.

[14] Stewart, B.; Harriman, A.; Higham, L. J. *Organometallics* **2011**, *30* (20), 5338–5343.

[15] Ford-Moore, A. H.; Perry, B. J. *Org. Synth.* **1951**, *31*, 111.

[16] (a) Ittel, S. D. *Inorg. Synth.* **1990**, *28*, 98–104. (b) Meier, M.; Basolo, F. *Inorg. Synth.* **1990**, *28*, 104–107.

[17] Holmes, R. R. *J. Inorg. Nucl. Chem.* **1960**, *12* (3–4), 266–275.

[18] Bettermann, G.; Krause, W.; Riess, G.; Hofmann, T. *Ullman's Encycl. Ind. Chem.* John Wiley & Sons **2012**, 325–360. ISBN: 9783527306732.

[19] Svara, J.; Weferling, N.; Hofmann, T. *Ullman's Encycl. Ind. Chem.* John Wiley & Sons **2012**, 325–360. ISBN: 9783527306732.

[20] Simon, A.; Borrmann, H.; Horakh, J. *Chem. Ber.* **1997**, *130*, 1235–1240.

[21] Cossairt, B. M.; Cummins, C. C. *J. Am. Chem. Soc.* **2009**, *131*, 15501.

[22] (a) Schwarzmaier, C. Doctoral Dissertation, Universität Regensburg, **2012**. (b) Dapporto, P.; Midollini, S.; Sacconi, L., *Angew. Chem.* **1979**, *91*, 510–510. (c) Gröer, T.; Baum, G.; Scheer, M., *Organometallics* **1998**, *17*, 5916–5919. (d) Rios, I. d. l.; Hamon, J.-R.; Hamon, P.; Lapinte, C.; Toupet, L.; Romerosa, A.; Peruzzini, M. *Angew. Chem. Int. Ed.* **2001**, *40*, 3910–3911. (e) Krossing, I.;

Wüllen, L. *Chem. Eur. J.* **2002**, *8*, 700–711. (f) Santiso-Quinones, G.; Reisinger, A.; Slattery, J.; Krossing, I. *Chem. Commun.* **2007**, 5046–5048. (g) Russell, C. A.; Sanguramath, R. A.; Slattery, J. M. *Chem. Commun.* **2012**, *48*, 1970–1972. (h) A. P. Ginsberg, W. E. Lindsell, *J. Am. Chem. Soc.* **1971**, *93*, 2082–2084.

[23] (a) Dorfman, Y. A.; Aleshkova, M. M.; Polimbetova, G. S.; Levina, L. V.; Petrova, T. V.; Abdreimova, R. R.; Doroshkevich, D. M. *Russ. Chem. Rev. (Engl. Transl.)* **1993**, *62*, 877–896. (b) Peruzzini, M.; de los Rios, I. ; Romerosa, A.; Vizza, F. *Eur. J. Inorg. Chem.* 2001, 593–608. (c) Peruzzini, M.; Abdreimova, R. R.; Budnikova, Y.; Romerosa, A.; Scherer, O. J.; Sitzmann, H. *J. Organomet. Chem.* **2004**, *689*, 4319–433. (d) Cossairt, B. M.; Piro, B. M.; Cummins, C. C. *Chem. Rev.* **2010**, *110*, 4164–4177. (e) Scheer, M.; Balaźs, G.; Seitz, A. *Chem. Rev.* **2010**, *110*, 4236–4256. (f) Caporali, M.; Gonsalvi, L.; Rossin, A.; Peruzzini, M. *Chem. Rev.* **2010**, *110*, 4178–4235. (g) Armstrong, K. M.; Kilian, P. *Eur. J. Inorg. Chem.* **2011**, 2138–2147. (h) Caporali, M.; Barbaro, P.; Gonsalvi, L.; Ienco, A.; Yakhvarov, D.; Peruzzini, M. *Angew. Chem. Int. Ed. Engl.* **2008**, *47*, 3766–3768.

[24] Rauhut, M. M.; Semsel, A. M. *J. Org. Chem.* **1963**, *28*, 471–473.

[25] Baudler, M.; Adamek, C.; Opelia, S.; Budzikiewicz, H.; Ouzounis, D. *Angew. Chem. Int. Ed. Engl*. 1988, **27**, 1059–1061.

[26] Scherer, O. J.; Hilt, T.; Wolmershäuser, G. *Organometallics* **1998**, *17*, 4110–4112.

[27] Borger, J. E.; Ehlers, A. W.; Lutz, M.; Slootweg, J. C.; Lammertsma, K. *Angew. Chem. Int. Ed*. **2014**, *53*, 12836–12839.

[28] Heinl, S.; Reisinger, S.; Schwarzmaier, C.; Bodensteiner, M; Scheer, M. *Angew. Chem. Int. Ed*. **2014**, *53*, 7639–7642.

[29] Camp, C.; Maron, L.; Robert G. Bergman, R. G.; Arnold, J. *J. Am. Chem. Soc*. **2014**, *136* (50), 17652–17661.

[30] Masuda, J. D.; Schoeller, W. W.; Donnadieu, B.; Bertrand, G. *J. Am. Chem. Soc.* **2007**, *129*, 14180–14181.

[31] Peruzzini, M.; Ramirez, J. A.; Vizza, F. *Angew. Chem. Int. Ed.* **1998**, *37*, 2255–2257.

[32] (a) Joannis, A. *Compt. Rend.* **1894**, *119*, 557–559. (b) Huber, A.; Kuschel, A.; Ott, T.; Santiso-Quinones, G.; Stein, D.; Bräuer, J.; Kissner, R.; Krumeich, F.; Schönberg, H.; Levalois-Grützmacher, J.; Grützmacher, H. *Angew. Chem. Int. Ed.* **2012**, *51*, 4648–4652. (c) Podewitz, M.; van Beek, J. D.; Wörle, M.; Ott, T.; Stein, D.; Rüegger, H.; Meier, B. H.; Reiher, M.; Grützmacher, H. *Angew. Chem. Int. Ed.* **2010**, *49*, 7465–7469. (d) Schäfer, V. H.; Fritz, G.; Hölderich, W. *Z. Anorg. Allg. Chem.* **1977**, *428*, 222–224. (e) Heift, D. Doctoral Dissertation, ETH Zurich, **2013**. (f) Brandsma, L.; van Doorn, J. A.; de Lang, R.-J.; Gusarovac, N. K.; Trofimov, B. A. *Mendeleev Commun.* **1995**, *5*, 14–15. (g) Jacobs, H.; Hassiepen, K. M. *Z. Anorg. Allg. Chem.* **1985**, *531*, 108–118.

Chapter V: Functionalization of P_4 using main-group hydrides

1. Reduction of P_4 using lithium borohydride

In order to achieve our goal of converting P4 to useful single-phosphorus synthons, we examined the surprisingly empty field of the reduction of P4 using hydrides. In an initial test reaction, we examined the reduction of P4 by the commercially available lithium borohydride (Scheme V-1).1 The addition of lithium borohydride to white phosphorus in ethanol resulted in a mixture of phosphine and P2H4 in a ratio of 1:1.6. The yield, while surprisingly high for the direct hydride activation of P4, still resulted in the loss of over half of the phosphorus to polyphosphides.

Changing the solvent to butylamine, however, led to the production of HP4- in high yield (Scheme V-1). The yields of 74 % were vastly higher than the literature-reported yields mentioned in the previous section, when Baudler first synthesized them on the scale of 4 % yield, without an implicated proton source.

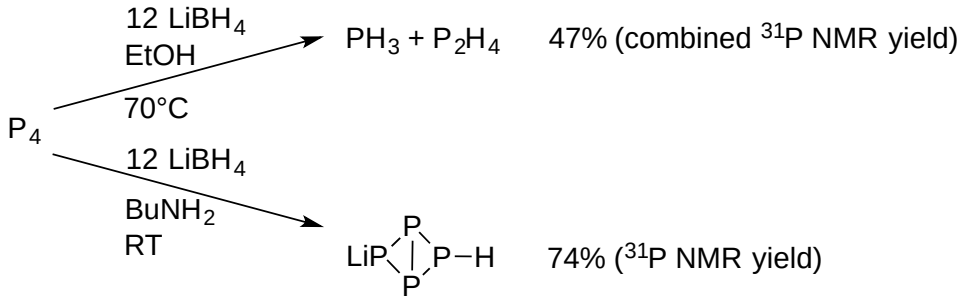

Scheme V-1. Reduction of P_4 by borohydrides in ethanol or butylamine.

However, the reaction did not result in the controlled formation of multiple P–H bonds. HP_4^- is unstable and further reacts to form mixtures of polyphosphide compounds and PH_3 in low yield, even at low temperature.[2] Nonetheless, these results highlight the potential of this surprisingly unprecedented method of using main group hydride sources to form P–H bonds from P_4. They demonstrated that it is possible to selectively convert a much larger fraction of P_4 to P–H bonds in a controlled manner than had been previously shown, and that the formation of polyphosphides might be limited by adjusting the reaction conditions. We postulated that a more reactive hydridic reagent would result in selective multiple P–H bond formation.

2. Reduction of P_4 with superhydride

The reaction of white phosphorus with lithium triethylborohydride ($LiBEt_3H$, "superhydride") formed a product **1** indicated by a triplet ^{31}P NMR signal at –98 ppm ($^1J_{P\text{-}H}$ = 260 Hz), as well as some very broad signals that hardly cleared the baseline, indicating the presence of highly coupled P-containing byproducts. The triplet collapsed to a singlet upon ^1H decoupling, indicating the formation of two P–H bonds. This suggested that the product was $LiPH_2$ (Figure V-1). However, the dimethoxyethane adduct of lithium phosphanide, $LiPH_2$(DME), displays a ^{31}P NMR signal at –283 ppm,[3] far upfield of the peak observed for compound **1**. Moreover, $LiPH_2$ and its DME adduct are known to degrade into Li_2PH and PH_3 when held at room temperature for several hours.[4] The product observed at –98 ppm, however, was stable in solution for at least six months. It was even found to be stable in dry air, though it was moisture-sensitive. An ^{11}B NMR shows a single peak at –10.4 ppm, indicating the presence of a borane atom (Figure V-1).

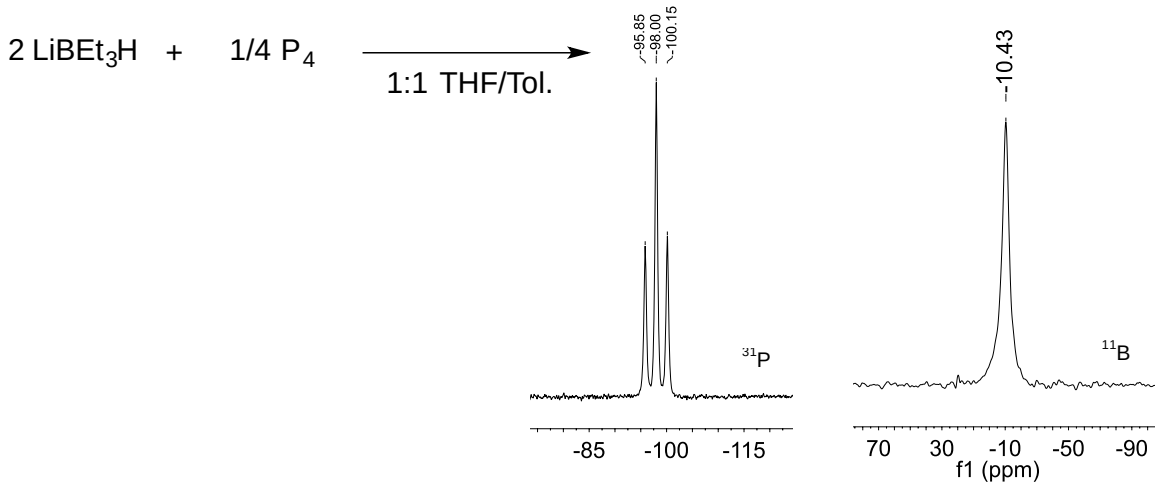

Figure V-1. NMR spectra of reduction product of P_4 upon reaction with superhydride (left: ^{31}P, with ^1H coupling; right: ^{11}B).

Upon application of vacuum, the triplet at –98 ppm shifted upfield (Figure V-2). We first saw the appearance of a triplet at –186 ppm, and eventually saw a second triplet at –294 ppm. Also of note is the decreasing full-width half-maximum (FWHM) of the peaks, suggesting decreasing coupling between phosphorus and, presumably, borane as we moved further upfield. The initial triplet at –98 ppm has rather broad peaks, while those at –186 ppm are somewhat more narrow, and those at –294 are narrower still. Moreover, we saw a consistent decrease in the P–H coupling constant.

The peak at –98 ppm has a $^1J_{P\text{-}H}$ of 263 Hz, while the peak at –186 ppm has a $^1J_{P\text{-}H}$ of 185 Hz and the peak at –294 ppm has a $^1J_{P\text{-}H}$ of 157 Hz. The peak at –294 ppm had a chemical shift and $^1J_{P\text{-}H}$ similar to those of the literature-reported $LiPH_2(DME)$, and also exhibited similar reactivity. Over the course of several hours, the species decomposed to PH_3 and, presumably, Li_2PH (seen as a precipitate) as expected. From this information, we deduced that the surprisingly stable compound at –98 ppm is the di(triethylborane) adduct of lithium phosphanide, $LiPH_2(BEt_3)_2$. Under vacuum, these borane adducts detached to form the monoborane and finally the naked $LiPH_2$ compound.

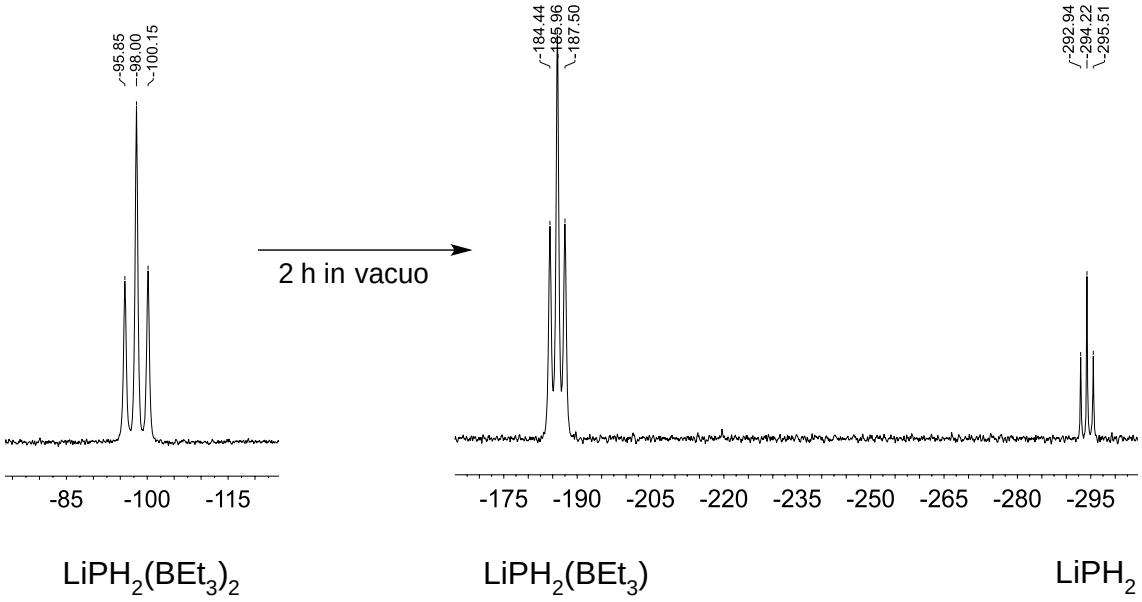

Figure V-2. Loss of BEt_3 adducts from $LiPH_2(BEt_3)_2$ (**1**) upon application of vacuum.

As further confirmation, the addition of two equivalents of pyridine to the bis(borane) adduct gives us the triplet at –186 ppm exclusively, presumably from the equilibrium-controlled displacement of one borane adduct (Figure V-3). Addition of another four equivalents of pyridine, for a final stoichiometry of six equivalents of pyridine per equivalent of phosphanide, results in the loss of the second borane adduct to yield the triplet at –294 ppm exclusively, which then decomposes.

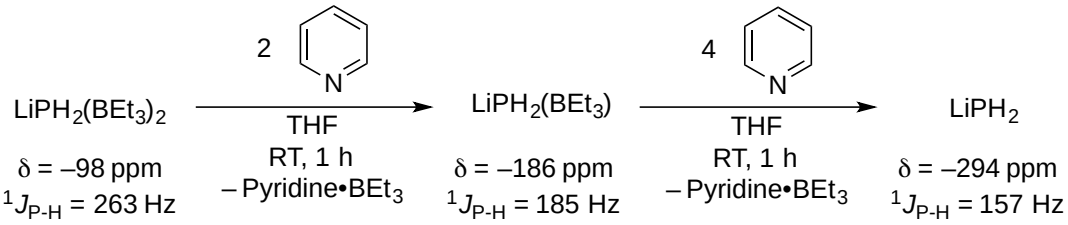

Figure V-3. Sequential loss of borane adducts by reaction with pyridine.

A ^{1}H NMR obtained in THF-d_8 upon concentration of the product using pentane confirmed the identity of the diborane adduct of $LiPH_2(BEt_3)_2$. Thus, we find that for each phosphorus atom, two equivalents of hydride react to form a phosphanide. This phosphanide is then stabilized by borane formed in solution from the loss of "LiH."

A closer look at the reaction revealed it to be a redox reaction, and that every equivalent of phosphanide also produced an extra electron (Scheme V-2). Free electrons have been shown to reduce P_4, leading to the formation of polyphosphides. As a result, we observed only a modest yield of about 33 % phosphanide product (NMR yield with respect to triphenylphosphine internal standard).

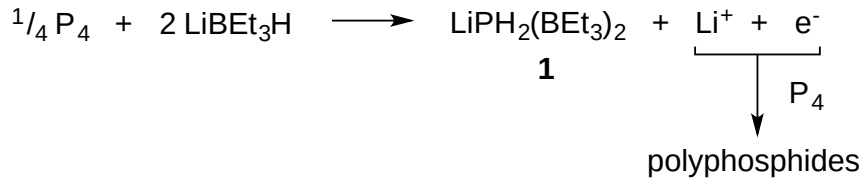

Scheme V-2. Balanced redox reaction of P_4 with $LiBEt_3H$.

We were able to limit the conversion of P_4 to polyphosphides by cooling the superhydride down to –100 °C and slowly adding the P_4 over several minutes, and then permitting the reaction to warm up slowly to room temperature. These conditions nearly doubled the yield of phosphanide to 61 % pure NMR yield. No further increase in yield could be obtained by changing parameters such as solvent, temperature, time, or stoichiometry.

Overall, an unprecedented 61 % of the starting P_4 tetrahedron was incorporated into the desired product, which contained two new P–H bonds per atom of P (*i.e.*, eight P–H bonds per P_4 molecule). This yield is much higher than the yields typically seen in the conversion of P_4, as discussed in the previous chapter. We can also compare these results to the only clear example of hydride reduction of P_4 that

we have found, Peruzzini's reduction of P_4 using Ir or Rh. Not only did that system produce only 25 % of usable phosphorus per starting P_4, but it also required transition metals. Here, we are able to more than double the amount of usable P using a simple main group reagent. We will also demonstrate below why a borane-stabilized phosphanide may be considered more useful than PH_3.

In order to isolate the phosphanide species, the crude solution was concentrated *in vacuo*. The application of vacuum was halted before it resulted in the loss of stabilizing borane ligand, through the process described in Figure V-2. By simply reducing the volume of solvent, the solution approached saturation. After several days, the formation of very pale yellow crystals was observed, along with the precipitation of a red powder along the walls of the Schlenk flask. The pale yellow crystals were identified as P_7Li_3 (broad singlet at –117 ppm at 60 °C), [5] which accounted for 23 % of the starting P atoms. The addition of a bidentate amine ligand, tetramethylethylenediamine (TMEDA), yielded crystals that were stable enough for X-ray diffraction were obtained upon (Figure V-3). In the absence of TMEDA, the crystals decomposed instantly upon exposure to air, before they could be mounted on a diffractometer. Although P_7Li_3 can be used for its own rich chemistry, we did not explore its use.

The remaining polyphosphide was a largely insoluble red powder, which presumably accounted for the remaining phosphorus balance. A final precipitation by diethylether ensured the removal of any lingering polyphosphide. In all, 61 % of the P went toward $LiPH_2(BEt_3)_2$ and 23 % P toward Li_3P_7. Thus, only 16 % of the P was lost to the insoluble red powder resulting from the uncontrolled fragmentation and oligomerization that is common in the chemistry of P_4.

The red precipitate obtained during the isolation of $LiPH_2(BEt_3)_2$ was isolated and dried *in vacuo*. The resulting red powder was found to be very slightly soluble in dimethylformamide and acetone. It was analyzed by mass spectrometry and by solid-state ^{11}B, ^{31}P, ^{13}C, ^{7}Li and ^{1}H MAS NMR. These analyses revealed that the solid contained BEt_3 as well as P and Li. We thus proposed that it was a polyphosphide compound with coordinated BEt_3. However, the amorphous structure of the solid, combined with its poor solubility, prevented us from obtaining a more precise structure for this solid. Its behavior distinguished it from commercial red phosphorus, as might be expected given the presence of non-phosphorus elements.

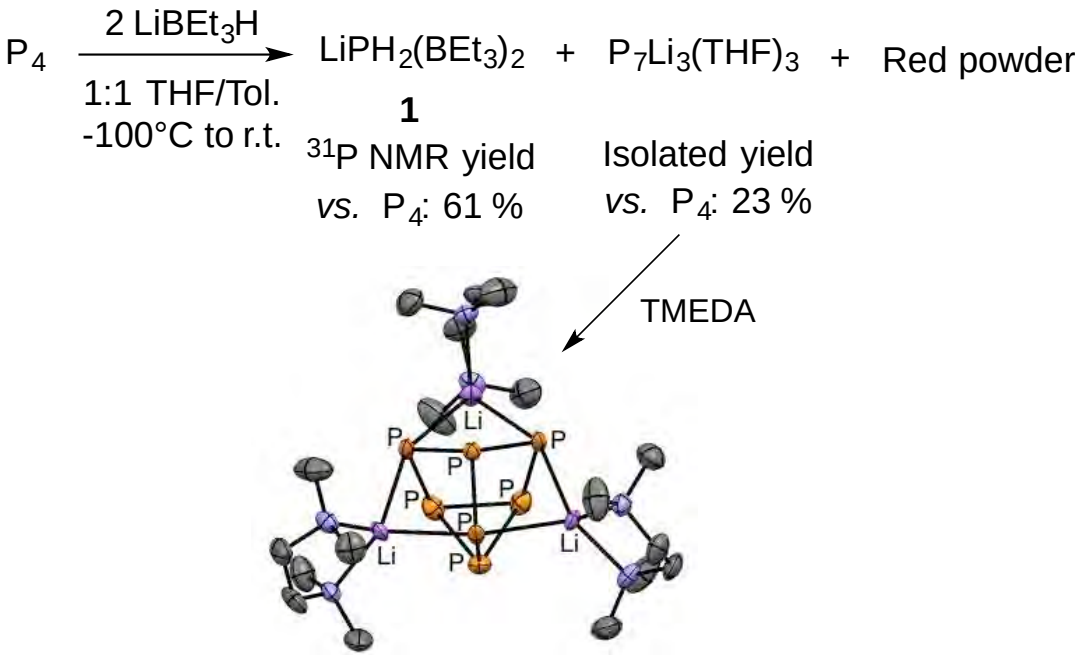

Figure V-4. Optimized reaction conditions for synthesis of compound **1**.

We thus had in hand a stable phosphanide species, which represented great potential for further synthetic use. Although the phosphanide needed to be stored in the form of a highly concentrated oil in order to maintain the stabilizing borane ligands, it did not decompose in solution. The phosphanide could be stored in a glove box for at least six months in a very concentrated form that may be seen as the THF adduct of the phosphanide-borane species. Upon addition of pentane to a concentrated solution of compound **1** in THF, the solution grows cloudy. After several hours, a very viscous oil precipitates and settles to the bottom. Careful phase separation with a pipette permits the removal of pentane with dissolved THF. The thick oil that remains is $LiPH_2(BEt_3)_2(THF)_x$. Calculations suggest the presence of two molecules of THF per phosphanide complex.

Despite extensive attempts, crystals of the product could not be obtained. Conditions tested included not only standard screens of solvents, concentrations, and temperatures, but also the use of various crown ethers, Kryptofixes, and other chelating ligands such as TMEDA, the replacement of the Li^+ cation by Na^+ or by better stacking cations such as tetraphenylphosphonium, and by coordination to tungsten pentacarbonyl. However, a calculated structure was obtained for the related species, $LiPH_2(BMe_3)_2(OMe_2)_2$. This gives us an approximation of the solid-state structure of the $LiPH_2(BEt_3)_2(THF)_2$ species (Figure V-5).

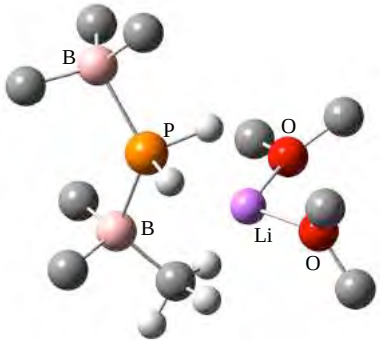

Figure V-5. Calculated structure of $LiPH_2(BMe_3)_2(OMe_2)_2$. Some hydrogen atoms omitted for clarity.

This structure gives us several interesting pieces of information. Most notably, we see that the lithium cation interacts not with the P^-, but with the hydrogen atoms attached to the negatively charged P. There also appears to be some interaction between the protons of a methyl group on one borane moiety with Li^+. This evident asymmetry may be the reason for the absence of clear ^{31}P–^{11}B coupling in both ^{31}P and ^{11}B NMR.[6] Nonetheless, the absence of two distinct resonances for ^{11}B atoms indicates sufficient rotation, even at low temperature (–60 °C).

The reduction of P_4 was attempted with several similar main group hydrides. The use of sodium triethylborohydride resulted in a much lower yield (34 % by NMR) of $NaPH_2(BEt_3)_2$, even after optimization. $NaB(CN)H_3$ yielded no product at all, while $KBPh_3H$ yielded numerous peaks by ^{31}P NMR that were highly coupled. Among them could be seen a set of peaks presumed to correspond to $KHP_4(BPh_3)_x$.

Commercial lithium triethylborohydride typically contains impurities of $LiBEt_2H_2$ and $LiBEtH_3$, which can be difficult to remove after the completion of the reaction. Fortunately, its synthesis is trivial from lithium hydride and triethylborane.[7] This provides a much cleaner source of $LiBEt_3H$ than the commercially available product. Nonetheless, the commercially available reagent may be used for convenience.

The phosphanide species has numerous advantages over PH_3, including low volatility, pyrophoricity, and toxicity. Both the phosphanide anion and the apparently labile borane adduct promised interesting reactivity for this new and stable species. We began by probing the functionalization of the P–H bond, as well as "PH_2" transfer, as described in the next section.

3. Reactions of $LiPH_2(BEt_3)_2$ towards organophosphines

We initially examined the reactivity between compound **1** and several organic halide substrates. We expected the phosphanide anion to behave as a nucleophile and to deliver primary phosphines upon reaction with one equivalent of substrate (Scheme V-3). The substrates propenylchloride, 2-methyl-2-propenylchloride, and benzylchloride were examined. In each case, ^{31}P NMR spectroscopy showed a wide distribution of primary, secondary, and tertiary products in very low yield, even upon addition of three or more equivalents of substrate. Multiple unknown byproducts were also observed. Separation proved impossible.

$$\underset{\mathbf{1}}{LiPH_2(BEt_3)_2} + RCl \xrightarrow[-\,2\,BEt_3]{} RPH_2 + LiCl$$

Scheme V-3. Expected reaction between **1** and organic halide.

We also expected to see the nucleophilic addition of the phosphanide anion to unsaturated bonds. A *t*-butoxide-supported $NaPH_2$ species was seen to react with a CO source (carbon monoxide, iron(0) pentacarbonyl, or ethylene carbonate) to form sodium phosphaethynolate (Scheme V-4),[8] and we expected our borane-supported lithium phosphanide to behave similarly.

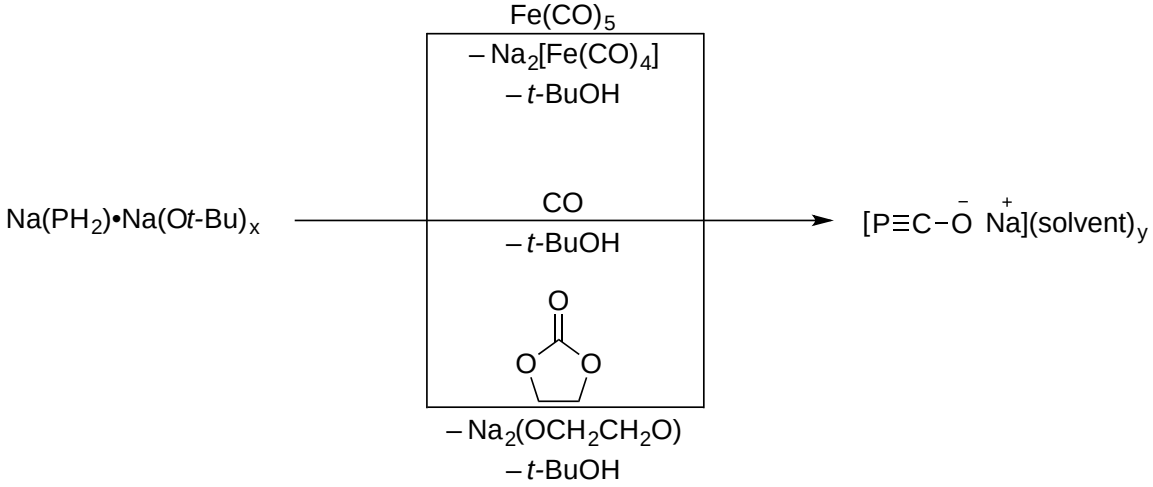

Scheme V-4. Formation of sodium phosphaethynolate from sodium phosphanide.[8]

Disappointingly, the addition of $LiPH_2(BEt_3)_2$ to molecules containing unsaturated bonds (e.g., benzophenone, ethylene carbonate, cyclohexenone, carbon disulfide, carbon dioxide, and dicyclohexylcarbamide) resulted in the formation of numerous unidentifiable products, even in the presence of bases such as sodium *t*-

butoxide, or mild proton sources such as *t*-butanol. The reaction of **1** with acetonitrile (MeCN) resulted only in the formation of 84 % NMR yield of PH_3, rather than in the nucleophilic attack of the PH_2 moiety on the CN triple bond. Literature precedent indicates the ability of $LiPH_2$ to scavenge adventitious protons.[9]

As mentioned above, the borane-supported phosphanide was both stable (*ie*, not prone towards disproportionation) and air-stable (*ie*, stable towards ambient oxygen). However, we observed the formation of PH_3 over the course of several days when left open to humid air. Based on this, we deduced that a nucleophilic PH_2^- moiety would also react with a proton source such as water. We thus examined the controlled reaction of $LiPH_2$ with H_2O, and observed the quantitative and vigorously exothermic formation of PH_3.

The parallel reaction of **1** with D_2O was expected to yield PH_2D, but instead, we observed a mixture of all possible products of proton exchange (Figure V-4). This introduced the possibility of forming not only primary phosphines, but also secondary and tertiary ones.

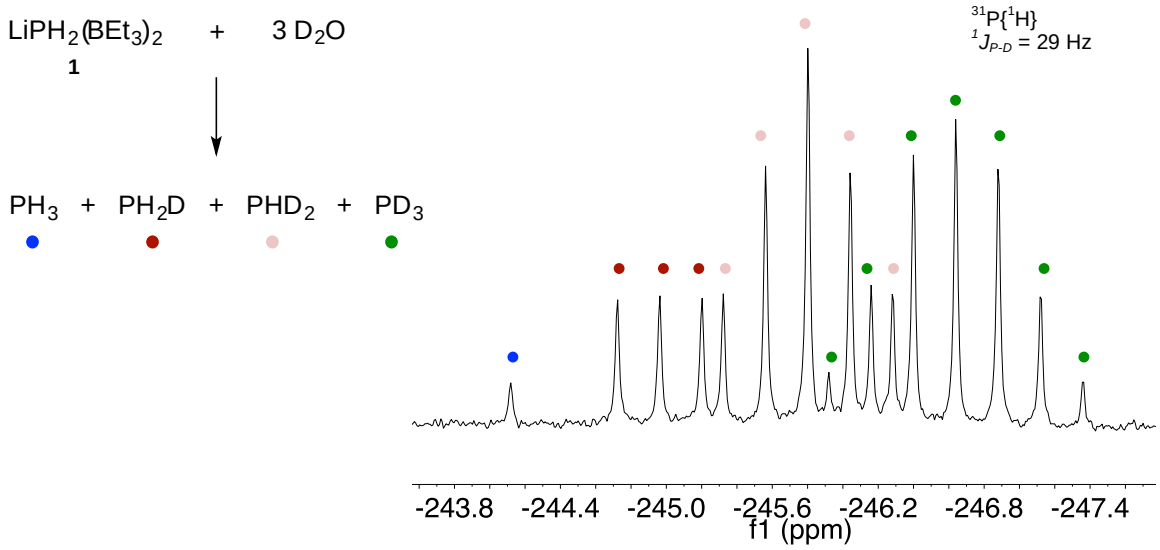

Figure V-4. Reaction of $LiPH_2(BEt_3)_2$ with D_2O, producing mixture of PH_3, PH_2D, PHD_2, and PD_3.

PD_3 could also be selectively synthesized by starting with lithium superdeuteride and reacting the deuterated phosphanide with D_2O (Figure V-5).

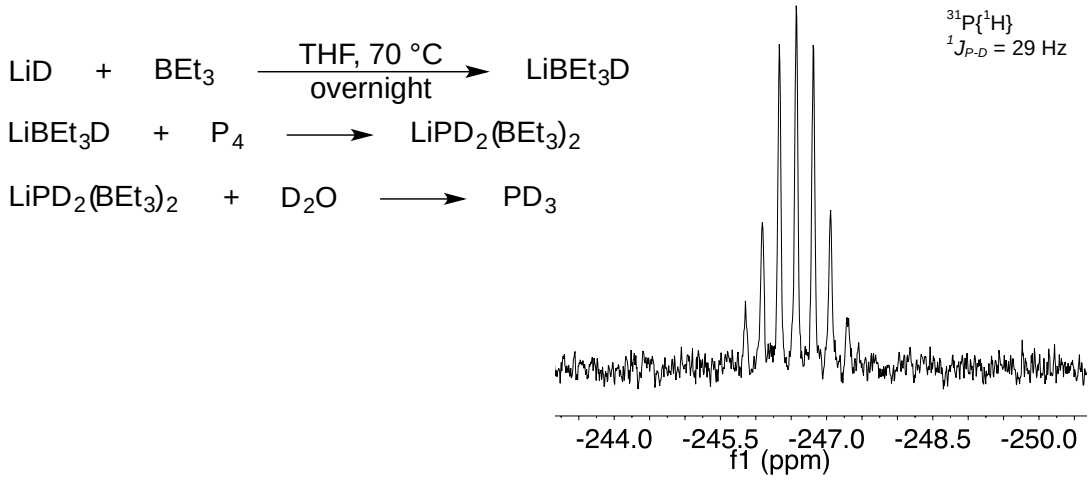

Figure V-5. Reaction of $LiPD_2(BEt_3)_2$ with D_2O, producing PD_3.

Having established that water may serve as a proton source for the phosphanide anion, other sources of H^+ were examined. We found that MeOH, EtOH, *i*-$BuNH_2$, and H_2O all resulted in the quantitative formation of PH_3 (Scheme V-5). Interestingly, $LiPH_2(BEt_3)_2$ appeared to be selective for primary amines and alcohols, and it did not react with *i*-PrN_2H, *i*-PrOH, or *t*-BuOH. This is likely due to the steric hindrance of the borane adducts.

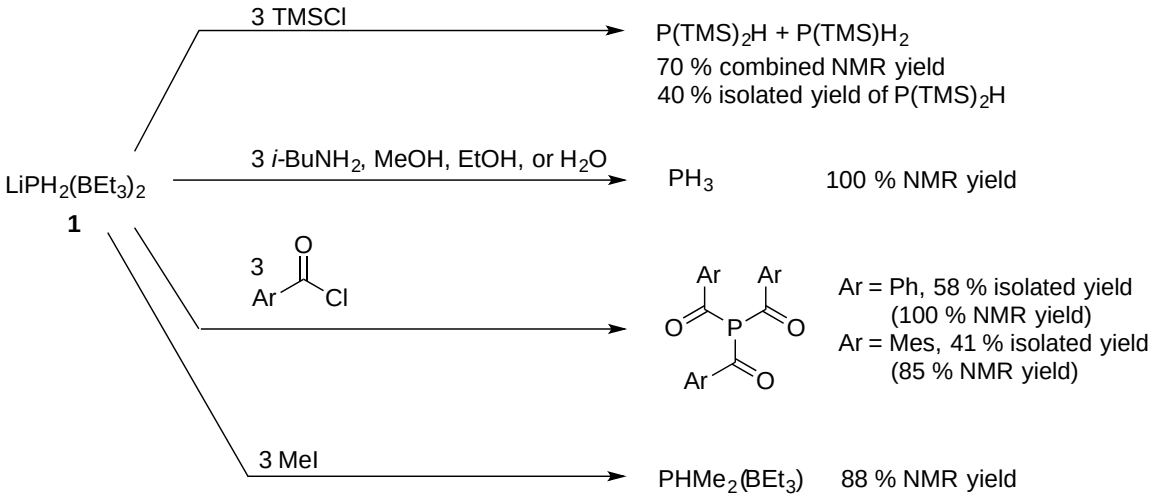

Scheme V-5. Reactions of $LiPH_2(BEt_3)_2$ with various electrophiles. NMR yields with respect to triphenylphosphine internal standard.

We also observed reactions between the phosphanide and other electrophiles (Scheme V-5). The addition of TMSCl results in a mixture of the mono- and

bis(TMS) phosphine products in a ratio of 1:1.7, respectively, from which $HP(TMS)_2$ may be isolated by distillation in 40 % yield. As expected, this product is very pyrophoric and undergoes dimerization to $P_2(TMS)_4$ upon heating, thus rendering the distillation process slow and dangerous.

The addition of aroyl chlorides, meanwhile, results in quantitative or near-quantitative conversion to tris(aroyl)phosphine. The addition of fewer than three equivalents of aroyl chloride resulted in a mixture of the tris(aroyl)phosphine and unreacted phosphanide. This is an interesting contrast to the observations of Grützmacher, who obtained the bis(mesitoyl)phosphine upon addition of two or more equivalents of mesitoyl chloride (Scheme V-6).[10] We believe this is due to the differential stabilization of the present phosphanide species *vs.* the phosphanide used by Grützmacher. The sodium phosphanide generated by Grützmacher is weakly stabilized by sodium *t*-butoxide. Upon reaction of a first mesitoyl chloride, the species is deactivated in terms of its ability to perform nucleophilic attack, since it has been converted from a phosphanide anion to a neutral primary phosphine. Meanwhile, the borane-supported lithium phosphanide is already quite stable. Reaction with a first equivalent of electrophile likely requires the loss of the stabilizing and somewhat sterically encumbering triethylborane adducts. This renders the primary phosphine more reactive towards mesitoyl chloride than the borane-stabilized starting material. The remaining electrophile thus reacts preferentially with the intermediate primary and secondary phosphine rather than with the remaining borane-stabilized starting material, resulting in very different reactivity.

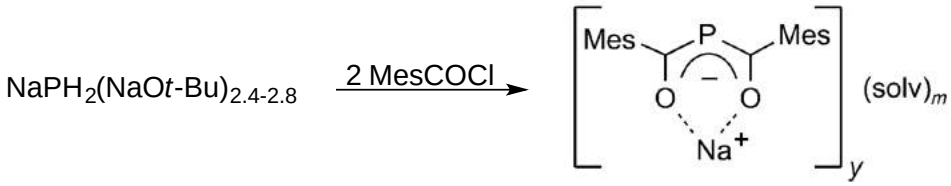

Scheme V-6. Reaction of $NaPH_2(NaO$*t*$-Bu)_x$ with mesitoyl chloride.[10]

Reaction of compound **1** with MeI resulted in near-quantitative conversion by NMR to the secondary dimethylphosphine stabilized by triethylborane, along with the presence of a small amount of byproduct. However, PMe_2H could not be isolated. Efforts to do so resulted in the loss of the BEt_3 adduct, followed by the disappearance of the phosphine peak by ^{31}P NMR.

As in the case of the secondary and tertiary amines and alcohols, secondary (e.g., chlorocyclohexane) or tertiary (e.g., *t*-butylchloride) organic halides also underwent no reaction with the phosphanide.

Compound **1** thus behaves, to some degree, like an easily accessible form of "P^-." We hoped it could also behave as a less dangerous form of $P(TMS)_3$. $P(TMS)_3$ is highly pyrophoric and flammable, and its synthesis is nontrivial.[11] One use of $P(TMS)_3$ is the transformation of a pyrylium salt to a phosphinine (Scheme V-7).[12] Like many organophosphines, phosphinines serve as an important class of ligands. Their aromatic nature imbues the ligands with interesting electronic properties.

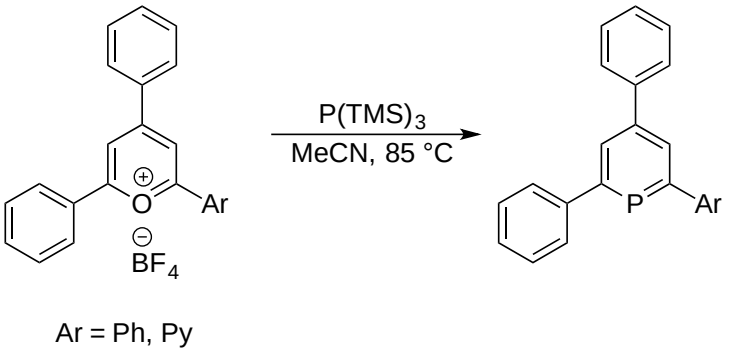

Scheme V-7. Formation of phosphinine from pyrylium salt.[12]

The difficult nature of $P(TMS)_3$ has led to efforts to form the phosphinine by reaction of the pyrylium salt with $NaPH_2(NaO$*t*$-Bu)_x$. However, this led to indiscriminate proton abstraction and resulted in the formation of PH_3 along with the destruction of the pyrylium salt. Hoping that the $LiPH_2(BEt_3)_2$ species would be a more gentle form of PH_2^-, we examined the reaction between the pyrylium salt and the borane-stabilized phosphanide. Unfortunately, the stabilization appeared to be too strong, and no reaction was observed at all, even after heating overnight at 70 °C, or heating in a microwave at 100 °C over several hours.

In the hopes that the removal of one BEt_3 adduct would sufficiently augment the reactivity of the stabilized phosphanide to react with the pyrylium salt, two equivalents of pyridine were added to $LiPH_2(BEt_3)_2$ to form $LiPH_2(BEt_3)$. This species also remained unreactive towards the pyrylium salt. Pyridine as solvent led to the formation of a peak at –34.3 ppm by ^{31}P NMR, which does not correspond to the phosphinine product. Even the addition of NaO*t*-Bu, which we hoped would form $LiPH_2(NaO$*t*$-Bu)_x$ *in situ*, resulted in products that did not correspond with the desired phosphinine. It seemed that at least in the case of the transformation of the pyrylium

salt to phosphinine, **1** is a poor substitute for $P(TMS)_3$.

Nonetheless, the P–H bonds were shown to be labile, and we were able to show that the phosphanide may serve as a precursor to organophosphines. This route provides a much more stable and easy-to-use intermediate than PH_3, as it is much less toxic or pyrophoric. These reactions were attempted both with purified and crude solutions of $LiPH_2(BEt_3)_2$, and the results were nearly identical in all cases. Thus, this provides a one-pot process to go from P_4 to organophosphines.

Another interesting feature of $LiPH_2(BEt_3)_2$ is the potential displacement of BEt_3, whose lability was observed upon extensive drying and upon addition of pyridine. This suggested that the adduct could be replaced by other, potentially more interesting adducts, which we then explored.

4. Reactions of $LiPH_2(BEt_3)_2$ towards borane replacement

The addition of excess triphenylborane to $LiPH_2(BEt_3)_2$ resulted in no change to the ^{31}P or ^{11}B shifts of the starting complex. ^{11}B NMR confirmed the presence of free triphenylborane. The same lack of reactivity was observed with $B(s\text{-}Bu)_3$, as well as with the strongly coordinating $B(C_6F_5)_3$.

We were also interested in exploring the possibility of using compound **1** as a P–B polymer precursor. Polymers with bonds between elements of groups 13 and 15 are particularly interesting, as they are isoelectronic with their carbon analogues but may possess interesting physical and chemical properties due to their difference in electronegativity.[13] Most current methods for the synthesis of P–B polymers begin with PR_3BR_3-type precursors and require metal catalysts, and often produce low molecular weight and/or polydisperse products.[14] A new approach by Marquadt *et al.* employs the thermal decomposition of PR_2BH_2-type precursors.[15] The replacement of the BEt_3 adduct of $LiPH_2(BEt_3)_2$ with BH_3 could thus provide a novel entry into this chemistry.

The addition of a slight excess of BH_3SMe_2 (2.5 equivalents) to $LiPH_2(BEt_3)_2$ at < 21 °C (cool room temperature) resulted in a mixture of highly coupled peaks by ^{31}P NMR. When heated at 35 °C for two hours, the complex set of multiplets collapsed into two sets of peaks corresponding to $LiPH_2(BEt_3)(BH_3)$ and $LiPH_2(BH_3)_2$ in a ratio of 1:1.45, respectively. Heating at 35 °C overnight resulted in a ratio of 1:3.74, and heating at 75 °C overnight pushed the equilibrium all the way to pure

$LiPH_2(BH_3)_2$ in near-quantitative yield.

Simply heating $LiPH_2(BEt_3)_2$ with 2.5 equivalents of BH_3SMe_2 at 75 °C overnight also produced **2**. This product was also obtained by the addition of 24 equivalents of BH_3SMe_2 at room temperature overnight. However, this large excess of BH_3SMe_2 also resulted in the formation of B_2H_6, according to ^1H and ^{11}B NMR.

The novel compound $LiPH_2(BH_3)_2$ is characterized in $^{31}P\{^1H\}$ NMR by a septet at –108 ppm that shows coupling with two ^{11}B atoms ($^1J_{P\text{-}B}$ = 52 Hz) (Figure V-6). The ^{11}B spectrum shows the expected doublet of quartets at –40 ppm ($^1J_{P\text{-}B}$ = 52 Hz, $^1J_{B\text{-}H}$ = 94 Hz), and the ^1H spectrum shows a doublet of septets for the two equivalent protons of PH_2 at 2.7 ppm ($^1J_{P\text{-}H}$ = 288 Hz, $^3J_{H\text{-}H}$ = 7 Hz). The ^1H NMR spectrum also points to two molecules of THF bound to the Li atom, and four broad resonances for the BH_3 moieties (–0.1, 0.2, 0.5 and 0.8 ppm). Upon decoupling with ^{11}B, these four resonances collapse into a doublet of triplets due to coupling with phosphorus and protons ($^2J_{P\text{-}H}$ = 12 Hz, $^3J_{H\text{-}H}$ = 7 Hz), indicating that the six hydrogen atoms in the BH_3 moiety are equivalent.[16]

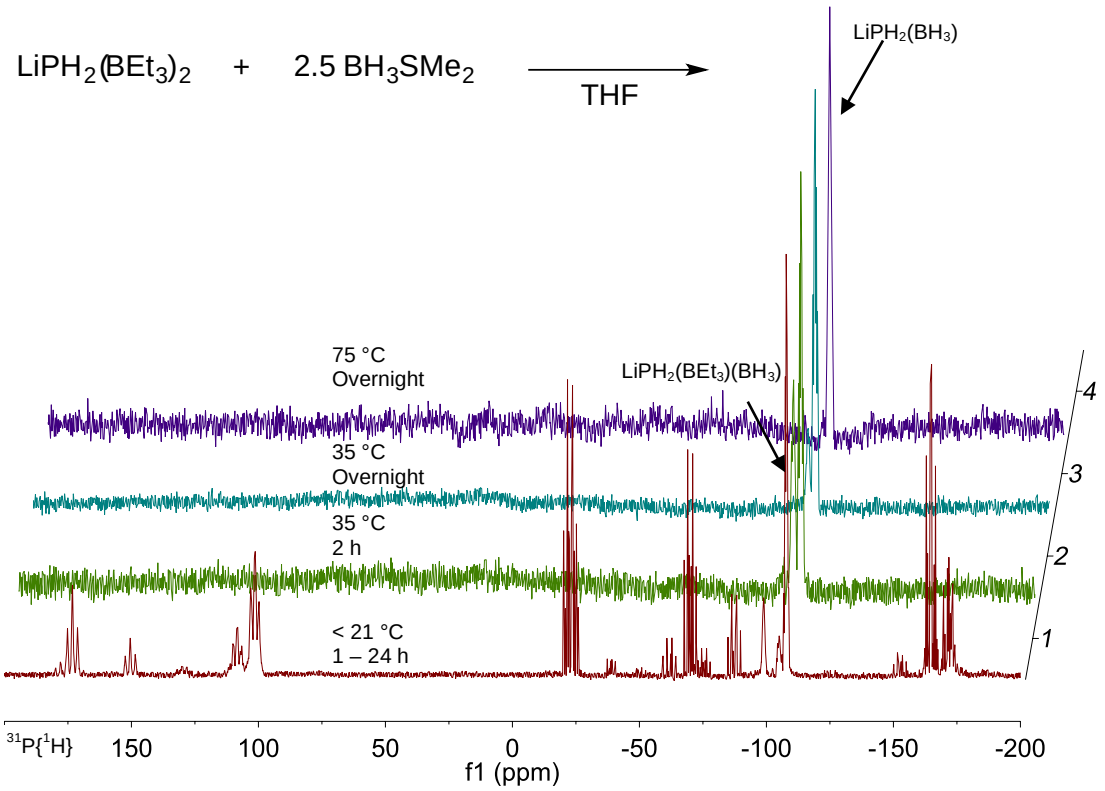

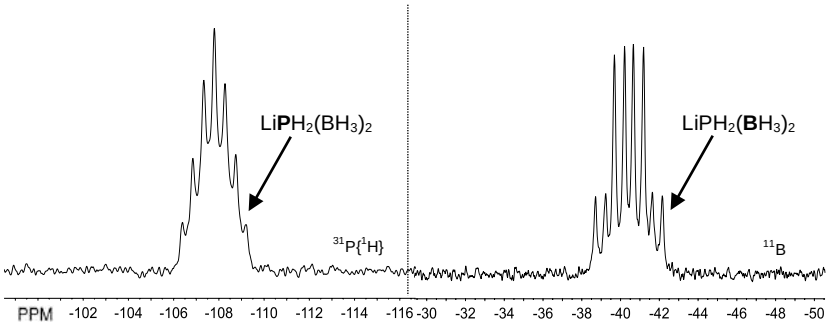

Figure V-6. Formation of $LiPH_2(BH_3)_2$ from $LiPH_2(BEt_3)_2$.

The crude phosphanide nmixture was washed repeatedly in acetone, pentane, and ether until it turned from a colorless oil to a white powder. As in the case of $LiPH_2(BEt_3)_2$, however, no crystals could be obtained, despite extensive screening. However, calculations performed on a model structure provided an indication of what the structure might be (Figure V-7). Once again, THF was modeled by OMe_2.

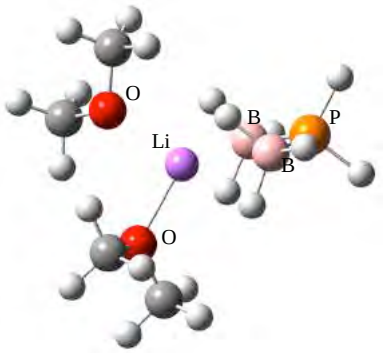

Figure V-7. Calculated orientation of $LiPH_2(BH_3)_2(OMe_2)_2$.

The calculated orientation suggests that in the case of the bis(BH_3) adduct, the lithium ion is coordinated not by the phosphorus moiety, as is the case for $LiPH_2(BEt_3)_2$, but by four of the six borane hydrides. Since the ^1H NMR showed just one set of borane peaks, there is likely swift rotation around the P–B bond even at low temperature (–60 °C).

The synthesis of a mixed $LiPH_2(BH_3)(BEt_3)$ species was attempted by initial formation of $LiPH_2(BEt_3)$ from the addition of two equivalents of pyridine. However, the pyridine-triethylborane adduct could not be separated from $LiPH_2(BEt_3)$. Addition of one to three equivalents of BH_3SMe_2 simply displaced the BEt_3 coordinated by the pyridine, and the phosphanide reverted to its original, bis(triethylborane) state (Scheme V-7).

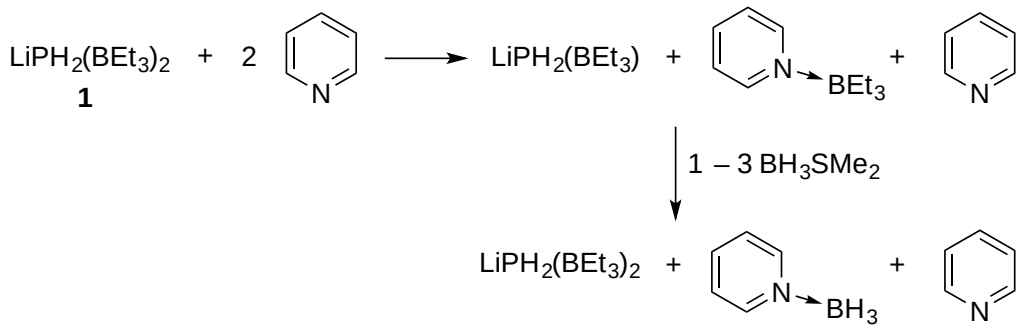

Scheme V-7. Attempted formation of $LiPH_2(BEt_3)(BH_3)$ by addition of 2 equiv. pyridine and up to three equivalents of BH_3SMe_2.

$LiPH_2(BH_3)_2$ is shockingly stable for a P^- species. Not only is it stable to air, but unlike the triethylborane adduct, it is also relatively moisture-stable, converting to PH_3 with a huge excess of water only over the course of weeks. It showed no reaction at all with any of the other reagents that reacted with $LiPH_2(BEt_3)_2$, nor did it react with the weak acid lutidinium triflate. Indeed, the only nucleophilic reaction observed with $LiPH_2(BH_3)_2$ occurring on a reasonable time scale was with hydrochloric acid, with which it reacted violently to form PH_3. Reaction with the strongly nucleophilic *n*-butyllithium resulted in the formation of $P(n\text{-}Bu)_3$ in very poor yield (5 % by NMR with respect to a PPh_3 internal standard) through a poorly understood mechanism. No other phosphorus peaks could be seen by ^{31}P, suggesting the formation of many highly coupled phosphorus oligomers.

As previously mentioned, reaction of **1** with MeCN produced PH_3. However, when $LiPH_2(BH_3)_2$ was heated to 75 °C in MeCN, it formed a polymeric white precipitate. The polymer was not further characterized, but the absence of any phosphorus or boron peak in the supernatant suggested that the polymer was comprised of phosphorus and boron.

In summary, we have developed the first successful hydride transfer to P_4 using main group hydrides, allowing the controlled generation of P–H bonds. Using $LiBH_4$ as the hydride source and amine as solvent, the reaction stops after the formation of a single P–H bond from P_4, despite the use of excess hydride. With the more hydridic $LiBEt_3H$, the borane-stabilized $LiPH_2(BEt_3)_2$ species is formed in good yield. Most importantly, preliminary results on the reactivity of this latter compound show its versatility in serving as a "PH_2^-" or "P^{3-}" source. The coordination of the phosphanide to transition metals might be of future interest. The use of the

phosphanide to synthesis metal phosphide nanoparticles may also be of interest.

The generation of $LiPH_2(BH_3)_2$ was possible via borane replacement. $LiPH_2(BH_3)_2$ can be seen as resulting from the formal addition of $LiBH_4$ on P_4. Performing the reaction in two stages through the intermediate $LiPH_2(BEt_3)_2$ allowed us to circumvent the stop at the HP_4Li stage observed upon direct addition of $LiBH_4$ to P_4. Preliminary results suggest that $LiPH_2(BH_3)_2$ may serve as a precursor to a P–B polymer. Further investigations into this polymeric species and a probe of the scope of P–B polymers that may be designed using this reaction are envisioned.

5. References

[1] Bhattacharyya, K. X.; Dreyfuss, S.; Saffon-Merceron, N.; Mézailles, N. *Chem. Commun.* **2016**, *52* (29), 5179–5182. Experiments with $LiBH_4$ performed by S. Dreyfuss.

[2] (a) Baudler, M.; Adamek, C.; Opelia, S.; Budzikiewicz, H.; Ouzounis, D. *Angew. Chem. Int. Ed. Engl*., **1988**, *27*, 1059–1061. (b) M. Baudler, B. Wingert, *Z. Anorg. Allg. Chem.*,**1992**, *611*, 50–55.

[3] Schäfer, V. H.; Fritz, G.; Hölderich, W. *Z. Anorg. Allg. Chem.*, **1977**, *428*, 222–224.

[4] Grützmacher, H.; Ott, T.; Dietliker, K. (Basf Se), WO2011003772 A1, 2011.

[5] Baudler, M.; Ternberger, H.; Faber, W.; Hahn, J. *Z. Naturforsch.*, **1979**, *34b*, 1690–1697.

[6] Conversation with C. Bijani, 30/11/2015.

[7] Krishnamurthy, S.; Brown, H. C. *J. Org. Chem.* **1983**, *48* (18), 3085–3091.

[8] Puschmann, F. F.; Stein, D.; Heift, D.; Hendriksen, C.; Gal, Z. A.; Grützmacher, H.-F.; Grützmacher, H. *Angew. Chem. Int. Ed. Engl.* **2011**, *50* (36), 8420–8423.

[9] Fritz, G. *Adv. Inorg. Chem.* **1987**, *31*, 171–214.

[10] Huber, A.; Kuschel, A.; Ott, T.; Santiso-Quinones, G.; Stein, D.; Bräuer, J.; Kissner, R.; Krumeich, F.; Schönberg, H.; Levalois-Grützmacher, J.; Grützmacher, H. *Angew. Chem. Int. Ed. Engl.* **2012**, *51* (19), 4648–4652.

[11] Kosarev, S. A. and Collier, S. J. 2011. Tris(trimethylsilyl)phosphine. *e-EROS Encyclopedia of Reagents for Organic Synthesis.*

[12] Loibl, A.; de Krom, I.; Pidko, E. a; Weber, M.; Wiecko, J.; Müller, C. *Chem. Commun.* **2014**, *50* (64), 8842–8844.

[13] For example: (a) Jäkle, F. *Chem. Rev.* 2010, **110**, 3985–4022. (b) Bosdet, M. J. D.; Piers, W. E.; Sorensen, T. S.; Parvez, M. *Angew. Chem. Int. Ed. Engl.* 2007, **46**, 4940–4943. (c) Staubitz, A.; Robertson, A. P. M.; Sloan, M. E.; Manners, I. *Chem. Rev.* 2010, **110**, 4023–4078.

[14] Schäfer, A.; Jurca, T.; Turner, J.; Vance, J. R.; Lee, K.; Du, V. A.; Haddow, M. F.; Whittell, G. R.; Manners, I. *Angew. Chem. Int. Ed.* 2015, **54**, 4836–4841.

[15] Marquardt, C.; Jurca, T.; Schwan, K.; Stauber, A.; Virovets, A. V.; Whittell, G. R.; Manners, I.; Scheer, M. *Angew. Chem. Int. Ed. Engl.* 2015, **54**, 13782–13786.

[16] Consiglio, G. B.; Queval, P.; Harrison-Marchand, A.; Mordini, A.; Lohier, J.-F.; Delacroix, O.; Gaumont, A.-C.; Gérard, H.; Maddaluno, J.; Oulyadi, H. *J. Am. Chem. Soc.* 2011, **133**, 6472–6480.

6. Experimental Details

Generalities

All reactions were routinely performed under an inert atmosphere of argon or nitrogen using standard Schlenk and glovebox techniques and dry deoxygenated solvents. Solvents were obtained from an MBraun Solvent Purifying system SPS 800. Nuclear magnetic resonance spectra were recorded on a Bruker AC-300 SY spectrometer operating at 300.13 MHz for ^{1}H, 75.5 MHz for ^{13}C and 121.5 MHz for ^{31}P. Solvent peaks were used as an internal reference relative to Me_4Si for ^{1}H and ^{13}C chemical shifts (ppm); ^{31}P chemical shifts are relative to an 85% H_3PO_4 external reference. Coupling constants are given in Hertz. The following abbreviations are used: s, singlet; d, doublet; t, triplet; m, multiplet. $LiBEt_3H$ was either obtained commercially or prepared according to literature procedures (see ref. 7 of text). All other reagents and chemicals were obtained commercially and used as received.

Synthesis of HP_4Li

Experiment performed by Sébastien Dreyfuss. A J-Young NMR tube was charged with 0.3 mL of degassed butylamine, 11 mg of triphenylphosphine (PPh_3, internal standard, 42 μmol), 100 μL of a 0.1M white phosphorus solution in toluene (10 μmol of P_4), and 60 μL of a 2M lithium borohydride solution in THF (120 μmol). The reaction is followed by ^{31}P-NMR. After 30 min at room temperature, HP_4Li is formed in 74 % yield with respect to the internal PPh_3 standard. ^{31}P-NMR:

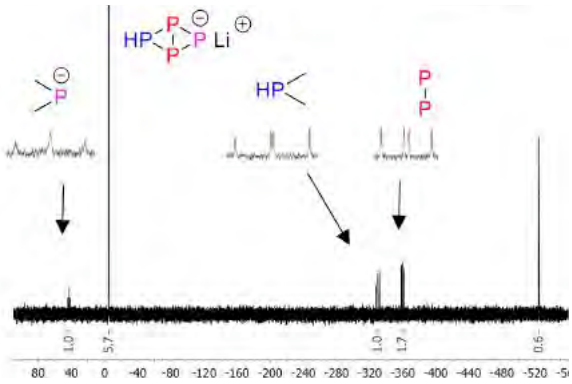

Figure Exp5.1: 31P{1H}-NMR spectrum of HP_4Li, formed after 30 min of reaction between P_4 and $LiBH_4$ at room temperature. PPh_3 was used as an internal standard (initial ratio $[PPh_3]_0/[P_4]_0 = 4.6$).

Synthesis of P_2H_4 and PH_3

Experiment performed by Sébastien Dreyfuss. A J-Young NMR tube was charged with 0.3 mL of degassed EtOH, a capillary containing a PPh_3 solution in C_6D_6, 100 µL of a 0.1M white phosphorus solution in toluene (10 µmol of P_4), and 60 µL of a 2M lithium borohydride solution in THF (120 µmol). The reaction is followed by ^{31}P-NMR. After 20 min at 70°C, PH_3 and P_2H_4 are formed in a 47% yield with respect to the PPh_3 standard. $^{31}P\{^1H\}$-NMR (121,5 Hz, $d_1 = 40$ s): $\delta = -244.3$ ppm (s, PH_3), $\delta = -214.5$ ppm (s, P_2H_4).

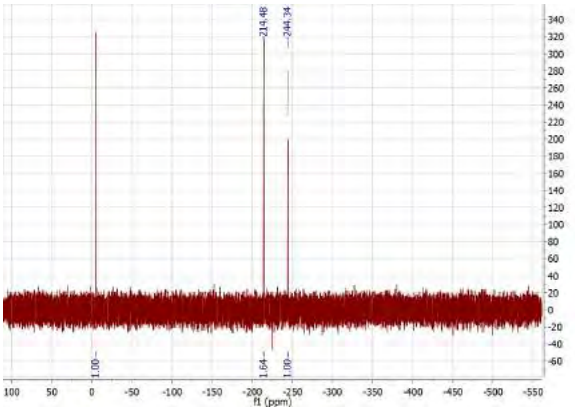

Figure Exp5.2: Formation of P_2H_4 and PH_3.

Synthesis of $LiPH_2(BEt_3)_2$

A dry Schlenk flask was charged with 15 mmol lithium triethylborohydide

($LiBEt_3H$) solution in THF (1 M, 15 mL), then cooled to –100 °C in a cryostat. To this, 1.9 mmol white phosphorus solution in toluene (7.5 mmol phosphorus) was added slowly (0.4 M, 18.75 mL). The reaction was warmed to room temperature slowly over four hours, over which time it turned red-orange. Purification was performed by reducing the volume of solution to 10 mL in vacuo, then permitting slow crystallization of $Li_3P_7(THF)_3$, as verified by ^{31}P NMR and X-ray crystallography (vide infra), over the course of three days. The crystals were dried in vacuo for a final mass of 111 mg (0.25 mmol). During this time, a red-orange solid also precipitated and clung to the walls of the Schlenk flask. This precipitate was isolated and dried in vacuo for a final mass of 287 mg powder (vide infra). The remaining solution was pale yellow in color. This was filtered and then reduced in vacuo for 20 min to result in a viscous oil. The oil was washed with toluene, with which it is immiscible, in order to wash off excess $LiBEt_3H$. After several minutes of vigorous stirring, the clear toluene layer was pipetted off. The paler yellow oil of clean $LiPH_2(BEt_3)_2$ was either stored as such or redissolved in the desired volume of THF for consequent use. Yield by NMR with respect to internal triphenylphosphine standard, with a relaxation time of 20 sec.: 61 %. ^{31}P NMR (121.5 MHz, THF): δ = –98.4 ppm (t, $^1J_{P\text{-}H}$ = 260 Hz). ^{11}B NMR (96.3 MHz, THF): δ = –10.4 ppm (s). ^1H NMR (300.1 MHz, THF): δ = 1.9 ppm (d, 2 H, $LiP\mathbf{H}_2(B(CH_2CH_3)_3)_2$, $^1J_{P\text{-}H}$ = 260 Hz), 0.56 (m, 18 H, $LiPH_2(B(CH_2C\mathbf{H}_3)_3)_2$), –0.23 (m, 12 H, $LiPH_2(B(C\mathbf{H}_2CH_3)_3)_2$).

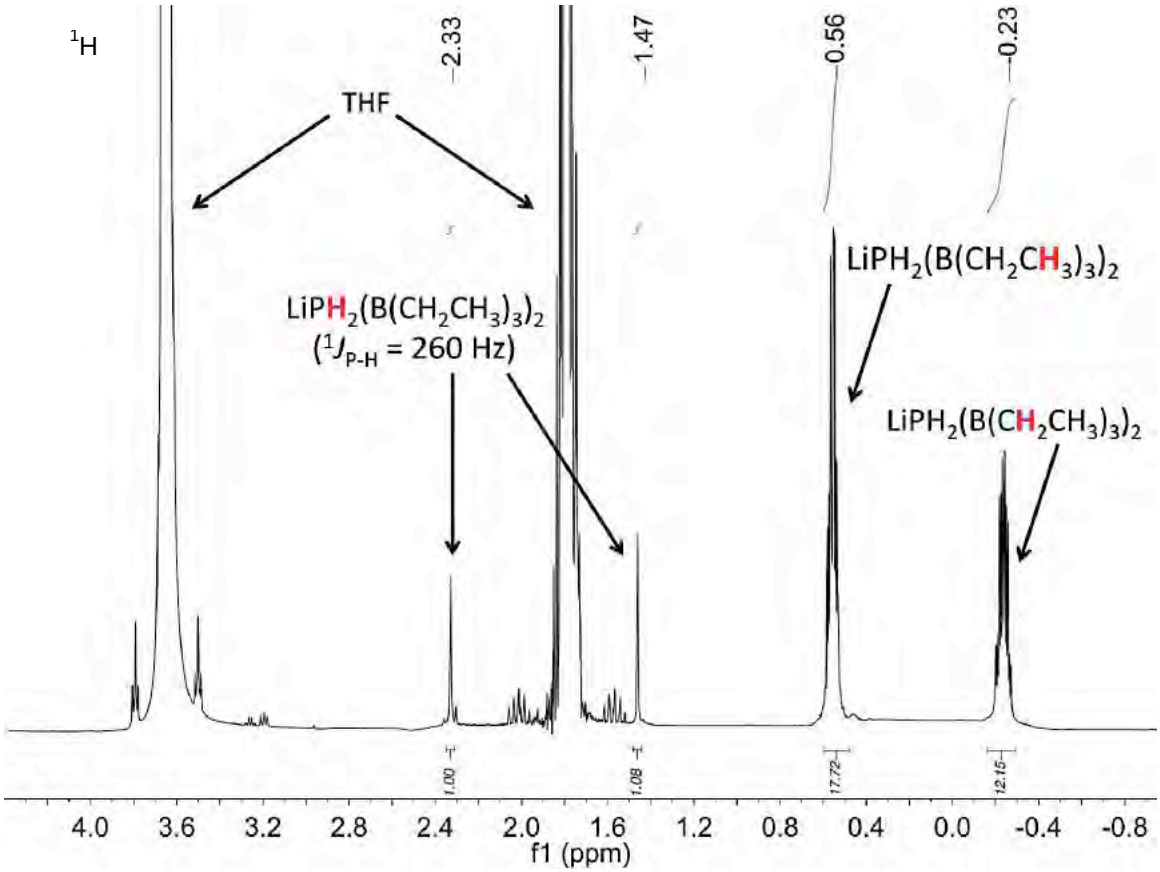

Figure Exp5.3: ^{1}H NMR of $LiPH_2(BEt_3)_2$ (^{31}P and ^{11}B NMR spectrum in text).

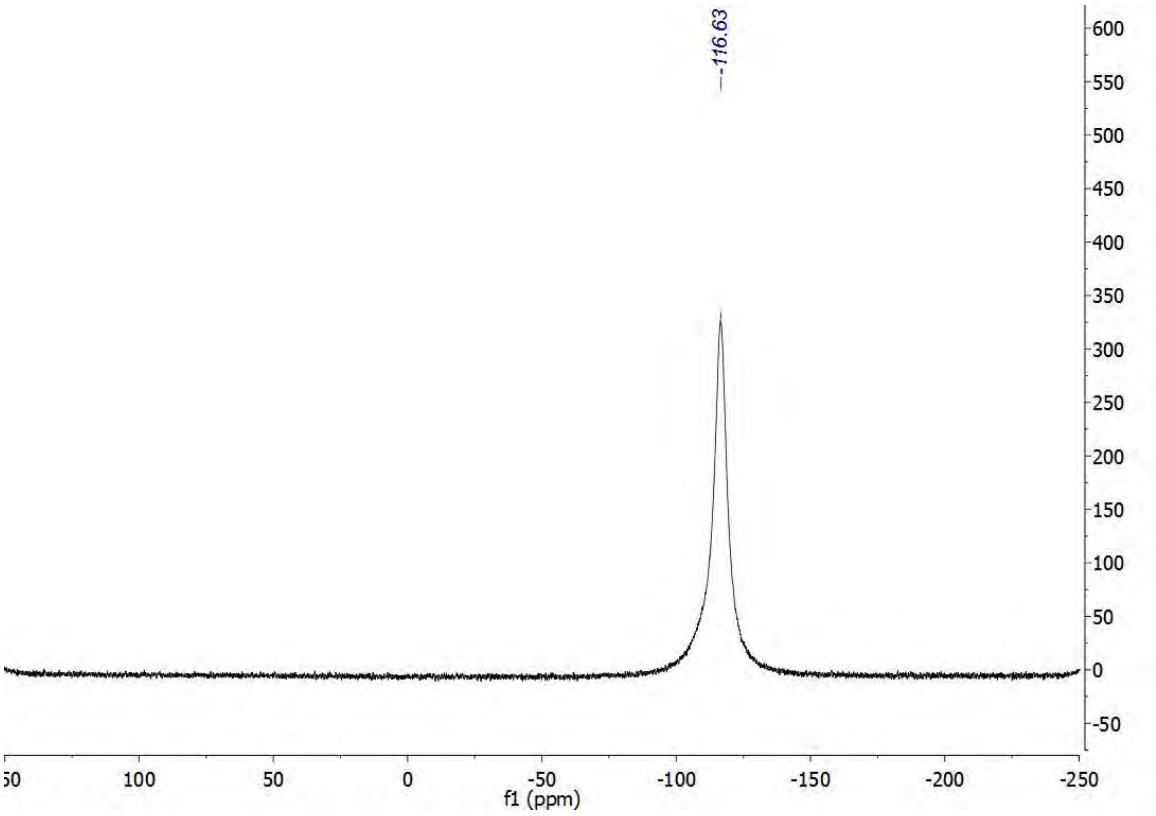

Figure Exp5.4: $^{31}P\{^{1}H\}$ NMR of $Li_3P_7(THF)_3$ at 60 °C.

Isolation of Li_3P_7 with addition of TMEDA

The crystals of $Li_3P_7(THF)_3$ obtained while purifying $LiPH_2(BEt_3)_2$ (as described above) were very sensitive and lost THF very fast after being removed from the solution. To obtain more stable crystals which are suitable for X-ray analysis, 1 equiv. of tetramethylethylenediamine (TMEDA) with respect to $LiPH_2(BEt_3)_2$ was added to the solution prior to the crystallization.

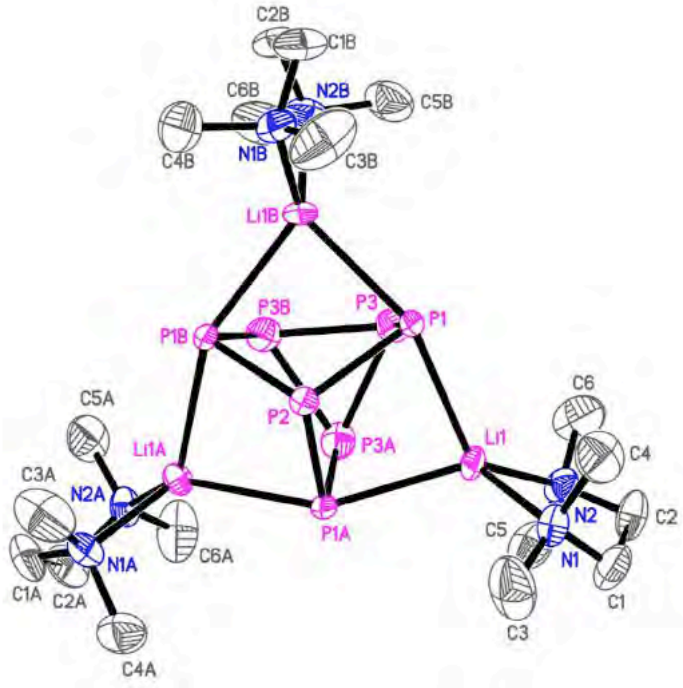

Figure Exp5.5: Molecular structure of $Li_3P_7(TMEDA)_3$ with thermal ellipsoids drawn at the 50% probability level. Hydrogen atoms have been omitted for clarity.

The data for this compound were collected at low temperature (173K) on a Bruker-AXS D8-Venture diffractometer equipped with a CMOS Area detector using MoKα radiation (λ = 0.71073Å). Phi- and omega- scans were used. The data were integrated with SAINT, and an empirical absorption correction with SADABS was applied.[1] The structure was solved by direct methods (SHELXS-97)[2] and refined using the least-squares method on F^2[2]. All non-H atoms were refined with anisotropic displacement parameters. The H atoms were refined isotropically at calculated positions using a riding model.

[1] SADABS, Program for data correction, Bruker−AXS.
[2] Sheldrick, G. M., 2008, Acta Cryst. A64, 112-122.

Selected data for Li_3P_7 **:** $C_{18}H_{48}Li_3N_6P_7$, M = 586.23, trigonal, space group $P\bar{3}$, a = b = 11.3403(3) Å, c = 15.1182(5) Å, V = 1683.76(11) Å^3, Z = 2, crystal size 0.20 x 0.20 x 0.15 mm^3, 27833 reflections collected (3423 independent, R*int* =

0.0533), 107 parameters, *R*1 [I>2s(I)] = 0.0445, *wR*2 [all data] = 0.1151, largest diff. peak and hole: 0.784 and –0.267 eÅ^{-3}.

Analysis of red precipitate obtained from isolation of $LiPH_2(BEt_3)_2$

The red precipitate obtained during the isolation of $LiPH_2(BEt_3)_2$ was isolated and dried in vacuo. The resulting red power was found to be very mildly soluble in dimethylformamide and acetone. It was analyzed by mass spectrometry (ESI positive and negative ionization), by solid-state ^{11}B, ^{31}P, ^{13}C, ^{7}Li and ^{1}H MAS NMR. These revealed that the solid contains BEt_3 as well as P and Li. We can thus propose that it is a polyphosphide compound with BEt_3 coordinated. Unfortunately, we cannot propose a more precise structure for this solid.

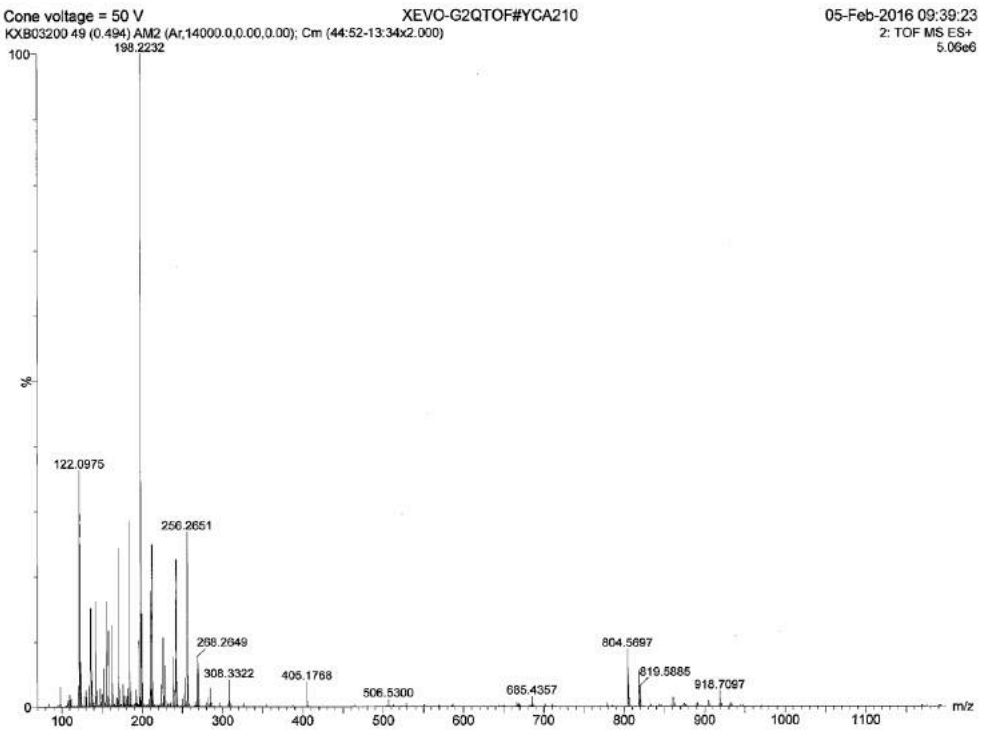

Figure Exp5.6: ESI positive ionization mass spectrum of red polyphosphide in solution in DMF/acetone.

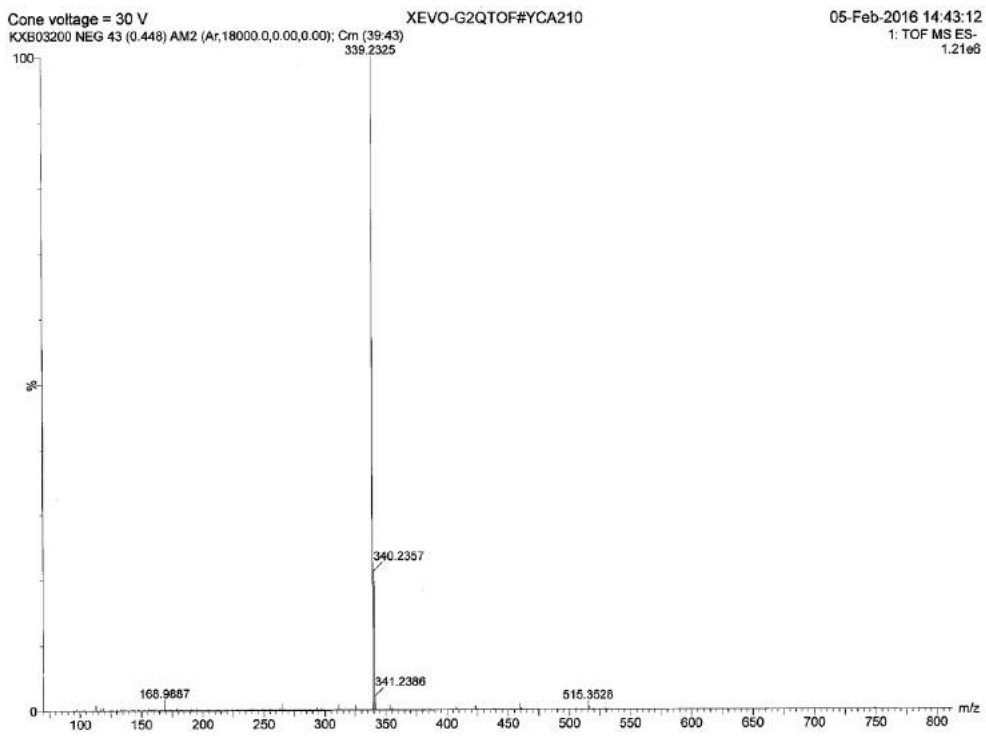

Figure Exp5.7: ESI negative ionization mass spectrum of red polyphosphide in solution in DMF/acetone.

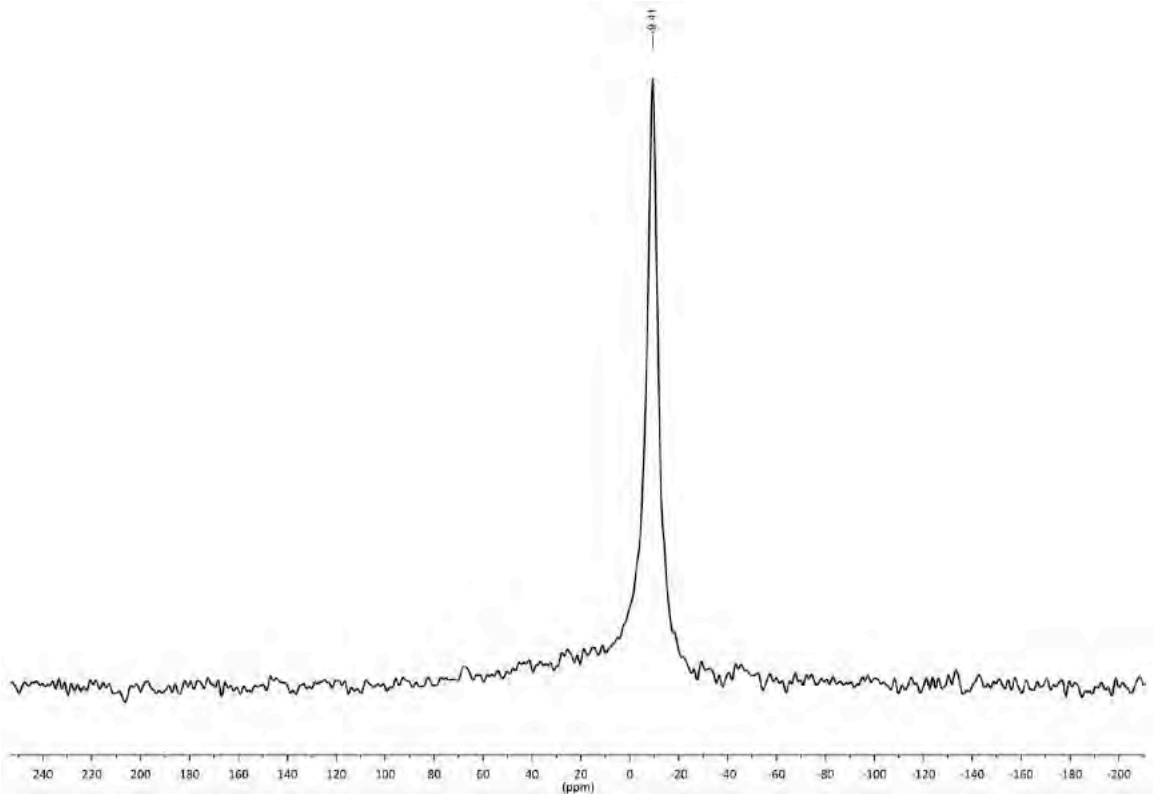

Figure Exp5.8: ^{11}B MAS NMR. Peak corresponds to BEt_3L (L = polyphosphide). Peak shape suggests high symmetry at boron but disorder in powder (i.e.,

amorphous).

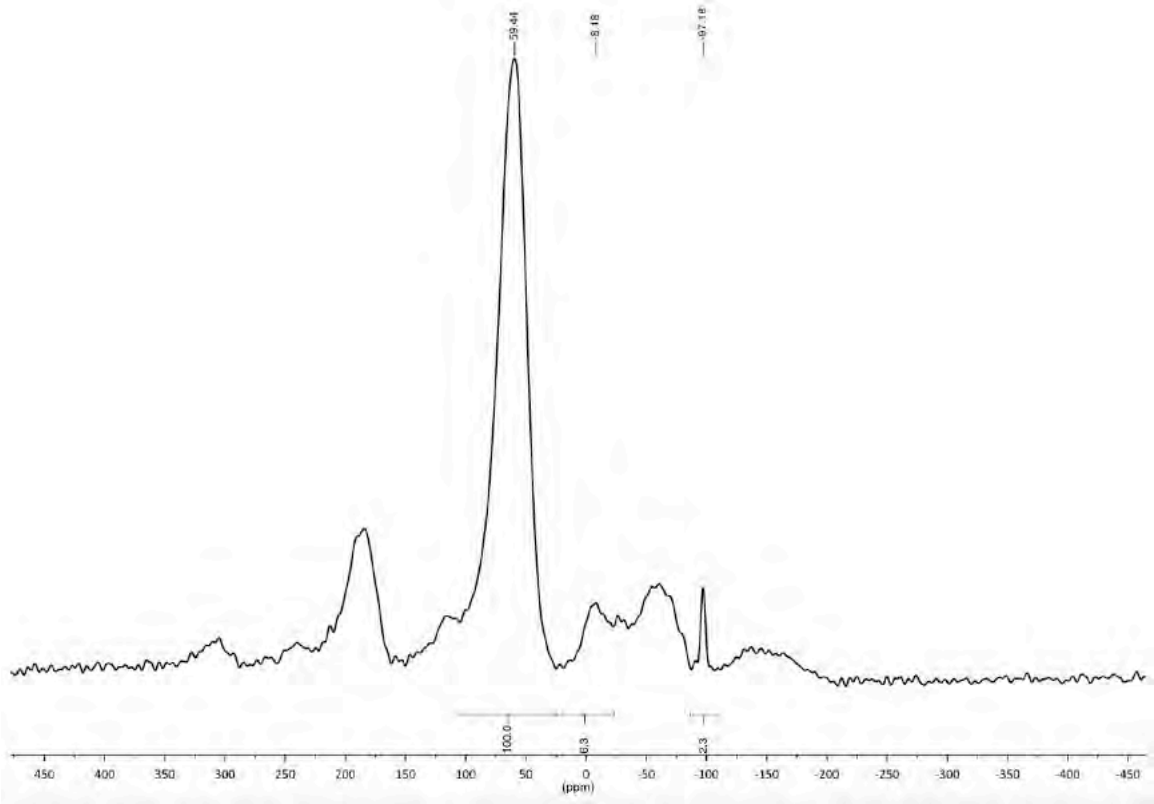

Figure Exp5.9: ^{31}P MAS NMR. The three labeled peaks correspond to the red solid; the others correspond to rotational bands.

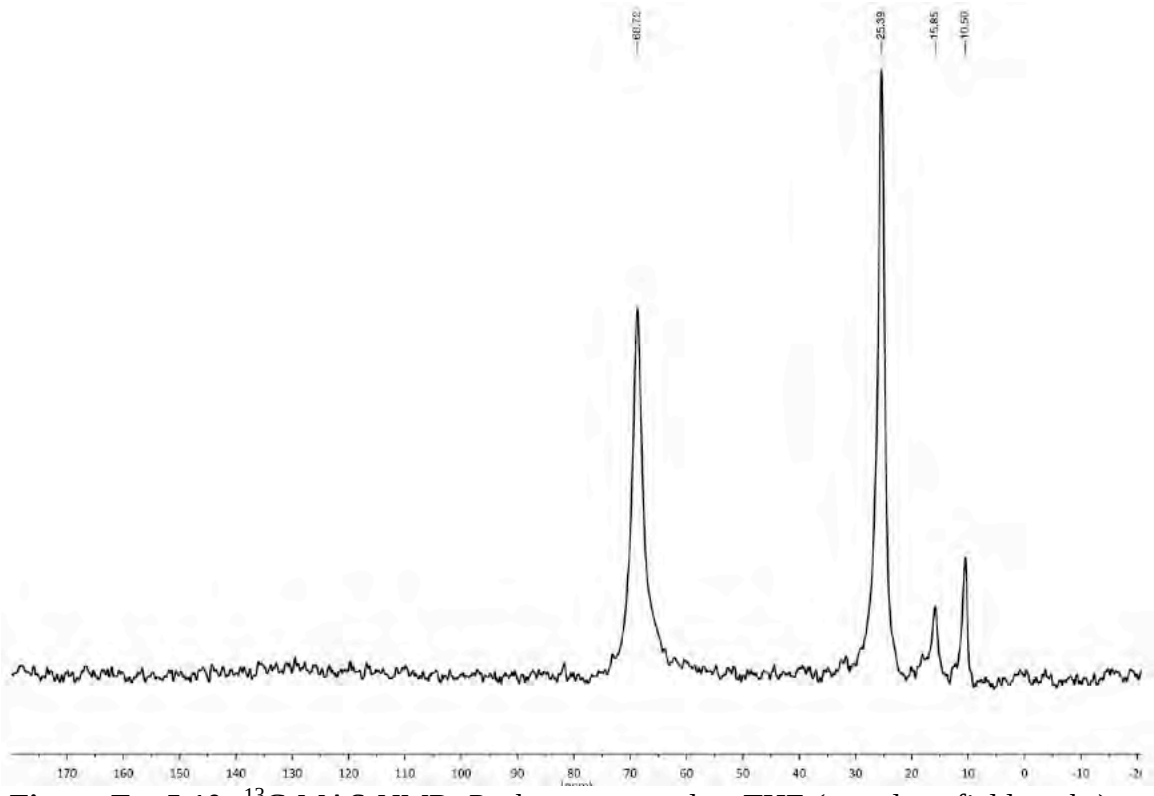

Figure Exp5.10: ^{13}C MAS NMR. Peaks correspond to THF (two downfield peaks) and BEt_3L (two upfield peaks).

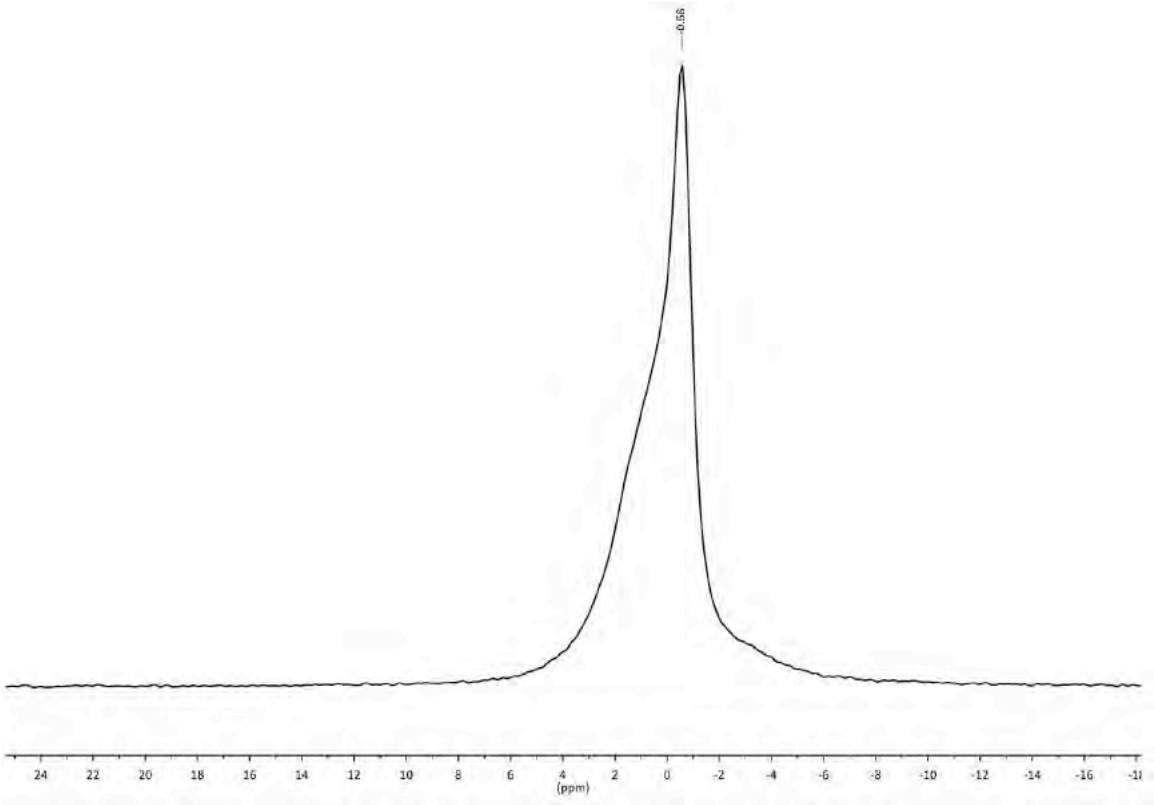

Figure Exp5.11: ^{7}Li MAS NMR. Two overlapping peaks corresponding to two different Li^{+} species.

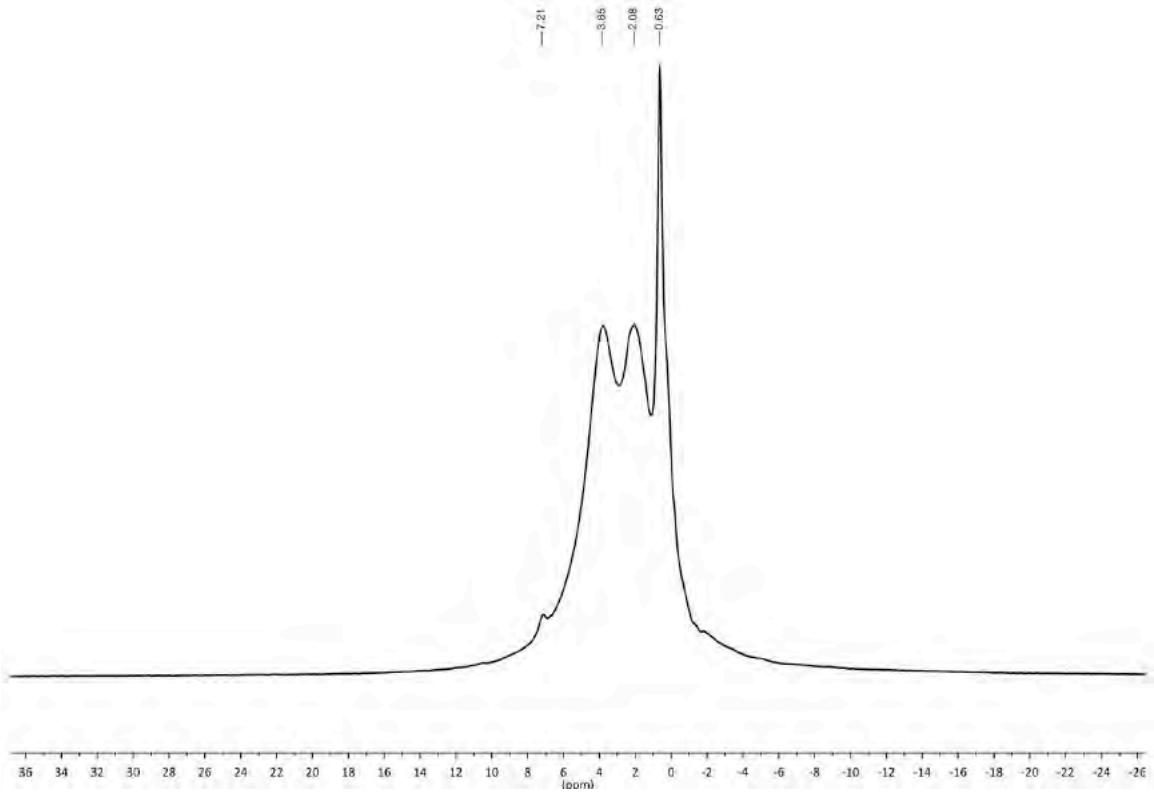

Figure Exp5.12: ^{1}H MAS NMR. Peaks may correspond to THF and BEt_3L, among others.

Removal of triethylborane adduct from $LiPH_2(BEt_3)_2$ under vacuum

A dry Schlenk charged with 0.5 mmol $LiPH_2(BEt_3)_2$ solution in THF (0.25 M, 2 mL) was placed under vacuum, resulting initially (30 min) in a mixture of $LiPH_2(BEt_3)_x$, x = 1 (^{31}P NMR (121.5 MHz, THF): δ = –186.0 ppm, t, $^1J_{P\text{-}H}$ = 194 Hz) or 2, and later (3 h) in a mixture of x = 0 (δ = –294.2 ppm, t, $^1J_{P\text{-}H}$ = 157 Hz) or. Free $LiPH_2$ degraded over a matter of hours, while $LiPH_2(BEt_3)$ persisted over several days.

Removal of triethylborane adduct from $LiPH_2(BEt_3)_2$ with pyridine

To a dry J-Young NMR tube charged with 100 μmol $LiPH_2(BEt_3)_2$ solution in THF (0.5 M, 200 μL) and 500 μL diluting THF was added pyridine (200 μmol, 16 μL). After 1 h, ^{31}P NMR indicated exclusively the monoborane adduct.

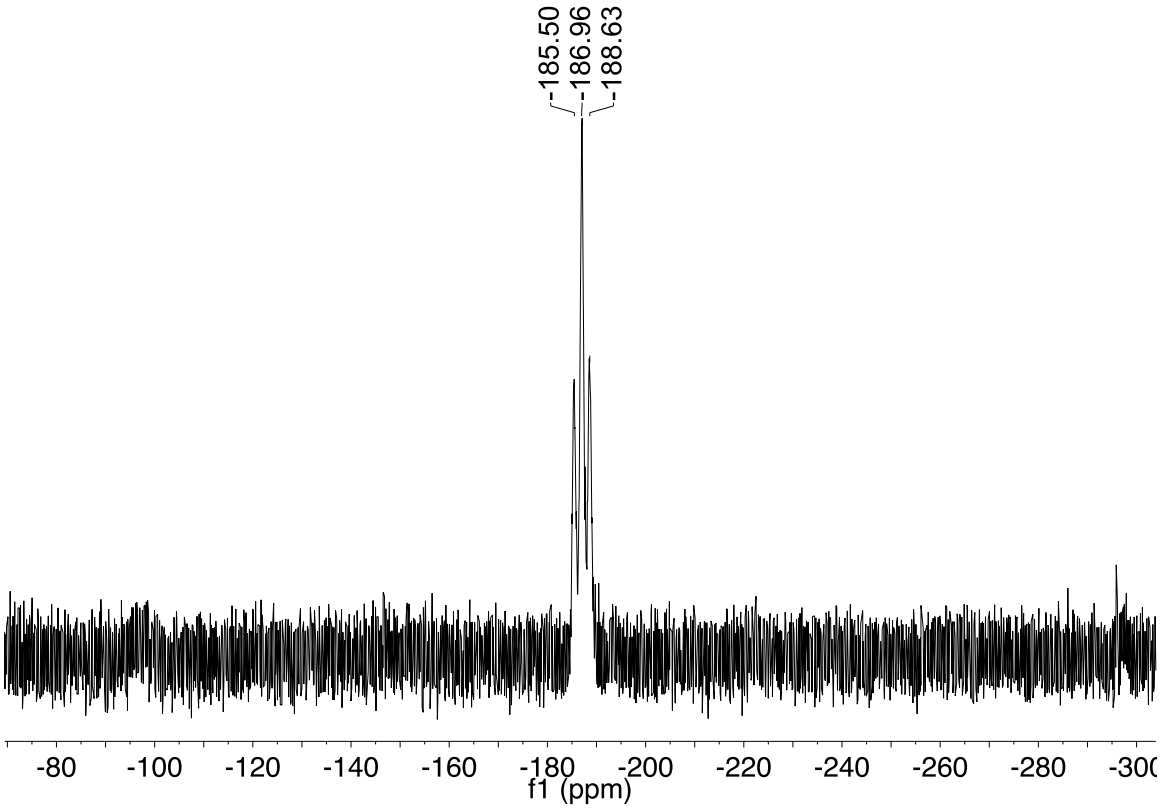

Figure Exp5.13: ^{31}P NMR of $LiPH_2(BEt_3)$.

Into this same J-Young NMR tube was added 400 μmol additional pyridine (32 μL). After 1 h, ^{31}P NMR indicated the presence of free $LiPH_2$ species and a

reduction in the amount of monoborane adduct. The free $LiPH_2$ species could not be exclusively obtained.

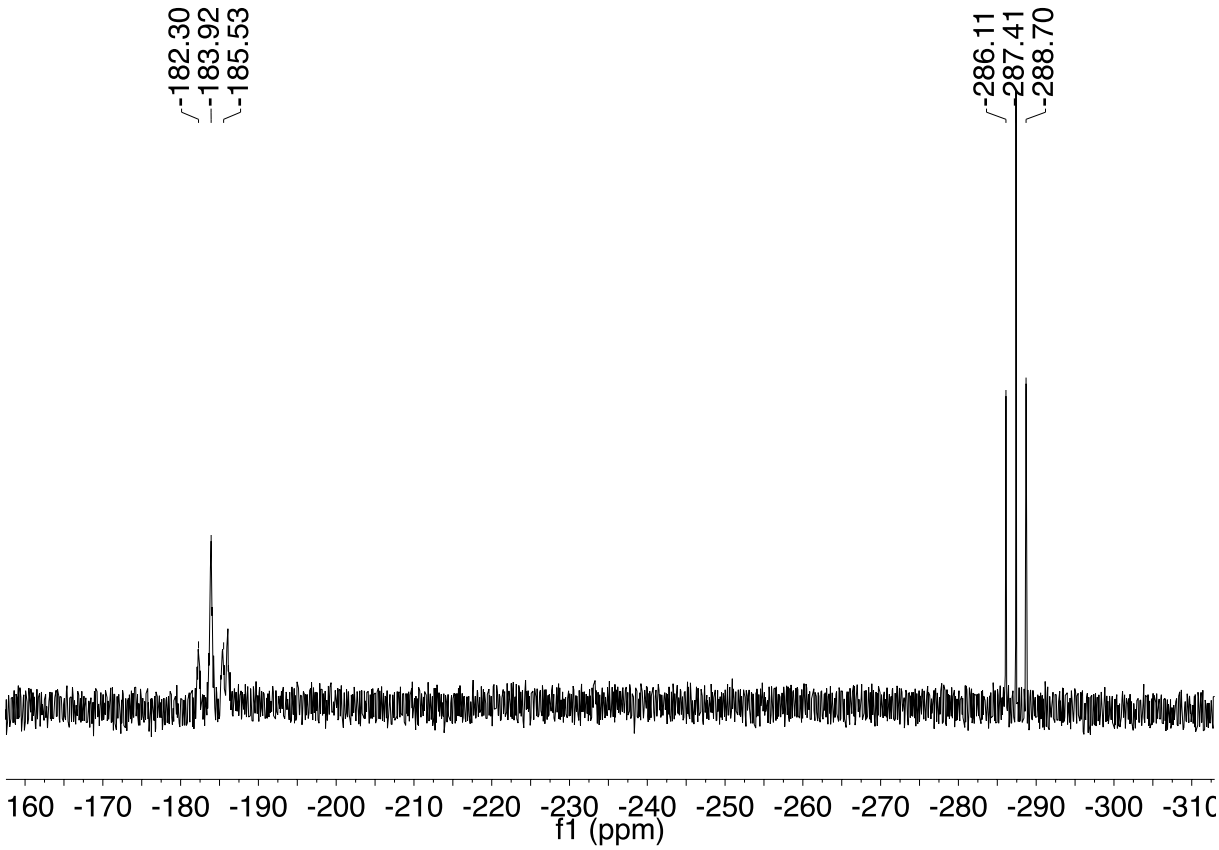

Figure Exp5.14: ^{31}P NMR of $LiPH_2$.

Reaction of $LiPH_2(BEt_3)_2$ with methyliodide, 1-propenylchloride, 2-methyl-2-butenylchloride, and benzyl chloride

A dry Schlenk was charged with 100 µmol $LiPH_2(BEt_3)_2$ solution in THF (0.77 M, 130 µL), which was diluted using THF to 1 mL. To this was added 300 µmol organic halide. The solution was stirred for 1 h. Yields for substrates 1-propenylchloride, 2-methyl-2-butenylchloride, and benzyl chloride were too low and too convoluted by byproduct peaks to quantify. The yield for the formation of $PHMe_2(BEt_3)$ was found to be 88 % by NMR with respect to an internal standard of PPh_3, with a d1 = 60 sec (δ = –35 ppm).

Formation of PH_3, PH_xD_{3-x}, and PD_3

In the cases of PH_3 and PH_xD_{3-x}, a dry Schlenk was charged with 0.5 mmol $LiPH_2(BEt_3)_2$ solution in THF (0.25 M, 2 mL). To this, 0.05 mL H_2O or D_2O, respectively, were added slowly. ^{31}P NMR showed exclusive formation of PH_3 (^{31}P NMR (121.5 MHz, THF): δ = –246.7 ppm, q, $^1J_{P\text{-}H}$ = 187 Hz) or a mixture of PH_xD_{3-x} (^{31}P NMR (121.5 MHz, THF): δ = –246.0 ppm, m), respectively. PH_3 is also obtained from similar reactions of $LiPH_2(BEt_3)_2$ with methanol, ethanol, and butylamine, but not with *tert*-butanol or diisopropylamine.

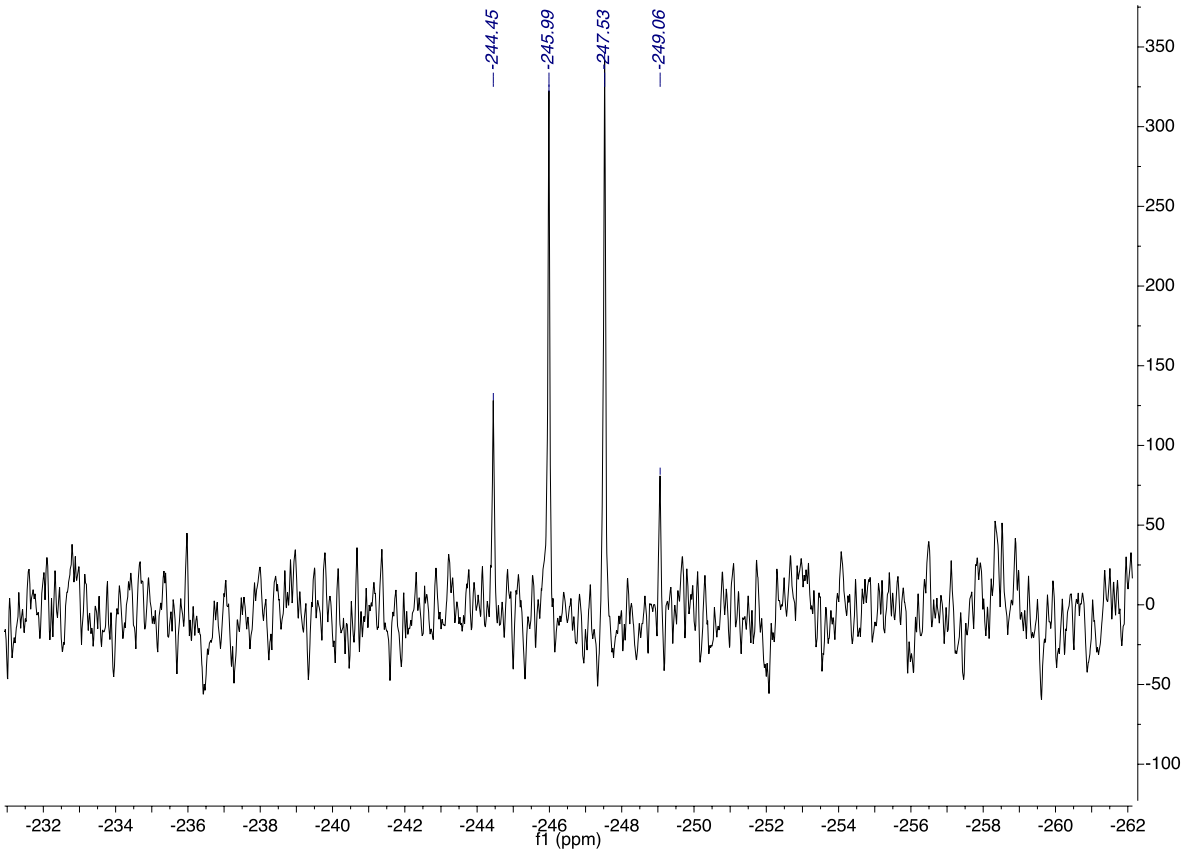

Figure Exp5.15: ^{31}P NMR spectrum of PH_3.

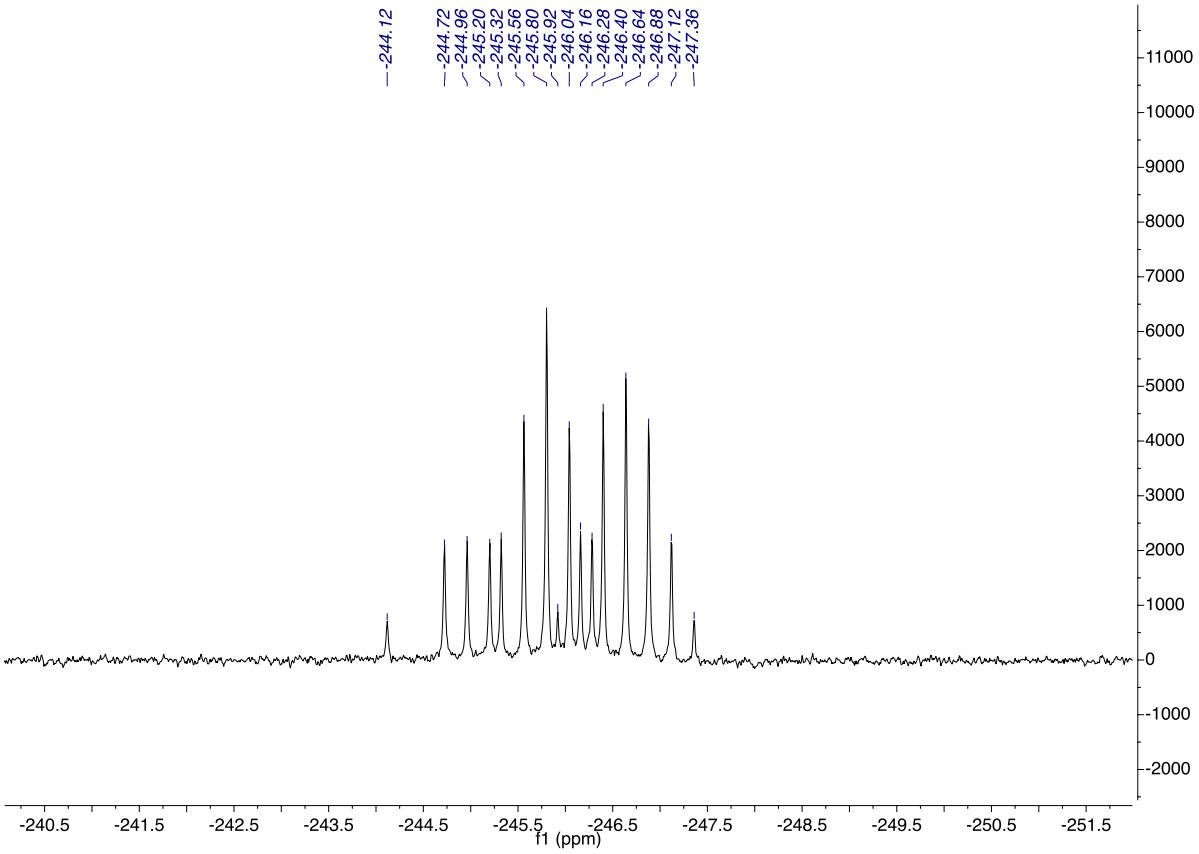

Figure Exp5.16: $^{31}P\{^{1}H\}$ NMR spectrum of PH_xD_{3-x}.

PD_3 was formed according to the scheme below:

$$LiD + BEt_3 \xrightarrow[\text{overnight}]{\text{THF, 70 °C}} LiBEt_3D$$

$$LiBEt_3D + P_4 \longrightarrow LiPD_2{\bullet}(BEt_3)_2$$

$$LiPD_2{\bullet}(BEt_3)_2 + D_2O \longrightarrow PD_3$$

Scheme Exp5.1: Formation of PD_3.

Lithium triethylborodeuteride ($LiBEt_3D$) was synthesized according to literature procedures.[1] A dry Schlenk charged with 0.5 mmol $LiBEt_3D$ in THF (1 M, 0.5 mL) was cooled to -100 °C in a cryostat. To this, 0.25 mmol white phosphorus solution in toluene was added slowly (0.73 M, 0.343 mL). Upon returning to room temperature, 0.05 mL D_2O added slowly. ^{31}P NMR showed exclusive formation of PD_3 (^{31}P NMR (121.5 MHz, THF): δ = –246.6 ppm, septet, $^{1}J_{P\text{-}D}$ = 29 Hz).

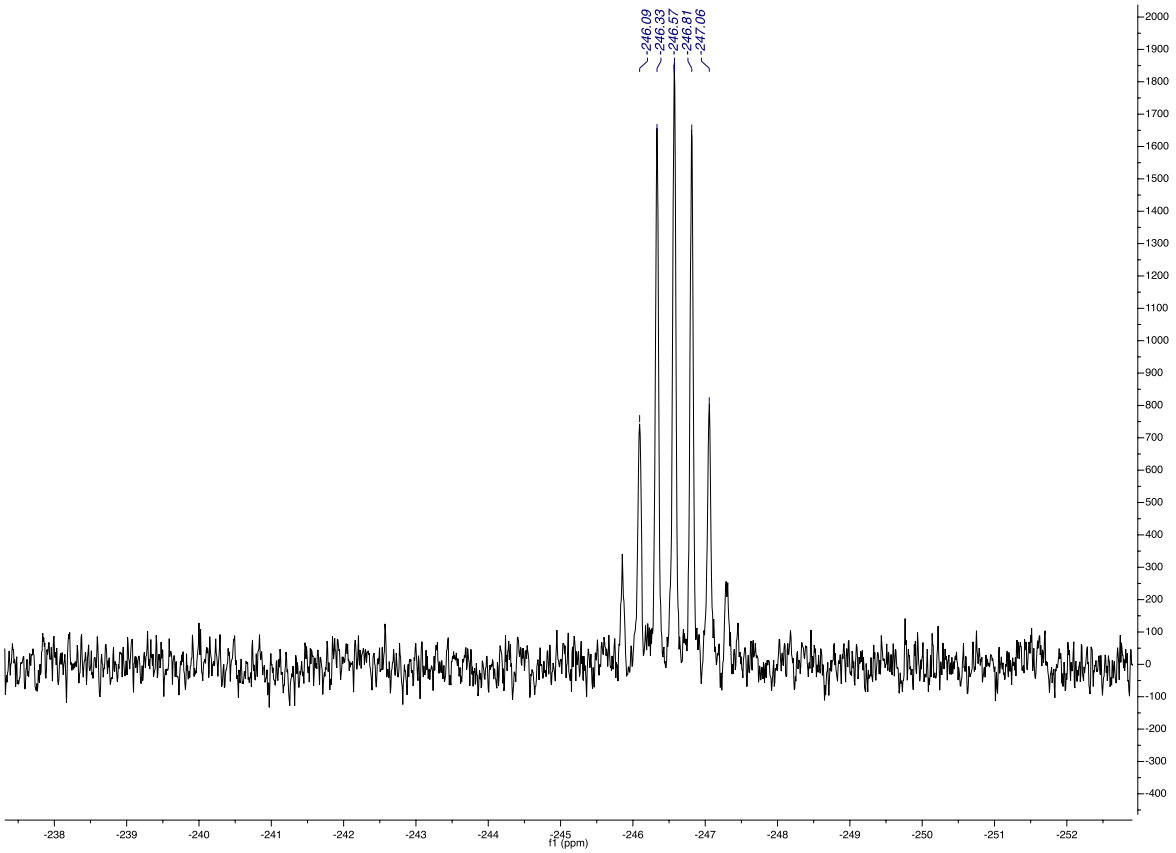

Figure Exp5.17: ^{31}P NMR spectrum of PD_3.

Reaction of $LiPH_2(BEt_3)_2$ with trimethylsilyl chloride (TMSCl)

A dry Schlenk was charged with 3.83 mmol $LiPH_2(BEt_3)_2$ solution in THF (0.77 M, 5 mL). To this was added 11.5 mmol TMSCl (1.458 mL). The yellow solution darkened to deep purple. NMR yield of $HP(TMS)_2$ (δ = –237.2 ppm) and $H_2P(TMS)$ (δ = –237.5 ppm) together with respect to an internal standard of PPh_3 showed a yield of 70 %, in a ratio of 1.7 to 1, respectively (ie, 44 % yield of $HP(TMS)_2$, 26 % yield of $H_2P(TMS)$). An attempt of heat distillation resulted in partial conversion to $P(TMS)_3$. Vacuum distillation of the reaction mixture resulted in a clear, flammable liquid that was found to be clean $HP(TMS)_2$ by ^{31}P NMR, with a mass of 230 mg (yield: 40 %).

Reaction of $LiPH_2(BEt_3)_2$ with aroyl chloride

A dry Schlenk was charged with 1.0 mmol $LiPH_2(BEt_3)_2$ solution in THF (0.25 M, 4 mL). To this was added 3 mmol aroyl chloride (benzoyl chloride, BzCl,

and mesitoyl chloride, 2,4,6-trimethylbenzoyl chloride). In the case of benzoyl chloride, 100 % yield, as judged by ^{31}P NMR, was obtained (δ = 64.6 ppm), while for mesitoyl chloride, 85 % yield was seen (δ = 86.1 ppm). The crude solutions were dried in vacuo and extracted with toluene. The mixtures were filtered by cannula transfer, with a glass microfiber filter (25-mm diameter) affixed to the source side of the cannula with Teflon tape. The volumes of the filtrates were reduced to 2 mL each, and layered with 5 mL pentane. The layered mixtures were stored in a 2-°C refrigerator over several days. The resulting precipitates were separated from the supernatant by decanting, and dried in vacuo for an isolated yield of $P(Bz)_3$ of 201 mg (58 %) and of P(2,4,6-trimethylbenzoyl)$_3$ of 194 mg (41 %).

Note: Addition of 2 equiv. aroyl chloride resulted in mixture of PR_3 and starting material.

Attempted synthesis of phosphinine from $LiPH_2(BEt_3)_2$ and pyrylium salt

A dry Schlenk was charged with 100 µmol $LiPH_2(BEt_3)_2$ solution in THF (0.77 M, 130 µL), which was diluted using THF to 1 mL. To this was added 100 µmol pyrylium salt (1,3,5-triphenylpyrylium tetrafluoroborate, 39.6 mg; or 1-pyridyl-3,5-diphenylpyrylium tetrafluoroborate, 39.7 mg). The solution was stirred for up to overnight at RT or overnight at 70 °C with no change in the $LiPH_2(BEt_3)_2$ peak by ^{31}P NMR. The addition of up to 500 µmol pyridine (40.3 µL) resulted in the formation and consequent disappearance of free $LiPH_2$, but no phosphinine. The addition of up to 500 µmol sodium *t*-butoxide (48.1 mg) resulted in the degradation of $LiPH_2(BEt_3)_2$ and the formation of uncharacterized products, but again no phosphinine.

An identical reaction was scaled up to 5 mL. 500 µmol $LiPH_2(BEt_3)_2$ solution in THF (0.77 M, 650 µL), diluted to 5 mL using THF, was added to a dry vial with a stir bar. To this was added 500 µmol pyrylium salt (1,3,5-triphenylpyrylium tetrafluoroborate, 198.0 mg; or 1-pyridyl-3,5-diphenylpyrylium tetrafluoroborate, 198.5 mg). The solution was heated to 100 °C in an Anton Paar Monowave 300 microwave apparatus in a pressure-sealed borosilicate glass microwave tube for 4 h. The $LiPH_2(BEt_3)_2$ remained untouched by ^{31}P NMR.

Synthesis of $LiPH_2(BH_3)_2(THF)_2$

A dry Schlenk was charged with 4.5 mmol $LiPH_2(BEt_3)_2$ solution in THF (0.25 M, 18 mL). To this was added 2.5 equiv. BH_3•SMe_2 (0.427 mL) at room temperature, and the solution was heated at 75 °C. Upon overnight heating, the solution had turned colorless. The title product was isolated by drying in vacuo, redissolution in acetone, drying, rinsing with pentane, redissolution in diethyl ether, and drying in vacuo. The oil was redried in vacuo to result in 568 mg $LiPH_2(BH_3)_2(THF)_2$ (91 % yield).

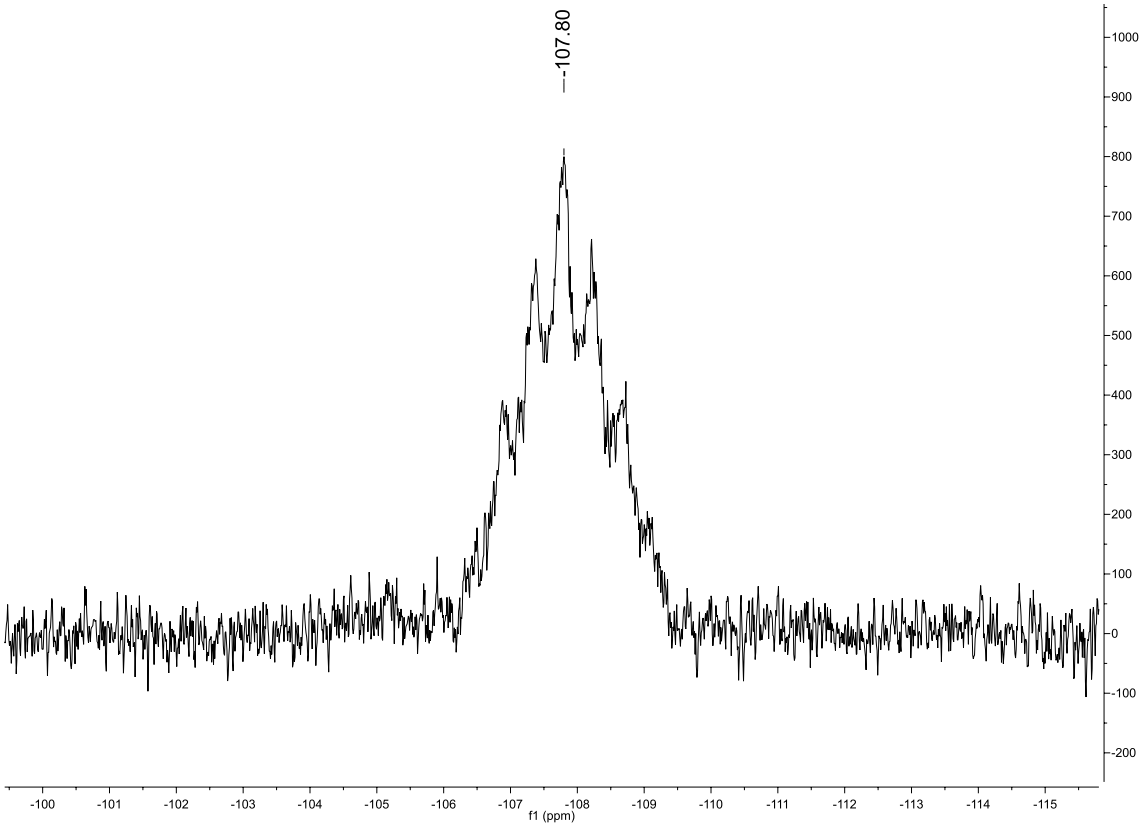

Figure Exp5.18: $^{31}P\{^1H\}$ spectrum of $LiPH_2(BH_3)_2(THF)_2$ (δ = –107.8 ppm, septet, $^1J_{P\text{-}B}$ = 52 Hz).

An initial cleaning followed by drying in vacuo over a couple hours at RT yielded the spectrum below, which has some impurities around 0.9 ppm that obscure the BH_3 protons of $LiPH_2(BH_3)_2(THF)_2$. This spectrum clearly shows two THF molecules attached to the complex. This impurity does not contain B, as the ^{11}B spectrum only shows the signal for the title product. We assign the impurity to solvent trapped in the oily product.

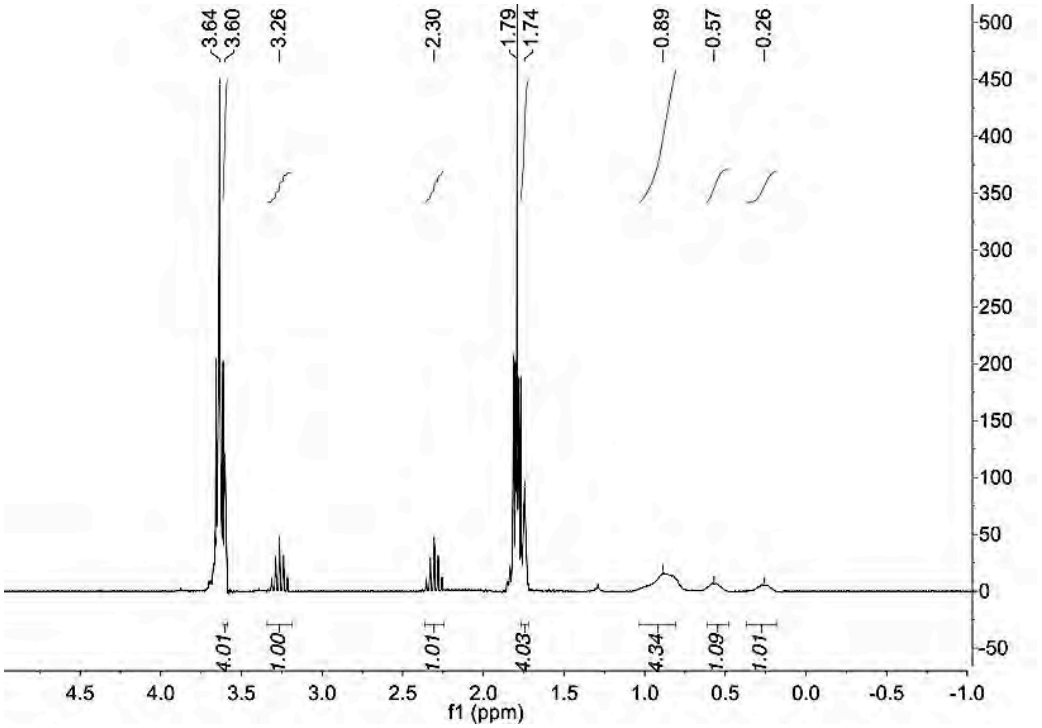

Figure Exp5.19: ^{1}H NMR spectrum of $LiPH_2(BH_3)_2(THF)_2$ containing solvent trapped in oily matrix

In an effort to clarify the area of BH_3 protons, the sample was dried over two hours in vacuo at 80 °C. This resulted in the partial loss of coordinated THF. It shows the expected 1:1:1:1 pattern for the BH_3 protons in the ^{1}H NMR spectrum.

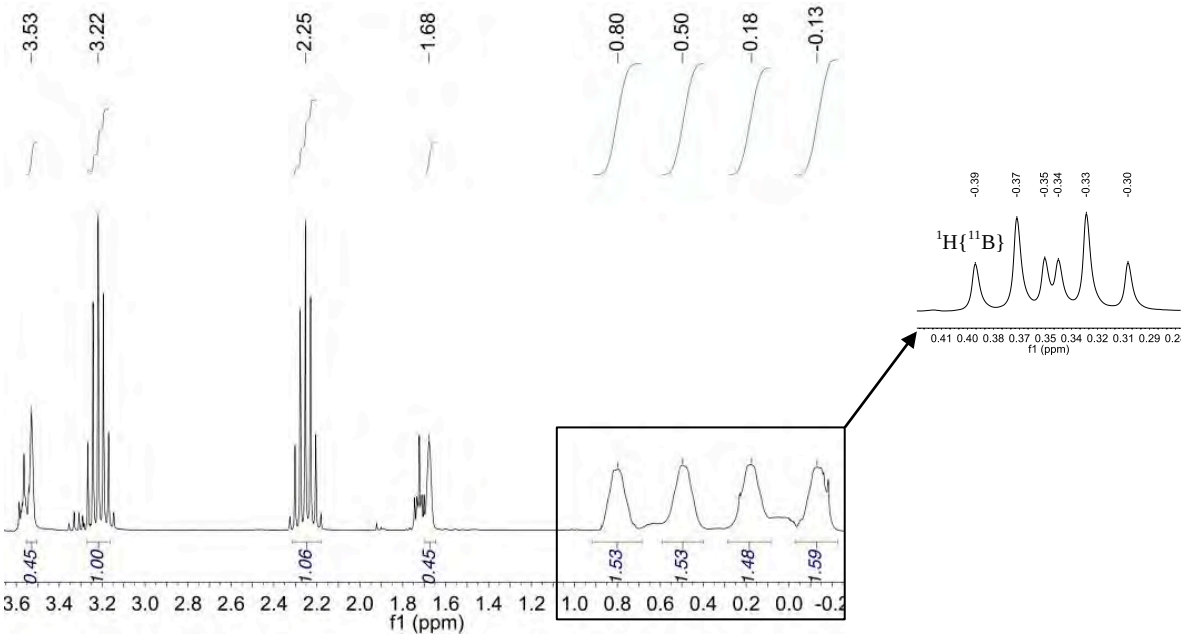

Figure Exp5.20: ^{1}H NMR spectrum of $LiPH_2(BH_3)_2$ (doublet of septets for Li**P**$\mathbf{H}_2(BH_3)_2$ at 2.7ppm, $^{1}J_{P\text{-}H}$ = 288 Hz, $^{3}J_{H\text{-}H}$ = 7 Hz; broad peaks at –0.13, 0.18,

0.50 and 0.80 ppm for $LiPH_2(B\mathbf{H}_3)_2$, $^1J_{B\text{-}H}$ = 94 Hz). Insert: $^1H\{^{11}B\}$ of $B\mathbf{H}_3$ region (doublet of triplets for $LiPH_2(B\mathbf{H}_3)_2$, $^2J_{P\text{-}H}$ = 12 Hz, $^3J_{H\text{-}H}$ = 7 Hz).

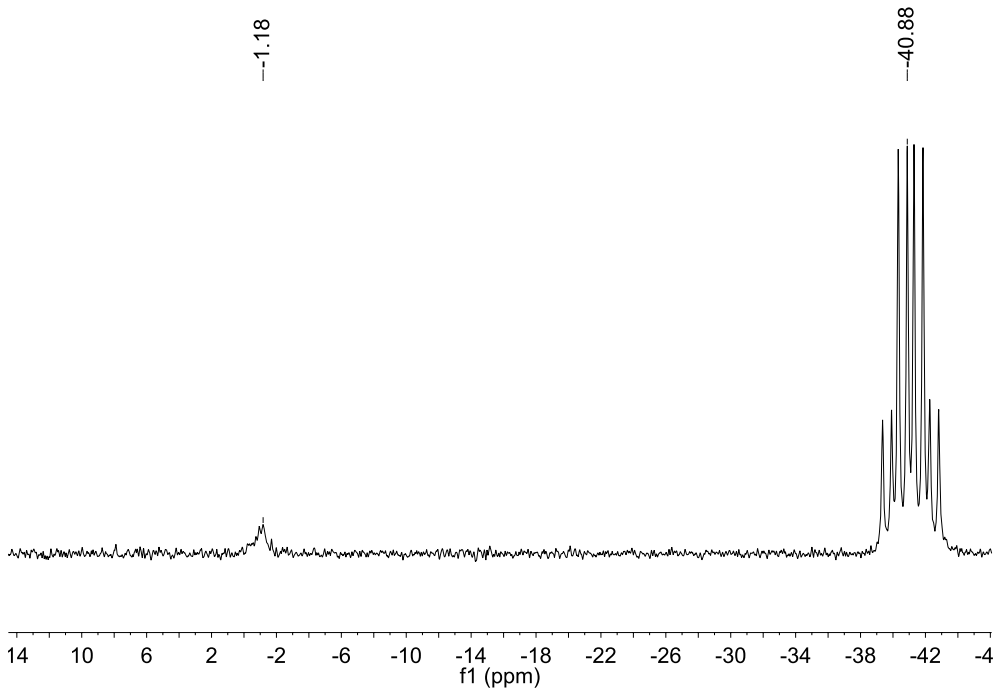

Figure Exp5.21: Extensive drying in vacuo at 80 °C resulted in the partial decomposition of the product, as shown by the appearance of a new signal at –1.2 ppm in the ^{11}B spectrum.

Attempted synthesis of $LiPH_2(BEt_3)(BH_3)$

A dry Schlenk flask was charged with a solution of 0.27 M $LiPH_2(BEt_3)_2$ (677.5 μmol, 2.5 mL) in THF. To this was added pyridine (1.36 μmol, 109 μL). After 1 h, a ^{31}P NMR spectrum showed only $LiPH_2(BEt_3)$ (Figure Exp5.13). To this mixture, 5 equiv. BH_3SMe_2 (3.39 mmol, 321 μL) were added. ^{31}P NMR indicated the exclusive presence of $LiPH_2(BEt_3)_2$. ^{11}B NMR showed $LiPH_2(BEt_3)_2$, BH_3SMe_2, and BH_3(pyridine).

Computational methods

Geometry optimizations and transition state calculations were performed using the Gaussian09. The M06L exchange-correlation functional was employed with a def2tzvp basis set on Ni, 6-311+g** on H, and 6-31g* on C and N. A full frequency calculation was performed on each structure to establish true minima, or maxima for transition states. Computed energies were corrected for thermal free energies. Structural models were generated from GaussView 03.

General Conclusion

This body of work has shown the versatility of white phosphorus as it pertains to the formation of both metal phosphide nanoparticles and organophosphines.

In the first project, we examined the formation of metal(0) nanoparticles. Starting with a previous synthesis of Ni(0) nanoparticles that used nickel(II) bis(acetylacetonate) that passed through a nickel(0) amino-imino intermediate, we eliminated the ligand-centered condensation reaction that resulted in the coproduction of water. Instead, we began directly with a nickel(II) diamide precursor that more directly formed the same intermediate. By doing so, we rendered the procedure more versatile, opening the door to parallel syntheses for water-sensitive metals, such as iron(0) or cobalt(0). Even more importantly, we carefully examined this nickel(II) diamide precursor using organometallic tools, which enabled us to understand that this species formed an oligomeric complex in solution. We also examined the effects of various other reaction parameters, such as temperature, solvent, and additives such as trioctylphosphine, oleylamine, or lithium bromide. Imaging techniques such as TEM, and analytical techniques such as X-ray diffractometry and wide-angle X-ray scattering gave us a better idea of the precise composition of the nanoparticles. This in turn permitted a clearer idea of the mechanism of nanoparticle formation. Promising initial catalytic activity leaves an open avenue for future research.

To these metal(0) nanoparticles, we added white phosphorus to form metal phosphide nanoparticles, again focusing our studies on Ni_2P. A timed test showed the separation of the larger, polycrystalline Ni(0) NPs to smaller particles, which then reaggregated. This suggested that P insertion occurs along grain boundaries, a suggestion that was supported by the addition of a large excess of the strongly binding trioctylphosphine ligand, which resulted in the exclusive production of much smaller Ni_2P nanoparticles (4.2 nm in diameter *vs.* 12.0 nm). Preliminary examinations suggest that Fe_2P and Co_2P may be formed using a similar procedure, but further analysis is required to confirm their formation and to explore reaction parameters.

In the second project, we provided the first literature example of the reduction of white phosphorus by a main-group hydride reagent. We obtained in high yield a lithium phosphanide species supported by two triethylborane molecules, which proved to be remarkably stable. By modifying reaction parameters, we were able to

limit the formation of polyphosphides, which are common byproducts that plague reactions involving white phosphorus, particularly those without bulky ligands. This phosphanide species was used in the formation of organophosphines. Further research may be envisioned in order to examine the use of PH_2^- as a bridging phosphorus ligand for metal complexes.

The triethylborane adducts were replaced by borane adducts, resulting in an even more stable species. This new species, which contains both protic [LiP$\mathbf{H}_2(BH_3)_2$] and hydridic [$LiPH_2(B\mathbf{H}_3)_2$] hydrogen atoms, may be used to form P–B polymers. The complex may also be interesting for hydrogen storage purposes.

Thus, we demonstrated the versatility of white phosphorus, and examined its reactivity in original systems to obtain new products. Both projects resulted in many promising leads that deserve further attention in the future.

Résumé de Thèse

Partie I: Synthèse des nanoparticles

1. Historique de la recherche sur les nanoparticules

Les nanoparticules (NPs) sont généralement définies comme des particules entre 1 –100 nm de diamètre.[1] Dans cette gamme de tailles, les particules présentent des nouvelles propriétés qui les différencient des matériaux massifs correspondantes. La petite taille des nanoparticules leur procure des propriétés chimiques, électriques, optiques et magnétiques inhabituelles.

L'étude des NPs synthétiques a augmenté de façon presque exponentielle au cours des deux dernières décennies.[11] Durant ces années, une plus grande compréhension des propriétés de la taille et la structure des nanoparticules s'est développée.[2] Divers facteurs affectent les propriétés des nanoparticules, notamment la taille, la cristallinité et les ligands de surface. Ces différentes propriétés peuvent être exploitées par une variété des applications, chaque types de nanoparticules étant adaptés à une utilisation précise. Cependant, peu d'aspects de la chimie derrière leurs synthèses ont été bien explorés. Nous voulions utiliser ce qui est déjà connu sur le mécanisme de synthèse des nanoparticules pour concevoir plus intelligemment la synthèse de nouvelles particules.

Comme la taille des NPs change leur fonction, il est important d'avoir une dispersion de taille étroite. Leur croissance dépend fortement de l'énergie de surface des particules, rendant le choix des ligands de surface critique. Les ligands de surface stabilisants peuvent soit inhiber les processus de maturation, soit les guider vers une taille thermodynamiquement favorable.[3] Cependant, l'utilisation de ligands pour contrôler la taille de la particule peut avoir des inconvénients dans des applications en aval. Par exemple, les ligands peuvent bloquer les sites catalytiquement actifs, ce qui rend les particules moins intéressantes, malgré leur monodispersité.

Un problème majeur avec la synthèse des NPs est la reproductibilité. De très facteurs, peu important en synthèse moléculaire, tels que la vitesse d'agitation, pourraient entraîner de grandes différences dans les produits obtenus.[4] La source des précurseurs peut également faire une grande différence dans la taille et la forme des NPs,[5] et des petites différences dans la vieillsement de la solution, de l'ordre de la minute, ont des effets mal compris.[6] Ainsi, le développement des méthodes robustes qui peuvent résister à de petites variations des conditions réactionnelles devient de

plus en plus nécessaire à mesure que les applications des nanoparticules deviennent plus variées et s'intègrent dans divers aspects de la technologie et de la science moderne.

À mesure que les nanoparticules deviennent mieux comprises, elles deviennent plus couramment utilisées.[2] Par exemple, les nanoparticules peuvent être utilisées comme catalyseurs hétérogènes.[7] L'utilisation des catalyseurs hétérogènes permet leur séparation facile après la fin d'une réaction, et permet souvent l'utilisation des conditions plus rigoureuses sans la dégradation du catalyseur. Les nanoparticules démontrent une réactivité et une sélectivité importante, et leur rapport surface/volume élevé les rend plus actifs.

Un grand intérêt s'est porté sur l'utilisation des métaux à moindre coût, tels que Ni, Fe et Co. Ces NPs du métal(0) sont utilisés pour les applications divers, de la catalyse[8] au développement de nanomatériaux plus complexes.[9] Les phosphures métalliques (M_xP_y) sont également intéressants pour une variété d'applications, y compris la catalyse, l'utilisation de leurs propriétés magnétiques,[10] les piles, et l'électrocatalyse.[11,12] Plusieurs NPs M_xP_y, tels que Ni_2P, CoP, et Fe_2P, sont des catalyseurs d'évolution de l'hydrogène hautement actifs, ou des catalyseurs de l'évolution de l'oxygène, divisant l'eau électrochimiquement pour générer de l'énergie électrique.[13]

Les phosphures métalliques se comportent très différemment de leurs NPs métalliques correspondantes. Par exemple, les NPs Ni_2P peuvent catalyser la réduction du phénylacétylène en s'arrétant au styrène (Schéma R-1).[14] En revanche, NPs Ni(0) sont capables de réduire le phénylacétylène exclusivement en éthylbenzène sous hydrogène. Cette atténuation de l'activité d'hydrogénation du Ni_2P a été attribuée à l'effet d'absorption des électrons du phosphore sur le nickel.

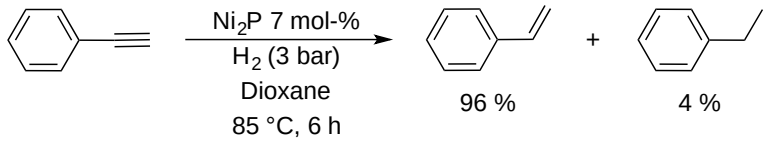

Schéma R-1. Hydrogénation partielle du phénylacétylène en prédominance au styrène.

La disponibilité facile et la toxicité faible du Ni(0),[15] avec sa versatilité chimique, le rend important et donc la cible principale de notre recherche.

2. Travaux précédents sur les nanoparticules de nickel(0)

Des travaux précédents dans l'équipe ont abouti au développement d'une méthode robuste pour synthétiser de manière reproductible des NPs de Ni monodisperses à taille ajustable par la réduction de $Ni(acac)_2$ par oléylamine, à haute température et en présence de TOP. La taille des particules s'étalle de 2 et 30 nm de diamètre en faisant varier la stoechiométrie de TOP et de l'oléylamine par rapport à la quantité de Ni (Figure R-1). Des quantités croissantes de TOP dans la solution conduisaient à une diminution de la taille des particules due à la stabilisation de surface. Des quantités croissantes d'oléylamine ont également conduit à une diminution de la taille des particules. Parce qu'elle sert comme agent réducteur, de plus grandes quantités d'oléylamine ont conduit à une nucléation plus rapide, et donc à la production rapide de nombreuses NPs plus petites.

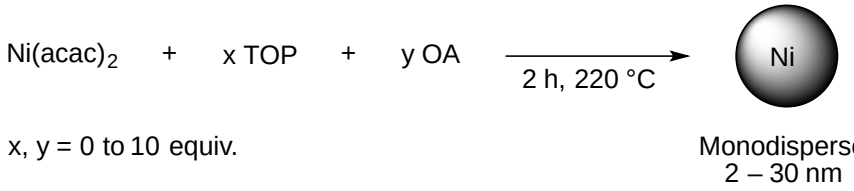

Figure R-1. NPs Ni(0) de la réduction à haute température du $Ni(acac)_2$ par l'oléylamine en présence de TOP. (L = ligand, soit TOP soit oléylamine)

Une étude mécanistique a montré que de l'eau était formée par la déshydratation des ligands acac pendant la réaction (Schéma R-2).[16]

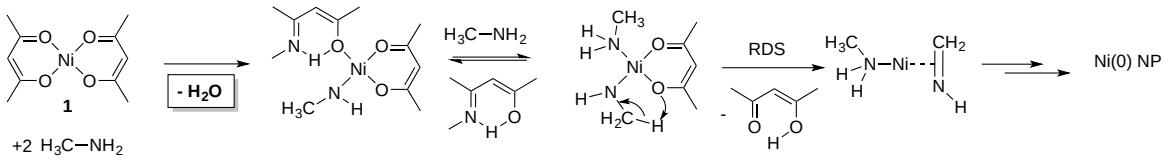

Schéma R-2. Mécanisme de réduction des précurseurs métalliques en NPs métalliques, conduisant à la co-formation d'eau.

Bien que la présence d'eau n'empêche pas la formation des NPs de Ni(0), l'élimination de l'eau pour les applications en aval pose un défi. En plus, une synthèse générique des NPs à partir d'autres précurseurs métalliques serait empêchée par l'oxydation facile d'autres espèces, telles que le fer, par l'eau. En effet, la réduction du fer(III) tris(acac) pour former des NPs par cette méthode conduit à Fe_3O_4 ou à

d'autres espèces de Fe oxydées, plutôt que Fe(0).[17] On a donc cherché à développer une méthode de synthèse des nanoparticules sans eau qui conserverait la robustesse de la procédure ci-dessus tout en nous permettant d'étendre la procédure à une variété de métaux, indépendamment de leur susceptibilité à l'oxydation par l'eau.

La réduction du $Ni(acac)_2$ par l'oléylamine a été démontrée passer à travers d'une espèce Ni(II) contenant un ligand acac, un ligand amide, et un ligand amine (Schéma R-2). Il est important de noter que la formation d'eau et la réduction de Ni(II) en Ni(0) sont deux étapes indépendantes. L'eau est formée aux premiers stades dans une réaction de condensation au niveau des ligands, tandis que le Ni reste dans l'état d'oxydation (II). L'étape clé de réduction implique un transfert de l'hydrogène en position β du ligand amide au ligand acac, entraînant la perte d'un équivalent d'acétylacétone (Schéma R-2).

Afin de conserver la robustesse de la réduction de $Ni(acac)_2$ tout en éliminant la production d'eau, on a cherché une voie plus directe à l'intermédiaire Ni(0) à partir d'une espèce $Ni(amide)_2$. Mécanistiquement, la réduction utiliserait le transfert de β-hydrogène d'un ligand amide à l'autre, comme le montre le Schéma R-3.

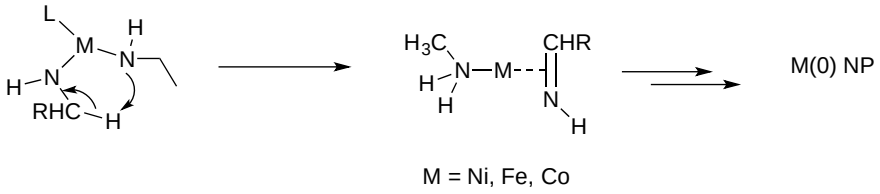

Schéma R-3. Formation de $M(NH_2CH_2R)(HN=CHR)$ de l'amidure de metal(II) aux NPs metal(0).

Alors que nos travaux avançait, Kovalenko, *et al.* ont réussi à transformer une variété des chlorures métalliques, de la plupart du groupe principal, en NPs métal(0) (M = In, Ga, Bi, Sb, Zn, Cu, Sn et leurs alliages) en formant *in situ* des amides métalliques.[18] On a donc décidé de se concentrer sur les espèces de nickel (II) bis (amide) comme précurseur, synthétisées soit indépendamment soit *in situ*.

3. Travaux actuels: Nanoparticules de Nickel(0) à partir de diamide de nickel(II) isolé

Le complexe **1** ($1/n[Ni(NHR)_2]_n$) a été synthétisé par simple réaction du produit commercial $NiBr_2(DME)$ (DME = 1,2-diméthoxyéthane) avec l'oléylamide de

lithium. Le bromure de lithium (LiBr) formé simultanément a ensuite été précipité avec du pentane. Après séchage, le produit formait une huile violette foncée. La spectroscopie RMN ^{1}H a mis en évidence des pics alkyles et vinyliques qui étaient distincts de ceux de l'oléylamine de départ et de l'oléylamide de lithium. Le produit était vérifié par l'analyse élémentaire.

Le précurseur isolé a formé des NPs Ni(0) noires après chauffage à 150 °C dans le toluène pendant 0,5 h. La microscopie électronique à transmission (MET) a montré que ces nanoparticules étaient polydisperses, ce qui est compatible avec une faible stabilisation du ligand. Des calculs ont suggéré que la réduction a eu lieu par l'abstraction d'un hydrogène en position β d'un ligand amide pour un autre, aboutissant à la formation d'un intermédiaire Ni(0) amino-imino. La taille des particules était beaucoup plus petite que celles synthétisées à partir de $Ni(acac)_2$ (4,8 nm *vs.* 30 nm).[19] Bien que le contrôle de la taille soit médiocre, la présente synthèse a montré que les espèces de diamide de nickel(II) pouvaient être réduites en NPs Ni(0), et plusieurs directions ont été envisagées pour tester les effets des ligands sur la taille et la forme des NPs Ni.

Des travaux antérieurs ont montré que l'oléylamine était un ligand peu coordinant aux NPs Ni synthétisés à partir de $Ni(acac)_2$ à 220 ° C, car elle se désorbait facilement de la surface métallique.[19] Dans des conditions de réaction plus douces (150 ° C), la désorption du ligand serait moins favorable.[20] Nous avons donc postulé qu'un ajout d'oléylamine pourrait donner un certain contrôle sur la taille et la forme des NPs. Des quantités différentes d'oléylamine libre ont été ainsi rajoutées au milieu réactionnel. L'addition de 0,1 ou 0,5 équivalents n'a pas fait apparaître de différences notables dans les NPs obtenues. Lors de l'addition d'un équivalent d'oléylamine, on a observé des NPs facettées et auto-organisées. Cette réaction produit une distribution bimodale des NPs, focalisée autour du 5,9 ± 0,9 nm et 9,5 ± 1,1 nm (Figure R-2). Une raison potentielle pour cette distribution bimodale est la présence de deux types de ligands différents à la surface. On postule que l'un de ces ligands est l'oléylamine peu stabilisante,[21] et le second est l'imine formée lors de la réduction du centre métallique (Schéma R-2). Ce résultat prometteur suggère que la taille et la forme des nanoparticules peuvent être contrôlées par l'utilisation de ligands supplémentaires, plus fortement coordinants.

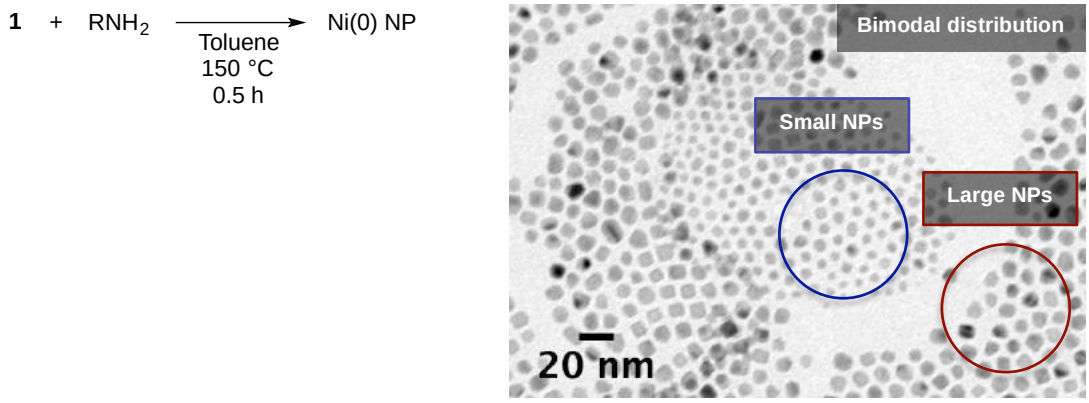

Figure R-2. Formation de Ni(0) NP à partir de la décomposition de nickel dioleylamide dans le toluène avec 1 équiv. oléylamine libre à 150 °C pendant 0,5 h. Distribution bimodale de nanoparticules plus petites et rondes de D = 5,9 ± 0,9 nm et plus grandes et facettées de D = 9,5 ± 1,1 nm.

Afin d'étudier plus en détail ce phénomène, on a ensuite examiné l'addition des ligands plus stabilisants. L'addition de la trioctylphosphine (TOP) hautement stabilisante a produit des nanoparticules sphériques monodisperses. Varier le nombre d'équivalents de TOP permet de contrôler la taille des NPs Ni(0) de 4,2 nm à 10,9 nm (*vs.* diamètres de 9 à 25 nm précédemment observés lors de l'addition de 0,1 à 0,5 équivalent de TOP aux NPs Ni obtenus à partir de $Ni(acac)_2$).[19]

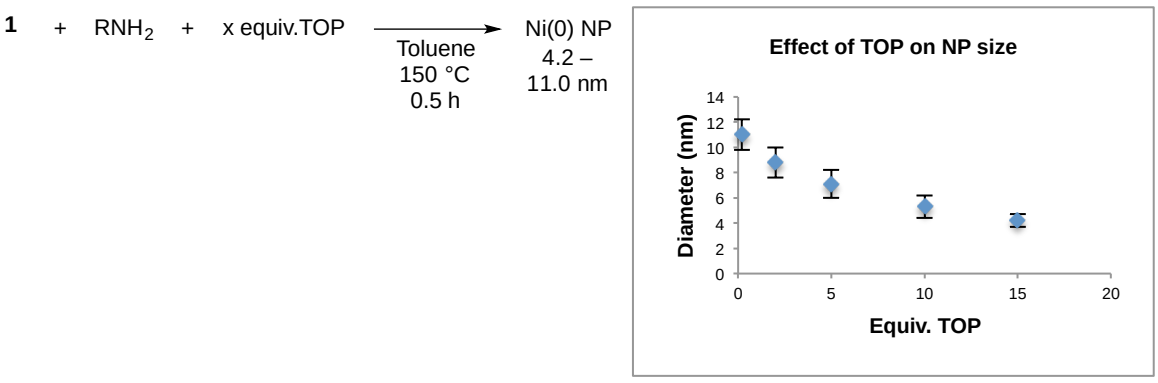

Figure R-3. Formation de NPs Ni de la décomposition du nickel(II) dioleylamide en NPs Ni(0) dans le toluène avec des quantités variables de TOP.

4. Nanoparticules du Ni(0) provenant de la formation *in situ* de dioléylamide de nickel(II)

Ayant développé une méthode robuste pour la formation de NPs Ni, on a cherché à simplifier davantage la synthèse. On a ainsi étudié la formation de nanoparticules à partir de dioléylamide de nickel(II) fait *in situ* à partir du $NiBr_2$(DME). Une expérience analogue à celle présentée sur la Figure R-3, en utilisant 0,2 équivalent de TOP, a produit de petites particules (D = 4,3 ± 1,0 nm) au lieu des particules attendues (D = 11,0 ± 1,2 nm). En effectuant la réaction à une température plus élevée, dans l'oléylamine, qui a un point d'ébullition beaucoup plus élevé, on obtient des particules plus grosses (D = 11,0 ± 1,1), comparables en taille et en dispersité aux particules obtenues en utilisant 0,2 équivalents de TOP avec **1** isolé (Figure R-4).

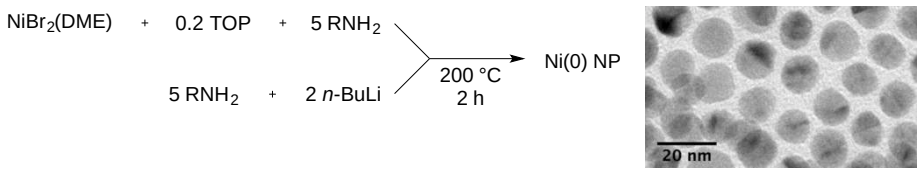

Figure R-4. $NiBr_2$(DME) pré-mélangé avec 5 équiv. oléylamine et 0,2 équiv. TOP, ajouté au mélange de 2 équiv. N-butyllithium avec 5 équiv. oléylamine de plus, chauffée à 200 °C pendant 2 h (D = 11,0 ± 1,1 nm).

Les images MET ont montré la présence de zones plus foncées et plus claires à l'intérieur d'une particule. Ces données indiquent que les NPs ne sont pas monocristallines. Ceci a été confirmé par la diffusion de rayons X à grand angle (WAXS), qui a montré que les particules sont composées de domaines cristallins d'environ 3 nm (Figure R-5).

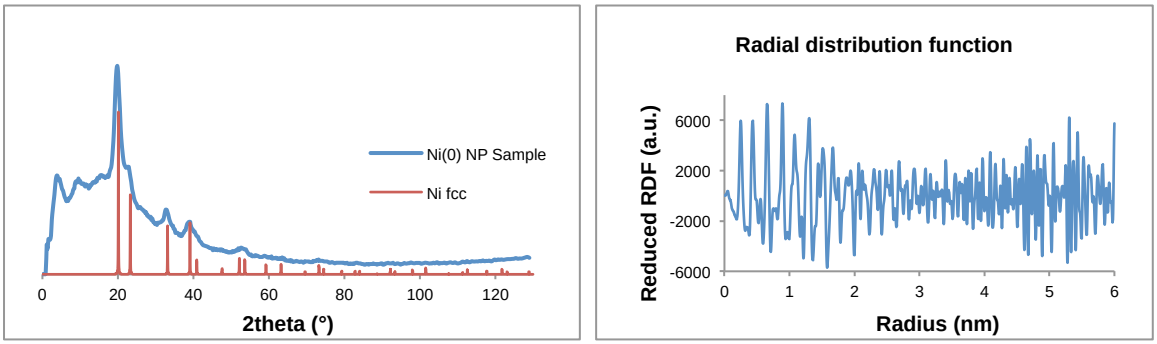

Figure R-5. Gauche: Diffractogramme WAXS de NPs Ni(0) montrés dans Figure R-4. Droite: Fonction de répartition radiale (RDF) des particules, révélant la taille des zones cristallines.

La structure polycristalline des NPs suggère que les particules croissent par un mécanisme agrégatif. Un mécanisme de maturation d'Ostwald, où les petites particules sont sacrifiées au profit des grandes, donne des particules monocristallines. Par contre, la coalescence de plusieurs petites particules, chacune avec sa propre structure cristalline, donnerait des particules polycristallines comme on le voit.

En effet, l'analyse de la formation de particules au cours du temps montre qu'après 10 minutes, les particules ont une taille de 3,0 ± 0,6 nm, correspondant aux domaines cristallins individuels (Figure R-6), avant de se rassembler pour former les particules représentées dans Figure R-4.

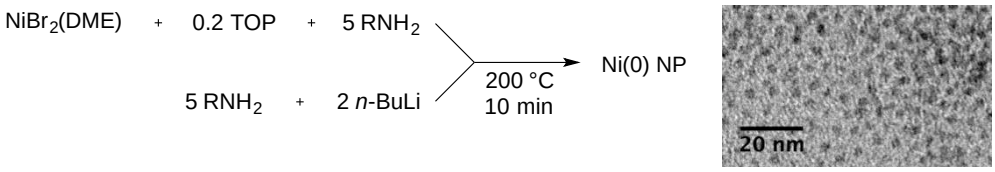

Figure R-6. $NiBr_2(DME)$ pré-mélangé avec 5 équiv. oléylamine et 0,2 équiv. TOP, ajouté au mélange de 2 équiv. N-butyllithium avec 5 équiv. oléylamine de plus, chauffée à 200 °C pendant 10 min. (D = 3,0 ± 0,6 nm).

5. Effet de la taille des précurseurs sur la taille et la forme des nanoparticules

Le précurseur proposé, le dioléylamide de nickel(II), est une espèce Ni(II) dicoordinées à 16 électrons lorsque chaque ligand amide est traité comme un donneur à trois électrons en utilisant le modèle covalent de comptage d'électrons. Une telle

espèce est insaturée et est typiquement instable, tendant vers la dimérisation/oligomérisation.[22] Les seules espèces monomériques existante sont stabilisées par des ligands volumineuses. Même le bis(diphénylamide) de nickel(II) forme des dimères, typiquement par l'intermédiaire de groupements amides pontants. Le dioleylamide de nickel(II) a peu de protection stérique, ce qui suggère qu'il pourrait également former des espèces agrégées en solution. On a ainsi postulé que l'espèce **1** serait plus exactement désignée par 1/n[Ni (oléylamide)$_2$]$_n$.

Pour identifier le précurseur exact de NPs Ni, une étude de RMN de diffusion 2-D (DOSY) a été réalisée sur des précurseurs de type Ni(NHR)$_2$ obtenus dans les conditions différentes. Dans les spectres RMN ^{1}H DOSY, les molécules migrent en fonction de leur rayon hydrodynamique r_H, une valeur qui peut être considérée comme l'équivalent du rayon d'un complexe en solution, s'il y a un minimum d'interactions entre le complexe et le solvant. La diffusion d'une espèce en solution est inversement proportionnelle à son rayon; donc, un plus grand coefficient de diffusion D donne un rayon hydrodynamique plus petit. Les deux valeurs sont corrélées par l'équation suivante:

$$r_H = \frac{k_B T}{6\pi\eta D}$$

Equation R-1. Equation corrélant le rayon hydrodynamique, r_H, avec le coefficient de diffusion. D = coefficient de diffusion (m^2/s), k_B = constante de Boltzmann, T = température, et η = viscosité.

Les études DOSY présentées ici ont été effectuées dans le toluène qui est un solvant non coordinant, afin de réduire les effets du solvant. L'espèce isolée **1** (synthétisée et stockée sous forme d'huile visqueuse pendant quelques jours à quelques mois) s'est révélée être une espèce polymère d'environ 6 nm de rayon (Figure R-8a). Ceci a été démontré par le coefficient de diffusion du pic diagnostique à 5,6 ppm (D = 6,06E-7 cm^2/s), correspondant au fragment vinylique du ligand oleyamine. La traînée montrée dans le spectre DOSY supporte la nature polydispersée de l'espèce, et/ou peut également être indicative de différentes conformations des chaînes vinyliques dans des espèces oligomèriques de même taille.

Par contre, un spectre RMN DOSY de **1** synthétisé *in situ* pris après 0,5 h a montré qu'il était monomère (Figure R-8b). Le plus grand coefficient de diffusion de

Figure R-9b (D = 3,08E-6 cm^2/s) a montré que les espèces correspondantes à ce coefficient diffusaient plus rapidement en solution, et correspondaient à un rayon hydrodynamique d'environ 1,3 nm.

L'échantillon de **1** non isolé, dont le spectre RMN est représenté sur la Figure R-8b, polymérisait en solution pendant trois jours à température ambiante pour former des oligomères de taille 2,5 à 13,1 nm de rayon (Figure R-8c), comme indiqué par les coefficients de diffusion beaucoup plus petits (D = 1,55E-6 à 2,52E-7 cm^2/s). Cette polymérisation à température ambiante est renforcée par la taille du complexe **1** isolé. Ce complex, représenté sur la Figure R-7a, est typiquement synthétisé à la température ambiante pendant une nuit, et donc est plus petit que l'oligomère qui se forme après trois jours.

On a essayé de comprendre si les NPs Ni(0) formées après chauffage étaient le résultat d'une réduction de métal dans le polymère de départ, ou si les polymères réformés des oligomères et/ou des espèces monométalliques avant la réduction ont eu lieu. Pour ce faire, on a examiné les solutions du polymère $[Ni(RNH)_2]_n$ après chauffage pendant une courte période de temps. Cela a permis l'initiation du processus de réduction, mais s'est arrêté rapidement, empêchant la formation.

Lors du chauffage à 150 °C pendant cinq minutes, la taille des polymères dans les échantillons représentés par les Figures R-7a et R-7c est réduite à des espèces monomèriques (Figure R-7d montre la séparation des polymères observés dans Figure R-7c à des monomères de r_H = 0,7 nm, démontrée par un coefficient de diffusion de D = 5,56E-6 cm^2/s). Cette expérience suggère que quel que soit l'état d'agrégation de l'espèce $[Ni(RNH)_2]_n$ au début de la réaction, la première étape de la formation des NPs est la dépolymérisation des espèces polymèriques de Ni(II) en monomère avant que le métal ne soit réduit.

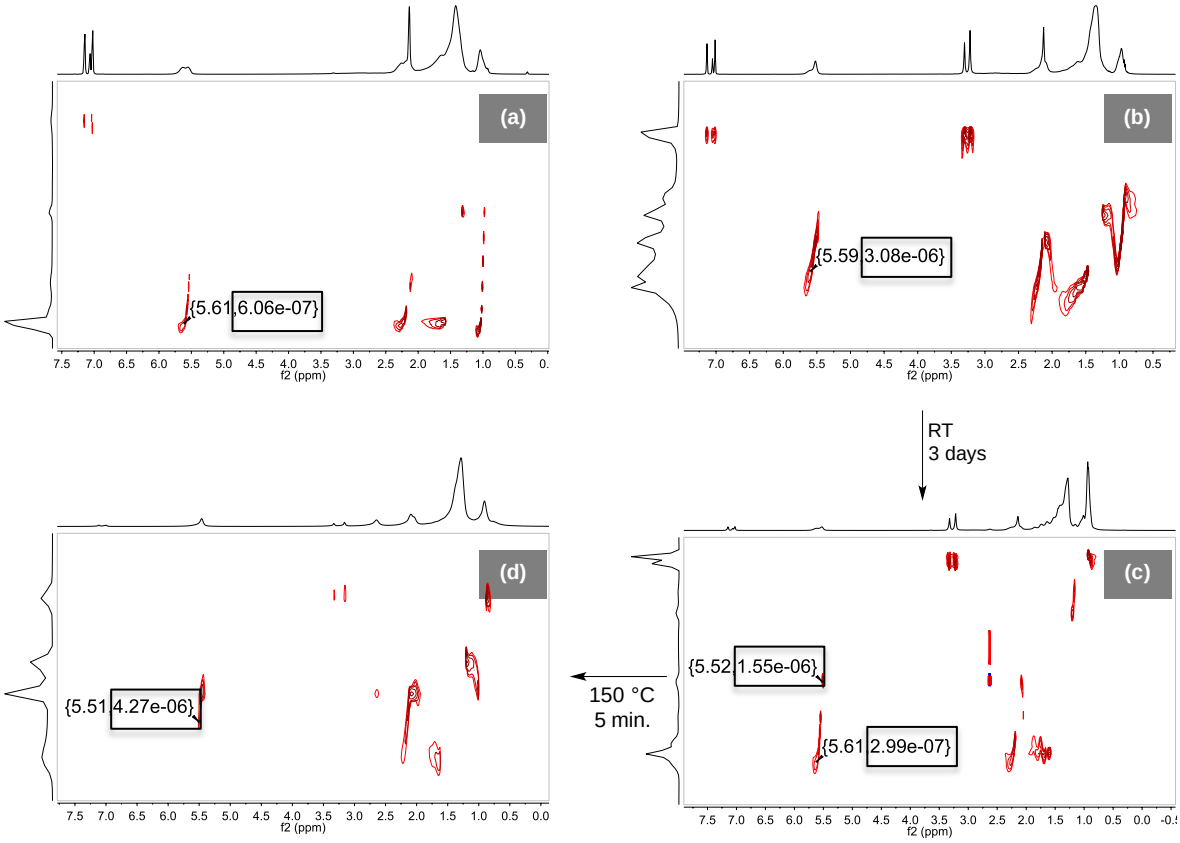

Figure R-7. DOSY RMN dans le d8-toluène de (a) Complexe **1** (r_H = 6 nm); (b) $NiBr_2$(DME) après addition d'un mélange de 2 équiv. *n*-BuLi et 2 équiv. oléylamine après 40 min. (r_H = 1,3 nm); (c) l'échantillon B après trois jours à RT (*rH* = 2,5 ou 13,1 nm); et (d) l'échantillon C chauffé à 150 °C pendant 5 min (rH = 0,9 nm).

On a supposé que l'élimination de cette première étape de dépolymérisation dans la formation des NPs à partir de **1** est la cause des différences dans les particules obtenues à partir de **1** synthétisé et isolé *vs.* fait in situ. La procédure utilisant **1** isolé avait le toluène comme solvant (Figure R-3). Par contre, la procédure utilisant **1** fait *in situ* nécessitait l'utilisation d'oléylamine comme solvant (Figure R-4). En effet, l'addition de huit équivalents d'oléylamine libres au mélange réactionnel représenté ci-dessus Figure R-8b limite la croissance de la taille du polymère sur trois jours à 2,2 nm, comme démontré par un coefficient de diffusion de D = 1,76E-6 cm^2/s. On s'attendait à ce que la présence des huits équivalents d'oleylamine libre (solvant) va donner plus de stabilisation au complexe de Ni(II) de départ. Ceci, à son tour, ralentirait la réduction de **1** à NPs Ni(0), et conduirait ainsi à la même voie réactionnelle que celle de la décomposition de **1** isolé. En séparant plus clairement les

processus de dépolymérisation et nucléation, les nanoparticules résultantes devraient être plus monodisperses.

Afin de vérifier la théorie de la maturation des solutions, deux séries d'expériences ont été réalisées. Dans un premier essai, **1** a été synthétisé *in situ* dans une solution de toluène et vieilli pendant une nuit. Il a ensuite été chauffé à 150 °C dans les conditions utilisées pour **1** isolé (Figure R-8).

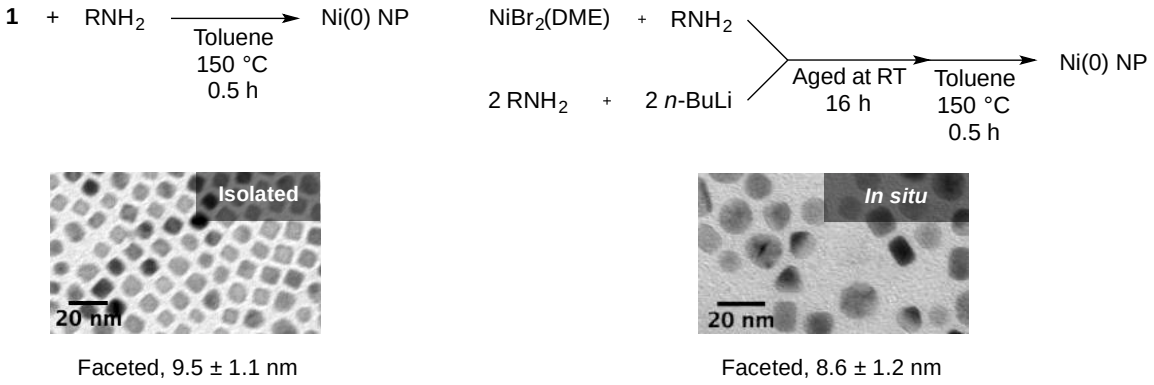

Figure R-8. NPs Ni(0) de **1** isolé (D = 9,5 ± 1,1 nm pour les grandes particules facettées) et une solution vieillie de **1** généré *in situ* (D = 8,6 ± 1,2 nm), auquel cas les deux séries de précurseurs devraient être semblables en taille. Les deux solutions précurseurs sont réduites dans le toluène à 150 °C.

Les particules résultantes ne sont pas identiques, mais elles sont beaucoup plus proches en taille et en forme à celles qu'on aurait obtenu sans vieillissement. Alors que la solution vieillie ne produit pas une quantité substantielle de petites nanoparticules sphériques telles que produites à partir de la solution de **1** isolé, les NPs facettées sont de taille, de dispersion de taille, et de facettage similaires. En revanche, une solution non vieillie de **1** fait *in situ* a produit des particules très différentes, comme brièvement décrit ci-dessus (Figure R-9).

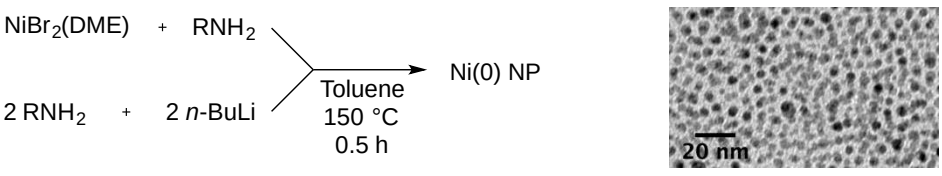

Figure R-9. NPs résultant d'une solution non vieillie de **1** (D = 4.3 ± 1.0 nm). Réduite dans le toluène à 150 °C.

Dans un second essai, une solution de **1** a été synthétisée dans le benzène, vieillie pendant une nuit, puis séchée sous vide. Le mélange résultant a été redispersé dans l'oléylamine et chauffé à 200 °C pour former des NP. Dans une réaction parallèle, **1** isolé a également été dispersé dans l'oléylamine et chauffé à 200 ° C (Figure R-10).

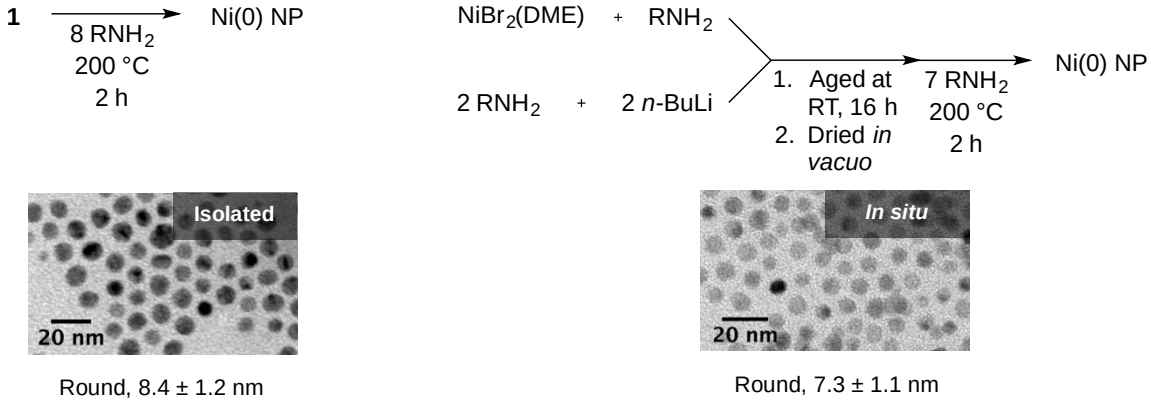

Figure R-10. NPs résultant de **1** isolé (D = 8,4 ± 1,2 nm) et d'une solution vieillie de **1** générée *in situ* (D = 7,3 ± 1,1 nm), auquel cas les deux séries de précurseurs devraient être de taille similaire. Les deux solutions précurseurs sont réduites en oléylamine à 200 °C.

On voit encore que les particules résultantes, bien que non identiques, étaient de taille, de dispersion, et de forme similaires. Ceux-ci peuvent être comparés aux particules dérivées de 1 non vieilli (D = 11,0 ± 1,1 nm), comme le montre la Figure R-4.

Ces réactions suggèrent fortement que l'état polymère de départ du précurseur 1 a un impact significatif sur la forme et la taille des nanoparticules obtenues. On suppose que les différences restantes peuvent être attribuées à des facteurs tels que la présence de LiBr et de DME en solution.

6. Extension aux nanoparticules du Fe and Co

Afin d'examiner la généralité de cette méthode de synthèse des nanoparticules, nous avons tenté de synthétiser des NPs de Fe et de Co. Les méthodes les plus efficaces de synthèse de NPs de Fe à partir de $Fe(CO)_5$ nécessitent la méthode d'injection à chaud,[23] qui est peu reproductible, en partie à cause du point d'ébullition bas du complexe métallique (103 °C). Ces synthèses sont typiquement à faible rendement, et les nanoparticules résultantes, de 6 à 20 nm, portent les ligands de CO

fortement liés à la surface, ce qui réduit la réactivité des surfaces actives pour une utilisation ultérieure (par exemple, la catalyse). La synthèse des NPs de Fe à partir de $Fe[N(SiMe_3)_2]_2$ évite ces problèmes et aboutit en effet à la synthèse de super-réseaux tridimensionnels hautement ordonnés de nanocubes de Fe de bords de 7 nm.[24] Cependant, la synthèse du précurseur est non triviale, et la réaction nécessite une pression d'hydrogène sur 48 h. Nous avons cherché à développer une méthode plus simple de synthèse de NPs de Fe qui permettrait également d'éviter les problèmes découlant de la décomposition du précurseur de carbonyle.

Une étude bibliographique de la synthèse de NPs de Co montre moins d'exemples de particules monodisperses.[25] Les particules de Co(0) ont été le plus souvent obtenues à partir de la décomposition du dicobalt(0) octacarbonyle (D < 10 nm)[26] ou de la réduction du chlorure de cobalt(II) en utilisant soit du borohydrure de sodium (D = 10 – 20 nm), soit de l'hydrogène (D = 50 – 78 nm).[27] Le précurseur de carbonyle présente plusieurs des mêmes problèmes décrits ci-dessus pour $Fe(CO)_5$, mais les précurseurs non carbonylés ne produisent généralement pas de particules monodisperses.

Une optimisation limitée des conditions de réaction a été réalisée dans les deux cas, en grande partie basée sur les résultats de l'optimisation à partir de la formation de NPs Ni(0). Les espèces isolées de dioleylamides de fer(II) ou de cobalt(II) ont effectivement produit des NPs Fe(0) de 5,2 ± 1,6 nm et Co(0) de 4,7 ± 1,6 nm. La modification de divers paramètres n'a pas significativement amélioré la monodispersité.

En utilisant la méthode des « deux pots » utilisée pour la synthèse des NPs Ni avec le bromure de fer(II) et le bromure de cobalt(II), on obtient une conversion quantitative en NP de 6,8 ± 0,8 nm pour Fe et 4,5 ± 0,6 nm pour Co (Figure R-11). La petite taille de ces particules sphériques et monodisperses, ainsi que l'absence de ligands carbonylés, les rendent extrêmement prometteuses pour des applications en catalyse.

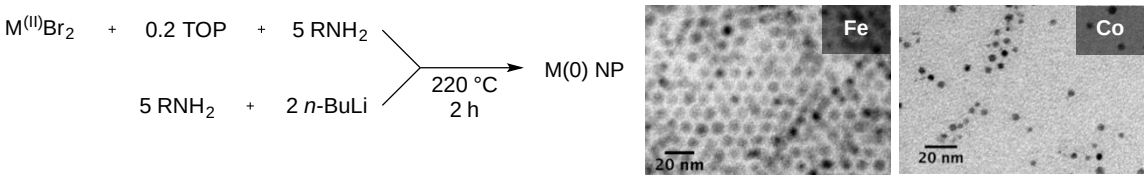

Figure R-11. Méthode « deux pot »: NPs Fe (D = 6,8 ± 0,8 nm) et Co (D = 4,5 ± 0,6 nm) dérivées de MBr_2 pré-mélangées avec 5 équiv. oléylamine, ajoutée à un mélange de 2 équiv. *n*-butyllithium avec 5 équiv. oléylamine supplémentaires, chauffée à 220 °C pendant 2 h.

7. Catalyses avec les nanoparticules du metal(0)

Plusieurs réactions préliminaires ont été tentées afin de montrer l'utilité de ces nanoparticules pour la catalyse. On a montré que les espèces Ni(II) moléculaires catalysent efficacement l'hydrosilylation des alcènes. Cependant, la littérature ne montrait aucun exemple d'hydrosilylation catalysée par NPs de Ni(0) au moment de notre travail ; le premier exemple est apparu dans la littérature en 2016 par Hu.[28] Ainsi, comme preuve préliminaire de concept, nous avons examiné l'hydrosilylation du 1-octène en utilisant les NPs de Ni synthétisés à partir de **1** réalisé in situ (Schéma R-4).

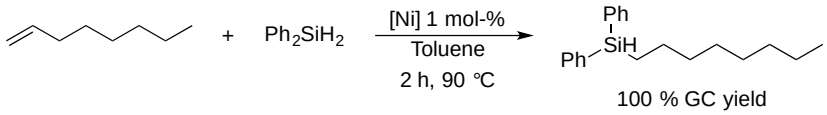

Scheme R-4. Hydrosilylation de 1-octène catalysé par NPs de Ni de 11,0 nm, dérivées de la synthèse de **1** *in situ*.

Un autre exemple de catalyse avec ces NPs de Ni est l'hydrogénation du phénylacétylène. Comme décrit ci-dessus, des travaux antérieurs ont montré que les NP Ni de 25 nm dérivés de $Ni(acac)_2$ réduisent complètement le phénylacétylène en éthylbenzène. Dans des conditions plus douces, en utilisant seulement 1 bar de H_2 au lieu de 6 bar, les NPs de Ni synthétisés à partir de **1** synthétisé *in situ* sélectionnaient principalement pour la production de styrène (Schéma R-5). Par chromatographie en phase gazeuse (GC), 89% du produit de réduction est le styrène, alors que seulement 11% de l'éthylbenzène entièrement hydrogéné est obtenu. En général, ce type de distribution est observé avec les NPs de Ni_2P et, dans une certaine mesure, avec les

NP de $Ni_{3.5}P$.[29] Cela suggère que les sites de surface des NPs de Ni utilisés dans ce travail sont empoisonnées, bien qu'elles ne contiennent pas de phosphore. Les NPs utilisés dans la réaction démontrée dans le Schéma R-4 contiennent de l'oléylamine et TOP comme ligands de surface, comme ceux utilisés dans le présent travail, mais le mélange réactionnel précédent ne contenait pas de LiBr. On peut donc postuler que les sites de surface insaturés sont bloqués par des ligands bromure dérivés du LiBr en solution.

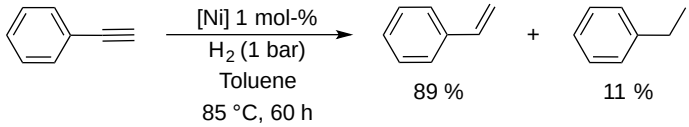

Scheme R-5. Réduction du phénylacétylène à un mélange de styrène et d'éthylbenzène catalysé par NPs Ni de 11,0 nm, dérivées de la synthèse de **1** *in situ*.

Un exemple très préliminaire mais important de catalyse avec les NPs de Fe est présenté. Il s'agit à la réduction du diazote. Le problème de la réduction de l'azote est notoirement difficile d'après la littérature.[30] Nishibayashi a été capable d'atteindre 25 équivalents de tris(trisilylméthyl)amine du diazote pour chaque équivalent de catalyseur de $Fe(CO)_5$ en utilisant de Na et trisilylméthylchlorure.[31]

Une réaction similaire a été tentée avec les NPs Fe synthétisées dans ce travail par la formation *in situ* de dioleylamide de fer(II) (Schéma R-6). Après trois jours de chauffage à 50 °C, une petite quantité de $N(TMS)_3$ a été observée. Le système n'était pas catalytique; en effet, on a obtenu environ 44 % de rendement de $N(TMS)_3$ par rapport aux atomes de Fe. Bien que ces résultats soient très modestes, c'est le premier exemple de l'utilisation des NPs Fe pour la réduction du N_2 à notre connaissance. Ainsi, le processus mériterait un examen plus approfondi.

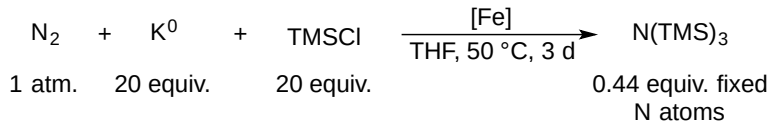

Scheme R-6. Réduction de N_2 à $N(TMS)_3$ avec les NPs de Fe de 6,8 nm, dérivées de dioléylamide de fer(II) fait *in situ*. Les équivalences sont par rapport aux atomes de Fe.

8. Syntheses dans la littérature de Ni_2P

En raison de leur importance dans de nombreuses applications, de différentes méthodes de synthèse ont été développées pour les NPs de Ni_2P. Ces méthodes peuvent être classées selon la source de phosphore employée (Figure R-12). [32–40]

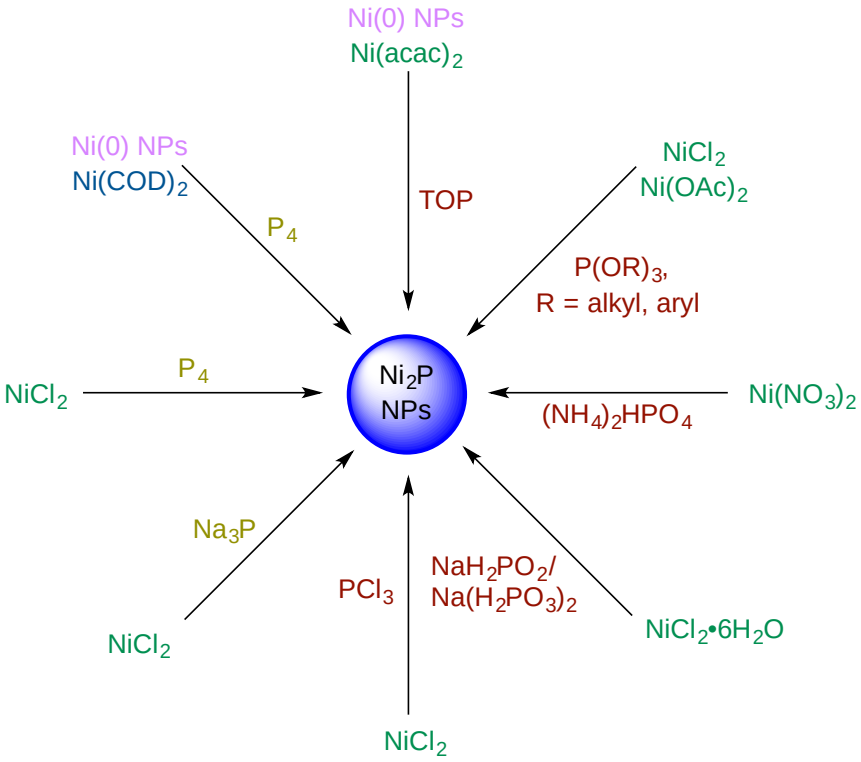

Schéma R-7. Résumé des précurseurs de métaux et des sources de phosphore pour la formation des NPs de Ni_2P.

Dans l'équipe, l'utilisation de P_4 comme source de phosphure a été développé.[41] Les NPs de Ni_2P peuvent être obtenues par addition directe de 1/8 d'équivalent de P_4 stoechiométrique au nickel(0) bis(cyclooctadiène), ce qui a immédiatement entraîné la formulation d'un solide noir amorphe. Un chauffage de ce solide noir en présence de TOPO a permis l'obtention de Ni_2P cristallin. Les NPs de Ni(0) peuvent être traitées avec des quantités stœchiométriques de P_4 jusqu'à 220 °C pour obtenir des particules cristallines de Ni_2P de 4,8 à 25 nm ou de 50 à 80 nm, en fonction des ligands de surface et des conditions réactionnelles.

9. Synthèse actuel du Ni_2P

Malgré les différentes propriétés de surface des NPs de Ni(0) décrites ci-dessus par rapport à celles synthétisées précédemment, comme démontré par les différents comportements vis-à-vis la réduction du phénylacétylène, nous avons tenté de former des NPs Ni_2P à partir des NPs Ni(0) synthétisées à partir du dioleylamide de nickel(II) préparé *in situ*. Comme précédemment observé, le chauffage simple des nanoparticules isolées ou non purifiées en présence de P_4 et d'oleylamine a entraîné la formation stœchiométrique des NPs de Ni_2P (Figure R-12).

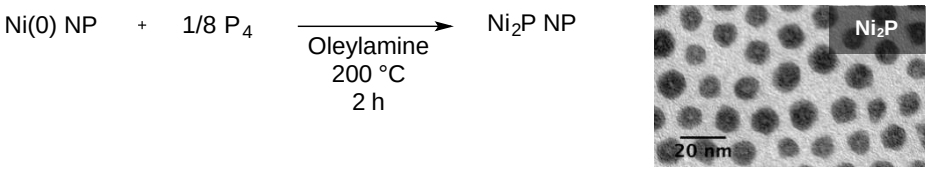

Figure R-12. Formation des NPs Ni_2P (D = 12,0 ± 1,1 nm) à partir des NPs Ni(0) isolées (D = 11,0 ± 1,1 nm).

Les études de XRD et WAXS ont donné peu d'informations sur la structure des NPs Ni_2P, ce qui suggère que le produit est amorphe. Le WAXS a suggéré que l'incorporation de phosphore a abouti à l'amorphisation des particules, commençant à la surface et s'incorporant vers le centre. Nous avons donc utilisé la RMN ^{31}P pour surveiller la consommation de P_4, en utilisant la triphénylphosphine comme étalon interne. Nous avons observé la consommation complète de P_4 après 60 minutes de chauffage.

Les images MET des particules résultantes ont montré des changements morphologiques significatifs. Ils ont démontré une légère augmentation de taille et des centres creux. Le chauffage des particules dans les mêmes conditions en l'absence de P_4 n'a pas entraîné de tels changements d'aspect et de taille, confirmant qu'elles étaient le résultat de la réaction avec P_4.

Le chauffage des particules de Ni_2P sous argon à 200 °C pendant quatre heures a induit un effet de cristallisation/mûrissement, aboutissant à un diffractogramme de rayons X avec des pics correspondant à Ni_2P (Figure R-13). L'analyse de Scherrer des largeurs de pic indiquait des diamètres de particules d'environ 20 nm.

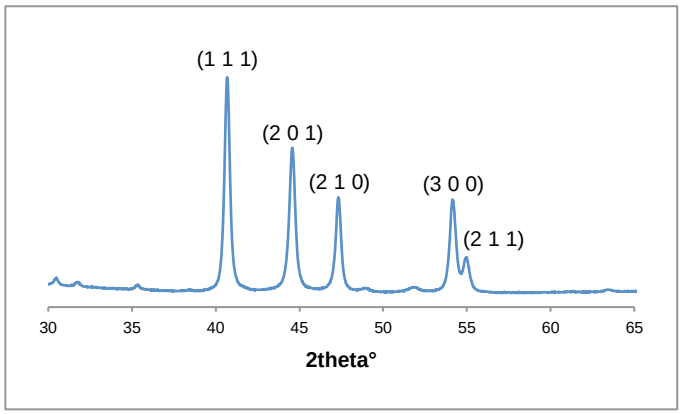

Figure R-13. Diffractogramme RX des NPs de Ni_2P cristallins lors du recuit de particules amorphes sous Ar pendant 4 h.

Afin de mieux comprendre le mécanisme de réactivité de P_4 avec Ni(0), l'évolution des particules a été observée dans le temps (Figure R-14). Les NPs de Ni(0) de 11 nm de diamètre se sont révélé être composées de zones cristallines de 3 nm par WAXS. Lors de la réaction avec P_4, on a observé d'abord la digestion des particules de 11 nm jusqu'à leurs zones cristallines de 3 nm. Ceci a été suivi par la coalescence des petites particules pour former des plus grandes, ce qui a permis l'obtension de NPs monodispersées après deux heures.

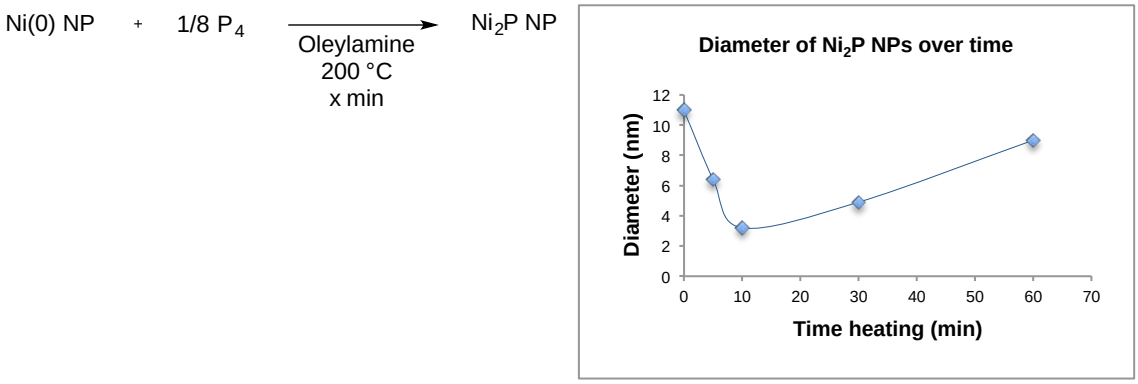

Figure R-14. Evolution des particules de Ni_2P dans le temps. Graphe des diamètres des particules après chauffage pendant 5 – 60 min. pour montrer la réduction de taille initiale suivie par la croissance conséquente.

La même réaction a été étudiée en présence de deux quantitiés différentes de TOP (0,5 et 15 équivalents ; Figure R-15). Avec 0,5 équivalents, deux populations de

NPs ont été obtenues : de grandes nanoparticules, résultants de la coalescence et vraisemblablement non stabilisé par la TOP, et des nanoparticules plus petites. En revanche, la présence d'un excès de TOP a abouti exclusivement à des particules plus petites.

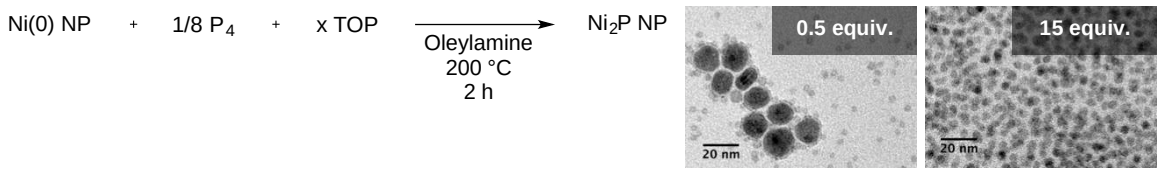

Figure R-15. Formation de particules de Ni_2P en présence de 0,5 équiv. (D = 3,2 ± 1,1 nm ou 11,5 ± 2,1 nm) et 15 équiv. (D = 4,1 ± 1,2 nm) TOP.

L'addition de P_4 à Ni(0) NP en présence de 15 équivalents de TOP pour juste 10 minutes a révélé la formation de collections de particules en forme des fleurs (Figure R-16). Ils montrent la désagrégation des NPs de Ni(0) initiales le long des frontières des zones cristallines. On peut postuler que les frontières des zones cristallines servent de voie de diffusion de P dans les NPs de Ni(0), comme on l'a vu à haute température dans des travaux antérieurs.[39b] Une fois désagrégées par l'insertion de P, les particules sont stabilisées par l'excès de TOP en solution, ce qui empêche leur regroupement. Au cours du temps, avec un chauffage plus long, les particules séparées ont été capables de se redistribuer en solution pour former les particules plus petites totalement désagrégées représentées sur la Figure R-15.

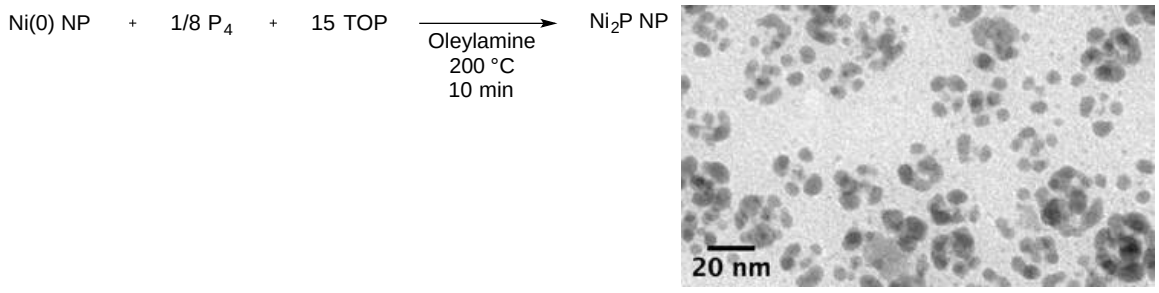

Figure R-16. La désagrégation des NPs Ni(0) avec P_4 en présence de 15 équiv. TOP (particules individuelles: D = 4,6 ± 1,3 nm ; agrégats globaux en forme de fleur: D = 25 – 30 nm, avec trop peu de particules pour une analyse statistiquement fiable).

L'étude dans le temps et l'étude de l'addition de TOP suggèrent que l'addition du P_4 aux NPs Ni(0) ne subit pas de mécanisme de diffusion, comme on aurait pu le

supposer à partir des centres creux. En revanche, il subit la digestion le long des frontières des zones cristallines, suivie par la réagrégation due aux énergies superficielles élevées.

La quantité de P_4 rajouté a été variée entre 0,25 équivalent P par Ni à 1 équivalent P par Ni, pour examiner si on pouvait former Ni_3P ou NiP_2. Cependant, des particules cristallines n'ont pas été obtenues, et ainsi les identités des produits n'ont pas pu être déterminées. Néanmoins, lorsque 1:1 P:Ni ont été chauffés ensemble, environ 0,5 équivalent de P_4 est resté après plusieurs heures de chauffage à 200 °C. Cela suggère que des quantités excessives de phosphore produisent exclusivement du Ni_2P, comme observé précédemment.[39b] Le recuit post-synthétique pourrait entraîner à nouveau la formation des NPs cristallines, ce qui permettrait d'utiliser la XRD pour évaluer l'identité du produit.

10. Extensions aux synthèses de Fe_2P et Co_2P

Ces réactions ont été étendues aux NPs de fer et de cobalt. Les NPs Fe(0) et Co(0) ont été préparées à partir du dioléylamide de fer(II) ou cobalt(II) synthétisé *in situ* (Figure R-17). Ces NPs ont été réagi avec P_4 pour former leurs phosphures correspondants. Dans chaque cas, la consommation de 0,5 équivalents de phosphore par spectroscopie RMN ^{31}P suggérait la formation des NPs M_2P (M = Fe, Co).

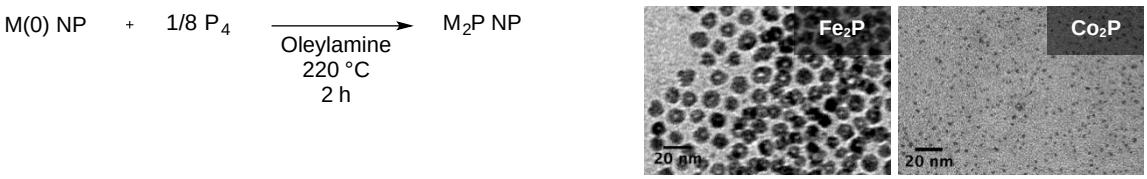

Figure R-17. Formation des NPs M_2P ; les schémas à gauche et les images TEM correspondantes à droite. Synthèse des NPs M_2P des M(0) NPs (Fe_2P de D = 10,3 ± 1,0 nm, Co_2P de D = 4,0 ± 0,3 nm, à partir du Fe(0) de D = 6,8 ± 0,8 nm, Co de D = 4,5 ± 0,6 nm).

Il est intéressant de remarquer que tous les trois phosphures de métal synthétisés (Ni, Fe et Co) avaient des centres creux, bien que cela soit difficile à voir dans l'image TEM ci-dessus de petites NP Co_2P. Les échantillons des NPs Fe(0) et Co(0) ont été chauffés en l'absence de P_4 dans des conditions autrement identiques, et aucun changement de conformation de ce type n'a été observé.

Comme avant, les particules étaient trop amorphes pour donner des pics XRD clairs, et l'incorporation de phosphore a été évaluée par RMN ^{31}P. 0,25, 0,5 et 1 équivalent de P ont été ajoutés par équivalent de M(0). Dans tous les cas, l'utilisation de 1:1 P:M a donné environ 0,5 équivalent de P_4 qui n'a pas réagi après 2 h de chauffage.

Ces résultats préliminaires de la formation des phosphures métalliques avec des NPs de Ni(0), Fe(0) et Co(0) synthétisés ci-dessus nécessitent une analyse plus poussée pour confirmer définitivement leur identité, notamment sous forme de XRD ou de WAXS. On s'attend à ce que le recuit post-réaction induise la cristallisation dans les NPs de Fe_2P et Co_2P, comme cela a été le cas pour Ni_2P. Le mécanisme de maturation des particules pendant le recuit doit également être examiné.

11. Conclusions de la synthèse des nanoparticules

On a montré la synthèse des nanoparticules de métal(0) monodisperses pour le Ni, le Fe, et le Co. Cette méthode robuste a évité de manière cruciale la production latérale d'eau, empêchant la formation des particules d'oxydes de Fe et Co. Ni a été examiné le plus complètement comme cas de test. La formation des NPs Ni a été réalisée en induisant thermiquement la réduction du dioléylamide de nickel(II), qui a été formé à partir du $NiBr_2$(DME). Ce précurseur moléculaire a été soit synthétisé séparément et isolé, soit synthétisé *in situ*. Les calculs montrent que la réduction se fait par l'abstraction d'un hydrogène en position β par un ligand amide, ce qui entraîne la formation d'un intermédiaire Ni(0) amino-imino.

L'oleylamine et le TOP ont servi comme ligands stabilisants pour les NPs, et la TOP a été utilisée pour ajuster la taille des particules résultantes. Le précurseur du dioleylamide de nickel(II) polymérisait en solution à température ambiante, ce qui a entraîné des différences entre les particules synthétisées à partir du précurseur isolé et celui formé *in situ*. Ce précurseur polymère a dépolymérisé lors du chauffage avant de subir une réduction et de former des nanoparticules de Ni(0).

Des recherches préliminaires ont été menées sur la formation des NPs Fe(0) et Co(0). Les transformations catalysées par ces différents types des NPs ont également été examinées, et les résultats ci-dessus donnent un début prometteur pour les travaux futurs.

On voit aussi que P_4 peut être utilisé comme source de phosphore pour la formation des NPs de M_2P, en utilisant des NPs de M(0) synthétisées à partir des sels de bromure de métal(II). Des études mécanistiques indiquent un mécanisme digestif de l'incorporation de P_4 dans les métaux, suivie d'une regroupement des particules plus petites. Ce travail constitue un fondement prometteur pour une synthèse facile et robuste d'une classe importante de NPs.

Partie II: Fonctionnalisation du phosphore blanc

1. Synthèse d'organophosphines à partir de P_4 : bibliographie

Le phosphore blanc (P_4) est un allotrope très réactif de phosphore qui est produit par la réduction des minéraux phosphatés.[42] Industriellement, le phosphore blanc est transformé en PCl_3 par réaction avec le dichlore, ou oxychloré en $POCl_3$, ou enfin est mis à réagir dans l'eau avec NaOH pour former PH_3 et NaH_2PO_2. La fonctionnalisation douce de P_4 en dérivés des organophosphine a été étudiée pendant de nombreuses années, en grande partie en utilisant des centres métalliques pour contrôler sa réactivité élevée. Des complexes insaturés des métaux de transition soigneusement conçus, caractérisés en général par des ligands volumineux et fortement donneurs d'électrons, permettent à la fois la coordination de P_4 et/ou l'insertion dans une liaison P–P avant fonctionnalisation.[43] Les complexes présentant des ligands moins stabilisants se décomposent facilement en espèces inconnues.

Par contre, lors de la réaction avec des nucléophiles forts tels que RMgX ou RLi, des mélanges complexes d'organophosphures ont été obtenus avec des rendements très faibles par des mécanismes de compétition mal connus (Schéma R-8).[44] Les nucléophiles neutres (comme les carbènes) et les organomagnésiens de réactivité atténuée ont permis plus de contrôle, et ont entraîné la formation de différents composés P_n avec des liaisons P–C. L'utilisation d'une paire de Lewis frustrée (FLP) à la fonctionnalisation P_4 a également été développée récemment. Des anions très volumineux favorisent la rupture du premier liaison P–P, tandis que l'acide de Lewis emprisonnait le nouveau anion bicyclotetrabutane.[45] Finalement, Cummins et Scheer ont

développé une approche de la fonctionnalisation des liaisons P–C à l'aide d'espèces de radicaux volumineux.[46]

Il apparaît donc que les réactifs volumineux ont été nécessaires pour contrôler la réactivité de P_4 afin d'empêcher des processus de fragmentation ou d'oligomérisation autrement favorables. Cependant, en termes de potentiel synthétique, il est souhaitable de rompre toutes les liaisons P–P dans le P_4 en faveur de la génération de liaisons P–A. Parmi ces liaisons P–A, les liaisons P–H possèdent une chimie très riche. De telles liaisons P–H ont été synthétisées dans la sphère de coordination de divers centres de métaux de transition, soit par transfert de métal-hydrure, soit par protonation de fragments P_n.[47] Notre but était de développer la fonctionnalisation directe de P_4 par des sources d'hydrure de groupe principal pour former des liaisons P–H.

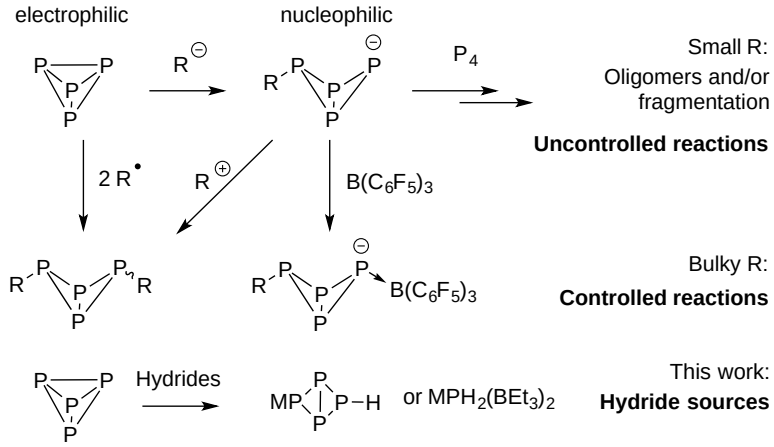

Schéma R-8. La réactivité contrôlée *vs*. fragmentation ou oligomérisation du P_4.

2. Travaux actuels: Réduction du P_4 par les hydrures du groupe principal

Pour réussir à cette stratégie de synthèse, un défi majeur doit être résolu, c'est à dire, la formation des polyphosphures par la réaction entre la fraction anionique P–H nouvellement formée et le P_4 électrophile de départ. Une des cibles les plus souhaitables est l'anion phosphanide (MPH_2), qui a été abondamment exploré dans la littérature.[48,49] Les méthodes de synthèse actuelles sont non triviales,[50] comme l'ajout d'une base forte à PH_3 dans l'ammoniac liquide,[12b] la réduction du P_4 ou du phosphore rouge en PM_3 dans l'ammoniaque liquide/DME suivie par la double protonation sélective,[50a] ou l'addition de M_0 à PH_3 dans l'ammoniac liquide.[50c] De plus, alors que Na/K/Rb/$CsPH_2$ sont thermiquement stables, $LiPH_2$ se dégrade à température

ambiante, progressant vers la dismutation en Li_2PH et PH_3.[50b,c] Dans le cadre de cette thèse, on montre que le P_4 peut réagir avec diverses sources d'hydrure pour former soit l'anion HP_4^- soit l'anion $LiPH_2(BEt_3)_2$ avec de bons rendements. Le plus intéressant, $LiPH_2(BEt_3)_2$ est thermiquement stable et a donc été utilisé comme une source versatile d'anion PH_2.

Dans une première approche, $NaBH_4$ ou $LiBH_4$ (12 équivalents) ont été mis à réagir avec du P_4 (1 équivalent) sous diverses conditions (Schéma R-9).[51]

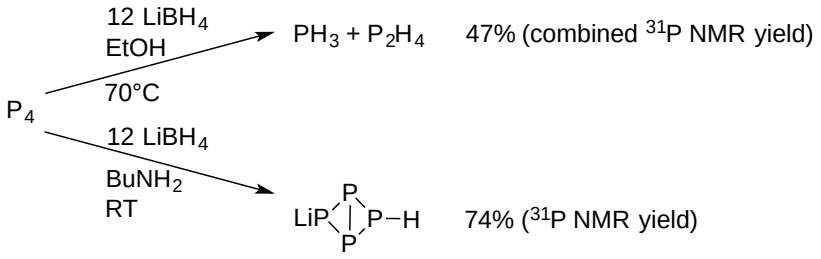

Schéma R-9. La réactivité de P_4 avec du MBH_4.

On a trouvé que le solvant jouait un rôle clé dans le contrôle du transfert d'hydrure. En effet, dans l'éthanol, un mélange de PH_3 et P_2H_4 a été formé avec un rendement combiné moyen (47 % par intégration par rapport à PPh_3 comme étalon externe, rapport vers 1,6:1 de P_2H_4 et PH_3) par chauffage à 70 °C. La réaction se produit dans la *n*-butylamine à température ambiante et entraîne la formation rapide d'un seul composé LiP_4H, en même temps que la disparition du signal P_4. Ce composé a été obtenu par Baudler avec un rendement très faible (4 %) lors de la réduction de P_4 avec Li ou avec (Na/K)/naphtalénure.[52] En revanche, LiP_4H a été formé ici avec un très bon rendement de 74 % par RMN par rapport à PPh_3 après 30 min. à température ambiante. Cependant, la réaction n'a pas entraîné la formation contrôlée de plusieurs liaisons P–H. Malheureusement, comme l'a souligné précédemment Baudler, HP_4^- évolue à température ambiante vers des mélanges de composés polyphosphorés et de PH_3.[52] Cependant, ces résultats mettent en évidence le potentiel des sources d'hydrure du groupe principal pour former des liaisons P–H à partir de P_4. Nous avons donc postulé qu'un réactif plus réducteur donnerait lieu à la formation sélective de multiples liaisons P–H.

Ainsi, le P_4 a été mis à réagir avec le superhydrure ($LiBEt_3H$). Une seule espèce, **2**, a été observée sous la forme d'un triplet large à –98 ppm par RMN ^{31}P (triplet, $^1J_{P\text{-}H}$ = 260 Hz), qui s'est réduit en un singulet lors du découplage ^1H,

indiquant la formation de deux liaisons P–H. Cependant, le déplacement chimique pour **2** est déblindé de 185 ppm par rapport à $LiPH_2$(DME) connu,[50b] ce qui suggère la coordination de BEt_3 sur $LiPH_2$. La réaction a été comprise comme impliquant un procédé rédox (Schéma R-10). La stœchiométrie requise pour générer la fraction $LiPH_2$ de ¼ P_4 et 2 $LiBEt_3H$ implique la libération d'un électron, qui peut alors réagir avec P_4 pour former diverses espèces de polyphosphures.

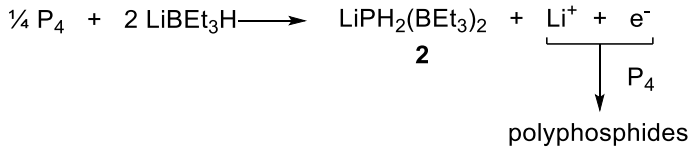

Schéma R-10. Procédé rédox équilibré conduisant à la formation de **2** et de polyphosphures.

Afin d'exploiter les différentes cinétiques de ces deux réactions pour favoriser la formation du phosphanide **2**, diverses températures et rapports de phosphore à hydrure ont été explorés. Dans des conditions optimisées, l'addition de deux équivalents du $LiBEt_3H$ par atome de P à –100 °C suivie d'un réchauffement lent sur 4 h à température ambiante a donné 61 % de phosphanide **2**. Une autre preuve de la formation du fragment $LiPH_2$ a été fournie par la réaction similaire avec $LiBEt_3D$ qui a conduit au composé deutéré attendu, contenant la fraction $LiPD_2$. La purification a été réalisée par concentration partielle sous vide, ce qui a entraîné la lente précipitation d'un solide rouge et la cristallisation concomitante d'un produit jaune pâle, Li_3P_7 (Schéma R-11).

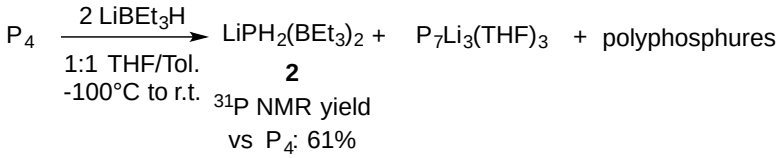

Schéma R-11. Synthèse optimisé de **2**.

La solution surnageante, contenant le composé **2**, a été séparée par filtration. La concentration de la solution sous vide pendant une courte période ne conduisait pas à la dégradation du composé **2**; cependant, quand elle a été mise sous vide pendant plusieurs heures, on a observé une perte séquentielle de BEt_3 stabilisant à partir du solide (Figure R-18b, Schéma R-13).

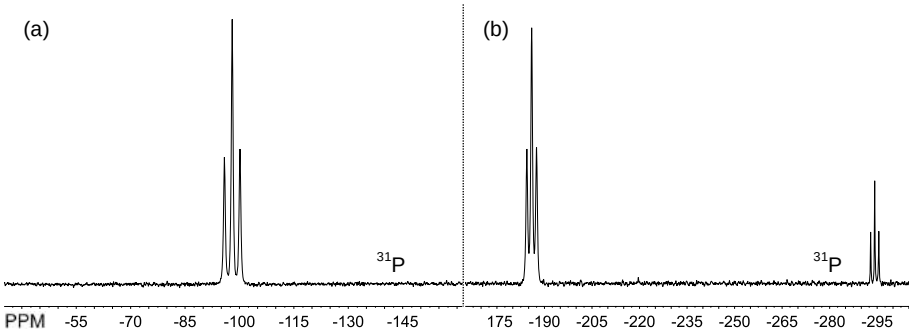

Figure R-18. (a) ^{31}P NMR spectrum of **2**: δ = –98.0 ppm. (b) ^{31}P NMR spectrum after 3 h vacuum: $LiPH_2(BEt_3)$ (δ = –186.0 ppm); $LiPH_2$ (δ = –294.2 ppm).

Un premier intermédiaire, également caractérisé par un triplet dans le spectre RMN ^{31}P à –186 ppm, a été attribué à $LiPH_2(BEt_3)$, suivi de l'apparition du signal à –294 ppm pour $LiPH_2$ libre.[50b] Le composé **2** a été donc maintenu en solution pour utilisation conséquente. Le spectre ^{1}H et ^{31}P enregistré à partir d'une solution concentrée (Figure R-18a) a confirmé que le composé **2** était $LiPH_2(BEt_3)_2$. Il est intéressant de noter que ce composé était stable en solution à température ambiante pendant au moins plusieurs mois sous atmosphère inerte, et était même stable à l'air sec (mais sensible à l'eau), contrairement à la pauvre stabilité observée de $LiPH_2$(DME), qui se dégrade en quelques jours à température ambiante.[53]

Les cristaux jaunes de Li_3P_7, obtenus avec un rendement isolé de 23 % par rapport aux atomes de P de départ, ont été analysés par RMN ^{31}P (singulet large à –117 ppm à 60 °C).[14] Afin d'obtenir des cristaux de qualité suffisante pour l'analyse par DRX, un équivalent de TMEDA par rapport à $LiPH_2(BEt_3)_2$ a été ajouté, ce qui a mené à l'obtention de cristaux de $Li_3P_7(TMEDA)_3$ (Figure R-19).[53]

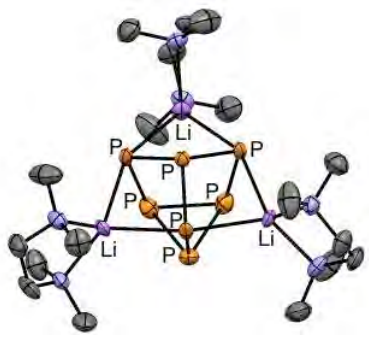

Figure R-19. Structure cristal du $Li_3P_7(TMEDA)_3$.

Après élimination des cristaux de Li_3P_7 et du précipité rouge, on a utilisé la solution pure résultante de phosphure stable pour sonder la fonctionnalisation de la liaison P–H, ainsi que le transfert du PH_2. Des exemples représentatifs sont présentés ci-dessous (Schéma R-12). Des réactions avec des sources de H^+, y compris MeOH, EtOH, *n*-$BuNH_2$, et H_2O, conduisaient à la formation quantitative de PH_3. La réaction de **2** avec des sources de D^+ donne un mélange statistique de PH_3, PH_2D et PHD_2. La réaction de P_4 avec $LiBEt_3D$ suivie par D_2O résulte exclusivement dans la formation de PD_3. De façon intéressante, **2** montre la sélectivité pour les amines primaires et les alcools, aucune formation de PH_3 avec des amines secondaires (*i*-Pr_2NH), ni avec des alcools secondaires ou tertiaires (*i*-PrOH ou *t*-BuOH), n'étant observée. De même, les réactions tentées avec des électrophiles secondaires et tertiaires, tels que le bromure de cyclohexyl et le chlorure de *t*-butyl, n'ont montré aucune réaction. La réaction de **2** avec de triméthylchlorosilane (TMSCl) a donné un rendement de RMN de 70% d'un mélange 1,7: 1 de $HP(TMS)_2$: $H_2P(TMS)$. A partir de ce mélange, on obtenait un rendement isolé pour $HP(TMS)_2$ de 40 % par distillation sous vide. La réaction de **2** avec iodure de méthyl a donné un rendement de 88 % de $HPMe_2(BEt_3)$ par RMN, mais ce produit ne pouvait pas être isolé.

Alors que les travaux antérieurs de Grützmacher *et al.* avec $NaPH_2(DME)_x(NaOtBu)$ ont montré la formation de $NaP(Me_3Bz)_2(DME)$ par réaction avec le chlorure de mésitoyle,[50a,53] la réaction de **2** avec les électrophiles chlorures de benzoyle et mésitoyle ont donné lieu à la formation de $P(Bz)_3$ et P(2,4,6-triméthylbenzoyle)$_3$ (quantitatifs et 85% par ^{31}P RMN, respectivement).

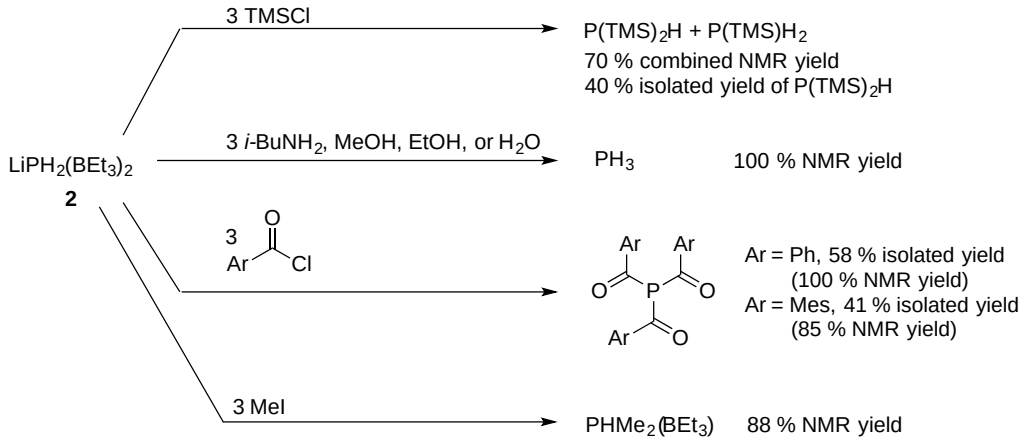

Schéma R-12. Réactivité de **2** avec les electrophiles.

Une caractéristique très intéressante de $LiPH_2(BEt_3)_2$ est le déplacement de BEt_3, dont la labilité a été observée lors d'un séchage étendu. Ceci pourrait être très précieux dans le contexte des polymères phosphine-borane. En effet, les polymères avec des liaisons entre les éléments des groupes 13 et 15 sont particulièrement intéressants car ils sont isoélectroniques avec leurs analogues de carbone mais ils peuvent posséder des propriétés physiques et chimiques différentes en raison de leur différence d'électronégativité.[54] Les méthodes les plus courantes pour la synthèse de P–B commencent avec des précurseurs de type PR_3BR_3 et nécessitent des catalyseurs métalliques. Ils entraînent souvent des produits de faible poids moléculaire et/ou polydispersés.[55] Une nouvelle approche de Marquadt *et al.* utilisait la décomposition thermique des précurseurs de type PR_2BH_2.[56] Le remplacement du produit d'addition BEt_3 de **2** par BH_3 pourrait donc constituer une nouvelle entrée dans cette chimie. En effet, la réaction avec un léger excès de BH_3, qui est un acide de Lewis plus fort que BEt_3, a conduit au déplacement quantitatif de BEt_3 de **2** et à la formation du composé **3** (Schéma R-13).

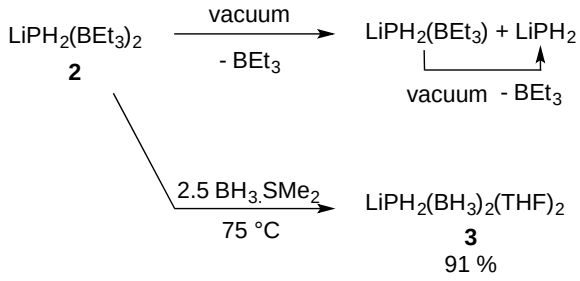

Scheme R-13. Labilité de BEt_3 dans **2** et la synthèse de **3**.

Ce nouveau composé est caractérisé en RMN $^{31}P\{IH\}$ par un septuplet à –108 ppm qui montre un couplage avec deux atomes ^{11}B ($^1J_{P\text{-}B}$ = 52 Hz) (Figure R-22a). Le spectre ^{11}B montre le doublet des quadruplets attendu à –40 ppm ($^1J_{P\text{-}B}$ = 52 Hz, $^1J_{B\text{-}H}$ = 94 Hz) (Figure R-20b), et le spectre ^1H montre un doublet de septuplets pour les deux protons équivalents de PH_2 à 2,7 ppm ($^1J_{P\text{-}H}$ = 288 Hz, $^3J_{H\text{-}H}$ = 7 Hz). Ce dernier spectre indiquait également qu'il y avait deux molécules de THF liées à l'atome de Li, et montrait quatre larges résonances pour les groupements BH_3 (–0,1, 0,2, 0,5 et 0,8 ppm). Lors du découplage avec ^{11}B, ces quatre résonances s'affaissent dans un doublet de triplets dû au couplage avec le phosphore et les protons ($^2J_{P\text{-}H}$ = 12 Hz, $^3J_{H\text{-}H}$ = 7 Hz), ce qui indique que les six atomes d'hydrogène dans le fragment BH_3 sont équivalents.[57] Contrairement au composé **2**, le composé **3** peut être isolé sous la forme

d'un poudre blanc avec un rendement de 91% sans perte des fragments de borane. Le composé **3** peut être vu comme résultat de l'addition formelle de $LiBH_4$ sur P_4. La réalisation de la réaction en deux étapes, à travers le composé **2**, a permis de contourner l'arrêt à l'étape de HP_4Li.

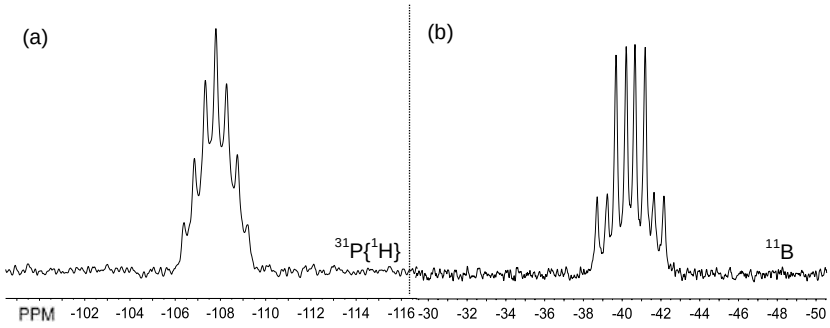

Figure R-20. Spectres RMN du **3** en (a) $^{31}P\{^1H\}$ et (b) ^{11}B.

En conclusion, on a développé ici le premier transfert d'hydrure à P_4 en utilisant les hydrures du groupe principal, permettant la génération contrôlée de liaisons P–H. En utilisant MBH_4, avec une amine comme solvant, la réaction s'arrêtait après la formation d'une seule liaison P–H à partir de P_4, malgré l'utilisation d'un excès de source d'hydrure. Avec $LiBEt_3H$, l'espèce stabilisée **2**, $LiPH_2(BEt_3)_2$, est formée avec un bon rendement par une réaction redox. Plus important encore, les résultats préliminaires sur la réactivité de ce dernier composé montraient sa versatilité pour servir comme source de PH_2^- ou P_3^-, ainsi que la production de $LiPH_2(BH_3)_2$, **3**, via le remplacement du borane.

Bibliographie

[1] Shin, S.; Song, I.; Um, S. *Nanomaterials* **2015**, *5* (3), 1351–1365.

[2] (a) Alivisatos, A. P. *J. Phys. Chem.* **1996**, *100* (95), 13226–13239. (b) Henglein, A. *Chem. Rev.* **1989**, *89* (8), 1861–1873. (c) Klabunde, K. J.; Sorensen, C. M.; Stoeva, S. I.; Prasad, B. L. V; Smetana, A. B.; Lin, X. M. *Met. Nanoclusters Catal. Mater. Sci. Issue Size Control* **2008**, *2*, 233–249.

[3] Prasad, B. L. V; Stoeva, S. I.; Sorensen, C. M.; Klabunde, K. J. *Chem. Mater.* **2003**, *15* (4), 935–942.

[4] Karaagac, O.; Kockar, H. *J. Supercond. Nov. Magn.* **2012**, *25* (8), 2777–2781.

[5] Carenco, S. Doctoral Dissertation, l'Université Pierre et Marie Curie, **2011**.

[6] (a) Kettemann, F.; Wuithschick, M.; Caputo, G.; Kraehnert, R.; Pinna, N.; Rademann, K.; Polte, J. *CrystEngComm* **2015**, *17* (8), 1865–1870. (b) Guan, Z.; Luo, W.; Xu, Y.; Tao, Q.; Wen, X.; Zou, Z. *ACS Appl. Mater. Interfaces* **2016**, *8* (8), 5432–5438.

[7] (a) Cuenya, B. R. *Acc. Chem. Res.* **2013**, *46* (8), 1682–1691. (b) Cuenya, B. R. *Thin Solid Films* **2010**, *518* (12), 3127–3150. (c) Astruc, D. *Transition-Metal Nanoparticles in Catalysis : From Historical Background to the State-of-the Art*; 2008.

[8] (a) Yan, J.-M.; Zhang, X.-B.; Han, S.; Shioyama, H.; Xu, Q. *Inorg. Chem.* **2009**, *48*, 7389–7393. (b) Saxena, A.; Kumar, A.; Mozumdar, S. *Appl. Catal. A* **2007**, *317*, 210– 215.

[9] (a) Rinaldi, A.; Tessonnier, J.-P.; Schuster, M. E.; Blume, R.; Girgsdies, F.; Zhang, Q.; Jacob, T.; Abd Hamid, S. B.; Su, D. S.; Schlögl, R. *Angew. Chem.* **2011**, *123*, 3371–3375.; *Angew. Chem. Int. Ed.* **2011**, *50*, 3313– 3317. (b) Zhu, L.-P.; Liao, G.-H.; Zhang, W.-D.; Yang, Y.; Wang, L.-L.; Xie, H.-Y. *Eur. J. Inorg. Chem.* **2010**, 1283–1288. (c) Sarac, M. F.; Wilson, R. M.; Johnston-Peck, A. C.; Wang, J.; Pearce, R.; Klein, K. L.; Melechko, A. V.; Tracy, J. B. *ACS Appl. Mater. Interfaces* **2011**, *3*, 936–940. (d) Carenco, S.; Le Goff, X. F.; Shi, J.; Roiban, L.; Ersen, O.; Boissière, C.; Sanchez, C.; Mézailles, N. *Chem. Mater.* **2011**, *23*, 2270–2277. (e) Carenco, S.; Surcin, C.; Morcrette, M.; Larcher, D.; Mézailles, N.; Boissière, C.; Sanchez, C. *Chem. Mater.* **2012**, *24*, 688–697.

[10] (a) Wang, H.; Jiao, X.; Chen, D. *J. Phys. Chem. C* **2008**, *112*, 18793–18797. (b) LaGrow, A. P.; Ingham, B.; Cheong, S.; Williams, G. V. M.; Dotzler, C.; Toney, M. F.; Jefferson, D. A.; Corbos, E. C.; Bishop, P. T.; Cookson, J.; Tilley, R. D. *J. Am. Chem. Soc.* **2012**, *134*, 855–858. (c) Han, M.; Liu, Q.; He, J.; Song, Y.; Xu, Z.; Zhu, J. M. *Adv. Mater.* **2007**, *19*, 1096–1100. (d) Jeon, Y. T.; Moon, J. Y.; Lee, G. H.; Park, J.; Chang, Y. *J. Phys. Chem. B* **2006**, *110* (3), 1187–1191.

[11] (a) Callejas, J. F.; Read, C. G.; Woske, C. W.; Lewis, N. S.; Schaak, R. E. *Chem. Mater.* **2016**, *28* (17), 6017–6044. (b) Carenco, S.; Portehault, D.; Boissière, C.; Mézailles, N.; Sanchez, C. *Chem. Rev.* **2013**, *113* (10), 7981–8065. (c) Eric J. Popczun, James R. McKone, Carlos G. Read, Adam J. Biacchi, Alex M. Wiltrout, Nathan S. Lewis, and Raymond E. Schaak. *J. Am. Chem. Soc.* **2013** *135* (25), 9267–9270.

[12] Sharon, M.; Tamizhmani, G. *J. Mater. Sci.* **1986**, *21* (6), 2193–2201.

[13] Callejas, J. F.; Read, C. G.; Woske, C. W.; Lewis, N. S.; Schaak, R. E. *Chem. Mater.* **2016**, *28* (17), 6017–6044.

[14] (a) Carenco, S.; Leyva-Pérez, A.; Concepción, P.; Boissière, C.; Mézailles, N.; Sanchez, C.; Corma, A. *Nano Today* **2012**, *7* (1), 21–28. (b) Chen, Y.; Li, C.; Zhou, J.; Zhang, S.; Rao, D.; He, S.; Wei, M.; Evans, D. G.; Duan, X. *ACS Catal.* **2015**, *5* (10), 5756–5765.

[15] Trumbo, P.; Yates, A. A.; Schlicker, S.; Poos, M. *Journal of the American Dietetic Association*. 2001, 294–301.

[16] (a) Carenco, S., Labouille, S., Bouchonnet, S., Boissière, C., Le Goff, X.-F., Sanchez, C., Mézailles, N. *Chem. Eur. J.*, **2012**, *18*(44), 14165–73. (b) Hou, Y.; Kondoh, H.; Ohta, T.; Gao, S. *Appl. Surf. Sci.* **2005**, *241* (1–2), 218–222.

[17] (a) Willis, A. L.; Chen, Z.; He, J.; Zhu, Y.; Turro, N. J.; O'Brien, S. *J. Nanomater.* **2007**, *14858*, 1–7. (b) Sun, S.; Zeng, H. *J. Am. Chem. Soc.* **2002**, No. 31, 8204–8205. (c) Nene, A. G.; Takahashi, M.; Somani, P. R. **2016**, 20–28.

[18] He, M.; Protesescu, L.; Caputo, R.; Krumeich, F.; Kovalenko. M. *Chem. Mater.* **2015**, *27*, 635–647.

[19] Carenco, S.; Boissiere, C.; Nicole, L.; Sanchez, C.; le Floch, P.; Mézailles, N. *Chem. Mater*. **2010**, *22*(4), 1340–1349.

[20] Mott, D.; Galkowski, J.; Wang, L.; Luo, J.; Zhong, C. J. *Langmuir* **2007**, *23* (10), 5740–5745.

[21] Mourdikoudis, S.; Liz-marzan, L. M. *Chem. Mater.* **2013**, *25* (9), 1465–1476.

[22] (a) Lipschutz, M. I.; Tilley, T. D. *Chem. Commun. (Camb).* **2012**, *48* (57), 7146–7148. (b) Hope, H.; Olmstead, M. M.; Murray, B. D.; Power, P. P. *J. Am. Chem. Soc.* **1985**, *107* (3), 712–713. (c) Faust, M.; Bryan, A. M.; Mansikkamäki, A.; Vasko, P.; Olmstead, M. M.; Tuononen, H. M.; Grandjean, F.; Long, G. J.; Power, P. P. *Angew. Chemie - Int. Ed.* **2015**, *54* (44), 12914–12917.

[23] (a) Henglein, A. *J. Phys. Chem.* **1982**, *86*(13), 2291−2293. (b) Rossetti, R.; Hull, R.; Gibson, J. M.; Brus, L. E. *J. Chem. Phys.* **1985**, *82*(1), 552−559. (c) Murray, C. B.; Norris, D. J.; Bawendi, M. G. *J. Am. Chem. Soc.* **1993**, *115*(19), 8706−8715. (d) Park, J.; Joo, J.; Kwon, S. G.; Jang, Y.; Hyeon, T. *Angew. Chem., Int. Ed.* **2007**, *46*(25), 4630−4660. (e) Van Embden, J.; Chesman, A. S. R.; Jasieniak, J. J. *Chem. Mater.* **2015**, *27* (7), 2246–2285.

[24] Kelsen, V.; Wendt, B.; Werkmeister, S.; Junge, K.; Beller, M.; Chaudret, B. *Chem. Commun.* **2013**, *49* (33), 3416–3418.

[25] Andersen, R. a; Faegri, K.; Green, J. C.; Haaland, A.; Lappert, M. F.; Leung, W. P.; Rypdal, K. *Inorg. Chem.* **1988**, *27* (10), 1782–1786.

[26] (a) Wu, L.; Li, Q.; Wu, C. H.; Zhu, H.; Mendoza-Garcia, A.; Shen, B.; Guo, J.; Sun, S. *J. Am. Chem. Soc.* **2015**, *137* (22), 7071–7074. (b) Michalek, F.; Lagunas, A.; Jimeno, C.; Pericas, M. A. *J. Mater. Chem.* **2008**, *18* (39), 4692–4697. (c) Yang, H. T.; Su, Y. K.; Shen, C. M.; Yang, T. Z.; Gao, H. J. *Surf. Interface Anal.* **2004**, *36* (2), 155–160. (d) Schällibaum, J.; Dalla Torre, F. H.; Caseri, W. R.; Löffler, J. F. *Nanoscale* **2009**, *1* (3), 374–381. (e) Hess, P. H.; Parker, P. H. *J. Appl. Polym. Sci.* **1966**, *10*, 1915–1927. (f) Zacharaki, E.; Kalyva, M.; Fjellvåg, H.; Sjåstad, A. O. *Chem. Cent. J.* **2016**, *10*, 10–11.

[27] (a) Jang, H. D.; Hwang, D. W.; Kim, D. P.; Kim, H. C.; Lee, B. Y.; Jeong, I. B. *Mater. Res. Bull.* **2004**, *39* (1), 63–70. (b) Liang, X.; Zhao, L. *RSC Adv.* **2012**, *2* (13), 5485–5487.

[28] Buslov, I.; Song, F.; Hu, X. *Angew. Chemie Int. Ed.* **2016**, *55*, 12295–12299.

[29] Carenco, S.; Leyva-Pérez, A.; Concepción, P.; Boissière, C.; Mézailles, N.; Sanchez, C.; Corma, A. *Nano Today* **2012**, *7* (1), 21–28.

[30] Yang, Z.; Ho, B. M.; Lukoyanov, D.; Yang, Z.; Dean, D. R.; Seefeldt, L. C. *Chem. Rev.* **2014**, *114* (8), 4041–4062.
[31] Yuki, M.; Tanaka, H.; Sasaki, K.; Miyake, Y.; Yoshizawa, K.; Nishibayashi, Y. *Nat. Commun.* **2012**, *3:1254*, 1–6.
[32] Henkes, A. E.; Vasquez, Y.; Schaak, R. E. *J. Am. Chem. Soc.* **2007**, *129* (7), 1896–1897.
[33] Chiang, R. K.; Chiang, R. T. *Inorg. Chem.* **2007**, *46* (2), 369–371.
[34] Wang, R.; Smith, K. J. *Appl. Catal. A Gen.* **2009**, *361* (1–2), 18–25.
[35] Feng, L.; Vrubel, H.; Bensimon, M.; Hu, X. *Phys. Chem. Chem. Phys.* **2014**, *16* (13), 5917–5921.
[36] Lü, B.; Bai, Y. J.; Feng, X.; Zhao, Y. R.; Yang, J.; Chi, J. R. *J. Cryst. Growth* **2004**, *260* (1–2), 115–117.
[37] Callejas, J. F.; Read, C. G.; Woske, C. W.; Lewis, N. S.; Schaak, R. E. *Chem. Mater.* **2016**, *28*(17), 6017–6044.
[38] Qian, X. F.; Zhang, X. M.; Wang, C.; Wang, W. Z.; Qian, Y. T. *Mater. Res. Bull.* **1998**, *33* (5), 669–672.
[39] Su, H. L.; Xie, Y.; Li, B.; Liu, X. M.; Qian, Y. T. *Solid State Ionics* **1999**, *122*, 157–160.
[40] Xie, Y.; Su, H. L.; Qian, X. F.; Liu, X. M.; Qian, Y. T. *J. Solid State Chem.* **2000**, *149*, 88–91.
[41] (a) Carenco, S.; Resa, I.; Le Goff, X.; Le Floch, P.; Mézailles, N. *Chem. Commun.* **2008**, No. 22, 2568–2570. (b) Carenco, S.; Hu, Y.; Florea, I.; Ersen, O.; Boissière, C.; Mézailles, N.; Sanchez, C. *Chem. Mater.* **2012**, *24* (21), 4134–4145.
[42] Cotton, F. A.; Wilkinson, G. *Advanced Inorganic Chemistry, Fifth Ed.*; John Wiley & Sons, New York, 1988, 386–386.
[43] (a) Dorfman, Y. A.; Aleshkova, M. M.; Polimbetova, G. S.; Levina, L. V.; Petrova, T. V.; Abdreimova, R. R.; Doroshkevich, D. M. *Russ. Chem. Rev. (Engl. Transl.)* **1993**, *62*, 877–896. (b) Peruzzini, M.; de los Rios, I. ; Romerosa, A.; Vizza, F. *Eur. J. Inorg. Chem.* 2001, 593–608. (c) Peruzzini, M.; Abdreimova, R. R.; Budnikova, Y.; Romerosa, A.; Scherer, O. J.; Sitzmann, H. *J. Organomet. Chem.* **2004**, *689*, 4319–433. (d) Cossairt, B. M.; Piro, B. M.; Cummins, C. C. *Chem. Rev*. **2010**, *110*, 4164–4177. (e) Scheer, M.; Balaźs, G.; Seitz, A. *Chem. Rev*. **2010**, *110*, 4236–4256. (f) Caporali, M.; Gonsalvi, L.; Rossin, A.; Peruzzini, M. *Chem. Rev.* **2010**, *110*, 4178–4235. (g) Armstrong, K. M.; Kilian, P. *Eur. J. Inorg. Chem.* **2011**, 2138–2147. (h) Caporali, M.; Barbaro, P.; Gonsalvi, L.; Ienco, A.; Yakhvarov, D.; Peruzzini, M. *Angew. Chem. Int. Ed. Engl.* **2008**, *47*, 3766–3768.
[44] Rauhut, M. M.; Semsel, A. M. *J. Org. Chem.*, **1963**, *28*, 471–473.
[45] (a) Borger, J. E.; Ehlers, A. W.; Lutz, M.; Slootweg, J. C.; Lammertsma, K. *Angew. Chem. Int. Ed.*, **2014**, *53*, 12836–12839. (b) Borger, J. E.; Ehlers, A. W.; Lutz, M.; Slootweg, J. C.; Lammertsma, K. *Angew. Chem. Int. Ed.*, **2016**, *55*, 2016, 613–617.
[46] (a) Cossairt, B. M.; Cummins, C. C. *New J. Chem.*, **2010**, *34*, 1533–1536. (b) Heinl, S.; Scheer, M. *Chem. Sci.*, **2014**, *5*, 3221–3225.
[47] (a) Peruzzini, M.; Ramirez, J. A.; Vizza, F. *Angew. Chemie Int. Ed.*, **1998**, *37*, 2255–2257. (b) Barbaro, P.; Peruzzini, M.; Ramirez, J. A.; Vizza, F. *Organometallics*, **1999**, *18*, 4237–4240. (c) Barbaro, P.; Ienco, A.; Mealli, C.; Peruzzini, M.; Scherer, O. J.; Schmitt, G.; Vizza, F.; Wolmershäuser,

G. *Chem. Eur. J.*, **2003**, *9*, 5195–5210. (d) Barbaro, P.; Bazzicalupi, C.; Peruzzini, M.; Seniori Costantini, S.; Stoppioni, P. *Angew. Chem. Int. Ed.*, **2012**, *51*, 8628–8631.

[48] Joannis, A. *Compt. Rend.* **1894**, *119*, 557–559.

[49] Par exemple: (a) Huber, A.; Kuschel, A.; Ott, T.; Santiso-Quinones, G.; Stein, D.; Bräuer, J.; Kissner, R.; Krumeich, F.; Schönberg, H.; Levalois-Grützmacher, J.; Grützmacher, H. *Angew. Chem. Int. Ed.*, **2012**, *51*, 4648–4652. (b) Mösch-Zanetti, N. C.; Schrock, R. R.; Davis, W. M.; Wanninger, K.; Seidel, S. W.; O'Donoghue, M. B. *J. Am. Chem. Soc.* **1997**, *119*, 11037–11048.

[50] (a) Podewitz, M.; van Beek, J. D.; Wörle, M.; Ott, T.; Stein, D.; Rüegger, H.; Meier, B. H.; Reiher, M.; Grützmacher, H. *Angew. Chem. Int. Ed.* **2010**, *49*, 7465–7469. (b) Schäfer, V. H.; Fritz, G.; Hölderich, W. *Z. Anorg. Allg. Chem.* **1977**, *428*, 222–224. (c) Brandsma, L.; van Doorn, J. A.; de Lang, R.-J.; Gusarovac, N. K.; Trofimov, B. A. *Mendeleev Commun.* **1995**, *5*, 14–15. (d) Jacobs, H.; Hassiepen, K. M. *Z. Anorg. Allg. Chem.* **1985**, *531*, 108–118.

[51] Expériences avec $LiBH_4$ faites par S. Dreyfuss.

[52] (a) Baudler, M.; Adamek, C.; Opelia, S.; Budzikiewicz, H.; Ouzounis, D. *Angew. Chem. Int. Ed. Engl.* **1988**, *27*, 1059–1061. (b) Baudler, M.; Wingert, B.; *Z. Anorg. Allg. Chem.***1992**, *611*, 50–55.

[53] Grützmacher, H.; Ott, T.; Dietliker, K. (Basf Se), WO2011003772 A1, 2011.

[54] Par exemple: (a) Jäkle, F. *Chem. Rev.* **2010**, *110*, 3985–4022. (b) Bosdet, M. J. D.; Piers, W. E.; Sorensen, T. S.; Parvez, M. *Angew. Chem. Int. Ed. Engl.* **2007**, *46*, 4940–4943. (c) Staubitz, A.; Robertson, A. P. M.; Sloan, M. E.; Manners, I. *Chem. Rev.* **2010**, *110*, 4023–4078.

[55] Schäfer, A.; Jurca, T.; Turner, J.; Vance, J. R.; Lee, K.; Du, V. A.; Haddow, M. F.; Whittell, G. R.; Manners, I. *Angew. Chem. Int. Ed.* **2015**, *54*, 4836–4841.

[56] Marquardt, C.; Jurca, T.; Schwan, K.; Stauber, A.; Virovets, A. V.; Whittell, G. R.; Manners, I.; Scheer, M. *Angew. Chem. Int. Ed.* **2015**, *54*, 13782–13786.

[57] Consiglio, G. B.; Queval, P.; Harrison-Marchand, A.; Mordini, A.; Lohier, J.-F.; Delacroix, O.; Gaumont, A.-C.; Gérard, H.; Maddaluno, J.; Oulyadi, H. *J. Am. Chem. Soc.* **2011**, *133*, 6472–6480.

How dull it is to pause, to make an end,
To rust unburnished, not to shine in use!
As though to breathe were life.
Alfred Lord Tennyson

The Functionalization of White Phosphorus towards Metal Phosphide Nanoparticles and Organophosphines

This manuscript presents an original synthesis of nickel(0) nanoparticles. The use of a nickel(II) dioleylamide precursor results in a versatile, robust, water-free method for the production of size-tunable particles between 4 – 11 nm in diameter. This method was extended to form small iron(0) and cobalt(0) nanoparticles. These particles were examined for catalytic activity, including the hydrosilylation of a terminal alkene, the selective hydrogenation of phenylacetylene to styrene, and the substoichiometric reduction of nitrogen to tris(trimethylsilyl)amine. White phosphorus (P_4) was stoichiometrically reacted with the metal(0) nanoparticles to form the corresponding metal phosphide nanoparticles.

White phosphorus was alternatively functionalized using superhydride ($LiBEt_3H$) to form a borane-stabilized phosphanide species, $LiPH_2(BEt_3)_2$. This species was used to synthesize various phosphines, including phosphine, tris(trimethylsilyl)phosphine, and triaroylphosphines. The labile triethylborane adducts were replaced by BH_3, resulting in the formation of $LiPH_2(BH_3)_2$, which may have applications in the formation of P–B polymers.

Key Words: Nanoparticles, nickel, organophosphines, white phosphorus

Fonctionnalisation du phosphore blanc pour la synthèse de nanoparticules de phosphures métalliques et d'organophosphines

Ce manuscrit présente une synthèse originale de nanoparticules de nickel(0). L'utilisation d'un précurseur de dioléylamide de nickel(II) conduit à un procédé versatile, robuste, et sans eau pour la production de particules ajustables en taille entre 4 et 11 nm de diamètre. Cette méthode a été étendue pour former de petites nanoparticules de fer(0) et de cobalt(0). Ces particules ont été examinées en ce qui concerne l'activité catalytique, y compris l'hydrosilylation d'un alcène terminal, l'hydrogénation sélective du phénylacétylène en styrène, et la réduction sous-stoechiométrique de l'azote en tris(triméthylsilyl)amine. Le phosphore blanc (P_4) a été réagi stoechiométriquement avec les nanoparticules métalliques pour former les nanoparticules de phosphure métallique correspondantes.

Le phosphore blanc a été alternativement fonctionnalisé en utilisant un superhydrure (LiBEt3H) pour former une espèce phosphanide stabilisée au borane, $LiPH_2(BEt_3)_2$. Cette espèce a été utilisée pour synthétiser diverses phosphines, y compris la phosphine, la tris(triméthylsilyl)phosphine, et les triaroylphosphines. Les adduits labiles de triéthylborane ont été remplacés par BH_3, ce qui a donné lieu à la formation de $LiPH_2(BH_3)_2$, qui peut avoir des applications dans la formation de polymères P–B.

Mots clés : Nanoparticules, nickel, organophosphines, phosphore blanc